Western&Graduate&PostdoctoralStudies

Electronic Thesis and Dissertation Repository

8-16-2021 3:00 PM

Mechanical Design and Development of a Compliant 5-DOF Manipulator Using Magneto-Rheological Actuators

Sergey Pisetskiy, *The University of Western Ontario*

Supervisor: Kermani, Mehrdad R., *The University of Western Ontario*
A thesis submitted in partial fulfillment of the requirements for the Doctor of Philosophy degree in Electrical and Computer Engineering
© Sergey Pisetskiy 2021

Follow this and additional works at: https://ir.lib.uwo.ca/etd

Part of the Robotics Commons

Recommended Citation

Abstract

Compliance in robotic systems became a very important and desirable characteristic in recent years. Existing compliant actuation approaches have either limited performance or significant mechanical and control complexity. Keeping high performance while maintaining the necessary level of compliance at low cost and minimum complexity is a challenging goal that should be achieved to boost the propagation of human-safe robots and systems capable to perform delicate tasks and operate in an unknown environment.

This study presents a novel, five degrees-of-freedom compliant manipulator. The compliancy of the manipulator is achieved using antagonistically working pairs of magneto-rheological (MR) clutches in each joint of the robot. The drive train of the manipulator consists of a single electrical motor located at the base of the robot and 5 pairs of antagonistic MR clutches. Multiple design concepts for the development of the manipulator's drive train are considered and the advantages and disadvantages of each concept were studied. The most efficient drive train concept is selected and further developed.

An improved design, complete analysis, and prototype development of a high torque-to-mass ratio magneto-rheological clutch are performed. The proposed MR clutches are intended as the main actuation mechanism for each joint of the robotic manipulator. Multiple steps to increase the toque-to-mass ratio of the clutch are evaluated and taken in the final design.

The proposed design of the MR clutch feature embedded Hall sensors for the indirect torque measurement. A new arrangement of the sensors with no effect on the magnetic reluctance of the clutch is presented. The magnetization of the MR clutch is improved by implementing a new hybrid design that features a combination of an electromagnetic coil and a permanent magnet for an improved torque-to-mass ratio. The gap size reduction in the hybrid MR clutch is introduced and its influence on maximum torque and dynamic range investigated. Finally, the design for a pair of MR clutches with a shared magnetic core for antagonistic actuation of the robot joint is presented and experimentally validated.

The details of each approach are discussed and the results of the finite element analysis are used to highlight the required engineering steps and to demonstrate the improvements achieved. Using the proposed design, several prototypes of the MR clutch with various torque capacities ranging from 15 N·m to 200 N·m are developed, assembled, and tested. The experimental results demonstrate the performance of the proposed design and validate the accuracy of the analysis used for the development.

The mathematical modeling and simulation of the transmission system for the robot is performed. Additionally, a positional joint-level control is developed and tested on the 1st and 2nd joints for the manipulator.

The behavior of implemented magneto-rheological antagonistic actuation approach is studied in terms of inherent passivity and velocity boundedness. Theoretical analysis of the subject is presented and experimentally validated through testing the performance of the antagonistic MR actuator in the 2nd joint of the 5-DOF robot. It is shown, that the MR actuated system is intrinsically passive but preserves excellent dynamics characteristics as long as the joint velocity remains within the necessary limits.

A novel design concept of a miniaturized MR clutch for prospective end-effector is developed. The design uses a set of spur gears as a means to control the torque. The details of the mechanical design of the spur gear MR clutch are discussed. The distribution of the magnetic

flux inside the MR clutch is studied using finite element analysis in COMSOL Multiphysics software. Experimental results using an assembled prototype validate the new concept feasibility. To clearly show the performance of the proposed design, the torque capacity of the novel MR clutch obtained experimentally is compared with that of a simulated disk-type MR clutch of a similar size.

Summary for Lay Audience

This study presents a novel five degrees-of-freedom compliant manipulator. The compliancy of the manipulator is achieved using antagonistically working pairs of magneto-rheological (MR) clutches in each joint of the robot. The drive train of the manipulator consists of a single electrical motor located at the base of the robot and 5 pairs of antagonistic MR clutches. Multiple design concepts for the development of the manipulator's drive train are considered and the advantages and disadvantages of each concept were studied. The most efficient drive train concept is selected and further developed.

An improved design, complete analysis, and prototype development of a high torque-to-mass ratio magneto-rheological clutch are performed. The proposed MR clutches are intended as the main actuation mechanism for each joint of the robotic manipulator. Multiple steps to increase the toque-to-mass ratio of the clutch are evaluated and taken in the final design.

The mathematical modeling of the transmission for the robot is performed. Positional joint-level control is developed and tested on the 1st and 2nd joints for the manipulator.

Co-Authorship Statement

This thesis is written by Sergey Pisetskiy, and reviewed and edited by Dr. Mehrdad R. Kermani.

Parts of this material were submitted and published in peer-reviewed conference proceedings and journals.

I would also like to acknowledge the contribution of Ziqi Yang in development and testing the joint control board, as well as his help with tests and experiments with the 5-DOF robot.

Acknowlegements

I would like to express my sincere appreciation and gratitude to my supervisor Dr. Mehrdad Kermani, for his guidance, encouragement, and support.

I am grateful to my colleagues and friends at the Western University Nikita Kuchinskiy, Mahyar Abdeetedal, Ziqi Yang, Masoud Moghani, Shuwei Qiu, Stefan Glibetic, Dan Sweiger and many others who have helped me during my Ph.D. journey.

To the memory of dear friend David L. Cade

Contents

List of Figures

List of Tables

List of Appendices

Chapter 1

Introduction

1.1 Motivation

In recent years, there has been an ever-increasing need for the development of human-friendly robotic systems. Close collaborations and direct interactions between humans and robots provide outstanding opportunities for collaborative manufacturing, interactive training, rehabilitation, and many other industrial and domestic applications. These applications entail new requirements to ensure a balance between the safety of the humans and desired performance of the robots.

Among all sources of danger, the risk of injury caused by a collision between a human and a robot is one of the biggest. The direct interactions between the human and robot makes collision unavoidable, and mitigating impacts from such collisions is one of the top priorities for research and development.

To develop a human-friendly system, the safety of physical human-robot interaction should be addressed at the earliest stage of development. An implementation of a proper force/torque control into the robotic system is required in some manner. This control gives the robot a sense of touch and ability to react to the external forces and torques as required. The implementation of the compliant actuators significantly improves the ability of the robot to execute tasks safely even with a malfunctioning control system. Possible solutions for such actuators include variable stiffness transmission approach, elastic actuation, Magneto-Rheological brakes and clutches, and distributed macro–mini actuation, to name a few.

The goal of this research is to develop and test a prototype of a fully compliant manipulator with improved performance and robustness. The prototype should be suitable for use in engineering research and able to demonstrate the advantages of the manipulator in performing tasks that require precise torque and position control along with full compliance of all its joints.

The Distributed Active Semi-Active (DASA) technology based on magneto-rheological (MR) technology is chosen as the main approach to achieve the required compliance of the robot. The basic concept of the DASA approach is in the separation of active and semi-active components. The active component (e.g. motor) can provide actuation for one or several semi-active components (MR clutches) located at the joints of the robot. A pair of MR clutches working in opposite directions can be used for antagonistic actuation of the joint. The semi-active clutches can be mechanically connected with the active component using different means

1

of transmission such as belt, shaft, gear, etc. In this case, the location of the active component can be chosen based on the required weight and inertia distribution in the system. The configuration of the robot with only one active component driving all semi-active compliant components in the system opens up the possibility of addressing safety requirements without increasing the cost and with no influence on the performance.

1.2   Compliant actuation

A safe interaction between humans and robots often requires both force/torque control and compliant behavior of the machine. Researches have made great progress in developing technologies for compliant robotics in recent decades.

In the case of physical interaction with a human body, the forces should not exceed certain safe limits. Implementation of the mechanical force/torque limiters ensures overload force protection. Such limiters based on nonlinear springs are described in [1, 2, 3].

Another approach for a human-friendly robotic system is the light-weight paradigm. One of the first robots developed under this paradigm is the Whole-Arm Manipulator (WAM) [4]. The WAM utilizes steel tendons to transmit the motion from the actuators located in the base of the robot to the links located above.

A similar cable -driven approach is used in the low inertia 2-DOF manipulator TDM (Tendon-Driven Manipulator). It utilizes a Projected PID algorithm to control cable-driven actuation of the light aluminum link [5]. In this case, a set of MR clutches was used to pull the tendons of the robot.

One of the most notable systems in the category of light-weight robots is the manipulator DLR-III. In this system, the use of light-weight carbon composite links actuated with Harmonic Drive gears in each joint has resulted in a high one-to-one payload to mass ratio of the robot [6, 7].

Different actuation systems have been proposed in order to decouple the robot link from the reflected actuator inertia. Such systems have received considerable attention due to the introduction of intrinsic compliance directly into a mechanical transmission. Series Elastic Actuator (SEA) [8] utilizes elastic elements between the link and the motor to introduce required compliance. Such elements significantly reduce the controllable bandwidth of the actuation and compromise the overall performance of the robot. Optimal trade-off between the safety, the required stiffness, and the accuracy should be found for the robotic system [9].

In order to better address the trade-off between the safety and the performance of the robot with elastic couplings, the Variable Stiffness Actuator (VSA) [10] was developed. Similar to SEA, the VSA has elastic elements in the transmission, however, VSA can control the stiffness of the elements during operation.

Series Damper Actuator (SDA) is another approach to compliant actuation that uses a variable damping technology [11]. A rotary damper in series with the motor drive ensures the force/torque control of the SDA actuator. The presented design is capable of achieving greater torque bandwidth over the SEA.

In the Variable Impedance Actuation (VIA) design [12] a variable elastic transmission is combined with a variable damping technology. This development further extended the VSA approach by allowing to change both elastic and damping properties of the actuator at the same

time during operation.

Compliant actuators such as pneumatic muscles [13], [14], [15] are able to exhibit excellent compliance and safety characteristics. Although their practical use in industry is somewhat limited due to an insufficient range of motion.

Magneto-rheological clutches as a prospective element for the mechanical transmission was initially introduced in 1948 [16]. The clutch can be designed to transmit high torques in comparison with actuators of similar mass and inertia. Unique ability to fast and precisely control transmitted torque without introducing non-linearities such as torque ripple makes MR clutches good candidate to a compliant actuator [17, 18].

A number of unique devices based on MR clutch actuation was developed for haptic applications [19, 20, 21, 22, 23]. Such systems are capable of providing effective and precise feedback to the operator but usually not designed to transmit high torques.

Integration of powerful magneto-rheological clutches into industrial systems receives increasing attention. More companies actively study the feasibility of implementing new MR technologies to replace or enhance existing solutions such as transmission system clutches for automotive and power equipment [24, 25], cooling systems [26], agricultural metering systems [27].

Rehabilitation equipment [20], exoskeletons [28], and collaborative robots [29, 5] are all the emerging areas that can benefit from MR technology implementation. These applications entail new requirements for a balanced approach to achieving compliant and safe interactions with humans and the environment while maintaining the desired level of robot performance.

1.3 Magneto-Rheological Fluids and Devices

An MR clutch is an intrinsically compliant device that provides an accurate and reliable method of controlling the transmitted torque. By controlling the viscosity of MR fluid inside the clutch, from liquid to near solid, using a variable magnetic field, the MR clutch regulates the coupling between an actuation source (e.g. an electric motor) and a load (e.g. a robot joint), adding full compliance to a coupling.

Due to intrinsic compliance of MR fluid, these devices are ideal for safe actuation.

The analyses and applications of the actuation based on MR clutch technology have been previously reported in [30, 22].

The MR clutch includes the input and output shafts, a single ferromagnetic disk connected to the input shaft, and two ferromagnetic output disks connected to the output shaft. We can refer to the input part of an MR clutch (i.e., input shaft and disks) as the rotor, the output part (i.e., output shaft and disks) as the stator. The rationale behind this naming is that the rotor is connected to the active source with continual rotation while the stator is connected to the load and rotates on-demand. The gap between the stator and the rotor is filled with the MR fluid. An electromagnetic coil within the stator generates a magnetic field to change the apparent viscosity (shear stress) of the MR fluid. The viscosity of the MR fluid generates a resistive force (stress) as the rotor shears through the fluid relative to the stator. The reactive force (stress) from the shearing of the fluid results in dragging the stator, hence transmitting the torque to the load. The torque transmitted through a surface element of a disk with infinitesimal width can be expressed as,

$$dT = 2\pi r^2 \tau dr \tag{1.1}$$

where dT is the differential transmitted torque, r is the radial distance of the surface element from the center of the disk, and τ is the MR fluid shear stress, whose value is approximated using Bingham visco-plastic model as follows, [31],

$$\tau = \tau_y(B) + \eta\omega r/l_f, \tau > \tau_y \tag{1.2}$$

in that $\tau_y(B)$ is the magnetic field dependent yield stress, η is the Newtonian viscosity of the MR fluid, ω is the angular velocity between rotor and stator, and l_f is the fluid gap size.

By integrating (2.1) on the entire surface of the disk, one can obtain the total transmitted torque corresponding to a single disk of the clutch. The MR clutch can include more than one disk to achieve the desired torque capacity. A comparison of different configurations of MR clutches can be found in [32, 33, 30].

Ferromagnetic materials used in the structure of the MR clutch course significant hysteresis of the magnetic flux during operation. The form of the hysteresis loop depends on many factors including material property and geometry of the system. Therefore, accurate control of the transmitted torque is a challenge due to the nonlinear relation between the current in the coil and the magnetic flux density in the MR fluid. However, the effect of hysteresis in the clutch can be avoided by the direct measurement of the magnetic flux in real-time. The measurement of the flux is done by one or several Hall sensors embedded in the MR clutch in the magnetic path. Using known relation between magnetic flux and shear stress of the MR fluid (e.g. from data-sheet [34]), the measurement of the magnetic flux could be effectively used to indirectly estimate the clutch torque without costly and bulky torque/force sensors. Thereby, a simple proportional-integral-derivative controller could be used for accurate control of the torque transmitted by the clutch. The precision of the described approach is superior to the control using an open-loop torque-to-current mapping and matches closed-loop control based on the feedback from torque sensor [35, 36].

Additionally, Hall sensors (i.e., Infineon TLE 4998s4) can be used to measure the temperature inside the clutch. The operating temperature affects the rheological properties of MR fluid [37] and taking it into account helps further improve the precision of the torque estimation.

1.4 Basic Principles of an Antogonistic DASA actuation approach

A pair of magneto-rheological clutches can be configured to provide antagonistic actuation to a load. In this case, the rotors of the MR clutches are rotated in opposite directions and the stators of both MR clutches are attached to a moving component (i.e. common shaft, robot link). Depending on the electromagnetic activation of each clutch, the torque can be applied by one or both MR clutches in either direction.

Several MR clutch pairs can be configured using an actuation concept termed Distributed Active Semi-Active Actuation (DASA) [38]. DASA concept will be used for actuating the designed manipulator. In DASA actuation a constant rotational motion of a single source of

power (e.g. a motor) is distributed to a number of loads (e.g. robot links) via a pair of antagonistically configured MR clutches. The pair of MR clutches spinning in opposite directions allows bi-directional actuation of the load.

1.5 Research Objectives

In the world of impending robotization, a new generation of high-performing compliant and safe robots is needed. The actuation approach based on DASA MR technology allows us to reconcile speed and precision with the intrinsic compliance of the system. Therefore, the purpose of this work is to study the capabilities of the MR technology in application to multi-degrees of freedom robots.

In particular, the aim is to develop and build a 5-DOF manipulator with the transmission distributing the mechanical power generated by a single motor to all 5 joints of the arm. The output torque of each joint should be controlled by the pair of counter-rotating MR clutches working in an antagonistic configuration.

The feasibility of constructing an inexpensive system with a high number of degrees of freedom based on DASA MR actuation can be demonstrated in the working prototype of the robotic arm. Extensive studying of the robot's performance can address concerns regarding the dynamic behavior, precision, stability, robustness, and control simplicity.

1.6 Contribution

The main contributions of the dissertation are as follows:

• An innovative design of an intrinsically compliant 5-DOF manipulator is developed. The robot is based on the Antagonistic Distributed Active-Semi Active (A-DASA) actuation approach described in previous works of our research group. The robot utilizes a single motor and various types of transmission to deliver a bi-directional rotation to all five joints. A pair of MR clutches with predefined performance is used as a compliant actuator in every manipulator's joint.

• An efficient design of the MR clutch with a high torque-to-mass ratio is developed. Multiple steps of progressive design improvement performed include: A new arrangement of Hall sensors inside the MR clutch; The hybrid magnetization using permanent magnets in conjunction with electromagnetic coils; Simulated and thoroughly optimized distribution of the magnetic flux inside the clutch core.

• An optimized compact design of an MR clutch pair with a joint magnetic core is developed. The design of the actuator is analyzed, experimentally validated, and introduced in the 5-DOF manipulator.

• The behavior of an antagonistic MR actuation approach is thoroughly studied. The passivity of the actuation is analytically proved based on the Lyapunov theory and experimentally validated in the number of tests with the robot.

• The torque control system for the compliant 5-DOF robot is developed. The system is implemented based on five STM32F2 controller boards interconnected to each other via CAN

Bus. The performance of the control system in terms of positional and torque precision is experimentally validated.

  • A new concept of MR clutch using squeeze mode of MR fluid is developed. The design based on planetary gear mechanism allows miniaturization of the clutch without posing significant restrictions in manufacturability. The prototype of a miniaturized MR clutch is developed and preliminary experimental results that validate the proposed design are obtained.

1.7   Thesis Outline

In Chapter 2 the development of the MR clutch improved design is presented. Chapter 3 discusses the mechanical design of the 5-DOF robot and its components. Chapter 4 presents the simulation of the robot transmission system, analysis of passive behavior of antagonistic MR actuator, describes the joint-level PID control, and results of experiments. Chapter 5 presents the development and test of the miniaturized "planetary" MR clutch and the concept of a compliant 7-DOF gripper on the miniaturized clutch design.

Bibliography

[1] J.-J. Park, Y.-J. Lee, J.-B. Song, and H.-S. Kim, "Safe joint mechanism based on nonlinear stiffness for safe human-robot collision," in *2008 IEEE International Conference on Robotics and Automation*. IEEE, 2008, pp. 2177–2182.

[2] J.-J. Park, H.-S. Kim, and J.-B. Song, "Safe robot arm with safe joint mechanism using nonlinear spring system for collision safety," in *2009 IEEE International Conference on Robotics and Automation*. IEEE, 2009, pp. 3371–3376.

[3] J.-J. Park and J.-B. Song, "Safe joint mechanism using inclined link with springs for collision safety and positioning accuracy of a robot arm," in *2010 IEEE International Conference on Robotics and Automation*. IEEE, 2010, pp. 813–818.

[4] K. Salisbury, W. Townsend, B. Ebrman, and D. DiPietro, "Preliminary design of a whole-arm manipulation system (wams)," in *Proceedings. 1988 IEEE International Conference on Robotics and Automation*. IEEE, 1988, pp. 254–260.

[5] J. Viau, P. Chouinard, J.-P. L. Bigué, G. Julió, F. Michaud, S. Shimoda, and J.-S. Plante, "Projected pid controller for tendon-driven manipulators actuated by magneto-rheological clutches," in *2015 IEEE/RSJ International Conference on Intelligent Robots and Systems (IROS)*. IEEE, 2015, pp. 5954–5959.

[6] G. Hirzinger, J. Bals, M. Otter, and J. Stelter, "The dlr-kuka success story: robotics research improves industrial robots," *IEEE Robotics & Automation Magazine*, vol. 12, no. 3, pp. 16–23, 2005.

[7] A. De Luca, A. Albu-Schaffer, S. Haddadin, and G. Hirzinger, "Collision detection and safe reaction with the dlr-iii lightweight manipulator arm," in *2006 IEEE/RSJ International Conference on Intelligent Robots and Systems*. IEEE, 2006, pp. 1623–1630.

[8] G. Pratt and M. Williamson, "Series elastic actuators," in *1995 IIEEE/RSJ International Conference on Intelligent Robots and Systems*. IEEE, 1995, pp. 399–406.

[9] K. Kong, J. Bae, and M. Tomizuka, "Control of rotary series elastic actuator for ideal force-mode actuation in human–robot interaction applications," *IEEE/ASME transactions on mechatronics*, vol. 14, no. 1, pp. 105–118, 2009.

[10] G. Tonietti, R. Schiavi, and A. Bicchi, "Design and control of a variable stiffness actuator for safe and fast physical human/robot interaction," in *Proceedings of the 2005 IEEE international conference on robotics and automation*. IEEE, 2005, pp. 526–531.

[11] C.-M. Chew, G.-S. Hong, and W. Zhou, "Series damper actuator: a novel force/torque control actuator," in *4th IEEE/RAS International Conference on Humanoid Robots, 2004.*, vol. 2. IEEE, 2004, pp. 533–546.

[12] A. Bicchi and G. Tonietti, "Dealing with the safety-performance tradeoff in robot arms design and control," *IEEE Robotics and Automation Magazine*, vol. 11, no. 2, 2004.

[13] D. G. Caldwell, G. A. Medrano-Cerda, and M. Goodwin, "Control of pneumatic muscle actuators," *IEEE Control Systems Magazine*, vol. 15, no. 1, pp. 40–48, 1995.

[14] C.-P. Chou and B. Hannaford, "Measurement and modeling of mckibben pneumatic artificial muscles," *IEEE Transactions on robotics and automation*, vol. 12, no. 1, pp. 90–102, 1996.

[15] B. Tondu and P. Lopez, "Modeling and control of mckibben artificial muscle robot actuators," *IEEE control systems Magazine*, vol. 20, no. 2, pp. 15–38, 2000.

[16] J. Rabinow, "The magnetic fluid clutch," *Electrical Engineering*, vol. 67, no. 12, pp. 1167–1167, 1948.

[17] A. S. Shafer and M. R. Kermani, "On the feasibility and suitability of mr fluid clutches in human-friendly manipulators," *IEEE/ASME Transactions on Mechatronics*, vol. 16, no. 6, pp. 1073–1082, 2010.

[18] N. Takesue, J. Furusho, and Y. Kiyota, "Fast response mr-fluid actuator," *JSME International Journal Series C Mechanical Systems, Machine Elements and Manufacturing*, vol. 47, no. 3, pp. 783–791, 2004.

[19] J. Blake and H. B. Gurocak, "Haptic glove with mr brakes for virtual reality," *IEEE/ASME Transactions On Mechatronics*, vol. 14, no. 5, pp. 606–615, 2009.

[20] T. Kikuchi, K. Oda, and J. Furusho, "Development of leg-robot for simulation of spastic movement with compact mr fluid clutch," in *2009 IEEE International Conference on Robotics and Automation*. IEEE, 2009, pp. 1903–1908.

[21] G. C. Latham, C. A. Fenny, J.-S. Plante, B. Atkins, G. Julio, M. Denninger, C. E. Covington, and P. Wilson, "Magnetorheological haptic trim actuator," May 23 2017, uS Patent 9,656,746.

[22] N. Najmaei, A. Asadian, M. R. Kermani, and R. V. Patel, "Design and performance evaluation of a prototype mrf-based haptic interface for medical applications," *IEEE/ASME Transactions on Mechatronics*, vol. 21, no. 1, pp. 110–121, 2015.

[23] M.-A. Bégin, M. Denninger, and J.-S. Plante, "Design and experimental validation of a 2dof sidestick powered by hyper-redundant magnetorheological actuators providing active feedback," in *2019 International Conference on Robotics and Automation (ICRA)*. IEEE, 2019, pp. 4011–4017.

[24] C. Kieburg, G. Oetter, M. Laun, C. Gabriel, and H. Steinwender, "Mr all-wheel-drive prototype car driving tests and durability requirements for the mr fluids used," in *11th Conference on Electrorheological Fluids and Magnetorheological Suspensions (ERMR)*, 2008.

[25] A. J. McDaniel, "Magneto-rheological brake-clutch apparatuses and methods," Feb. 22 2011, uS Patent 7,891,474.

[26] A. L. Smith, J. C. Ulicny, and L. C. Kennedy, "Magnetorheological fluid fan drive for trucks," *Journal of Intelligent Material Systems and Structures*, vol. 18, no. 12, pp. 1131–1136, 2007.

[27] J. W. Henry and S. D. Noble, "Agricultural metering system having a magnetorheological fluid clutch assembly," May 15 2018, uS Patent 9,970,490.

[28] M. Okui, S. Iikawa, Y. Yamada, and T. Nakamura, "Variable viscoelastic joint system and its application to exoskeleton," in *2017 IEEE/RSJ International Conference on Intelligent Robots and Systems (IROS)*.   IEEE, 2017, pp. 3897–3902.

[29] P. Fauteux, M. Lauria, B. Heintz, and F. Michaud, "Dual-differential rheological actuator for high-performance physical robotic interaction," *IEEE Transactions on Robotics*, vol. 26, no. 4, pp. 607–618, 2010.

[30] W. Li, P. Yadmellat, and M. R. Kermani, "Design optimization and comparison of magneto-rheological actuators," in *2014 IEEE International Conference on Robotics and Automation (ICRA)*.   IEEE, 2014, pp. 5050–5055.

[31] R. W. Phillips, "Engineering applications of fluids with a variable yield stress," Ph.D. dissertation, University of California, Berkeley, 1969.

[32] Q.-H. Nguyen and S.-B. Choi, "Optimal design of a novel hybrid mr brake for motorcycles considering axial and radial magnetic flux," *Smart Materials and Structures*, vol. 21, no. 5, p. 055003, 2012.

[33] ——, "Selection of magnetorheological brake types via optimal design considering maximum torque and constrained volume," *Smart Materials and Structures*, vol. 21, no. 1, p. 015012, 2011.

[34] "Mrf-140cg magneto-rheological fluid," Lord Technical Data, 2008. [Online]. Available: http://www.lordmrstore.com

[35] O. Erol, B. Gonenc, D. Senkal, S. Alkan, and H. Gurocak, "Magnetic induction control with embedded sensor for elimination of hysteresis in magnetorheological brakes," *Journal of Intelligent Material Systems and Structures*, vol. 23, no. 4, pp. 427–440, 2012.

[36] W. Li, P. Yadmellat, and M. R. Kermani, "Linear torque actuation using fpga-controlled magneto-rheological actuators," in *2014 IEEE International Conference on Robotics and Automation (ICRA)*.   IEEE, 2014, pp. 1060–1065.

[37] W. Song, S. Wang, S.-B. Choi, N. Wang, and S. Xiu, "Thermal and tribological characteristics of a disc-type magnetorheological brake operated by the shear mode," *Journal of Intelligent Material Systems and Structures*, vol. 30, no. 5, pp. 722–733, 2019.

[38] M. Kermani and A. Shafer, "Magneto-and electro-rheological based actuators for human friendly manipulators," Feb. 14 2017, uS Patent 9,566,715.

Chapter 2

5-DOF Manipulator: MR Clutches Development

Parts of the material in this chapter are published in "Journal of Intelligent Material Systemsand Structures", 2021" [1] and in "The 2018 IEEE/RSJ International Conference on Intelligent Robots and Systems (IROS)", 2018, Madrid, Spain [2].

This chapter presents design, analysis, and prototype development of magneto-rheological clutches intended as the actuation mechanism for the compliant robotic manipulator with 5 degrees of freedom. Multiple steps to increase the toque-to-mass ratio of the general clutch design are evaluated and implemented.

First, the arrangement of the Hall sensors is optimized to reduce their impact of the clutch magnetic reluctance.

Second, the performance of the MR clutch is improved by implementation of a hybrid magnetization approach.

Third, the gap size reduction in the MR clutch with hybrid magnetization is introduced and its influence on maximum torque and dynamic range investigated.

Finally, the design for a pair of MR clutches with a shared magnetic core for antagonistic actuation of the robot joint is presented.

The details of each approach are discussed and the results of the finite element analysis are used to highlight the required engineering steps and to demonstrate the improvements achieved. Using the proposed design approach, the MR clutch prototypes for each joint of 5-DOF robot are developed, assembled, and tested. The experimental results demonstrate the performance of the proposed design and validate the accuracy of the analysis used for the development.

2.1   Introduction

The demand for a compliant actuation system is motivated by growing needs for robotic systems capable of safe and effective operations in close proximity and physical contact with humans, animals, fruits, and vegetables, performing delicate tasks, and mastering unplanned interactions with the environment.

The actuation based on MR clutches is chosen because it offers unique advantages such as
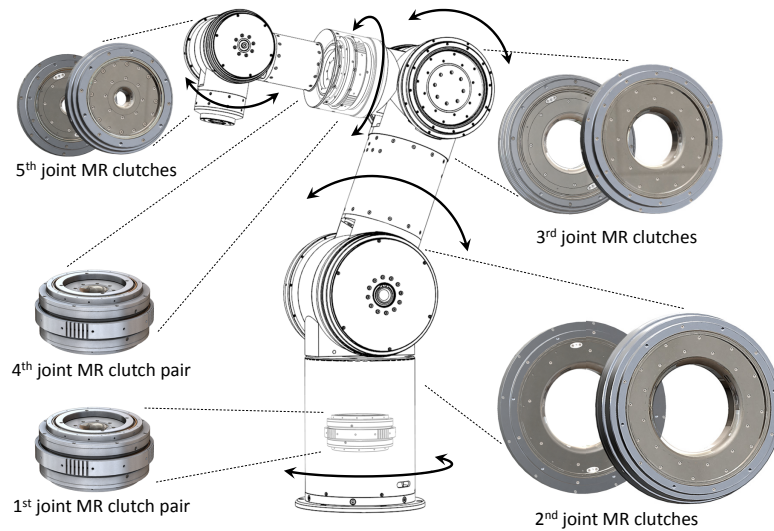
Figure 2.1: Prospective 5 DOF Robot and location of the MR clutches in the joints.

compactness, high torque-to-mass ratio, low power consumption, high operating speed, precision in torque control, and semi-active control of compliance. Furthermore, the use of MR clutch allows the creation of an actuation framework in which a single active source of power (e.g. an electric motor) can drive multiple loads (e.g. multiple robot joints) via multiple MR clutches [3]. For independent and simultaneous actuation of multiple loads, a pair of MR clutches are needed to drive each load in an antagonistic fashion.

2.1.1 MR clutch design objectives

The main objective of the work described in this chapter is the development of MR clutches with enhanced capabilities for each joint of the 5-DOF manipulator. The kinematic structure, the transmission, and details of the mechanical design for the manipulor described in Chapter 3.

The target payload of the manipulator is 10 kg at 800 mm full-reach. Each joint of the system is actuated using a pair of MR clutches coupled in an antagonistic configuration. Fig. 2.1 shows a CAD model of the proposed manipulator and the MR clutches used in each joint of the robot. The system in total includes 10 MR clutches that deliver direct torque to the corresponding joints without gear reduction. Given the intended payload and the reach of the robot, the desired torques at each joint starting from the base (from joint 1 to joint 5) are determined as 20, 200, 80, 20, and 15 N·m, respectively.

The antagonistic pair of MR clutches in joint 2, 3, and 5 are designed using separate clutches whereas the design of joint 1 and 4 allows use of a pair of antagonistic MR clutches connected together. The detailed design, optimization, analyses, and prototype development of these MR clutches are described next.
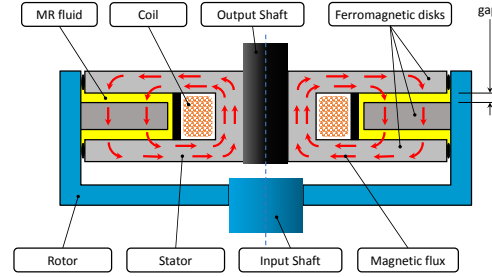
Figure 2.2: Cross-section view of a single-disk MR clutch.

2.1.2 Basic principles of a disk-type MR clutch

In order to develop a lightweight, strong, and reliable actuator, various types of MR clutches including drum-type, multi-drum, multi-disk, and drum-disk hybrid MR clutches were considered [4]. Given the characteristics of each type in terms of performance and manufacturability, a multi-disk MR clutch is identified to best meet the design requirements for the 5-DOF manipulator actuation.

An example of a disk-type MR clutch with a single rotor disk is shown in Fig. 2.2. The MR clutch shown in the figure includes the input and output shafts, a single ferromagnetic disk connected to the input shaft, and two ferromagnetic output disks connected to the output shaft. The input part of an MR clutch (i.e., input shaft and disks) is referred to as the rotor, the output part (i.e., output shaft and disks) as the stator. The rationale behind the naming is that the rotor is connected to the active source with continual rotation, while the stator is connected to the load and rotates on-demand. The gap between the stator and the rotor is filled with MR fluid.

An electromagnetic coil within the stator generates a magnetic field to change the apparent viscosity (shear stress) of the MR fluid. The viscosity of the MR fluid generates a resistive force (stress) as the rotor shears through the fluid relative to the stator. The reactive force (stress) from the shearing of the fluid results in dragging the stator, hence transmitting the torque to the load. The torque transmitted through a surface element of a disk with infinitesimal width can be expressed as,

$$dT = 2\pi r^2 \tau dr \qquad (2.1)$$

where dT is the differential transmitted torque, r is the radial distance of the surface element from the center of the disk, and τ is the MR fluid shear stress, whose value is approximated using Bingham visco-plastic model as follows, [5],

$$\tau = \tau_y(B) + \eta \omega r/l_f, \tau > \tau_y \qquad (2.2)$$

in that $\tau_y(B)$ is the magnetic field dependent yield stress, η is the Newtonian viscosity of the MR fluid, ω is the angular velocity between rotor and stator, and l_f is the fluid gap size.

By integrating (2.1) on the entire surface of the disk, one can obtain the total transmitted torque corresponding to a single disk of the clutch. The MR clutch can include more than one disk to achieve the desired torque capacity. A comparison of different configurations of MR clutches can be found in [6, 7, 4].

Ferromagnetic materials used in the structure of the MR clutch course significant hysteresis of the magnetic flux during operation. The form of the hysteresis loop depends on many factors including material property and geometry of the system. Therefore, accurate control of the transmitted torque is a challenge due to the nonlinear relation between the current in the coil and the magnetic flux density in the MR fluid. However, the effect of hysteresis in the clutch can be avoided by the direct measurement of the magnetic flux in real-time. The measurement of the flux is done by one or several Hall sensors embedded in the MR clutch in the magnetic path. Using known relation between magnetic flux and shear stress of the MR fluid (e.g. from data-sheet [8]), the measurement of the magnetic flux could be effectively used to indirectly estimate the clutch torque without costly and bulky torque/force sensors. Thereby, a simple proportional-integral-derivative controller could be used for accurate control of the torque transmitted by the clutch. The precision of the described approach is superior to the control using an open-loop torque-to-current mapping and matches closed-loop control based on the feedback from torque sensor [9, 10].

Furthermore, modern Hall sensors (i.e., Infineon TLE 4998s4) can be also used to measure the temperature inside the clutch. The operating temperature affects the rheological properties of MR fluid [11] and taking it into account helps further improve the precision of the torque estimation.

2.2　Analytical model of the MR clutch

To estimate the torque transmitted by the MR clutch, an analytical model is developed based on the reluctance of the magnetic circuit. The model is similar to the one described in [12]. The parameters for the model are shown in Fig. 2.3 for the MR clutch with two rotor disks and one stator disk. In the general case, the clutch has n rotor disks and $n-1$ stator disks. Magnetic reluctance is a ratio of the circuit length and the circuit area multiplied by the material permeability. For the model in Fig. 2.3 the total clutch reluctance is derived taking into account reluctance of each separate part as follows,

$$\mathcal{R}_{rd} = \frac{t_d}{\mu_s \pi (r_6{}^2 - r_4{}^2)}, \mathcal{R}_{sd} = \frac{t_d}{\mu_s \pi (r_5{}^2 - r_3{}^2)}, \tag{2.3}$$

$$\mathcal{R}_{rf} = \frac{t_d}{\mu_f \pi (r_4{}^2 - r_3{}^2)}, \mathcal{R}_{sf} = \frac{t_d}{\mu_f \pi (r_6{}^2 - r_5{}^2)}, \tag{2.4}$$

$$\mathcal{R}_f = \frac{t_f}{\mu_f \pi (r_6{}^2 - r_3{}^2)}, \mathcal{R}_c = \frac{t_c}{\mu_s \pi (r_2{}^2 - r_1{}^2)}, \tag{2.5}$$

$$\mathcal{R}_w = \int_{1/2(r_1+r_2)}^{1/2(r_3+r_6)} \frac{1}{\mu_s (2\pi r) t_w} dr = \frac{ln(\frac{r_3+r_6}{r_1+r_2})}{2\pi \mu_s t_w}, \tag{2.6}$$

where $\mathcal{R}_{rd}$, $\mathcal{R}_{sd}$, $\mathcal{R}_{rf}$, $\mathcal{R}_{sf}$, $\mathcal{R}_f$, $\mathcal{R}_c$, and $\mathcal{R}_w$, are the reluctance of the rotor disk, stator disk, fluid next to the rotor disk, fluid next to the stator disk, fluid between disks, core, and walls of the stator (flanges), respectively; t_d, t_f, t_c, and t_w are the thickness of the disk, fluid gap, core, and stator wall (flange), respectively; μ_s and μ_f are magnetic permeability of steel and MR fluid; r_1, r_2, r_3, r_4, r_5, and r_6 are radius of core opening, core itself, inner radius of the stator disk,

(a)   (b)
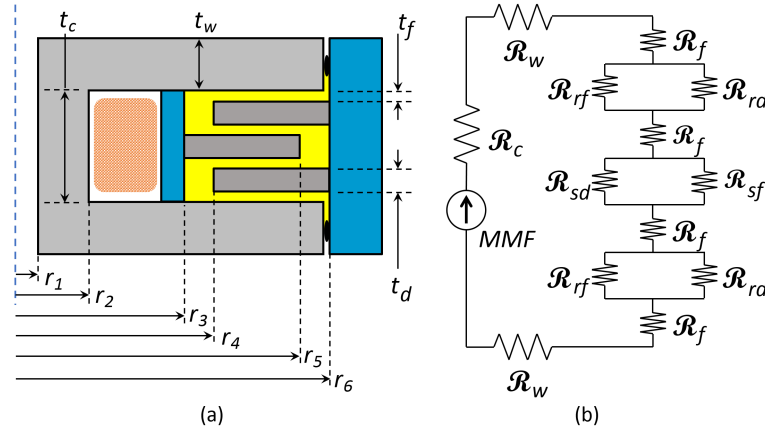
Figure 2.3: Cross-section geometry (a) and equivalent magnetic circuit (b) of a typical MR clutch

inner radius of the rotor disk, outer radius of the stator disk, and outer radius of the rotor disk, respectively.

Using Kirchhoff's law for the model in Fig. 2.3 (b), the total reluctance of the circuit for the clutch with two rotor disks and one stator disk is,

$$\mathcal{R} = \mathcal{R}_c + 2\mathcal{R}_w + 4\mathcal{R}_f + \frac{2\mathcal{R}_{rf}\mathcal{R}_{rd}}{\mathcal{R}_{rf} + \mathcal{R}_{rd}} + \frac{\mathcal{R}_{sf}\mathcal{R}_{sd}}{\mathcal{R}_{sf} + \mathcal{R}_{sd}} \tag{2.7}$$

However, in the general case for the clutch with n rotor discs and $(n-1)$ stator disks the total reluctance is,

$$\mathcal{R} = \mathcal{R}_c + 2\mathcal{R}_w + 2n\mathcal{R}_f + \frac{n\mathcal{R}_{rf}\mathcal{R}_{rd}}{\mathcal{R}_{rf} + \mathcal{R}_{rd}} + \frac{(n-1)\mathcal{R}_{sf}\mathcal{R}_{sd}}{\mathcal{R}_{sf} + \mathcal{R}_{sd}} \tag{2.8}$$

According to Ampere's law, the magnetic flux Φ in the circuit is calculated as,

$$\Phi = \frac{\mathcal{F}}{\mathcal{R}} = \frac{N \cdot i}{\mathcal{R}}, \tag{2.9}$$

where Φ is a magneto-motive force, N is a number of wire turns in the electromagnetic coil, and i is the current in the wire. The average magnetic flux density B in the MR fluid is computed as,

$$B = \frac{\Phi}{A} = \frac{N \cdot i}{\mathcal{R}\pi(r_6{}^2 - r_3{}^2)}, \tag{2.10}$$

The magnetic flux density B is used to calculate the MR fluid shear stress τ with equation (2.2). Finally, the differential torque is found with (2.1) and integrated on the entire surface of all the rotor disks (or the stator disks) to obtain the total transmitted torque of the MR clutch.

2.3   Improved design of the MR clutch

This section provides the details of the MR clutch design and several implemented improvement steps for increasing the clutch torque-to-mass ratio.
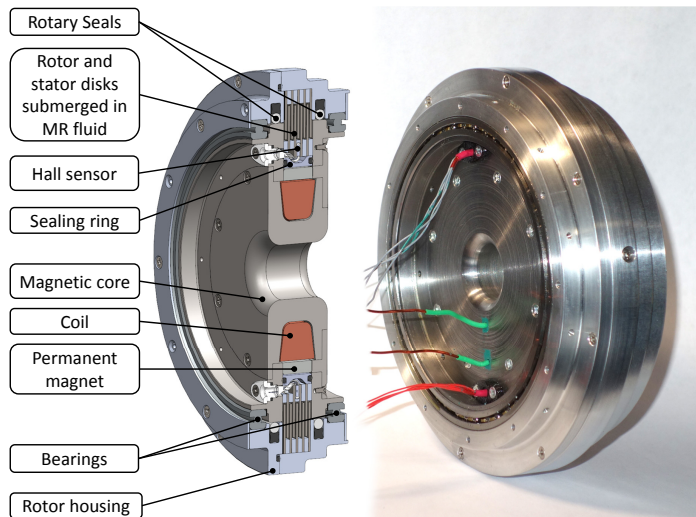
Figure 2.4: Section view of the 5$^{\text{th}}$ joint MR clutch.

To develop a lightweight, compact, and high-torque MR clutches suitable for the manipulator actuation, the multi-disk configuration of the clutch is selected. The selection is based on the results of previous studies in which a comparison of different design configurations of MR clutches was presented [4, 13].

We begin by providing the details of a multi-disk configuration of the MR clutches used in the 5$^{\text{th}}$ joint of the robot manipulator. A similar configuration is used for all the rest clutches used in other joints of the robot.

As described in the previous section, a multi-disk MR clutch consists of four main components, i.e., an input part including an input shaft and disks a.k.a rotor and an output part including an output shaft and disks a.k.a stator, an electromagnetic coil to generate a magnetic field within the magnetic core of the clutch, and the MR fluid itself. Fig. 2.4 shows the cross-section of a model of an MR clutch highlighting these components. The figure also shows a snapshot of an assembled MR clutch prototype. This particular design includes four input disks and five output disks made of carbon steel. The disks are separated using aluminum spacers at the inner and outer diameters. The aluminum spacers ensure a consistent gap size of 0.4 mm between the stator and rotor disks. The core of the clutch is also made of carbon steel and has an electromagnetic coil with 150 turns of 17 AWG wire (200 turns of 20 AWG in later version). As part of its magnetization, the stator also includes a permanent magnet in the shape of a ring. The permanent magnet is used as part of the weight reduction strategy and will be discussed later in the paper.

The gaps between the disks are filled with MR fluid injected using fill and drain ports on the rotor housing. Specially designed rotary seals and sealing O-rings are used to prevent the fluid from escaping the volume between the disks (active zone).

Our MR clutch design includes Hall sensors to provide feedback on the internal magnetic field used to estimate the torque of the MR clutch to allow accurate torque control without the use of any external torque measurement devices.
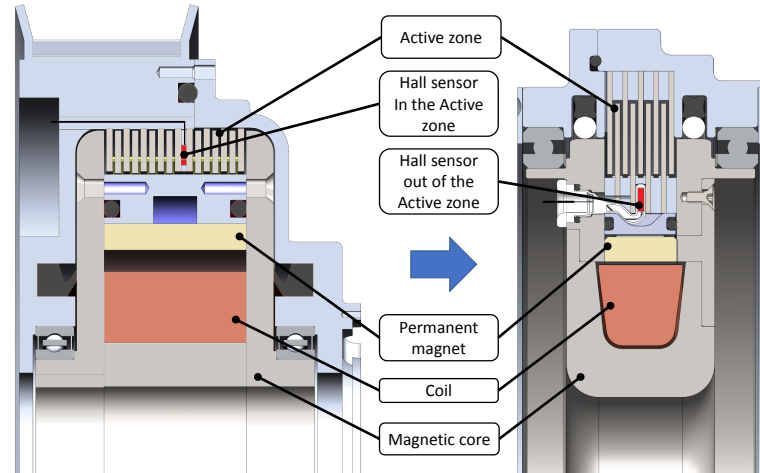
Figure 2.5: Comparison of the conventional Hall sensor location (left) with the proposed location outside of the MR clutch active zone (right).

2.3.1 Geometry Optimization using Finite Element Analysis

The purpose of the geometry optimization is to minimize the weight of the MR clutch within the preset constraints. The constraints were identified as follows,

- required transmitted torque,
- maximum clutch diameter,
- maximum clutch width,
- maximum wire current density in the coil,
- minimum gap size,
- available materials,
- limitations on relation between the clutch dimensions (e.g. $r_1 < r_2$ as in Fig. 2.3).

A parametric model is built in COMSOL Multiphysics® software for every MR clutch design. Proper ranges for the parameters are identified based on the preset constraints. Optimization is done by sweeping across all the parameters while analyzing the MR clutch weight for every combination. The combination corresponding to the minimum weight and generating the required torque was selected as the optimal set of parameters.

More in-depth details of the MR clutch geometry optimization can be found in [12].

2.3.2 New location for the Hall Sensors

One of the improvements that set apart the design of our MR clutch from conventional multi-disk MR clutches with Hall sensors is the location and arrangement of the sensors [2]. Unlike previously built MR clutches [14, 15], our proposed design includes two programmable Hall sensors (Infineon TLE 4998s4) outside the active zone of the clutch. To save space within the zone in-between the input and output disks, the Hall sensors are located outside the active zone in a cut within the aluminum spacers. Fig. 2.5 shows the new placement of the Hall sensor (right) and compares it with the conventional placement of the sensors (left).

The advantages of the proposed location for the Hall sensors are multifold. First, by placing
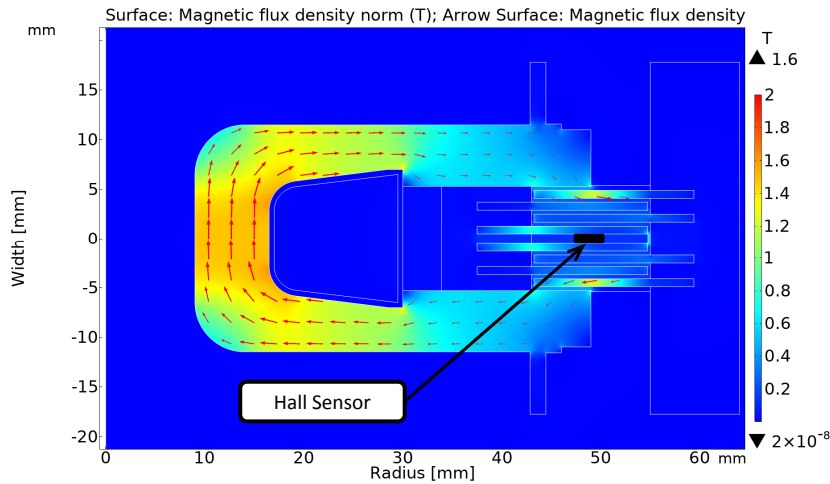
Figure 2.6: Magnetic flux density and flux contours of an MR clutch with the Hall sensor inside the active zone. Wire current of 2 A, total coil current of 300 A, transmitted torque 7.7 N·m, and 0.127 T flux density at the Hall sensor location.

the Hall sensor, outside the active zone of the MR clutch, the space used for housing the Hall sensors can be saved. In a conventional design, the Hall sensors are sandwiched in-between two carbon steel stator disks. This space can be used for an additional rotor disks, contributing to the higher torque of the MR clutch (see Fig. 2.6, 2.7, and 2.9). Second, placing additional carbon steel disk in the gap used for accommodating the Hall sensors results in a reduced reluctance of the magnetic circuit and increased magnetic flux (hence torque) for a given input current. Third, by placing the Hall sensor outside the active zone, a smaller fraction of the magnetic field is used for the measurement which allows measuring higher magnetic flux density in the active zone. This is an important issue since Hall sensors have a fixed dynamic range and often saturate.

The magnetic field density outside the active zone is less than that inside the active zone, but it is *proportional* to the magnetic field density in the active zone. This proportionality is only a function of the mechanical structure of the clutch and is a constant. Fig. 2.8 shows field density vs. current curves for the Hall sensor location and for two different locations within the active zone. It can be observed that the density in the chosen locations in the active zone can be obtained from the Hall sensor measurements using the coefficient of proportionality. The coefficient is unique for every point in the zone as well as for the average density. However, the proportionality can be determined in simulations and experimentally and later used to estimate the clutch torque for any current.

As a result of the proposed placement of the Hall sensor, the MR clutch with the sensors provides identical torque as a similar sensor-less clutch. And in comparing with the old design of the clutch with the Hall sensors it is almost 2 times higher transmitted torque at 1 A, 1.5 times at 2 A, and 1.4 times at 3 A wire current. To calculate the transmitted torque, the "Yield Stress vs. Magnetic Field Strength" graph published by LORD Corporation for MR fluid MRF-140CG was used (Y-H graph in [8]). However, to avoid some discrepancies between simulation and experimental results and to improve the accuracy of the simulations, the Y-H curve on the graph was adjusted to start from zero. The results for the designs are compared in Fig. 2.9.
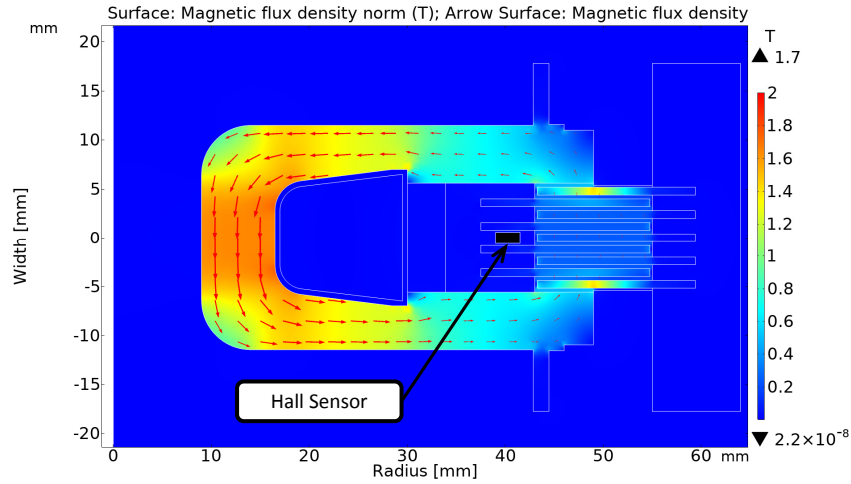
Figure 2.7: Magnetic flux density and flux contours of the MR clutch with Hall sensor outside the active zone. Wire current of 2 A, total coil current of 300 A, transmitted torque 12 N·m, and 0.045 T flux density at the Hall sensor location.
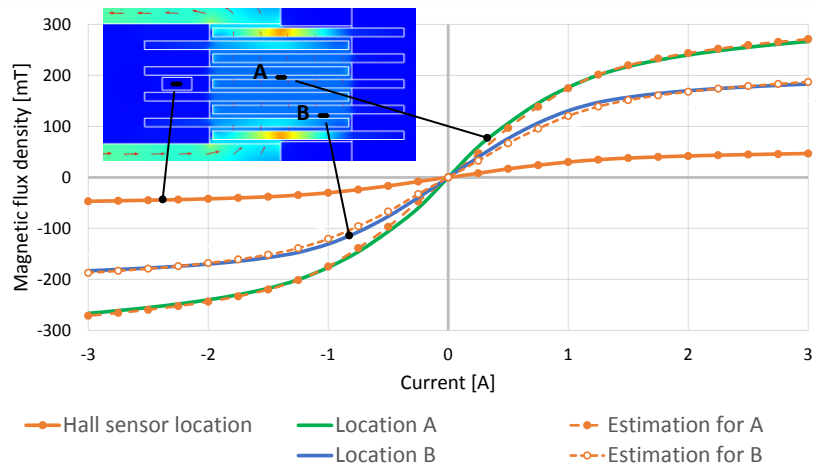
Figure 2.8: Magnetic flux density vs coil current at the Hall sensor location (solid orange curve), and in two locations (A and B) in the active zone (green and blue curves). Based on the flux density at the location of the Hall sensor, the densities at locations A and B are estimated (plotted in dotted orange curves).

In our design, the Hall sensors and the electromagnetic coil are mounted on the stator side of the MR clutch for convenience. This choice eliminates the need for a slip-ring mechanism for wire connections since it allows us to keep the Hall sensors and the coil stationary with respect to the load. This also improves the connection reliability, the ease of assembly, and the maintainability of the MR clutch.
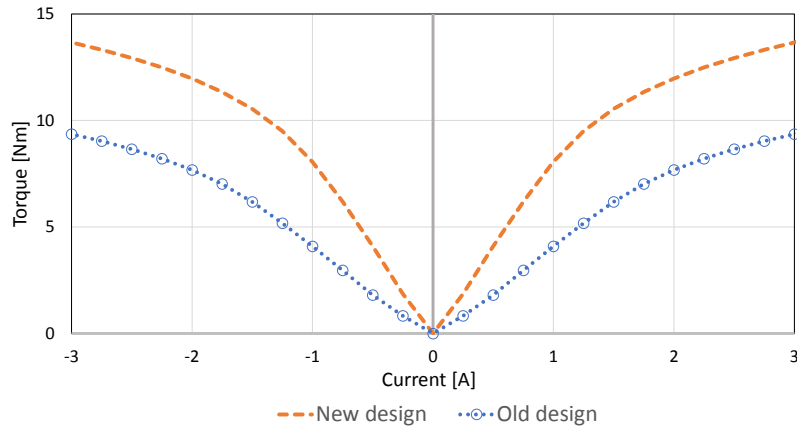
Figure 2.9: The relationship between the transmitted torque (N·m) and input current (A) for two designs with the Hall sensors inside and outside of the active zone (no permanent magnet installed).

2.3.3   Combined Magnetization

This section studies the effect of a combined (hybrid) magnetization of the MR clutch using a combination of an electromagnetic coil and a permanent magnet, and the improvements made as a result of this combination. In this approach, the permanent magnet provides the clutch with an initial magnetization, and the electromagnetic coil is used to adjust the strength of the magnetic field within the active zone to the exact desired value on demand. A comprehensive report on this approach and the discussion on the selection of parameters for the magnetic coil and the permanent magnet can be found in [12].

To better integrate the permanent magnet and the electromagnetic coil with the magnetic core of the MR clutch, the geometry of the clutch was carefully optimized using Finite Element Analysis (FEA) in COMSOL Multiphysics software. Fig. 2.10 shows the map of the magnetic flux distribution for the MR clutch with a permanent magnet installed (B = 1.35 T). Comparing the results in this figure with those shown in Fig. 2.7, one can see that the use of the permanent magnet results in a more uniform distribution of the magnetic field and the elimination of magnetic saturation within the magnetic core such as those seen in Fig. 2.7 (red area with the flux density above 1.4T). The results in both figures are generated for the magnet wire current of 2 A (the total coil current of 300 A for 150 turns of wire 17 AWG).

The permanent magnet installed at the selected location is more efficient in increasing the maximum magnetic flux in the active zone than the additional turns of coil that could fit in the allocated for the magnet space. The MR clutch in Fig. 2.11 includes a larger coil with additional 45 turns of wire in lieu of a permanent magnet. This coil fills up the space used to accommodate the magnet. The coil is energized with the same wire current of 2 A (total current of 390 A). It can be observed that the magnetic flux in the center of the core reaches values around 1.8 T and the material becomes saturated. In the active zone, the flux is 0.25..0.5 T. As a result, the torque transmitted by the clutch is only 14.2 N·m. For the same wire current of 2 A, the clutch shown in Fig. 2.10 transmits 20.7 N·m, and the magnetic flux in the center of the core is only 0.8..1.1 T.

Therefore, another important advantage of a combined magnetization is the ability to have
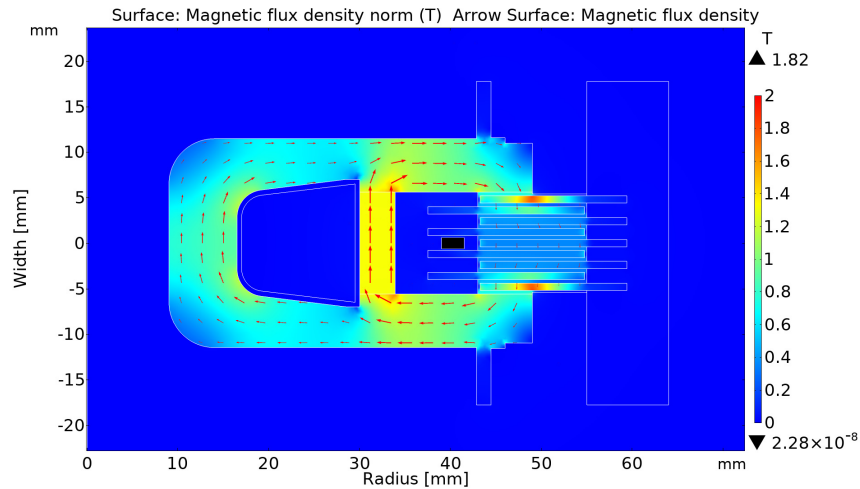
Figure 2.10: Magnetic flux density and flux contours of the MR clutch with the Hall sensors outside the active zone and combined magnetization with a permanent magnet. Wire current of 2 A, total coil current of 300 A, permanent magnet of 1.35 T, transmitted torque 20.7 N·m, and 0.08 T flux density at the Hall sensor location.

higher input currents without magnetic saturation of the coil, thus transmit greater torque, all thanks to the re-distribution of the magnetic flux within the clutch. Stated differently, for a given input current, a combined magnetization requires less ferromagnetic volume and can be lighter than its conventional counterpart.
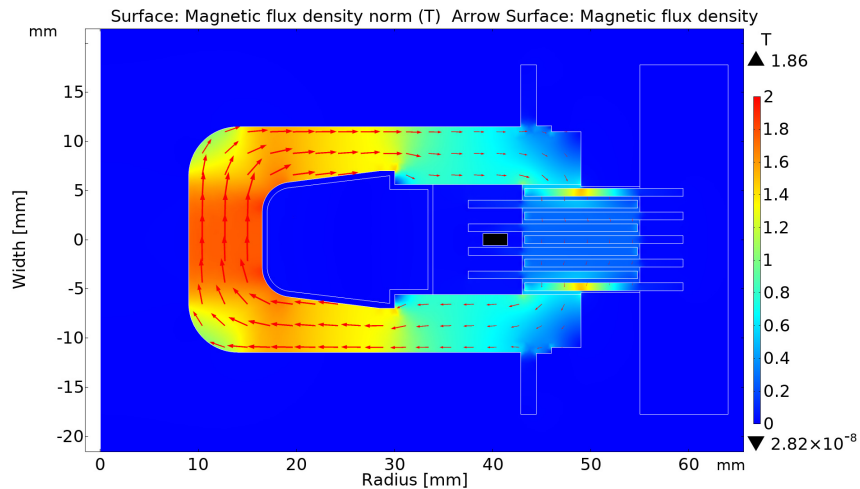
Figure 2.11: Magnetic flux density and flux contours of the MR clutch with the Hall sensors outside the active zone and magnetization with the coil reinforced with additional turns of wire placed instead of a permanent magnet (45 turns). Wire current of 2 A, total coil current of 390 A, no permanent magnet, transmitted torque 14.2 N·m, and 0.05 T flux density at the Hall sensor location.

Fig. 2.12 compares the generated torque of the MR clutches with combined magnetization

with that of a conventional MR clutch. The figure depicts the torque values versus the input currents for a design with no permanent magnet as well as for two designs with magnets of different strengths, i.e., a weak permanent magnet (0.5 T) and a strong permanent magnet (1.35 T). As seen, the maximum transmitted torque increases with the strength of the permanent magnet. The maximum torque for a 3 A input current with a strong permanent magnet can reach 26.3 N·m, whereas a weak permanent magnet and no permanent magnet can generate 19 N·m and 13.6 N·m, respectively. This is a 79% increase in the value of output torque. Considering the mass of the MR clutch (1.8 kg), the proposed combined magnetization offers a torque-to-mass ratio of 14.6 N·m/kg.

The "off-state" torque of the clutch appears with the addition of a permanent magnet and reaches 0.3 N·m. It should be taken into account in some applications.
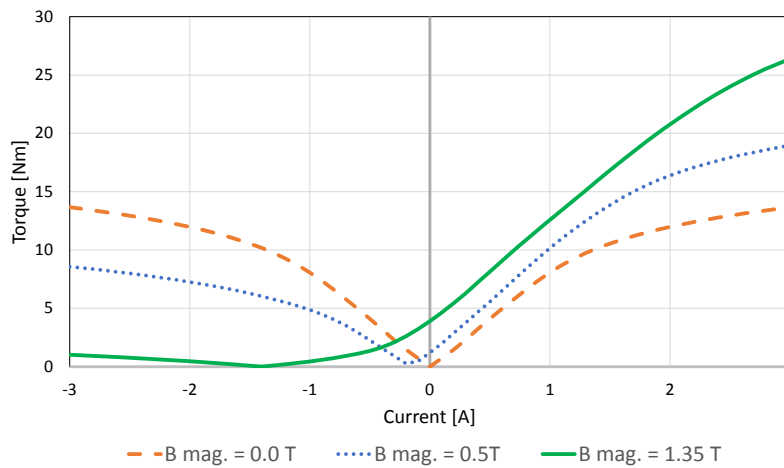
Figure 2.12: Transmitted torque (N·m) vs. input current (A) for the MR clutches with and without permanent magnets.

Another noticeable change of an MR clutch with permanent magnet is the asymmetrical values of the generated torque with respect to the input current. This characteristic, specific to MR clutch with combined magnetization, can be considered as an advantage or disadvantage depending on the application of the MR clutch. The permanent magnet results in a partial "on-state" (i.e., engagement) of the MR clutch even with no input current to the coil. This feature can be advantageous in applications requiring a fail-safe brake response (e.g., a robot joint). On the other hand, in applications that require using the MR clutch in "off-state" (i.e., disengaged) more often such as dual transmission of an electric vehicle, this feature requires a continual input current to the coil to counteract the magnetic flux of the permanent magnet and keep the clutch in the "off-state". This constant power consumption is an undesirable feature in some applications.

2.3.4   MR Fluid Gap

In this section, the effect of the MR fluid gap on the performance of the clutch with hybrid magnetization is briefly studied. It is a well-known fact that decreasing the size of the fluid gap directly increases the MR clutch transmission torque. A smaller gap size results in a lower

reluctance of the magnetic circuit, higher magnetic flux, and subsequently larger transmitted torque in the "on-state". However, the minimum drug torque in the "off-state" regime also increases due to a higher fluid strain rate at the same clutch angular speed, as well as a higher residual magnetic flux in the active zone.

Higher "off-state" torque negatively affects the dynamic range of the MR clutch and undesirable in most of the applications.

Fig. 2.13 shows the FEA results for an MR clutch with identical size (volume) as that shown in Fig. 2.10. The new clutch has a gap size of 0.2 mm (as opposed to 0.4 mm), and accommodates two times more disks (8 output disks instead of 4 disks). The disks of the new MR clutch are also thinner (0.4 mm instead of 0.8 mm) except for the middle disk (0.8 mm) used for housing the Hall sensors. One of the smallest packing sizes of the Hall sensor available in the market (Infineon TLE 4998s4) is 1 ± 0.05mm.
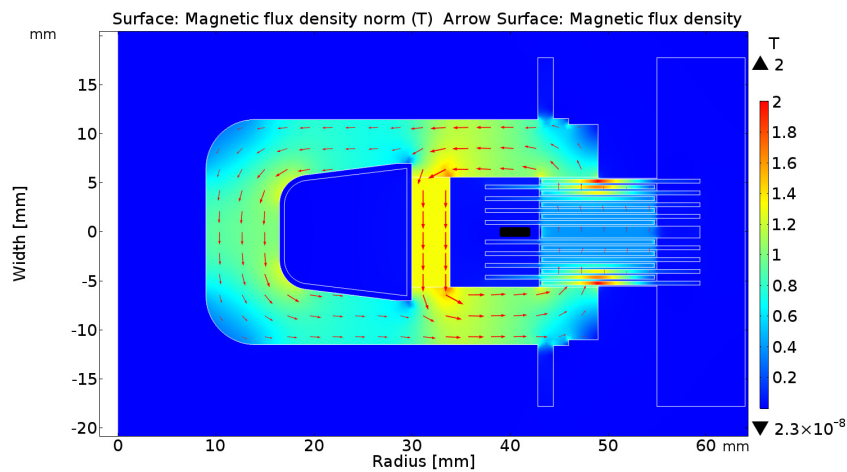
Figure 2.13: Magnetic flux density and flux contours of the MR clutch with the Hall sensors outside the active zone, permanent magnet, and 0.2 mm MR fluid gap. Wire current of 2 A, total coil current of 300 A, permanent magnet of 1.35 T, transmitted torque 40.56 N·m, and 0.048 T flux density at the Hall sensor location.

The estimated output torque of the new clutch with a reduced gap size versus the input current of the MR clutch is depicted in Fig. 2.14.

As observed, the reduction of the gap size can significantly increase the output torque of the MR clutch. The maximum torque of the clutch with a 0.2 mm gap size can reach to 49 N·m for 3 A input wire current. In comparison to the maximum torque of an identical MR clutch with a 0.4 mm gap size, this is an 85% increase in output torque. Considering the mass of the clutch, the torque-to-mass ratio of the new MR clutch is 27 N·m/kg.

However, the challenge of implementing a smaller gap is the manufacturing and assembly difficulties due to tighter tolerances requirements.

2.3.5 Joined Magnetic Core

The design of the MR clutch pairs used in the 1st and 4th joint of the robot manipulator is further enhanced using a joined magnetic core similar to some designs developed in the past (i.e. [16].
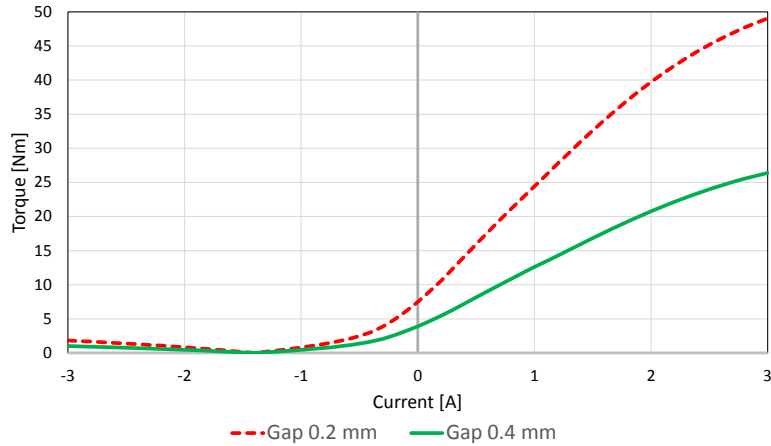
Figure 2.14: The relationship between the transmitted torque (N·m) and input current (A) for MR clutches with 0.2 mm and 0.4 mm gaps.

The clutches in the pairs in the 1st and 4th joint do not need to be apart to accommodate the transmission elements. The transmission shaft in these joints can be easily located in the opening of the clutch pairs because the clutches are oriented coaxially with the shaft. Thus, the design of the two clutches is fused to reduce the overall weight of the joint.

Fig. 2.15 demonstrates the new design of a pair with the joined core (right) in comparison with a conventional assembly of two separate MR clutches (left).
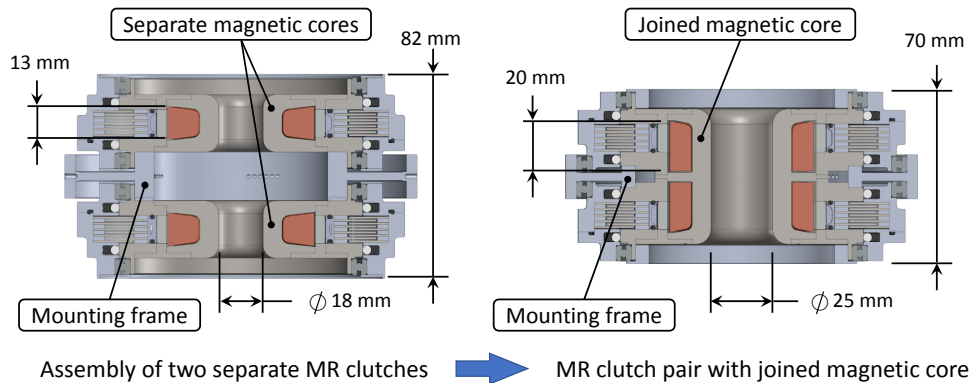
Figure 2.15: Comparison of a pair of conventional MR clutches (left) vs. a pair of MR clutches with joined magnetic core (right).

To accommodate specific design requirements of the 1st and 4th joint of the robot (due to the outer diameter of the coaxial shafts assembly), it was necessary to increase the diameter of the central hole in the magnetic core from 18 mm to 25 mm as shown in Fig. 2.15. To increase the inductance of the electromagnetic coil to the required level, the height of each coil was increased from 13 mm to 20 mm.

Despite this increase, the total weight of the joined MR clutch pair with the mounting frame remained the same 4.2 kg. Moreover, the height of the pair reduced to 70 mm compared to the 83 mm height of two individual MR clutches mounted together on the appropriate frame.

The shape of the joined magnetic core and the size and location of the electromagnetic coils were optimized using COMSOL Multiphysics software. Fig. 2.16, 2.17, and 2.19 show the magnetic flux density of the joined clutches for different values of input current in the top and bottom coils containing 260 turns of wire each.
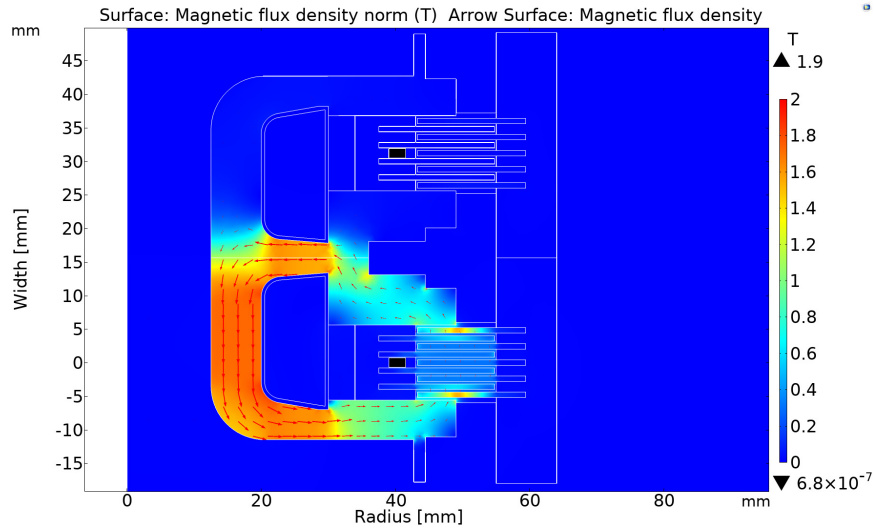
Figure 2.16: Magnetic flux density and flux contours of the joined MR clutch pair with no permanent magnet and 0.4 mm MR fluid gap. Wire current of -0.2 A and 2.0 A, the corresponding torque of 3.3 N·m and 17.6 N·m, and the corresponding flux density 0.0002 T and 0.093 T at the Hall sensor location in the top and bottom clutch respectively.

Fig. 2.16 shows the magnetic flux density in a pair of joined MR clutches with no permanent magnets and an input current of 2 A through the bottom coil. The bottom clutch generates 17.8 N·m torque in the desired direction. This generated torque is higher than its corresponding value in a separate single clutch with no permanent magnet installed (see the dashed orange line in Fig. 2.12). The magnetic field from the bottom coil spills over to the other part of the clutch resulting in an undesired torque of 4.3 N·m in the top clutch. This torque counteracts the original torque and decreases the total torque of the MR clutch pair down to 13.5 N·m. This value is similar to that generated in a single clutch with no permanent magnet at 2 A input current (see Fig. 2.12).

Minimizing the residual field in the top clutch helps to reduce the undesired opposing torque. An input current of -0.2 A can be introduced in the top coil to reduce the opposing torque from 4.3 N·m to 3.3 N·m. This current will also reduce the torque of the bottom clutch from 17.8 N·m to 17.6 N·m, however, a net torque of the MR clutch pair will increase from 13.5 N·m to 14.3 N·m.

Similar to the single MR clutch, the introduction of the permanent magnet can significantly increase the transmitted torque of the MR clutch pair. Fig. 2.17 shows the magnetic flux density of the pair with a permanent magnet of (B = 1.0 T) installed in each clutch and an input current of 2 A passing through the bottom coil. The input current results in 27.9 N·m in the desired direction of the bottom clutch. Similar to the previous case, an input current of -0.15 A can be used in the top coil to minimize the residual magnetic flux and to drop the undesired torque of

the top clutch from 4.5 N·m to 3.3 N·m. As a result, the net torque of the MR clutch pair is 24.6 N·m.

Nevertheless, even without minimizing the residual magnetic flux in the top clutch, the joined pair still generates a net torque of 23.5 N·m in the desired direction. This value is about 10% higher than the corresponding toque of a separate single MR clutch with 1.35 T permanent magnet installed (see the solid green line in Fig. 2.12).
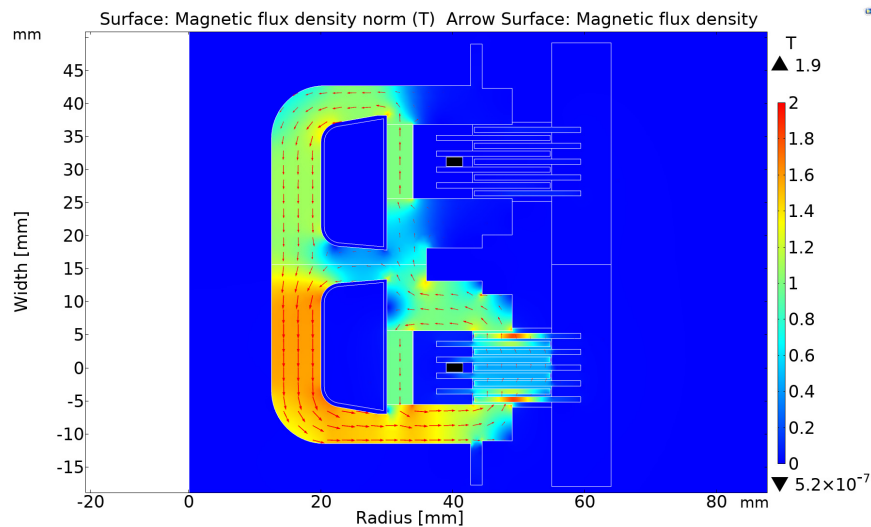
Figure 2.17: Magnetic flux density and flux contours of the joined MR clutch pair with permanent magnets of 1.0 T, and 0.4 mm MR fluid gap. Wire current of -0.15 A and 2.0 A, the corresponding torque of 3.3 N·m and 27.9 N·m, and the corresponding flux density 0.0001 T and 0.149 T at the Hall sensor location in the top and bottom clutch respectively.

To reverse the direction of the transmitted torque, the currents in the top and bottom coils can be swapped enabling the MR clutch pair to transmit the same amount of torque in the opposite direction.

We further studied the performance of the joined MR clutch pair in other scenarios. As described previously, the use of permanent magnets results in partial "on-state" of the MR clutches due to partial activation of each clutch. In an antagonistic configuration, these partial torques acting in opposite directions will cancel out each other for the symmetrical design of the pair. Regardless, we studied whether these torques can be nullified using the corresponding coil.

Fig. 2.18 displays the magnetic flux density of the MR clutch pair when no current is running through the electromagnetic coils. The magnetic flux density measured at 0.1 T within the active zone is due to permanent magnets alone. As a result, each clutch generates 5.4 N·m torque in opposite directions. The net torque of the MR clutch pair is, however, near zero.

To force the "off-state" of the MR clutch pair, the currents in the top and bottom coils should be sufficient to minimize the magnetic flux of the permanent magnets in the active zone of the MR clutch. Fig. 2.19 shows that to counteract the magnetic flux of permanent magnets an input current of -0.76 A in both top and bottom coils need to be used. This input current, however, cannot completely cancel out the magnetic flux of the permanent magnets leaving a
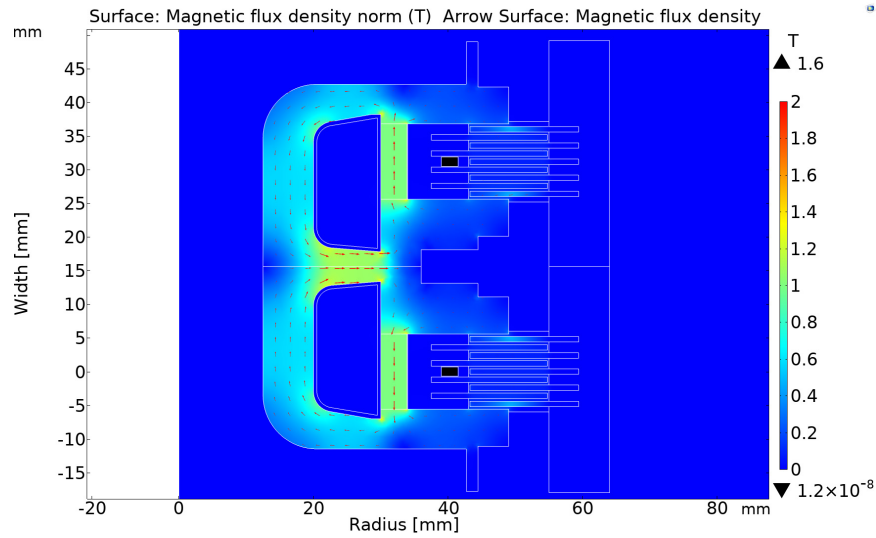
Figure 2.18: Magnetic flux density and flux contours of the joined MR clutch pair with permanent magnets of 1.0 T, and 0.4 mm MR fluid gap. No Wire current in either clutch, 5.4 N·m residual torque, and 0.017 T flux density at the Hall sensor location in each clutch.

residual magnetic flux density of 0.05 T in the active zone. The residual flux density will result in 3.2 N·m of generated torque in each clutch in opposite directions. The net torque of the MR clutch pair will be close to zero.
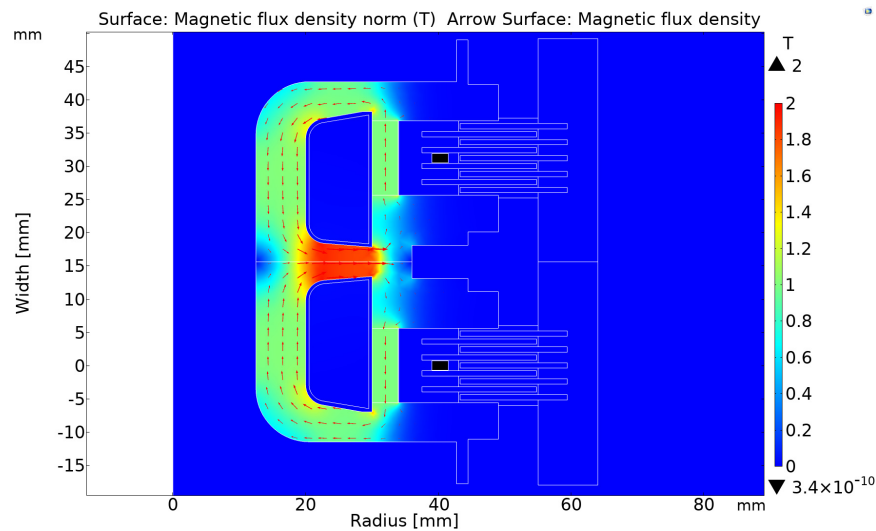
Figure 2.19: Magnetic flux density and flux contours of the joined MR clutch pair with permanent magnets of 1.0 T, and 0.4 mm MR fluid gap. Wire current of -0.76A in the top and bottom clutches, minimal magnetic flux in active zone, 3.2 N·m generated torque, and 0.00003 T flux density at the Hall sensor location in each clutch.

Last, we examined the performance of a pair of joined MR clutch with a fluid gap size of 0.2 mm. As explained earlier, reducing the gap size will free up space that can be used to

accommodate additional disks in the active zone. As such, the number of disks in each clutch on the stator side was increased from 4 to 8 and on the rotor side from 5 to 9.

Moreover, as also explained earlier, the existence of permanent magnets results in partial "on-state" of the MR clutches and some opposing torque on each clutch. Although the net output torque of the antagonistic pair is (near) zero, there is some energy dissipation on the motor side. The joined MR clutch pair is intended for joint 1 and joint 4 of the robot manipulator. The axis of rotation in joint 1 is vertical (see Fig. 2.1) and this joint is not loaded under the gravitational forces, hence the MR clutches in joint 1 are more often used in "off-state" regime than in "on-state". It is, therefore, more suitable to eliminate the partial "on-state" of the MR clutches and the energy dissipation associated with it. Thus, the permanent magnets were not included in the design of the joined MR clutch pair intended for joint 1 of the manipulator.

Fig. 2.20 shows these changes and the results of FEA for the magnetic flux density in the joined pair of MR clutches with the increased number of disks, a gap size of 0.2 mm, and no permanent magnets installed. The figure shows the results for the input current of 2 A and -0.22 A through the top and bottom coils, respectively. The generated torque in the top and bottom clutches are 32.5 N·m and 5.9 N·m, respectively and the net torque of the pair is 26.6 N·m.
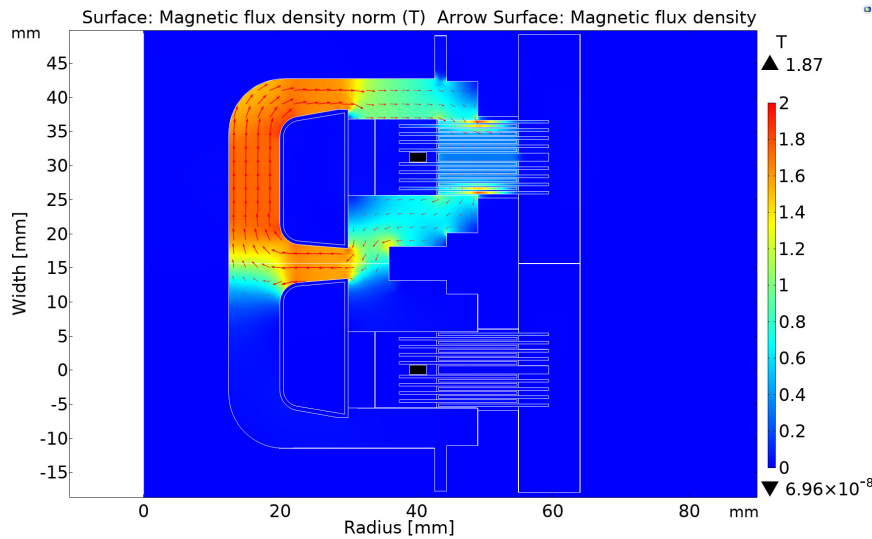
Figure 2.20: Magnetic flux density and flux contours of the joined MR clutch pair with no permanent magnet and 0.2 mm MR fluid gap. Wire current of 2.0 A and -0.22 A, the corresponding torque of 32.5 N·m and 5.9 N·m, and the corresponding flux density 0.012 T and 0.00001 T at the Hall sensor location in the top and bottom clutch respectively.

2.4   MR Clutches Prototypes

Using the results obtained in the previous sections the prototypes of the MR clutches for each joint of the manipulator were developed. All joints of the manipulator are actuated with a pair of antagonistic clutches. Joint 1 and joint 4 of the manipulator use a pair of antagonistic MR

Figure 2.21: Prototype of a joined pair of MR clutches.

clutches with joined magnetic core. A snapshot of an assembled joined MR clutch pair used in joint 1 and joint 5 is shown in Fig. 2.21.

The MR clutches used in joints 2, 3, and 5 have an identical design except for the number of disks and the diameter of the disks. The MR clutches used in joint 2 have the largest number of disks and have the largest diameters. These clutches have 10 rotor disks and 9 stator disks, with an outer diameter of 227mm. A cross-section of the MR clutch used in joint 2 of the manipulator and the snapshot of the prototype MR clutch is shown in Fig. 2.22 (left and middle pictures).

Rotary Seals

Rotor and stator disks submerged in MR fluid

Hall sensor

Permanent magnet

Magnetic core

Electro-magnetic Coil

Hall sensor

Bearings

Rotor housing

2nd joint MR clutch cross-section   2nd joint MR clutch   3rd joint MR clutch
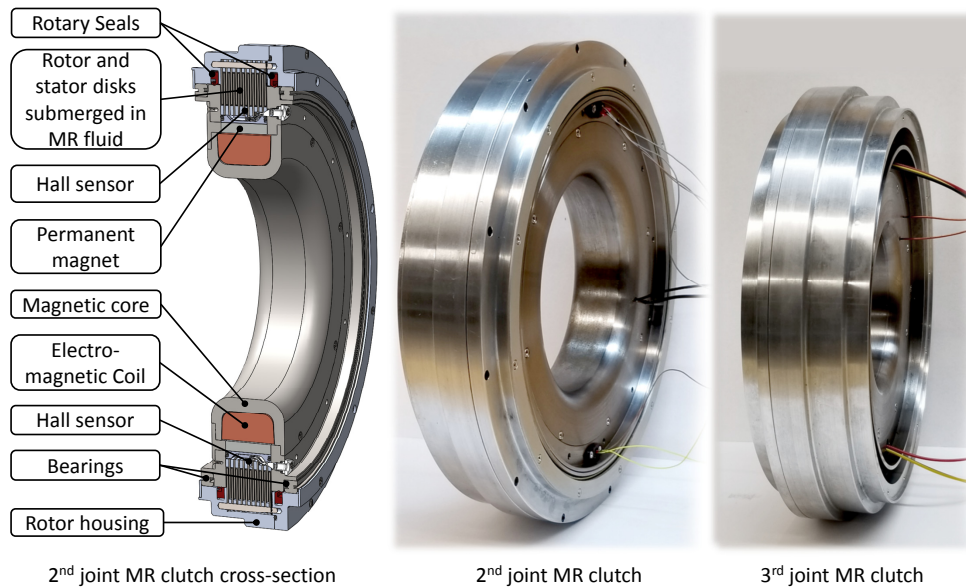
Figure 2.22: Section view of the 2nd joint MR clutch and a snapshots of MR clutch prototypes for the 2nd and 3rd joints.

The MR clutches used in joint 3 have 8 rotor disks, and 7 stator disks with an outer diameter of 186 mm. A snapshot of the MR clutch used in joint 3 of the manipulator is shown in Fig. 2.22 on the right.

The MR clutches used in joint 5 are identical to those used in joint 3 with 5 rotor disks, 4 stator disks, and an outer diameter of 132 mm as shown in Fig. 2.4.

Table 2.1 summarizes the characteristics of all the MR clutches used in each joint of the manipulator as well as adjusted required torque for each joint in a tabular form.

Table 2.1: Characteristics of separate MR clutches for robot joints

Joint of the robot	1	2	3	4	5
Max Required Torque[N·m]	20	200	80	20	15
Torque at 1.5A [N·m]	20	198	65	22	16
Torque at 2.0A [N·m]	22	223	83	24	20
Number of rotor disks	9	10	8	5	5
Number of stator disks	8	9	7	4	4
Number of coil turns	260	440	370	260	200
Gap size [mm]	0.2	0.4	0.4	0.4	0.4
Rotor Diameter [mm]	132	227	186	132	132
Weight [kg]	2.1	6.9	4.3	2.1	1.8

2.5 Experimental Validations

To validate the results obtained previously and to demonstrate the effectiveness of the proposed design, the MR clutch prototypes were experimentally examined and the data from these experiments were compared with the corresponding COMSOL simulation results. The MR clutches were filled with MR fluid MRF-140CG [8]. The experimental results for the clutches used in joint 1 and joint 5 of the manipulator are presented in this section. Similar results from other MR clutches were obtained but for the sake of brevity are not presented.

To perform the experiments, the base of the manipulator was used as a part of the experimental setup. The base of the manipulator includes a 2800-Watt brushless DC motor (Hacker Q80-13XS) and an HD gearbox. The base was equipped with a frame to mount a static load cell (Transducer Techniques SBO-1K) as shown in Fig. 2.23. An adapter with a 62 mm shoulder was used to firmly connect the load cell to the stator of the joined MR clutch pair used in the 1st joint.

A motor driver (Advanced Motion Control AZ12A8) was used to supply current to the electromagnetic coil of the top MR clutch in the joined MR clutch pair. In the experiments, the bottom clutch was not powered. An interface box (Infineon PGSISI-2 board) was used to read the data provided by the Hall sensors. A real-time control and data acquisition platform (dSPACE DS 1103) was used to control the motor driver and to acquire feedback data from the load cell.

A sinusoidal current with a frequency of 1 Hz and an amplitude of ±2.0 A was applied to one of the two electromagnetic coils of the prototype MR clutch pair while the output torque of the pair was measured. Fig. 2.24 shows the measured torque values versus the input current of the MR clutch (blue solid line) and compares these results with their corresponding simulated values obtained in COMSOL Multiphysics (orange dash line).
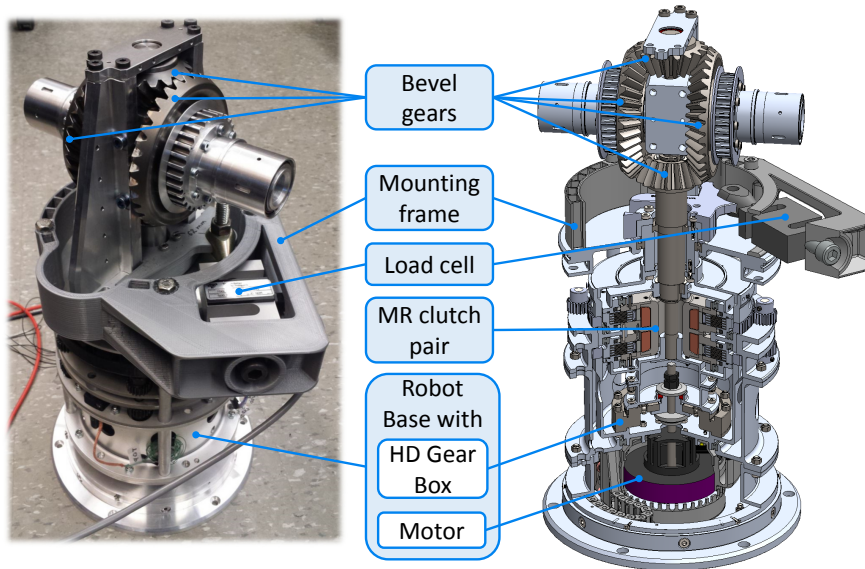
Figure 2.23: Experimental setup used for testing the 1st joint MR clutch pair.

As observed, there is a clear agreement between the simulated and the actual measured torque. The shift of the experimental curve down about 2 N·m relative to the simulated curve is due to excessive friction in the opposite rotating MR clutch. The friction appeared from some misalignment of the rotor and stator disks during the assembly procedure.
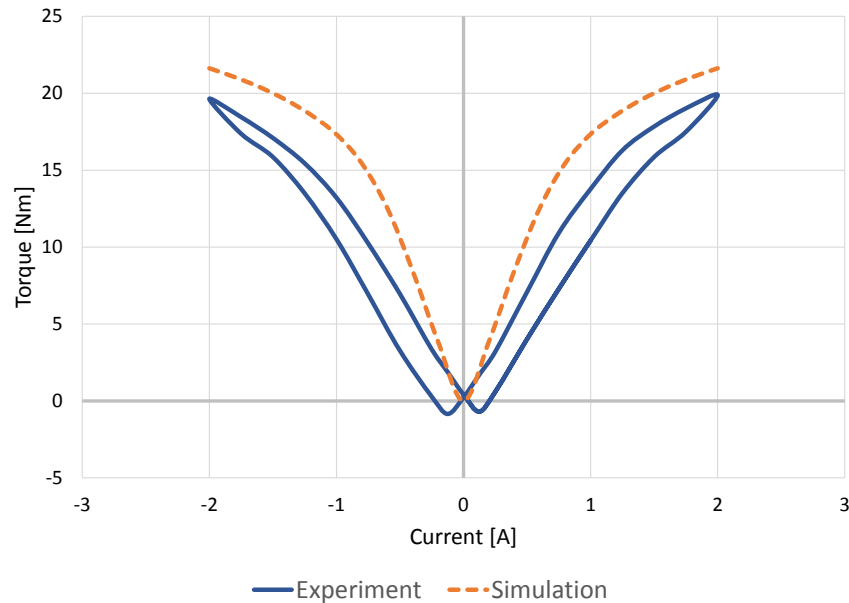
Figure 2.24: Experimental and simulated results of the joined pair of MR clutch used in the 1st joint: transmitted torque (N·m) vs. coil input current (A)

Similar experiments were performed using the MR clutch for the 5th joint. As in the previous case, the base of the manipulator was used as a part of the experimental setup. The base

was equipped with a frame to mount a static load cell (Transducer Techniques SBO-1K) as shown in Fig. 2.25. An adapter on the top of the clutch was used to firmly couple the stator of the clutch to the load cell. A similar adapter underneath the MR clutch was used to transmit the rotational input from the HD gearbox to the clutch rotor. Similar equipment was used to run the motor at a constant speed, provide (current) command signals to the MR clutches, and acquire feedback data from the load cell and Hall sensors.
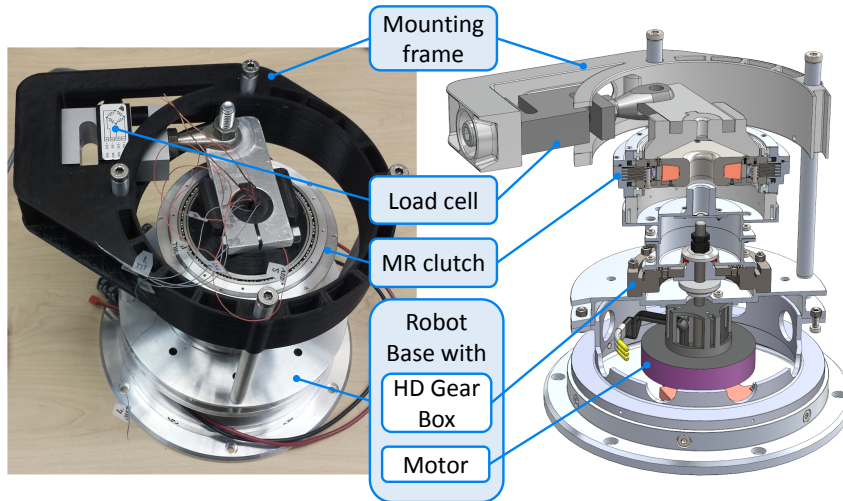
Figure 2.25: Experimental setup used for testing the 5th joint MR clutches.

A sinusoidal current with the frequency of 1 Hz and an amplitude of ±2.5 A was used to drive the electromagnetic coil of the prototype MR clutch while the output torque of the clutch was measured. Fig. 2.26 shows the measured torque values versus the input current of the MR clutch (blue solid line) and compares these results with their corresponding simulated values obtained in COMSOL Multiphysics (orange dash line).

The graphs demonstrate general agreement between the simulated and the actual measured data. Small discrepancies between the data occur for small values of input current (less than ±0.3 A). These discrepancies are due to the limitations of the COMSOL models in representing magnetic hysteresis of the ferromagnetic materials.

In a subsequent experiment, the feasibility of placing the Hall sensors outside the active zone of the MR clutch was also validated. To this end, a continuous current with several different magnitudes ranging from -3 A to 4.5 A was applied to the magnetic coil of the MR clutch and the corresponding magnetic flux densities measured by the Hall sensors were recorded. The data was compared with the one obtained from simulations. Fig. 2.27 compares the experimental (solid blue) and simulated (dashed orange) results. As observed, there is a good agreement between the results which validates our proposed placement of the Hall sensor outside the active zone of the MR clutch.

The Hall sensor measurements can be directly used as feedback in a simple PID controller to estimate the torque transmitted by the MR clutch. However, the relation between magnetic flux density and the yield stress of MR fluid may change over time due to the possible degra-
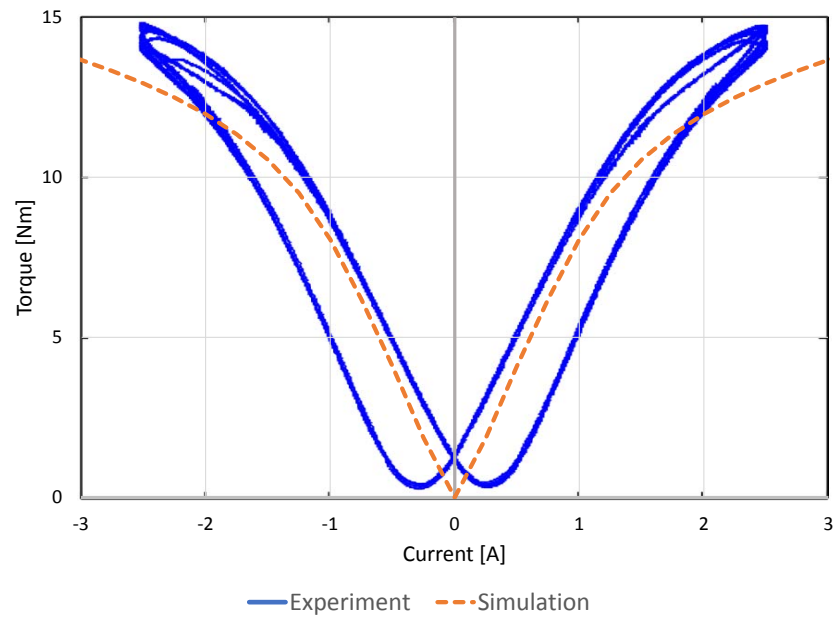
Figure 2.26: Experimental and simulated results for the MR clutches used in the 5th joint: transmitted torque (N·m) vs. coil input current (A).
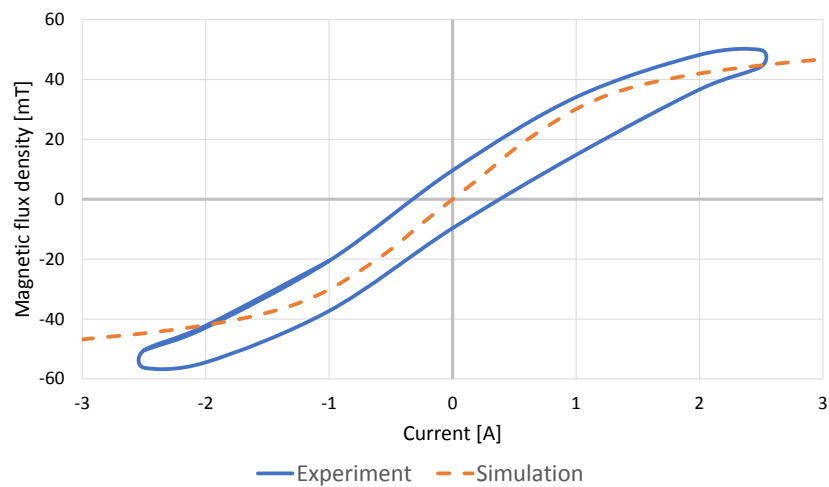
Figure 2.27: Experimental and simulated magnetic flux densities for the 5th joint MR clutch Hall sensor readings (mT) vs. coil input current (A).

dation of the fluid. Therefore, some adjustments or re-calibration of the controller might be needed after a certain period to make sure the torque precision stays at the required level.

Table 2.2: Comparison of the torque-to-weight ratio for MR clutches at the same current density (8 A/mm^2) in the electromagnetic coil

MR clutch (MRC) or MR brake (MRB)	(a) Joint 5 MRC for 5-DOF robot	(b) Joint 3 MRC for 5-DOF robot	(c) Joint 2 MRC for 5-DOF robot	(d) Hollowed M.-Drum MRB, [17]	(e) Serpentine flux path MRB, [18]	(f) 5N·m compact MRC, [19]	(g) 40N·m compact MRC, [19]	(h) MRB for RMRA, [20]
Type	Disk	Disk	Disk	Drum	Drum	Disk	Disk	Disk
Weight [kg]	1.8	4.3	6.9	0.232	2.2	0.237	2.2	0.6
Max torque [N·m]	21	92	223	1.08	10.9	5	40	31.5
Gap size [mm]	0.4	0.4	0.4	0.3	0.25	0.05	0.05	0.2
Number of gaps	18	16	20	4	1	18	50	27
Number of coil turns	200	370	440	305	800	191	200	965
Wire gauge	20 AWG	20 AWG	20 AWG	30 AWG	26 AWG	32 AWG	26 AWG	26 AWG
Wire current [A] for 8 A/mm^2 current density	4.13	4.13	4.13	0.4	1	0.25	1	1
Torque [N·m] for 8 A/mm^2 current density	27	104	393	0.475	9.8	2.1	44	29
Torque-to-weight ratio [N·m/kg] for 8 A/mm^2 current density	15.2	27.3	52.7	2.1	4.5	8.9	20.0	48
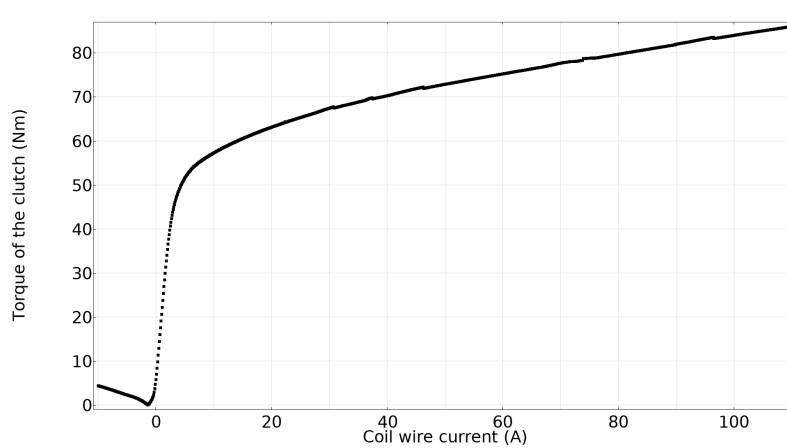
Figure 2.28: Transmitted torque (N·m) vs. wire current (A) for the 5th joint MR clutch (0.2 mm gap and with the permanent magnet installed) calculated for the wide range of the input current (COMSOL simulation).

2.6 Comparison of the different MR clutches reported in the literature

To evaluate the characteristics of the developed clutches, their torque performance was compared with several MR clutches and MR brakes previously reported in the literature.

It was noted that a simple comparison of the torque-to-weight ratio (TWR) or a torque-to-volume ratio (TVR) of different devices in many times did not provide an adequate result. It is because the value of the (maximum) input current through the electromagnetic coil has a significant effect on both TWR and TVR. To show this, let us consider the results for the 5th joint MR clutch shown in Fig. 2.28. As seen, the transmitted torque at the wire current of 100 A is about 84 N·m giving a TWR value of 47 N·m/kg. On the other hand, the same clutch, produces 40 N·m for the input current of 2.5 A, giving a TWR value of 22.2 N·m/kg. It could be impractical to pass 100 A through 21 AWG wire unless for a very short time, but this example demonstrates how the maximum current can sway the values of TWR and TVR.

To provide a fair comparison, we propose to compare the torque of the MR devices at the same current density through the electromagnetic coil. Fig. 2.29 shows the TWR of several different MR clutches versus the current density in the coil.

As observed, the TWR curve for each clutch reaches a certain position relative to other TWR curves beyond a certain current density (i.e., beyond 5 A/mm^2). This position remains relatively the same with respect to the TWR of other clutches for higher values of current density. Thus, it is more meaningful to compare the performance of the MR devices for the same current density that is within the maximum permissible current range for each particular clutch.

For the selected clutches and brakes, we performed the comparison at 8 A/mm^2 wire current density (marked with the orange vertical line in Fig. 2.29). The results of the comparison are shown in Table 2.2. It is not a comprehensive list of devices due to the lack of necessary information in the description of some of the clutches and brakes reported in the literature (e.g., the coil wire cross-section area (or gauge) or the number of turns in the coil is often
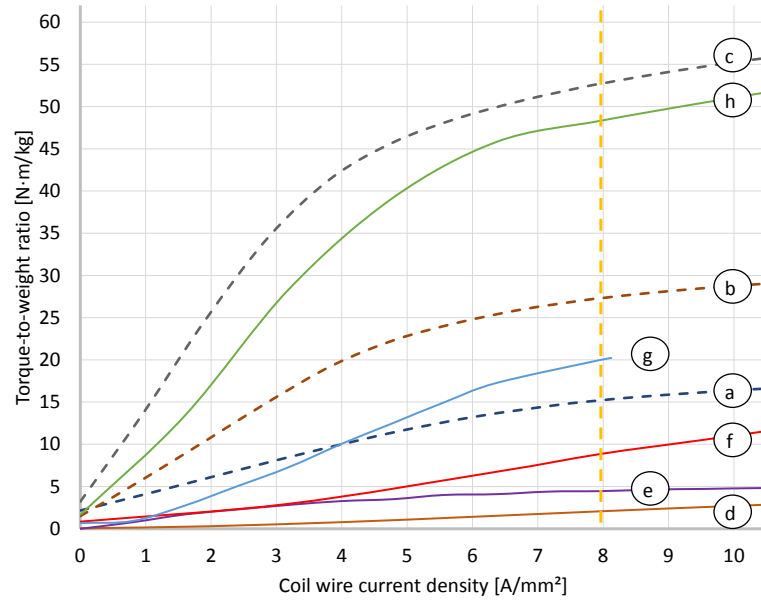
Figure 2.29: Torque-to-weight vs. wire current density for MR clutches and MR brakes: (a) - 5th joint MRC for 5-DOF robot; (b) - 3rd joint MRC for 5-DOF robot; (c) - 2nd joint MRC for 5-DOF robot; (d) - Hollowed M.-Drum MRB, [17]; (e) - Serpentine flux path MRB, [18]; (f) - 5N·m compact MRC, [19]; (g) - 40N·m compact MRC, [19]; (h) - MRB for RMRA, [20].

missing in publications).

The results clearly show the advantages of our presented design. Taking into account a relatively large gap size used in the clutches (0.4 mm for facilitating manufacturing), the small number of disks, and embedded Hall sensors, our proposed design shows an excellent torque-to-weight ratio that surpasses many alternative designs. Our 2nd joint MR clutch offers the highest TWR that rivals one of the highest previously reported data in the literature [20].

2.7 Conclusion

In this chapter the implementation of several design improvements, complete analysis, and prototype development for high torque-to-mass ratio MR clutches presented. Furthermore, the feasibility of building actuators with enhanced performance for compliant actuation is demonstrated.

A new arrangement for the Hall sensors outside the active zone is proposed. The feasibility of the proposed placement of the Hall sensor is experimentally validated.

The use of permanent magnets for partial magnetization of the MR clutch is presented and comprehensively analyzed. As a result of these design improvements and fine-tuning of the geometry of the MR clutch, a torque-to-mass ratio of 14.6 N·m/kg for the MR clutches (with 3.2 Watt power consumption) is obtained. The reduction of the gap size between the disks from 0.4 mm to 0.2 mm combined with increasing the total number of disks allows to further improve the torque-to-mass ratio of the MR clutches to 27 N·m/kg with the same power consumption.

Experimental results using prototype MR clutches confirm the validity of the proposed

approaches. The results show good agreement with those obtained from simulations and it confirms the correctness of the results obtained using FEA.

The design of a pair of antagonistic MR clutches with joined magnetic core presented along with a detailed analysis of the design to enhance the compactness of the actuator without jeopardizing its performance.

Some of the design issues that require further investigations and improvements include increased friction forces inside the MR clutch due to decreased gap size between the disks, additional power consumption to counteract the magnetic flux of the permanent magnets and avoid partial "on-state" of the MR clutch, possible change of MR fluid properties over time and subsequent change of the precision of the Hall sensor-based torque control.

Bibliography

[1] S. Pisetskiy and M. Kermani, "High-performance magneto-rheological clutches for direct-drive actuation: Design and development," *Journal of Intelligent Material Systems and Structures*, p. 1045389X211006902, 2021.

[2] S. Pisetskiy and M. R. Kermani, "Development of mr clutch for a prospective 5 dof robot," in *2018 IEEE/RSJ International Conference on Intelligent Robots and Systems (IROS)*. IEEE, 2018, pp. 5900–5905.

[3] M. Kermani and A. Shafer, "Magneto-and electro-rheological based actuators for human friendly manipulators," Feb. 14 2017, uS Patent 9,566,715.

[4] W. Li, P. Yadmellat, and M. R. Kermani, "Design optimization and comparison of magneto-rheological actuators," in *2014 IEEE International Conference on Robotics and Automation (ICRA)*.   IEEE, 2014, pp. 5050–5055.

[5] R. W. Phillips, "Engineering applications of fluids with a variable yield stress," Ph.D. dissertation, University of California, Berkeley, 1969.

[6] Q.-H. Nguyen and S.-B. Choi, "Optimal design of a novel hybrid mr brake for motorcycles considering axial and radial magnetic flux," *Smart Materials and Structures*, vol. 21, no. 5, p. 055003, 2012.

[7] ——, "Selection of magnetorheological brake types via optimal design considering maximum torque and constrained volume," *Smart Materials and Structures*, vol. 21, no. 1, p. 015012, 2011.

[8] "Mrf-140cg magneto-rheological fluid," Lord Technical Data, 2008. [Online]. Available: http://www.lordmrstore.com

[9] O. Erol, B. Gonenc, D. Senkal, S. Alkan, and H. Gurocak, "Magnetic induction control with embedded sensor for elimination of hysteresis in magnetorheological brakes," *Journal of Intelligent Material Systems and Structures*, vol. 23, no. 4, pp. 427–440, 2012.

[10] W. Li, P. Yadmellat, and M. R. Kermani, "Linear torque actuation using fpga-controlled magneto-rheological actuators," in *2014 IEEE International Conference on Robotics and Automation (ICRA)*.   IEEE, 2014, pp. 1060–1065.

[11] W. Song, S. Wang, S.-B. Choi, N. Wang, and S. Xiu, "Thermal and tribological characteristics of a disc-type magnetorheological brake operated by the shear mode," *Journal of Intelligent Material Systems and Structures*, vol. 30, no. 5, pp. 722–733, 2019.

[12] M. Moghani and M. R. Kermani, "A lightweight magneto-rheological actuator using hybrid magnetization," *IEEE/ASME Transactions on Mechatronics*, 2019.

[13] P. Yadmellat and R. V. Patel, "Frequency response analysis of magneto-rheological clutch designs," *Journal of Intelligent Material Systems and Structures*, vol. 29, no. 5, pp. 905–923, 2018.

[14] M. Moghani and M. R. Kermani, "Design and development of a hybrid magneto-rheological clutch for safe robotic applications," in *2016 IEEE International Conference on Robotics and Automation (ICRA)*.   IEEE, 2016, pp. 3083–3088.

[15] A. Shafer and M. R. Kermani, "Magneto-rheological clutch with sensors measuring electromagnetic field strength," Jan. 10 2017, uS Patent 9,539,731.

[16] P. Fauteux, M. Lauria, B. Heintz, and F. Michaud, "Dual-differential rheological actuator for high-performance physical robotic interaction," *IEEE Transactions on Robotics*, vol. 26, no. 4, pp. 607–618, 2010.

[17] H. Qin, A. Song, and Y. Mo, "Performance evaluation of a hollowed multi-drum magnetorheological brake based on finite element analysis considering hollow casing radius," *IEEE Access*, vol. 7, pp. 96 070–96 078, 2019.

[18] D. Senkal and H. Gurocak, "Serpentine flux path for high torque mrf brakes in haptics applications," *Mechatronics*, vol. 20, no. 3, pp. 377–383, 2010.

[19] T. Kikuchi, K. Otsuki, J. Furusho, H. Abe, J. Noma, M. Naito, and N. Lauzier, "Development of a compact magnetorheological fluid clutch for human-friendly actuator," *Advanced Robotics*, vol. 24, no. 10, pp. 1489–1502, 2010.

[20] H. Ma, B. Chen, L. Qin, and W.-H. Liao, "Design and testing of a regenerative magnetorheological actuator for assistive knee braces," *Smart Materials and Structures*, vol. 26, no. 3, p. 035013, 2017.

Chapter 3

5-DOF Manipulator: Mechanical Design

Parts of the material in this chapter are published in materials of "Workshop on Physical human-robot interaction: a design focus" at "2019 International Conference on Robotics and Automation (ICRA), 2019, Montreal, Canada." [1]

This chapter presents the architecture and mechanical design of a 5-DOF manipulator based on magneto-rheological clutch actuation. The compliant behavior of the manipulator is achieved using an antagonistically working pair of MR clutches in each joint of the robot. The drive train of the manipulator consists of a single brushless DC motor located at the base of the robot, a system of shafts, gears, and belts, and 5 pairs of antagonistic MR clutches. Multiple design concepts for the development of the manipulator's drive train are presented and the advantages and disadvantages of each concept are described. The most efficient drive train concept is further developed and the design of the entire manipulator including the mechanical structure of the links and joints, transmission mechanism, and motor power/data wiring is presented.

3.1 Introduction

The development of a multi-degrees of freedom robotic manipulator is a complex task that requires combining several research areas, solving different engineering tasks, and optimizing interconnected systems and components. In this work, the focus is set to designing a low-cost robotic system based on distributed antagonistic MR clutch actuation approach.

The performance of the distributed MR clutch actuation as a whole depends on the performance of the clutches. However, the quality of the transmission and primary source of motion (i.e. motor) has little or no effect on the actuation as long as the torque is enough and the speed of the clutch rotor is greater or equal to the required speed of the corresponding link. Mechanical, electro-mechanical, hydraulic, pneumatic, or any other actuation can be used as the primary actuation source with minimum or no negative effect on the torque control, position control, or the bandwidth of the actuator.

The actuated loads can be at different locations (non-collocated) with respect to each other and/or the primary source of motion. This provides significant flexibility in the design without compromising the actuation performance due to friction and/or backlash often seen in non-collocated actuation.

Due to the antagonistic nature of the actuator, the bandwidth of the actuation could be significantly higher than that of the conventional servo-actuators. In many cases, the overall mass of the actuation mechanism is lower than the combination of electromagnetic motors and reduction gearboxes for all the multiple joints.

3.1.1 Manipulator design requirements

At the very beginning of the project, the desired parameters for the manipulator are identified such as compliance, the number of degrees of freedom, the number of motors, the payload, and the outreach. Additionally, the desired robotic manipulator is intended for use in science and education, so it should be relatively simple to upgrade, repair, modify, and integrate into future research projects.

Taking into account parameters of the most popular and effective manipulators, such as UR3/5/10 [2] from Universal Robots, Kinova JACO robotic arm [3, 4, 5], Franka Emika [6], YuMi from ABB [7], KUKA collaborative robots [8, 9], an anthropomorphic elbow configuration (Fig. 3.1 (left)) with revolute joints is chosen as the kinematic arrangement for the prospective 5-DOF robotic arm.
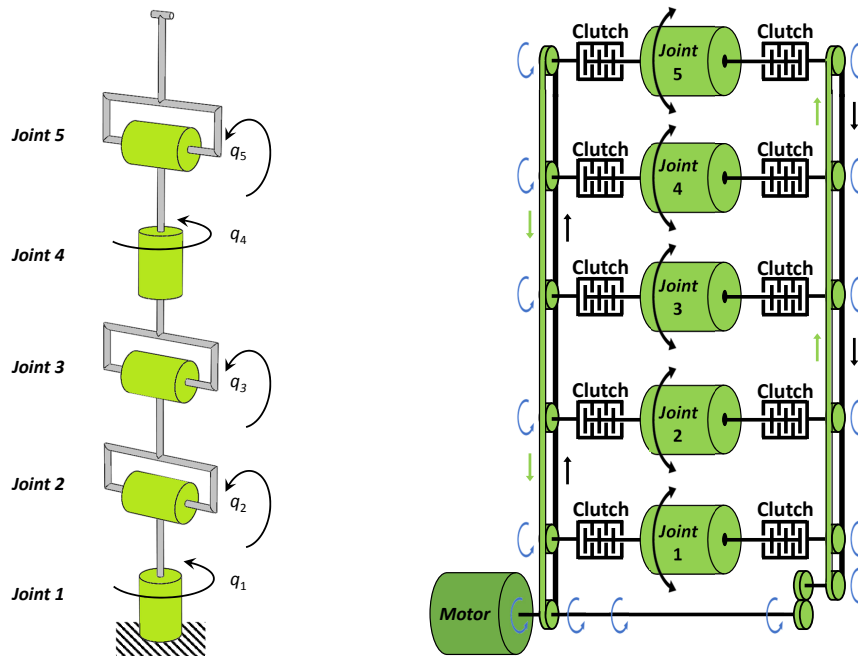
Figure 3.1: Symbolic representation of the chosen kinematic arrangement for a 5-DOF manipulator (left) and the distributed antagonistic actuation of MR clutches a; all 5 joints (right).

The intended manipulator is required to have a maximum payload of 10 kg, and a reach of 900 mm minimum. A single motor is intended to drive all 5 joints, each of which includes a pair of MR clutches in an antagonistic configuration. It is designed to use a distributive actuation approach schematically shown in Fig. 3.1 (right).

3.1.2 Additional design considerations

Additional design requirements are as follows,

- The encoders precision in the joints should allow pose pepeatability 0.2 mm.
- MR clutches should be easy to remove for repair and maintenance,
- MR clutches should have optional hybrid magnetization,
- Payload (i.e. end-effector) interface should have separate power and data lines,
- The flange to connect payload (i.e. end-effector) should be similar to KUKA LWR 4+
- The distance between joints 2 and 3, and between joints 3 and 5 should be 400 mm,
- Control boards for the joints should be interchangeable and easy to replace,
- All the wiring should be embedded inside the manipulator links.

3.2 Early design concepts

The proposed distributed antagonistic actuation approach (Fig. 3.1 (right)) can be implemented using various conventional transmission means such as belt, chain, cable, and others. One set of transmission components should provide continual CW rotation to one of the MR clutches in each pair, while another set should provide CCW rotation to the opposing MR clutch in the same pair. All the clutches should be actuated by a single motor rotating in only one direction.

Several different design concepts with various transmission systems were initially considered and evaluated. The three most promising concepts are compared in the following.

3.2.1 Concept 1: Single belt transmission

Concept 1 (Fig. 3.2) represents a transmission system using a single belt.

The motor and the gearbox of the manipulator are located in the first link. A single timing belt passes through all 5 joints of the manipulator.

The portion of the belt moving from joint 1 to joint 5 rotates one clutch of every joint in a one direction, while the portion moving back from joint 5 to joint 1 rotates the another clutch of every pair in the opposite direction. The axis of rotation of every clutches oriented parallel to the ground when the manipulator is in the initial vertical position. The 1st joint and the 4th joint use bevel gears to provide 90° rotation between the axes of rotation of MR clutches and that of the joint.

The axis of the motor and the gearbox are parallel to the ground. The motor is fixed below the gearbox and both components are attached outside of the 1st link leaving inside space for the belt and pulleys.

A single belt allows minimizing the diameter of the links, decreasing the height of the 1^{st}st link, reducing the number of receiving pulleys in the joints and using a single tension mechanism in the robot. On the other hand, a single belt requires a number of additional guiding pulleys to ensure sufficient contacts between the belt and the receiving pulleys. And small bending radii when passing through the guiding and tension pulleys reduces the belt durability. Furthermore, movement of joint 4 induces significant twisting of the timing belt inside 4th link. All these factors require improved flexibility of the timing belt and introduce additional stresses that may negatively affect the endurance of the transmission.
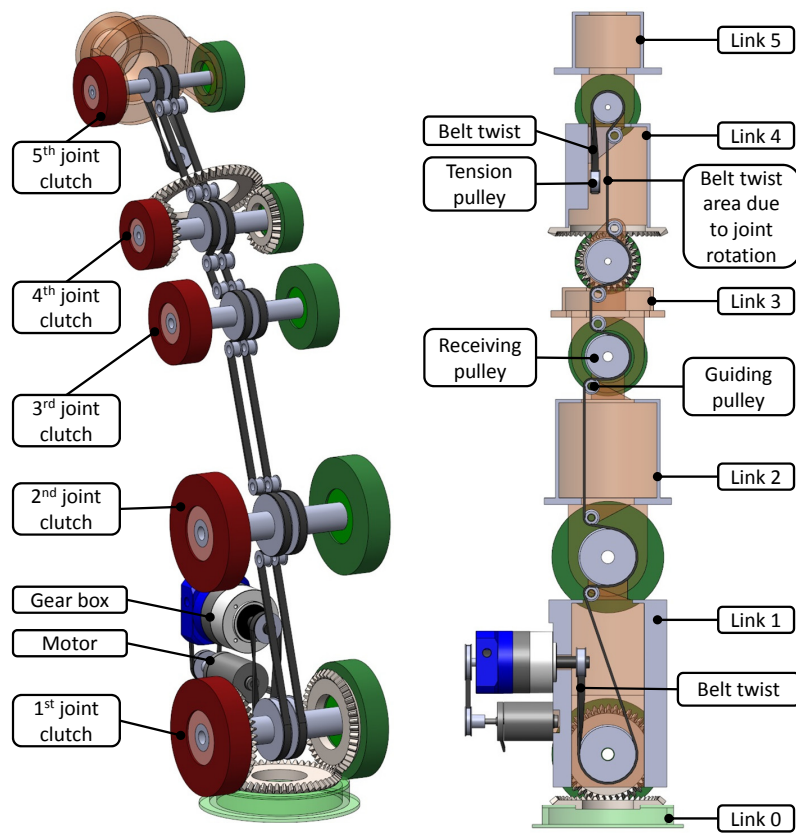
Figure 3.2: Concept 1: 5-DOF robot with a single belt transmission.

Finally, due to limited belt twisting ability, joint 4 may have some limitations in rotational angle.

3.2.2 Concept 2: Shaft transmission

Concept 2 (Fig. 3.3) represents a manipulator with the shaft transmission.
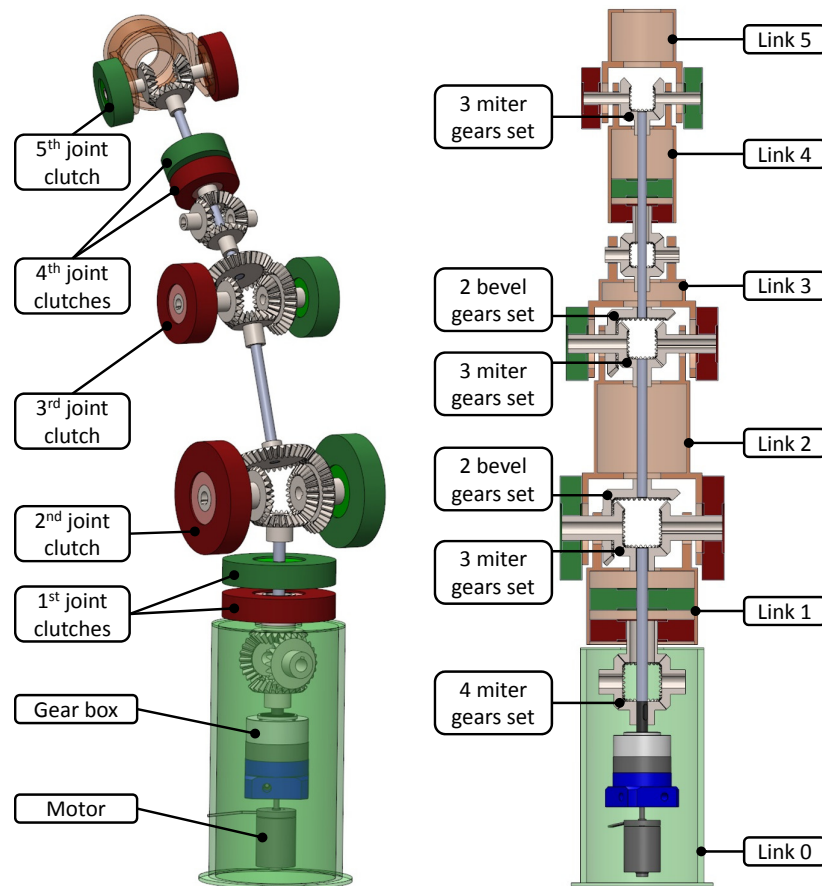
Figure 3.3: Concept 2: 5-DOF robot with the shaft transmission.

In this concept, miter and bevel gears are used at each joint to ensure rotation of the clutches in opposite directions. Additional bevel gear pairs are used at 2nd and 3rd joints to transmit the motion to upper links without compromising the joint flexibility.

The axis of rotation of clutches in joints 2, 3, and 5 are oriented parallel to the ground when the manipulator is in the initial vertical position. The clutches in joints 1 and 4 are oriented with their axis of rotation perpendicular to the ground. Two concentric shafts are used for the 1st and 4th joints to deliver opposite rotation from miter gears to the clutches.

The axis of the motor and the gearbox located in the base is perpendicular to the ground. The motor is fixed below the gearbox and both components are fixed inside the housing of link 0 of the manipulator.

Using shafts allows an increase in the range of joint movements without a negative effect on transmission endurance. Arrangement of the motor and gearbox inside the link 0 housing

reduces the footprint of the manipulator. On the other side, the height of the base has to be increased to accommodate all the components. Additionally, the utilization of the miter and bevel gear sets at every joint of the robot increases the total weight of the transmission.

3.2.3 Concept 3: Shaft and multiple belt transmission

Concept 3 (Fig. 3.4) represents a combination of shaft and multiple belt transmission.
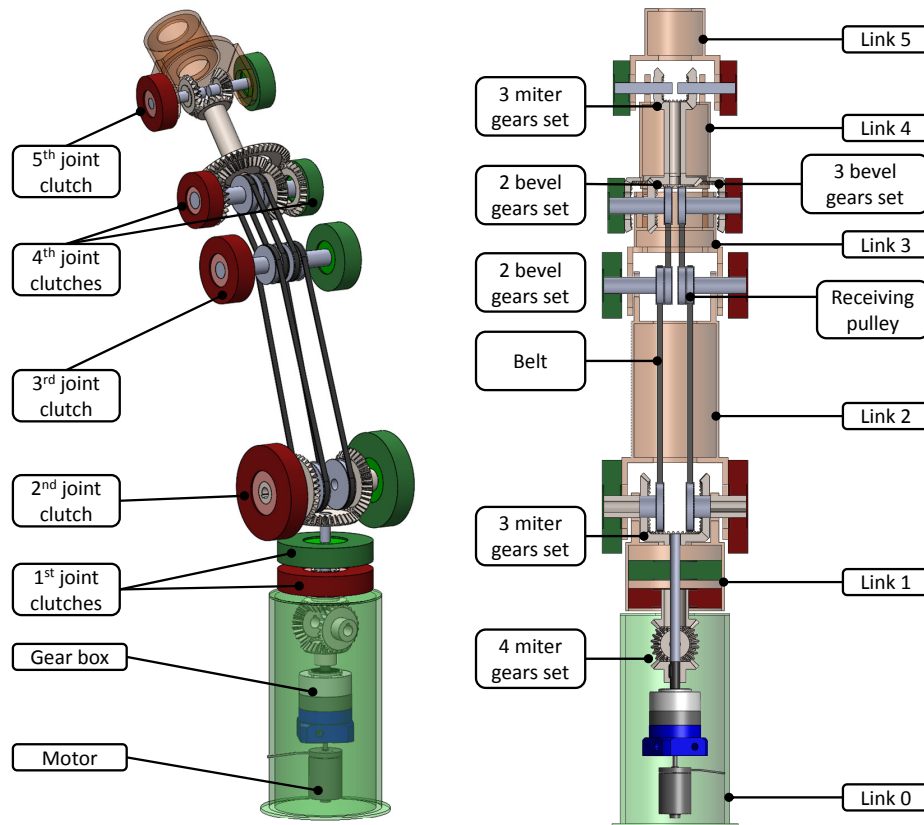
Figure 3.4: Concept 3: 5-DOF robot with shaft and multiple belt transmission.

In this concept, the rotational motion of a single motor is transmitted to the 1st and 2nd joints through the set of shafts and miter gears. However, transmission to the 3rd and 4th joints is performed through two pairs of belts. Transmission to the last 5th joint is realized again through a shaft and a set of miter gears.

The axis of rotation of clutches in joints 2, 3, 4, and 5 are oriented parallel to the ground when the manipulator is in the initial vertical position. Only the clutches in joint 1 are oriented with their axis of rotation perpendicular to the ground. Two concentric shafts are used in the 1st joint to deliver opposite rotation from miter gears to the clutches.

Similar to Concept 2, the axis of the motor and the gearbox located in the base is perpendicular to the ground. The motor is fixed below the gearbox and both components are fixed inside the housing of link 0 of the manipulator.

Using timing belts with aluminum pulleys between 2nd, 3rd and 4th joints instead of a shaft and an additional miter gear set allows to reduce the weight and complexity of the transmission.

In the presented timing belt transmission the joints movement does not aggravate the belt's endurance.

3.2.4   Concept 4: Optimized shaft and belt transmission

Concept 4 (Fig. 3.5) represents further development of the combined shaft and belt transmission.
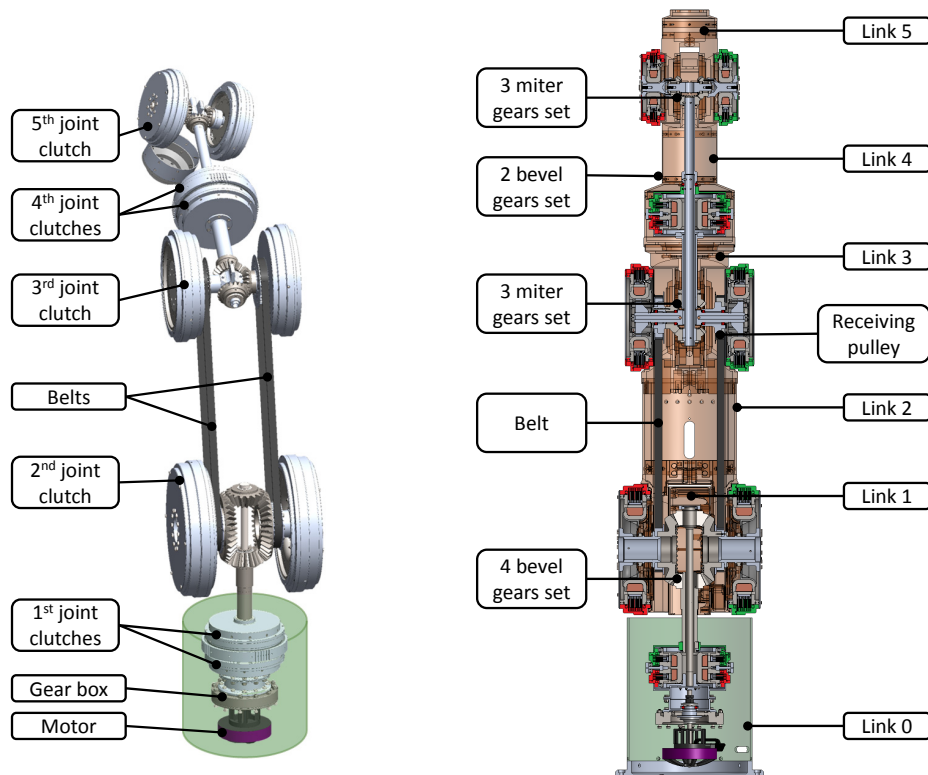
Figure 3.5: Concept 4: 5-DOF robot with combined shaft and belt transmission.

In the concept, only one pair of belts is used to transmit rotation between 2nd and 3rd joints. One set of 4 bevel gears located in the 2nd joint derives rotation in opposite directions for two joints at the same time: for the 1st and for the 2nd joint. A set of 3 miter gears in the 3rd derives antagonistic rotation for the 4th joint. Finally, 3 miter gears at the 5th joint receive unidirectional rotation from a shaft and derive rotation in opposite direction for the clutches in joint 5.

The axis of rotation of clutches in joints 2, 3, and 5 are oriented parallel to the ground when the manipulator is in the initial vertical position. The clutches in joints 1 and 4 are oriented with their axis of rotation perpendicular to the ground. Two concentric shafts are used for the 1st and 4th joints to deliver opposite rotation from bevel and miter gears to the clutches.

Using a single set of miter or bevel gears to actuate two joints at the same time allows to further reduce the weight and complexity of the robot transmission. In the timing belt transmission the joints movement does not aggravate the belt's endurance. The height of the base is reduced due to elimination of the miter gears for the 1st joint.

This last configuration of the transmission system is selected for the implementation in the 5-DOF manipulator design.

3.3   Selected robot concept and design considerations

Concepts 4 provides the best engineering trade-offs between efficiency, cost, simplicity, reliability, and maintainability and is chosen as the preferred transmission design concept for the 5-DOF manipulator. It is further developed into a detailed design. Fig. 3.6 presents the kinematic diagram of the robot next to the computer-aided (CAD) model of the transmission.
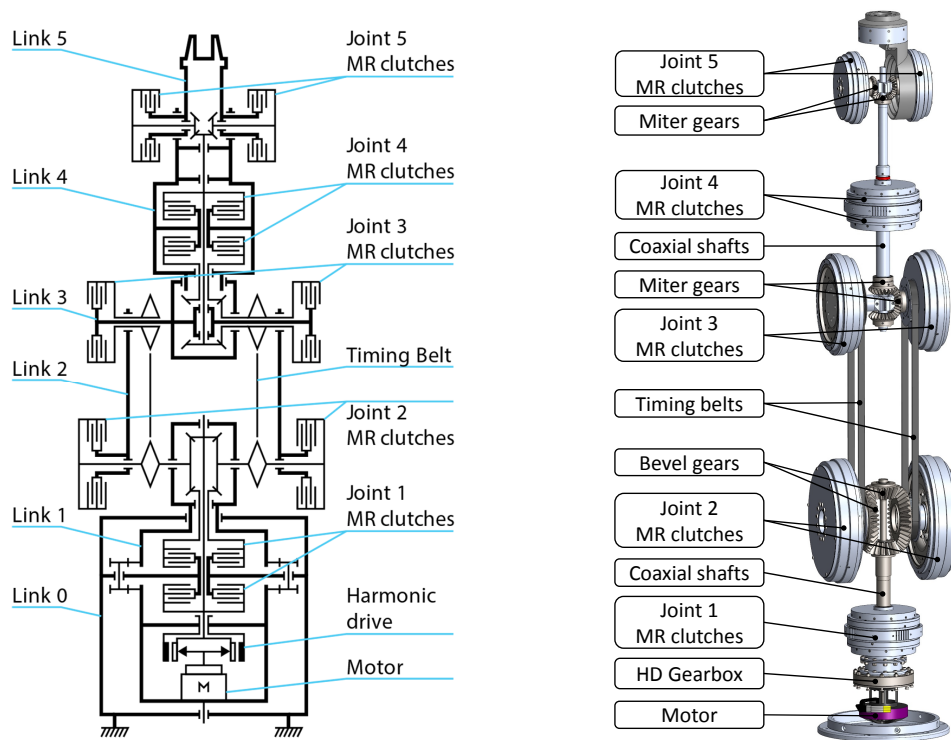
Figure 3.6: Kinematic diagram of the 5-DOF manipulator (left) and the computer aided (CAD) model of the transmission (right).

As it is shown on the kinematic diagram, the output of the motor with the gearbox provides rotation to the clutches of the 1st joint and a set of bevel gears (within the 2nd joint) using two coaxial shafts with the bevel pinions. The clutches of the 2nd joint are driven using two bevel gears coupled to the pinions. The clutches of the 3rd joint receive rotational motions from a belt system consisting of two timing belts moving in opposite directions. The clutches of the 4th joint are driven using a pair of coaxial shafts coupled to the miter gears in the 3rd joint. The miter gears are actuated by only one timing belt to avoid the joint mechanical lock.

Finally, the MR clutches of the 5th joint are driven using a single shaft and a set of miter gears in the joint. The single shaft is connected to the external hollow shaft that delivers rotation to the top clutch in the 4th joint.

3.3.1   Angular velocities modelling for serial transmission

Due to the serial nature of the chosen transmission concept, the speed of each subsequent element (MR clutch rotor) depends not only on the motor velocity but also on the speed of all the previous joints in series (see Fig. 3.7).
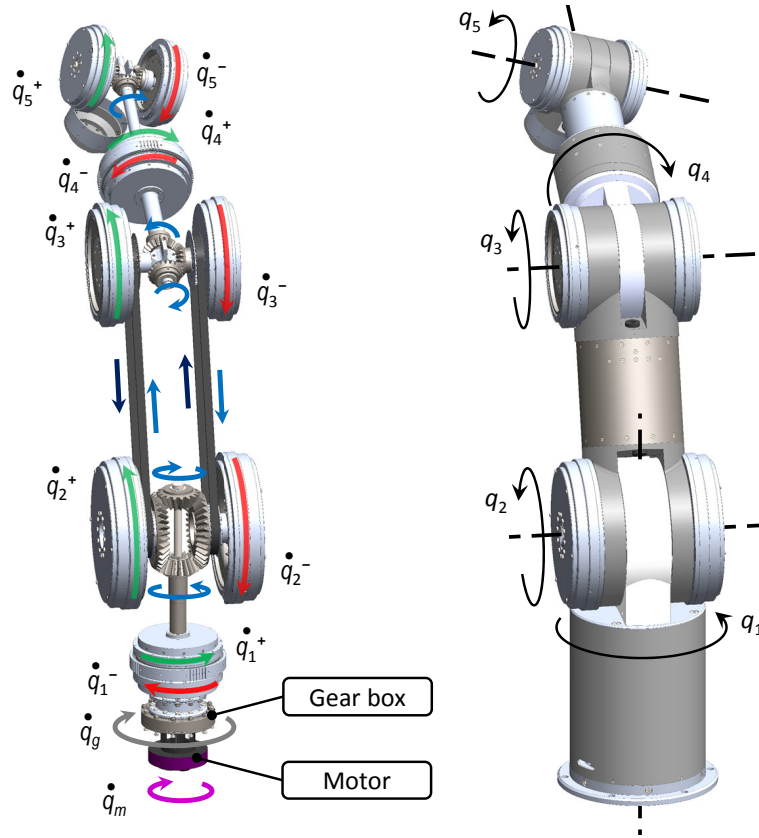
Figure 3.7: Angles for manipulator transmission modelling.

Based on the geometrical characteristics of the transmission components, the relationship between the velocities can be calculated in advance. The relationship should be taken into account in the control system to improve the performance of the manipulator.

For the chosen concept the robot transmission is modeled to calculate the relative angular velocity of rotor and stator for each clutch [10]. Clutch rotor-stator relative velocities depend on the speed of the motor and angular velocities of the robot links in series.

For the selected transmission configuration, the 1st and the 2nd joint are arranged in parallel, while joints 3, 4, and 5 are in series with joint 2. The relationship for angular velocities derived from the robot transmission scheme is given by,

$$
\begin{bmatrix} \dot{\theta}_1^{\pm} \\ \dot{\theta}_2^{\pm} \\ \dot{\theta}_3^{\pm} \\ \dot{\theta}_4^{\pm} \\ \dot{\theta}_5^{\pm} \end{bmatrix} = \pm \begin{bmatrix} n_{m/1} \\ n_{m/2} \\ n_{m/3} \\ n_{m/4} \\ n_{m/5} \end{bmatrix} \dot{q}_m + \begin{bmatrix} -n_{1/1} \\ 0 \\ 0 \\ 0 \\ 0 \end{bmatrix} \dot{q}_1 + \begin{bmatrix} 0 \\ -n_{2/2} \\ -n_{2/3} \\ -n_{2/4} \\ -n_{2/5} \end{bmatrix} \dot{q}_2 + \begin{bmatrix} 0 \\ 0 \\ -n_{3/3} \\ -n_{3/4} \\ -n_{3/5} \end{bmatrix} \dot{q}_3 + \begin{bmatrix} 0 \\ 0 \\ 0 \\ -n_{4/5} \\ +n_{4/5} \end{bmatrix} \dot{q}_4 + \begin{bmatrix} 0 \\ 0 \\ 0 \\ 0 \\ -n_{5/5} \end{bmatrix} \dot{q}_5 \qquad (3.1)
$$

where $\dot{\theta}_i^+ = \dot{q}_i^- - \dot{q}_i$ and $\dot{\theta}_i^- = \dot{q}_i^- - \dot{q}_i$ are relative angular velocities between rotor ($\dot{q}_i^{\pm}$) and stator ($\dot{q}_i$) of a pair of clutches at joint i, $\dot{q}_m$ is motor output angular velocity, $\dot{q}_i$ is the angular velocity of joint i, and $n_{i/j}$ is a gear ratio between joints i and j.

Taking into account the selected ratio for the gearbox (1:100), belt transmission (1:1), bevel (1:2), and miter gear sets (1:1), the relationship is as follows,

$$
\begin{bmatrix} \dot{\theta}_1^{\pm} \\ \dot{\theta}_2^{\pm} \\ \dot{\theta}_3^{\pm} \\ \dot{\theta}_4^{\pm} \\ \dot{\theta}_5^{\pm} \end{bmatrix} = \pm \begin{bmatrix} 0.01 \\ 0.005 \\ 0.005 \\ 0.005 \\ 0.005 \end{bmatrix} \dot{q}_m + \begin{bmatrix} -1 \\ 0 \\ 0 \\ 0 \\ 0 \end{bmatrix} \dot{q}_1 + \begin{bmatrix} 0 \\ -1 \\ -1 \\ -1 \\ -1 \end{bmatrix} \dot{q}_2 + \begin{bmatrix} 0 \\ 0 \\ -1 \\ -1 \\ -1 \end{bmatrix} \dot{q}_3 + \begin{bmatrix} 0 \\ 0 \\ 0 \\ -1 \\ +1 \end{bmatrix} \dot{q}_4 + \begin{bmatrix} 0 \\ 0 \\ 0 \\ 0 \\ -1 \end{bmatrix} \dot{q}_5 \qquad (3.2)
$$

The results of simulations performed using the derived model are presented in Chapter 4.

3.3.2   Refined design characteristics

Taking into account the kinematic arrangement and the selected concept with 5 revolute joints, the intended payload and maximum reach of the robot, approximate weight of the links and clutches, the desired torque at each joint is estimated. Starting from the base (joint 1) the required torques are determined as 20, 200, 80, 20, and 15 N·m, respectively (Table 2.1).

In the developed configuration, a harmonic drive gearbox (HD drive) with a 1:100 ratio is selected as a speed reducer for a gear reduction. The bevel gears in the 2nd joint provide an additional 2:1 gear reduction, a 90-degree change in orientation of the axis of rotation, and opposite direction of rotation for the top clutch in the 1st joint.

The HD gearbox and the inner shaft are required to transmit 180 N·m torque to the bevel gear set in the 2nd joint. The bevel gears and pinions are required to withstand 200 and 100 N·m torque respectively.

For the 1st joint the rotation in one direction is delivered to the bottom clutch rotor straight from the HD gearbox, the opposite rotation is delivered to the top clutch via a hollow shaft capable to transmit 25 N·m.

From the 2nd joint, a pair of timing belts (one for CW and one for CCW direction) deliver rotational motion (torque) to the 3rd joint pair of MR clutches with the ratio 1:1. The timing belt is required to withstand a pulling force of 2300 N.

Two coaxial shafts and a set of miter gears are used to continue torque transmission to the 4th joint pair of MR clutches. As in joint 2, the miter gears in joint 3 provide a 90-degree orientation change in the axis of rotation. As a result, the joint 3 and joint 4 are mutually orthogonal and share a common intersection point. The miter gears are required to transmit 35 N·m nominal torque.

Finally, a single hollow shaft and a set of miter gears complete the torque transmission to the 5th joint pair of MR clutches. The shaft and the miter gears are required to transmit 15 N·m nominal torque.

3.4   Mechanical design: Manipulator links

According to the chosen design concept and the design requirements, the manipulator has 6 links as shown in Fig. 3.8. Below, the mechanical design of each link is described in detail.
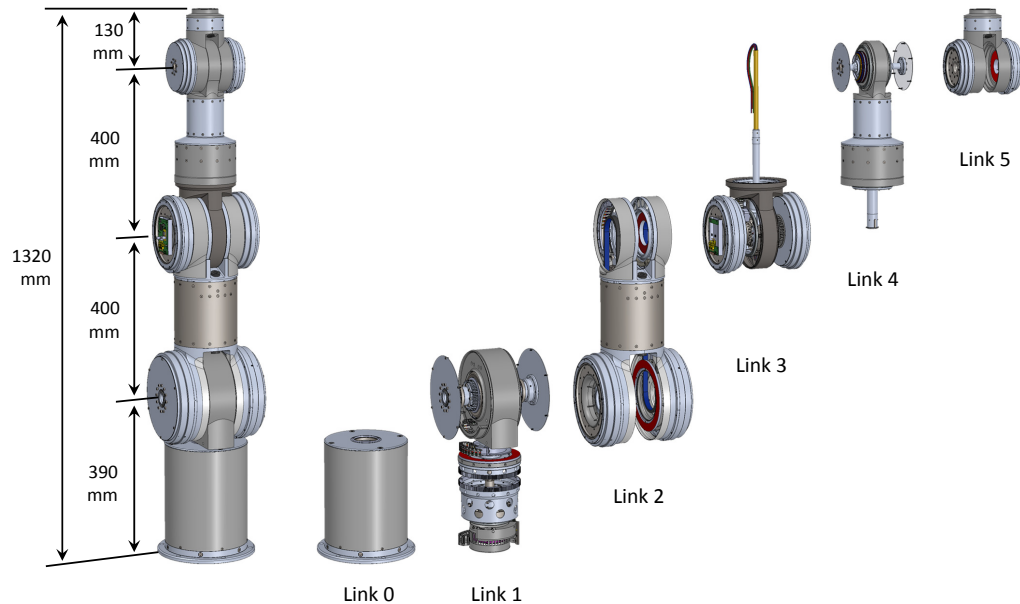
Figure 3.8: CAD model of the 5-DOF manipulator and separated links.

3.4.1   Mechanical design of Link 0 (Base)

Link 0 or a Base of the manipulator (Fig. 3.9) is designed as a rigid cylindrical structure.

The structural frame of the base consists of 3 cylindrical parts interconnected with the M5 bolts and 4 standoffs - structural elements that allow supporting all the load from the upper robot links and a payload. At the bottom, the base has a flange with 8 holes for M6 bolts to fix the manipulator on the horizontal surface. The top of the base is mounted on the standoffs and fixed with four M8 bolts. Between the base top and the upper cylindrical frame, there is a ring-shaped part with the bearing to support the 1st link of the robot. The part also holds a limiter mechanism preventing rotation of the 1st link above 360 degrees.

The stator of the MR clutch pair for the first joint is rigidly connected to the cylindrical frame of the base. The pair divides the inner space of the base into upper and lower areas. The additional spur gear system is used to mechanically connect the top and bottom portions of the 1st link as it is described in 3.5.1. The system consists of 6 pairs of spur pinions mounted on the Link 0 and two spur rings fixed to the Link 1 top and bottom parts.

The bottom flange of the base, as well as the top flange, has a ferromagnetic (carbon steel) strip attached to the inner surface. The strips are used to guide the top and bottom cable chains during the rotation of the Link 1.

Encoder stator (an active component of the encoder Zettlex INC-9-150-171001) is attached to the top base flange. The rotor of the encoder is fixed to the 1st link as shown in Fig. 3.10.
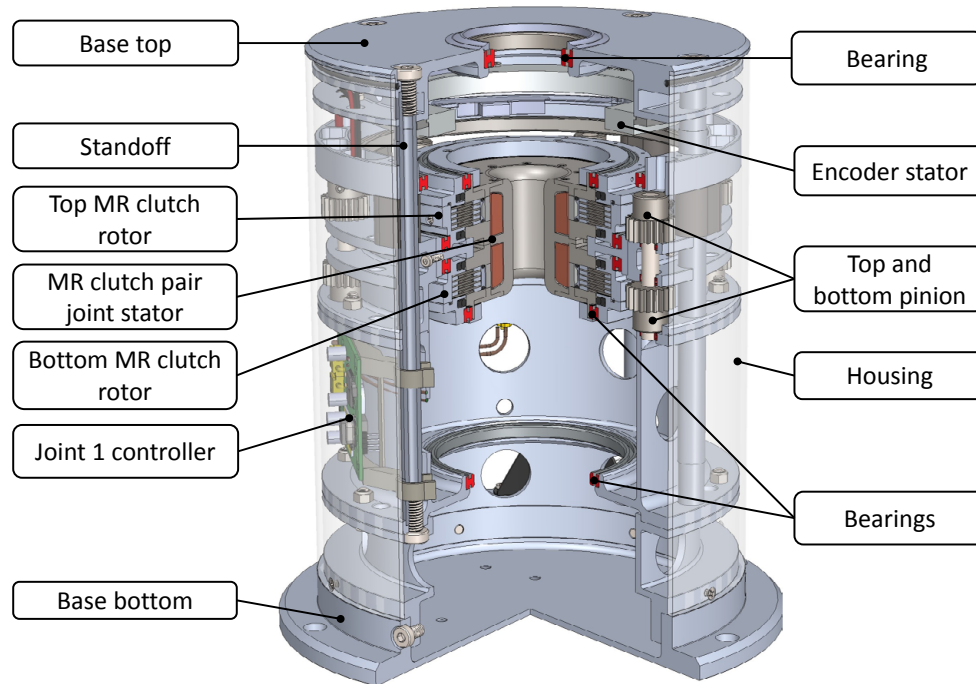
Figure 3.9: CAD model of link 0 (base) of the manipulator (zonal section view).

3.4.2   Mechanical design of Link 1

Link 1 of the manipulator (Fig. 3.9) consists of the joint 1 (lower) and joint 2 (upper) sub-assemblies.

The joint 1 sub-assembly of the link 1, in turn, has top and bottom parts. The bottom part comprises a motor Hacker Q80-13XS, harmonic drive SHD-25-100-2SH (ratio 1:100), and a bottom cable chain with wires to provide electrical power for the motor. The top part of joint 1 sub-assembly has two concentric shafts spinning in the opposite directions, an encoder rotor (a passive component of the encoder Zettlex INC-9-150-171001), and a top cable chain with wires to provide electrical power and data signals to the upper links. The control board for joint 1 is mounted on the side of the sub-assembly and fixed to the standoffs using a plastic board holder.

Both top and bottom parts of joint 1 sub-assembly have spur-rings for the link synchronized rotation as a whole piece. The synchronized movement of the top and bottom parts is explained in detail below in subsection 3.5.2 and demonstrated in Fig. 3.16. Additionally, the top and bottom parts have adapters to drive the 1st joint clutch rotors in opposite directions.

The upper (joint 2) sub-assembly of link 1 consists of a triangular aluminum frame protected with plastic housing. The bevel gear set is composed of 2 bevel gears (KKSP119002GFG) and 2 bevel pinions (KKSP119002GFP) mounted on the frame. The top bevel pinion is mounted on the solid inner shaft, while the bottom pinion is attached to the hollow shaft concentrically placed relative to the solid one. Two timing belt pulleys are mounted on the bevel gear hubs. An encoder stator (an active part of the 17-bit encoder Zettlex INC-9-175-171001) is mounted on one side of the triangular frame, on another side, the cable chain is located to guide the proper movement of the power and data wires passing to Link 2.
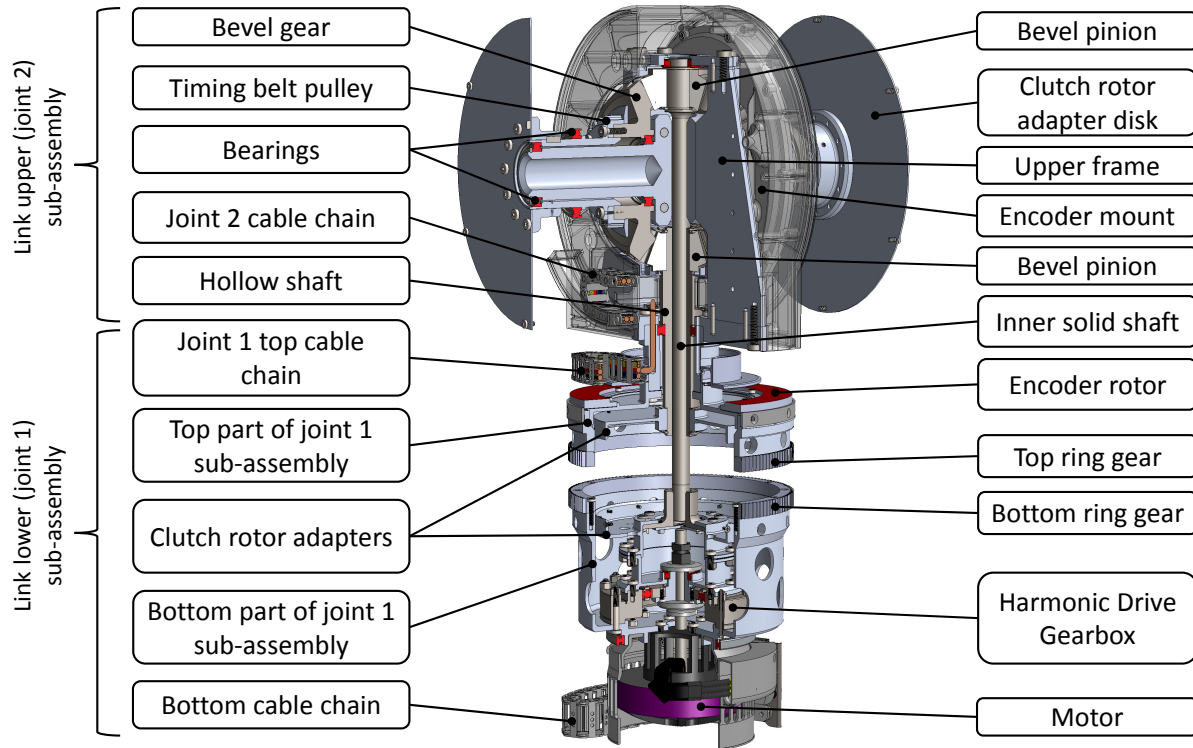
Figure 3.10: CAD model of the 1st link of the manipulator (zonal section view).

The clutch adapter disks are attached to the bevel gears after the timing belt pulleys. The disks transmit the rotation of bevel gears to the rotors of the 2nd joint MR clutches.

3.4.3   Mechanical design of Link 2

Link 2 of the manipulator (Fig. 3.11) comprises a housing with joint 2 fork assembly at one end and joint 3 fork at the other end.

Joint 2 fork is rigidly fixed to the stators of two 200 N·m MR clutches. An encoder rotor (a passive part of the 17-bit encoder Zettlex INC-9-175-171001) is mounted on one side of the fork, while the other side has a ferromagnetic (carbon steel) strip to attract and hold in place the 2nd cable chain.

The link housing plays the role of a structural component to withstand the bending, twisting, and compression forces during operation. Additionally, it holds and protects two timing belts of the transmission, joint 2 control board, wiring ducts, and the belt pretension system that is described in subsection 3.6.

The fork for joint 3 contains the joint 2 cable chain assembly and an encoder stator (the active part of encoder Zettlex INC-4-100-161001).

Both forks for joint 2 and joint 3 have rubber stoppers to limit the movement of link 2 and link 3 respectively.
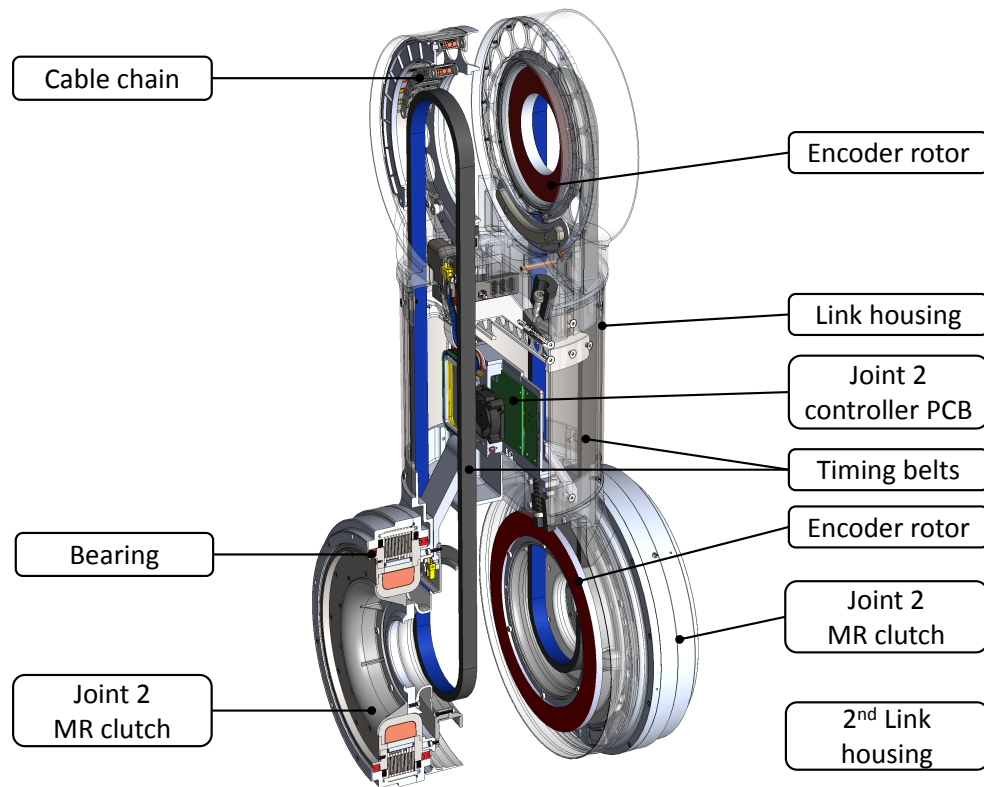
Figure 3.11: CAD model of the 2nd link of the manipulator (zonal section view).

3.4.4 Mechanical design of Link 3

Link 3 of the manipulator (Fig. 3.12) comprises a joint 3 frame and two 80 N·m MR clutches mounted on it. The rotors of both MR clutches are attached to the timing belt pulleys while the stators are rigidly connected to the frame. Via timing belts, the pulleys receive rotation in the opposite directions from the bevel gears in joint 2. The received movement is transmitted to the rotors of the 3rd joint clutches.

Additionally, one of the pulleys is connected to one of the gears of a 3 miter gear set. Two other miter gears in mesh actuate the hollow shafts that transmit the rotation in the opposite directions to the 4th joint MR clutches. The 3rd joint and joint 4 are mutually orthogonal and share a common axis intersection point.

The hollow opening of the inner hollow shaft is used to contain the power and data wiring running from joint 3 to joint 4 and 5. The wires are protected from the moving shaft by the thin-wall brass tube and PTFE liner.

One of the joint 3 MR clutches has the control board mounted on its side. All the wires coming from the clutches and encoder are stowed in the central openings of the joint 3 frame.

To measure the angle of joint 3, the encoder rotor (passive part of 16-bit encoder Zettlex INC-4-100-161001) is mounted on one side of the Link 3 frame. On the other side of the frame, a cable chain for wires passing to Link 4 is mounted.

To measure the angle of joint 4, the encoder rotor (passive part of 15-bit encoder Zettlex INC-4-75-151001) is mounted coaxially with the hollow shafts.
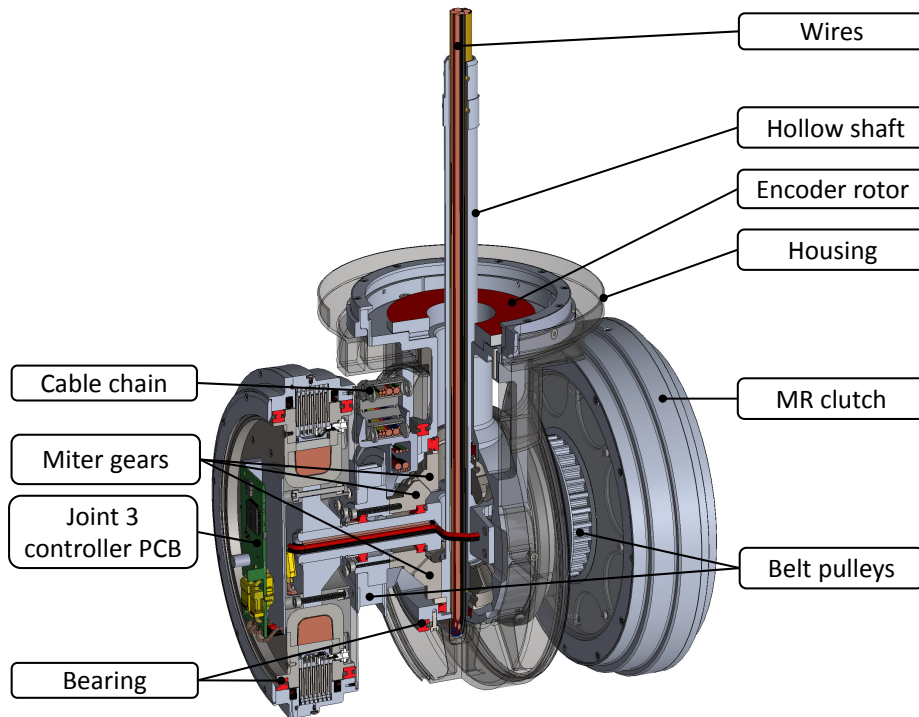
Figure 3.12: CAD model of the 3rd link of the manipulator (zonal section view).

The plastic housing of Link 3 protects the joint components and guides the wires passing to the upper links.

3.4.5 Mechanical design of Link 4

The lower part of link 4 (Fig. 3.13) comprises a pair of 20 N·m MR clutches mounted inside the cylindrical housing. The rotors of the clutches are connected with the adapters to the hollow shafts rotating in the opposite directions. Encoder stator (the active part of 15-bit encoder Zettlex INC-4-75-151001) for measuring the joint 4 angle is attached to the bottom flange of the link.

The middle part of link 4 has 2 control boards, one for joint 4 and one for joint 5. The controllers are located in link 5 above the MR clutches and mounted on a plastic frame. Both boards are interchangeable with each other and with the control boards from other manipulator joints.

The upper part of link 4A has an aluminum frame installed into the plastic housing with an encoder stator (the active part of 15-bit encoder Zettlex INC-4-75-151001) attached on one side. On the other side of the housing, there is a flexible nylon spiral to guide wires around the shaft and ensure its proper bending during joint movement.

There are 3 miter gears mounted on the 5th joint frame that receive the rotation from the hollow shaft and distribute it to the pair of MR clutch adapter disks spinning in the opposite direction. The plastic housing of the 5th joint head has channels to hold the wires coming from the 3rd joint through the hollow shaft and guide them to the control boards.

The joint 5 and joint 4 are mutually orthogonal and share a common axis intersection point.
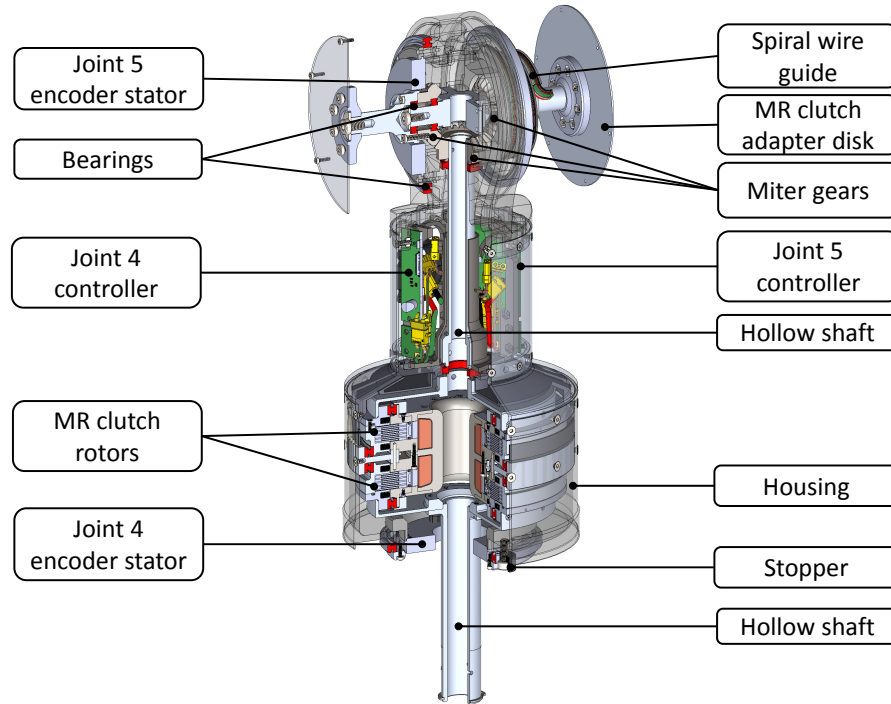
Figure 3.13: CAD model of the 4$^{\text{th}}$ link of the manipulator (zonal section view).

3.4.6 Mechanical design of Link 5

Link 5 of the manipulator (Fig. 3.14) is the simplest in its design.
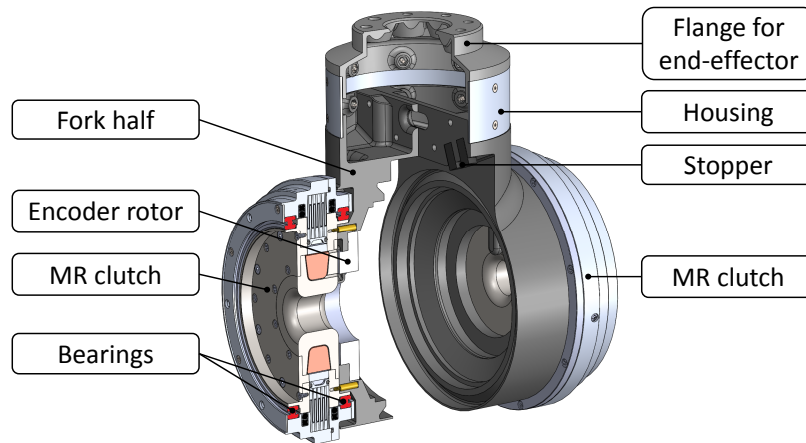
Figure 3.14: CAD model of the 5$^{\text{th}}$ link of the manipulator (zonal section view).

The link has a pair of 15 N·m MR clutches attached to the plastic fork, a short cylindrical housing, and a flange similar to KUKA LWR 4+ manipulator flange.

To measure the angle of joint 5, the encoder rotor (passive part of 15-bit encoder Zettlex INC-4-75-151001) is fixed to the fork next to the MR clutch. The MR clutch stator is attached to the fork using 6 brass standoffs.

3.5 Mechanical design: Joints

The manipulator has 5 revolute joints equipped with two MR clutches and an encoder each. The MR clutches rotate in the opposite directions in an antagonistic configuration. The encoder is used to measure the angular position of the joint. Below the description of the design of each joint is presented.

3.5.1 Mechanical design of Joint 1

The base (link 0) containing the 1st joint is the heaviest part of the robot. The section view of the base with joint 1 is shown in Fig. 3.15. The colors are added to the figure to assist with understanding the arrangement and relative motion of the mechanical components.
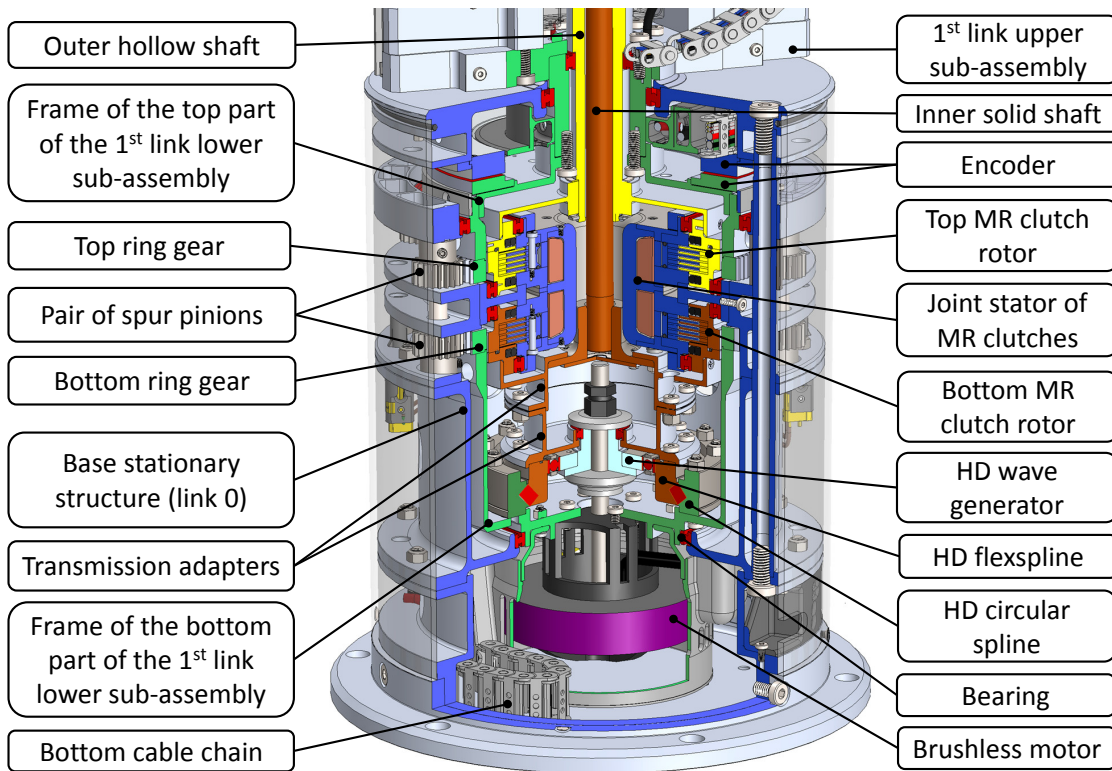
Figure 3.15: Manipulator base with joint 1 section view.

As shown, the inner space of the base (base frame is shown in blue color) is occupied with link 1 lower sub-assembly (link 1 frame is shown in green color) and a pair of MR clutches that rotate link 1 around the vertical axis. The single brushless motor Hacker Q80-13XS F3A that drives all 5 joints is rigidly fixed to the frame of the bottom part of the 1st link lower sub-assembly. The rotation of the motor (maximum 6520 RPM and peak power of 2.7 kW) is reduced by the HD drive SHD-25-100-2SH with the ratio 1:100 attached to the 1st link frame above the motor. The output of the HD drive is directly connected to the rotor of the bottom MR clutch and also to the inner solid shaft going to the 2nd joint through the opening in the center of the clutch pair. All the parts are depicted in ginger color.

The top MR clutch of the 1st joint is driven by the outer hollow shaft coming from the 2nd joint and spinning in opposite direction relative to the inner solid shaft. The hollow shaft, adapter, and top clutch rotor are shown in yellow color.

The frame of the 1st link lower sub-assembly is split into 2 parts to allow the MR clutch stators (also shown in blue) to be rigidly fixed to the base frame through the gap between the parts. To ensure the top and bottom parts of the sub-assembly rotates as one whole, the parts are kinematically connected through the spur gear arrangement. The arrangement consists of 6 pairs of spur pinions and two ring gears: top gear and bottom gear. The top ring gear is mounted on the top part of the 1st link lower sub-assembly, the bottom gear is attached to the frame of the bottom part. Through the pairs of spur pinions, the rotation of the top ring gear is transmitted to the same movement of the bottom ring gear. That ensures the rotation of two separate parts as one unit.

An absolute encoder Zettlex INC-9-150-171001 is mounted at the top of the manipulator base with its rotor attached to the 1st link frame and stator to the top flange of link 0 for angular position measurements.

The upper sub-assembly of the 1st link comprising joint 2 is described next.

3.5.2   Mechanical design of Joint 2

Joint 2 is assembled on the frame of link 1 upper sub-assembly as shown in Fig. 3.16. The colors are added to the figure to assist with understanding the arrangement and relative motion of the mechanical components.
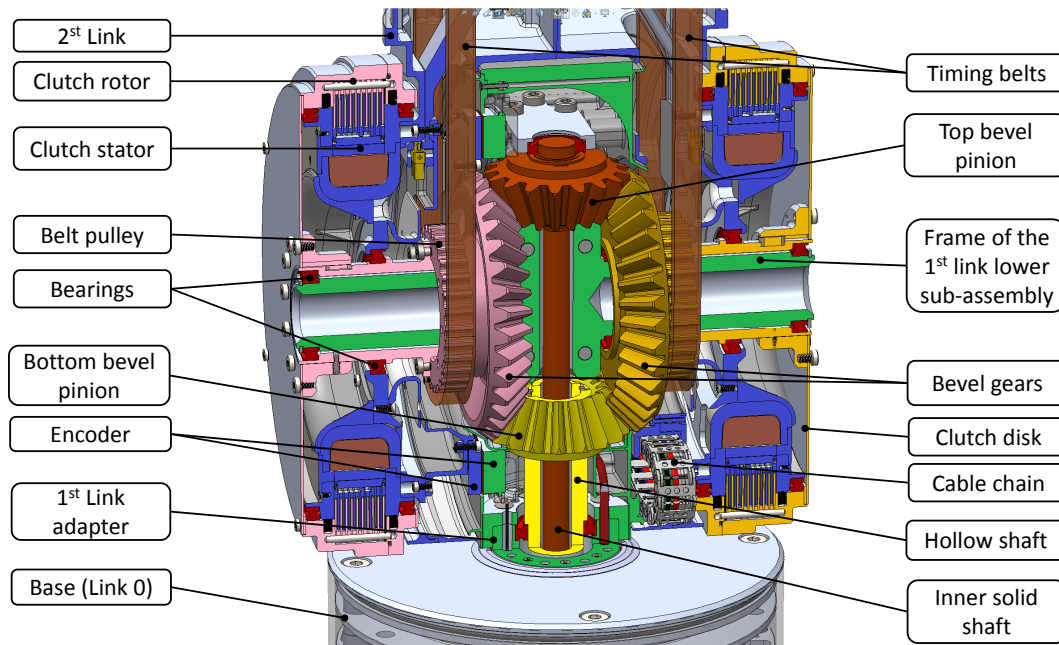
Figure 3.16: Joint 2 section view.

The frame of the 1st link upper sub-assembly (in green color) is mounted on the hollow link adapter (neck) that connects upper and lower sub-assemblies into one rigid structure. The link

comprises a set of bevel gears to produce rotation in two opposite directions for all the joints of the robot. The rotation of the solid inner shaft (driven by the harmonic drive) is transmitted to the bevel pinion on the top of the link. Both solid shaft and top bevel pinion are depicted in ginger color. Two bevel gears on both sides of the frame are in mesh with the pinion and rotate in opposite directions to each other. The reduction ratio between bevel pinion and bevel gear is 1:2. The bottom bevel pinion in mesh with bevels gears rotates in an opposite direction relative to the top pinion. The hollow shaft coming from the bottom pinion transmits the rotation to the rotor of the top MR clutch in the base. Both hollow shaft and bottom bevel pinion are depicted in yellow color.

In addition to the MR clutches, each side bevel gear is connected with the timing belt pulley to transmit the rotation in both directions to the upper joints.

To measure the angular position between link 1 and link 2, the absolute encoder Zettlex INC-9-175-171001 is attached to the link 1 upper frame.

Finally, a cable chain is used to protect and guide the wires during joint 2 movements.

3.5.3   Mechanical design of Joint 3 and Joint 4

Joint 3 MR clutches receive rotation in opposite directions from the 2nd joint using two timing belts as shown in Fig. 3.17. The colors are added to the figure to assist with understanding the arrangement and relative motion of the mechanical components.
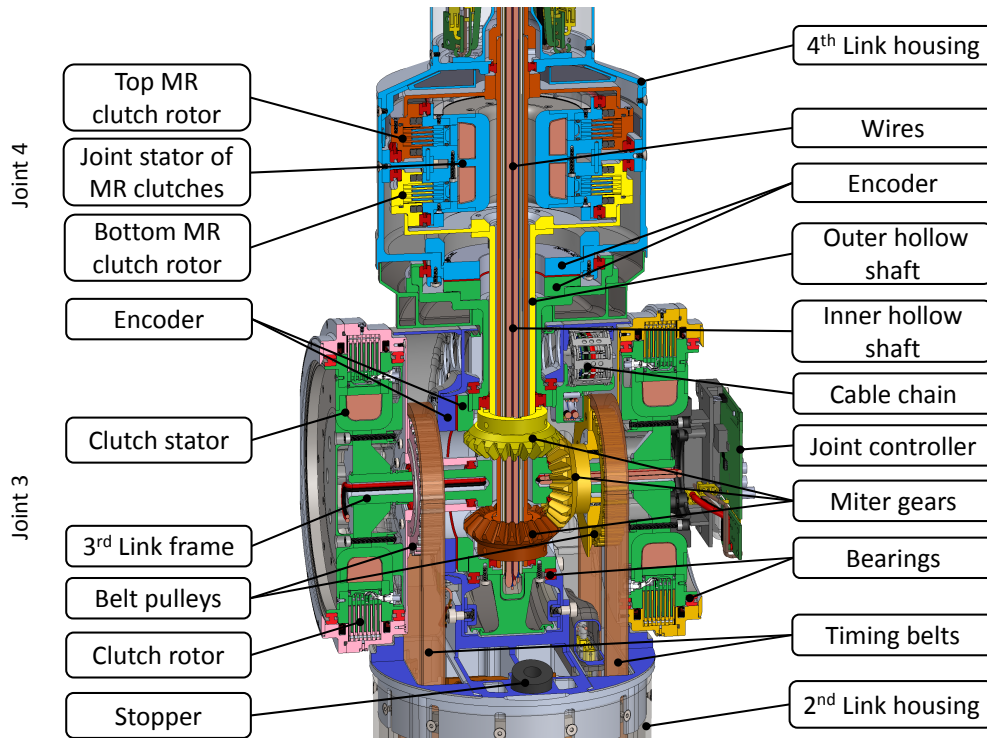

Figure 3.17: Joint 3 and 4 zonal section view.

The belt pulleys are connected to the clutch rotors. One of the pulleys (in orange color) is connected to the miter gear from the set of 3 gears. Two other miter gears (in yellow and

ginger color) are mounted on the concentric hollow shafts transmitting the rotation to the 4th joint. The inner hollow shaft (in ginger color) is connected to the bottom miter gear, the outer hollow shaft (in yellow color) is connected to the top gear. The set of miter gears is used to obtain the rotation at a 90-degree angle in two opposite directions for the MR clutches in joint 4. To measure the angular position between link 2 and link 3, the absolute encoder Zettlex INC-4-100-161001 is used with the stator attached to the 2nd link and the rotor fixed to the side of the 3rd link frame. A cable chain is attached to another side of the frame to protect and guide the wires during joint 3 movements.

Joint 4 (Fig. 3.17) ensures the "roll" rotation of the link 4 perpendicular to the axis of the 3rd joint. The inner hollow shaft transmits rotation from the bottom miter gear to the top MR clutch rotor (in ginger color) and further to the 5th joint, the outer hollow shaft delivers rotation to the rotor of the bottom clutch (depicted in yellow color).

To measure the angular position of the 4th joint, the absolute encoder INC-4-75-151001 is used. The rotor of the encoder is attached to the 3rd link frame, while the stator is attached to the housing of the 4th link (in light blue color).

The wiring running from the 3rd joint to the 5th joint are enclosed in the inner hollow shaft and experience twisting during joint 4 rotation.

3.5.4   Mechanical design of joint 5

The 5th joint receives rotation from the 4th joint through the hollow shaft as seen on Fig. 3.18. The colors are added to the figure to assist with understanding the arrangement and relative motion of the mechanical components.
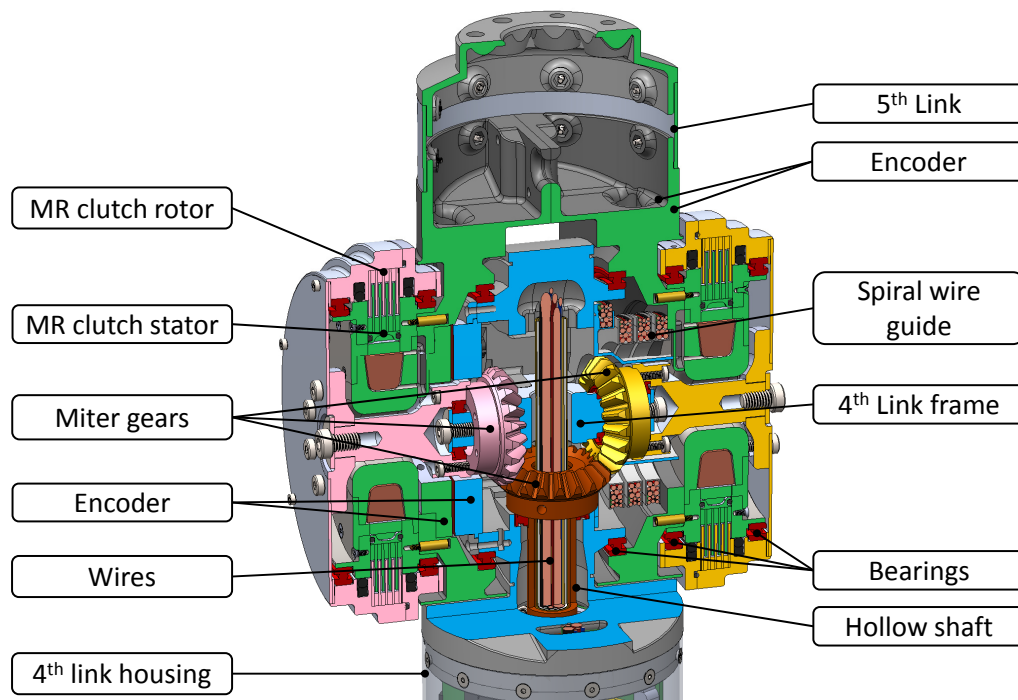
Figure 3.18: Joint 5 zonal section view.

The opening inside the hollow shaft is used to run the wires from joint 3 to joint 5.

The set of miter gears is used to obtain the rotation in opposite directions at a 90-degree angle to the hollow shaft for the MR clutches in joint 5. The rotors of MR clutches are connected to the miter gears with the shaft going through the center of the clutches.

The stator of the absolute encoder Zettlex INC-4-75-151001-ASI1-AC1-5-AN is fixed on the 4th link frame (in light blue color), while the rotor is attached to the 5th link fork structure (in green color).

The flexible nylon spiral guide ensures that wires running from the 4th to the 5th link are properly bending during joint movement.

3.6   Mechanical design: Timing belt pretension arrangement

Timing belts are lightweight and provide quiet, reliable, low maintenance performance, with superior resistance to contamination and wear. However, for normal and reliable operation, the belt tension should be properly adjusted. It is done by varying the distance between two pulleys connected through the belt.

In the presented design, the distance between a pulley in joint 2 and the respective pulley in joint 2 could be adjusted within 10 mm by moving wedges inwards and outwards as shown in Fig. 3.19.
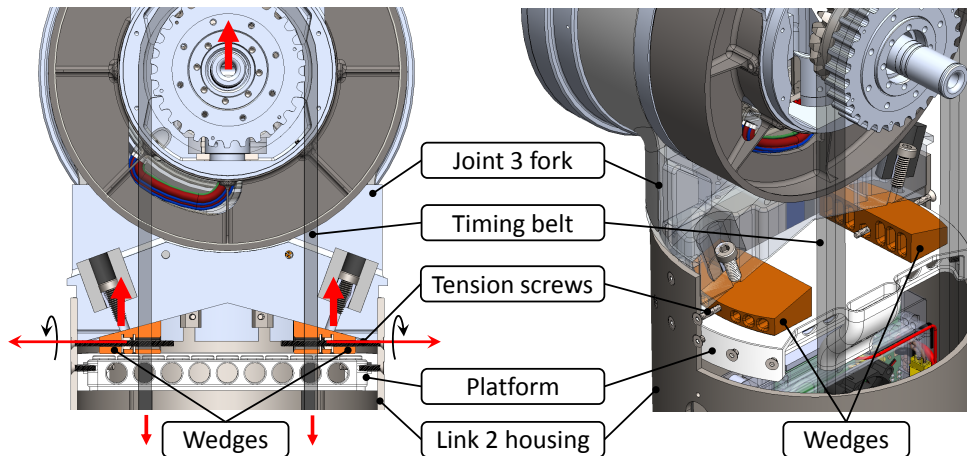
Figure 3.19: Timing belt pretension system.

The movement is performed by adjusting the screws that pull the wedges to the sides of the link 2 housing. The wedges reside on the platform rigidly fixed to the housing. The slanted top of each wedge pushes the joint 3 fork away and increases the overall length of the link 2 as well as the distance between pulleys. The tension of the belt should be checked at least once a year to avoid excessive wear of transmission system components.

3.7 Mechanical design: Materials and structural strength

The weight of the manipulator is a crucial parameter that affects the safety, power consumption, and controllable bandwidth of the system. To achieve the minimum possible weight, light alloys and plastics are extensively used in the construction. The majority of the structural components are made of aluminum alloys 6061, 2024, 6061-T6, 7075-T6. The high-loaded parts such as solid inner shaft (part 10000075B in Fig. 3.21) and shaft adapter (part 10000585A in Fig. C.9) in the base are manufactured from steel alloys to ensure required compactness. Housings, wire holders, brackets, covers, cable chain links are made of plastics (PLA, Nylon, ABS, Taulman Alloy 910). Components of the magnetic circuit in MR clutches are machined from ferromagnetic steel (AISI 1018, 1010).

For critical components, the finite element models (FEM) are created and stress simulations performed to ensure the structural integrity under the predicted loads.

The buckling simulation for one of four standoffs 10000002B that should be able to withstand compression load due to the weight and inertia of the manipulator and payload is shown in Fig. 3.20. The compression load of 800 N, higher than the weight of the manipulator (60 kg) was used in the simulation. The calculated safety factor is 7.7.

Part number:	10000002B
Name:	L00 Standoff
Material:	2024-T4
External torque:	0 N·m
External force:	800 N

Load factor: 7.7
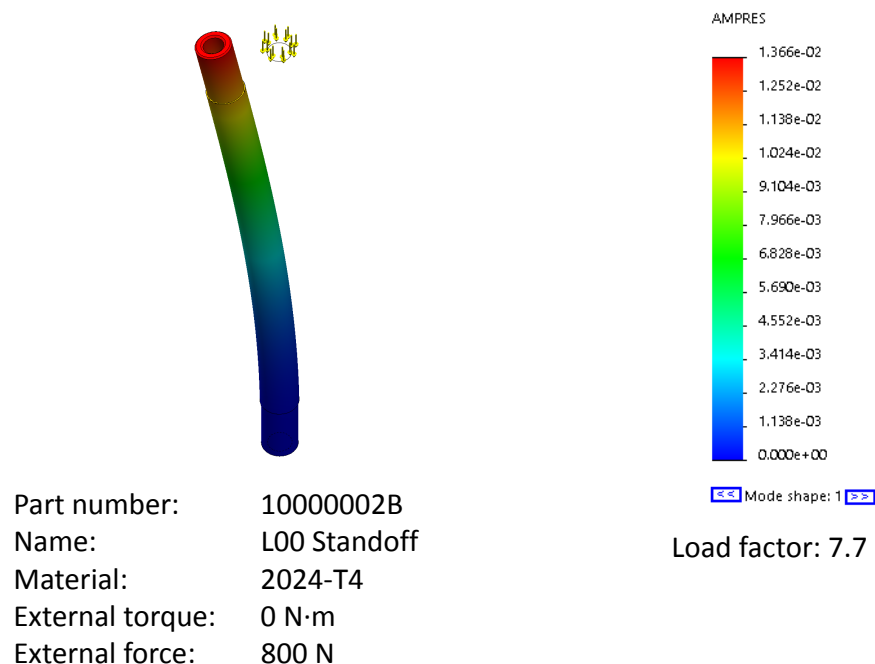
Figure 3.20: Buckling simulation for Link 1 standoff: 800 N·m external force.

The torque simulation for the inner solid shaft 10000075B transmitting the rotation from the HD gearbox to the bevel pinion in the 2nd joint is shown in Fig. 3.21. The torque 200 N·m is used for the simulation keeping in mind that the maximum peak torque can not be greater than 180 N·m. The geometry and material for the shaft were adjusted to ensure the proper strength of the part. The final material selected is alloy 300M, a modified version of 4340 alloy steel. 300M is used in applications that require high yield strength, such as torsion bars and drive shafts. The calculated safety factor for 200 N·m is 1.02.

Part number: 10000075B
Name: J1 Shaft Solid
Material: 300M
External torque: 200 N·m
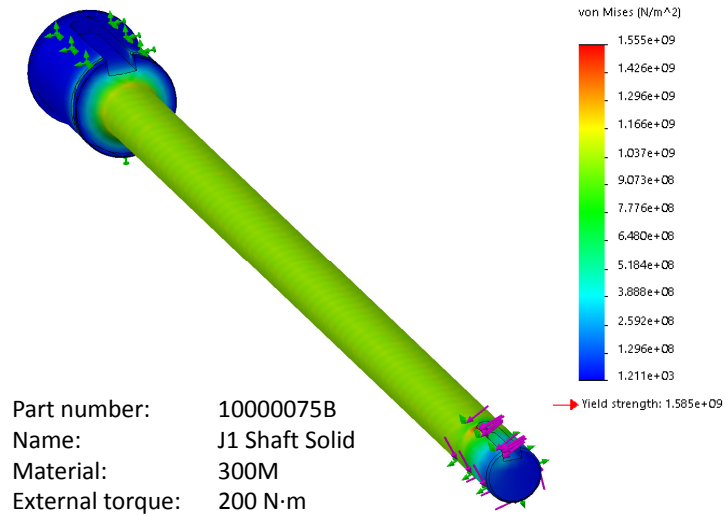
Figure 3.21: Static stress simulation for joint 1 solid shaft: 200 N·m external torque.

The bending simulation for the joint 2 frame shaft 10000006A that should be able to withstand bending load due to the weight and inertia of the upper links and payload is shown in Fig. 3.22. The bending load of 3000 N, about 5 times higher than the weight of the manipulator (60 kg) was used in the simulation to compensate for unknown load factors not available at the time of calculations. The calculated safety factor is 1.97.

Part number: 10000006A
Name: J2 Frame Shaft
Material: AL 7075-T6
External load: 3000 N
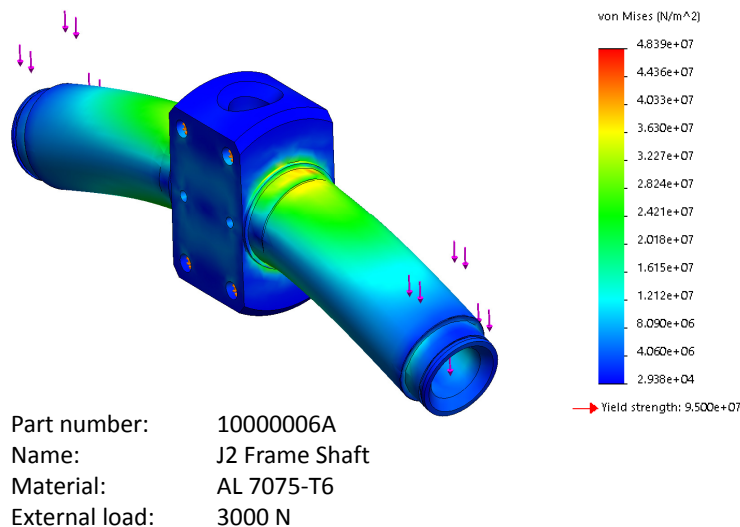
Figure 3.22: Static stress simulation for joint 2 frame shaft: 3000 N·m external force.

Simulation results for the less critical components are presented in Appendix C.

3.8   Mechanical design: Wiring

To control the actuation of the robot, each joint is equipped with its own control board as shown on the simplified electrical diagram in Fig. 3.23.
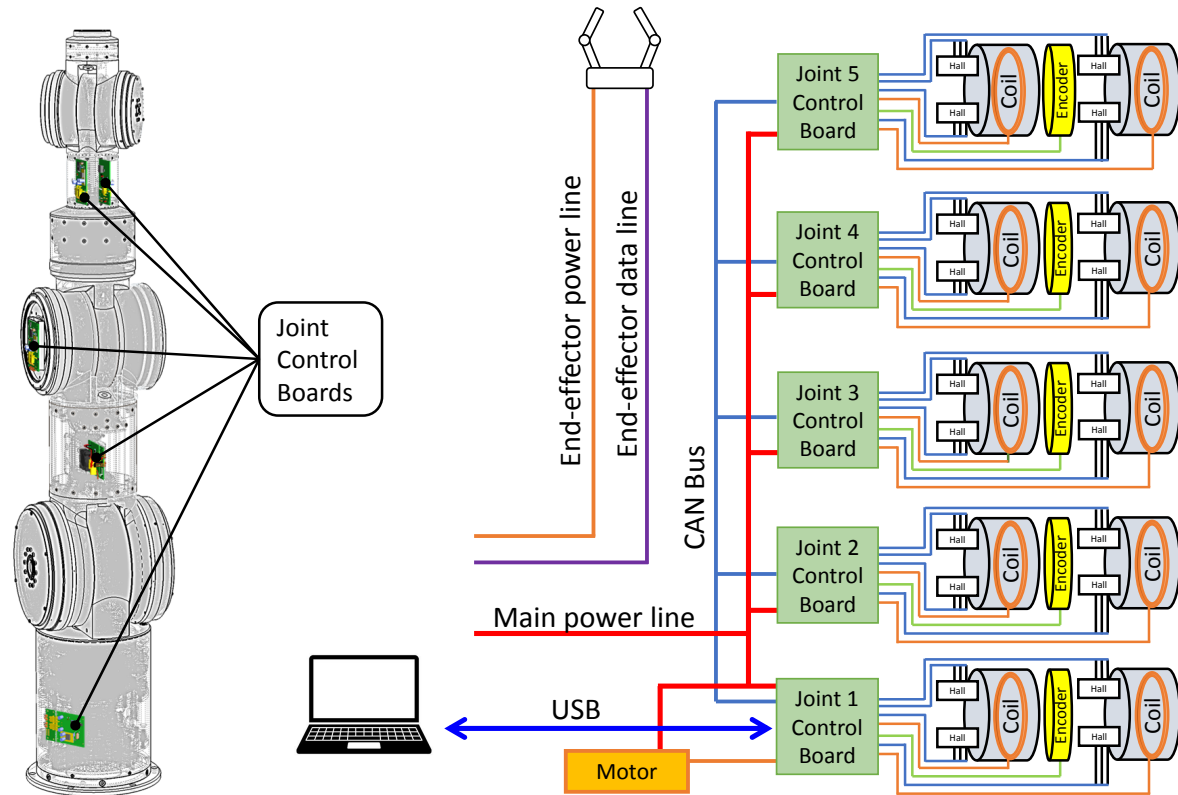
Figure 3.23: Location of the joint control boars in the manipulator (left) and simplified electrical diagram (right).

Every board receives data from the joint encoder, and from two pairs of hall sensors installed in the MR clutches. Received data is used as control feedback and based on the running control algorithms, the board supplies current to the coils of both MR clutches in the pair.

All the boards are interconnected with CAN Bus and all receive power from the same power line (36 V). The control board for the 1st joint also controls the robot motor and reads motor RPM via Electronic Speed Controller. The communication with the external computer is performed using the USB interface of the joint 1 control board. The location of the boards inside of the 5-DOF robot is shown on the left side of Fig. 3.23.

As shown in the diagram in Fig. 3.23 (left), two wires for electrical power and two wires for CAN bus are running through the whole manipulator.

Moreover, each board is connected to the pair of clutches and the encoder of the respective joint. The encoder is connected using wires: 5 V power supply, ground, and data. Each clutch is connected to the board with 2 wires to power the coil and with 6 wires running from Hall sensors (3 wires from each: 5 V power, ground, and data).

In addition to that, there are 2 pairs of wires running through the robot for the end-effector actuation: a pair for the electrical power and a pair for control and information data.

The control boards themselves (Fig. 3.24) are designed, assembled, and tested by Ziqi Yang. The boards are fully interchangeable, they feature STM32F4 microcontroller with 168 MHz frequency and 512 Kbytes of flash memory onboard.
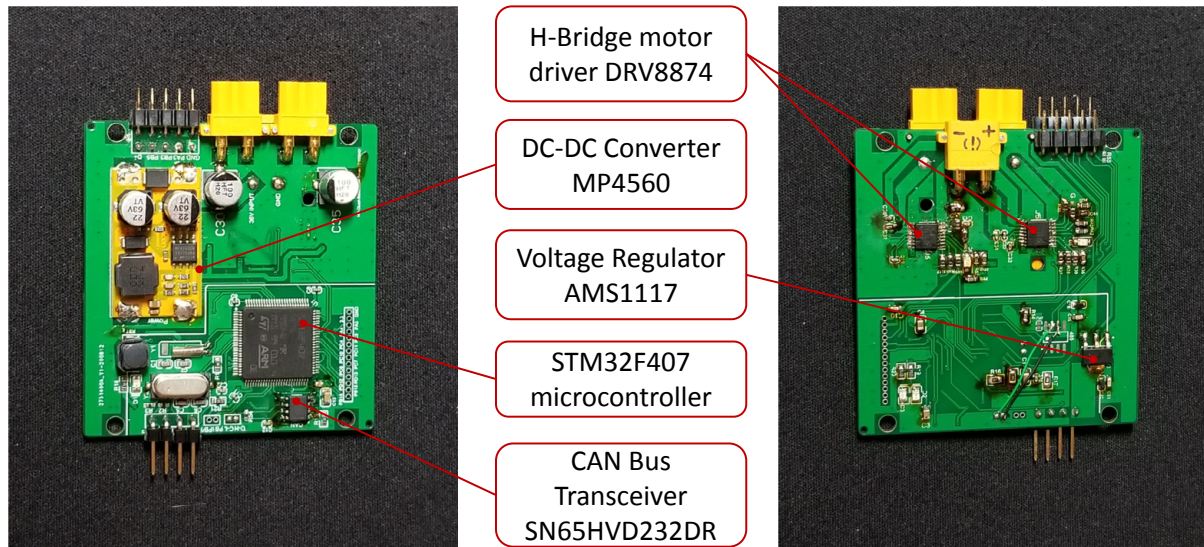
Figure 3.24: Joint control board based on STM32F4 microcontroller (developed by Ziqi Yang).

To control the current through the MR clutch coils each board has two H-Bridge motor drivers Texas Instruments DRV8847 with a maximum continuous output current of 3.3 A. The CAN bus transceiver SN65HVD232DR is used to establish reliable communication between all the boards in the robot. The DC-DC converter MP4560 is used to perform conversion of input voltage (up to 37 V) to required by electronics 5 V. Additional voltage regulator AMS1117 is used to convert 5 V to 3.3 V for some electronic components.

As seen in Fig. 3.23, the number of wires in the 5-DOF manipulator is significant, therefore, special care is taken to ensure the conductors are well insulated, not jammed or pinched between the robot parts, while control signals are safely and reliably transmitted within the robot components.

The wires running through a joint experience constant bending and/or twisting during joint movement. The bending radii of the wire strands should be large enough to ensure only elastic deformations are present in the material. For joints with continuous rotation or with no space for a large enough bending radius, the slip rings should be used instead of uninterrupted wires.

Analysis of the 5-DOF manipulator preliminary dimensions showed that all 5 joints have enough space to accommodate continuous wires working within the elastic region of the strands material. For joints 1, 2, and 3 the wiring is designed based on the cable chain approach as shown in Fig. 3.25-3.28.

3.8.1 Joint 1 wiring

Fig. 3.25 shows the cable chain at the very bottom of the base. It runs the wires from the stationary link 0 to the Electronic Speed Controller (ESC) of the motor attached to the moving

link 1 frame. The cable chain contains two power cables (12 AWG rated for up to 90 A current) and 3 ESC data wires (28 AWG).

Each link of the cable chain has 3 cylindrical permanents on one side. The magnets are used to attract the chain to the inner surface of the base or outer surface of the motor guard to keep the proper shape of the chain during joint movements. Ferromagnetic strips (carbon steel) are attached to the aluminum base and the nylon motor guard.
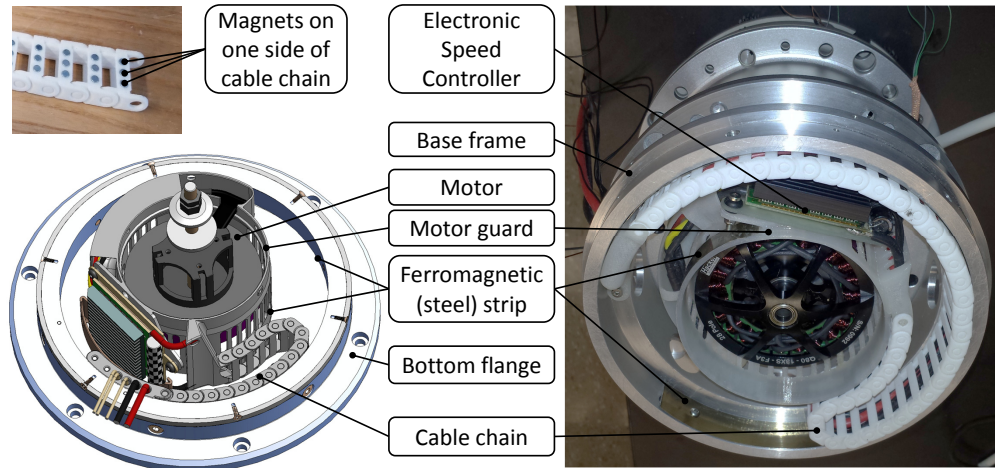
Figure 3.25: Cable chain for motor wiring (joint 1 rotation).

Fig. 3.26 shows the joint 1 cable chain at the top of the base. It runs the wires from the stationary link 0 to the 2nd joint of the manipulator. The top cable chain contains two power cables (14 AWG rated for up to 60 A current), 2 wires for CAN bus (28 AWG), 2 wires for payload power (20 AWG), and 2 wires for payload data (28 AWG).
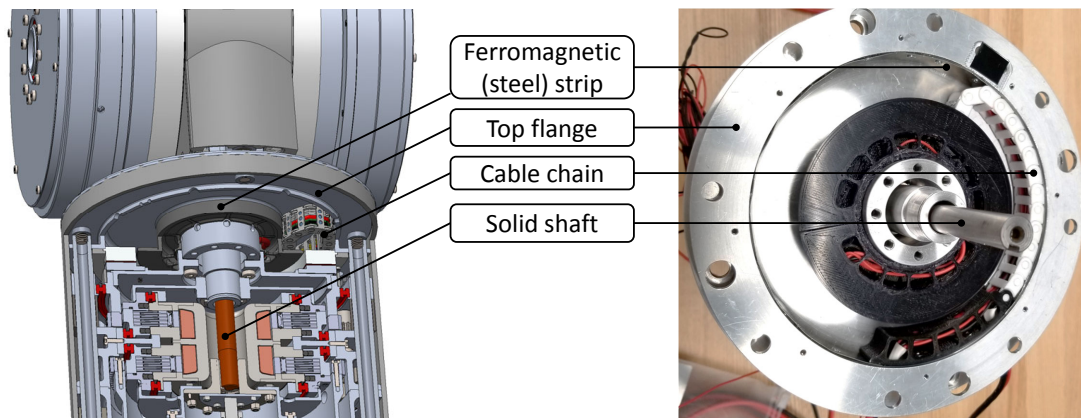
Figure 3.26: Cable chain for joint 1 rotation.

3.8.2   Joint 2 wiring

Fig. 3.27 shows the cable chain running wires around 2nd joint of the manipulator. It guides the wires from the link 1 structure to the 2nd link of the manipulator. Similar to the joint 1

cable chain, the joint 2 cable chain contains two power cables (14 AWG rated for up to 60 A current), 2 wires for CAN bus (28 AWG), 2 wires for payload power (20 AWG), and 2 wires for payload data (28 AWG). Additionally, the 2nd joint chain contains 3 wires (28 AWG) for the joint 2 absolute encoder.
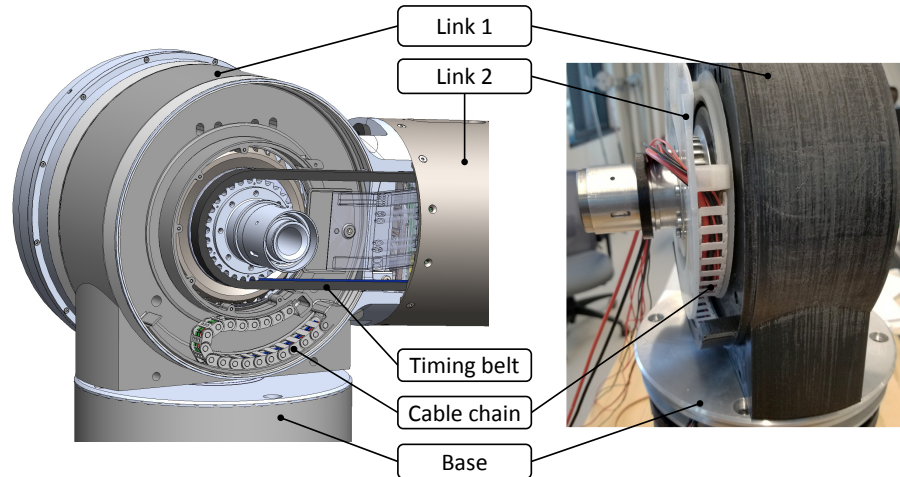
Figure 3.27: Cable chain for joint 2 rotation.

3.8.3   Joint 3 wiring

Fig. 3.28 shows the cable chain running wires around 3rd joint of the manipulator. It guides the wires from the link 2 structure to the 3rd link of the manipulator. Similar to the joint 1 cable chain, the joint 3 cable chain contains two power cables (14 AWG rated for up to 60 A current), 2 wires for CAN bus (28 AWG), 2 wires for payload power (20 AWG), and 2 wires for payload data (28 AWG).
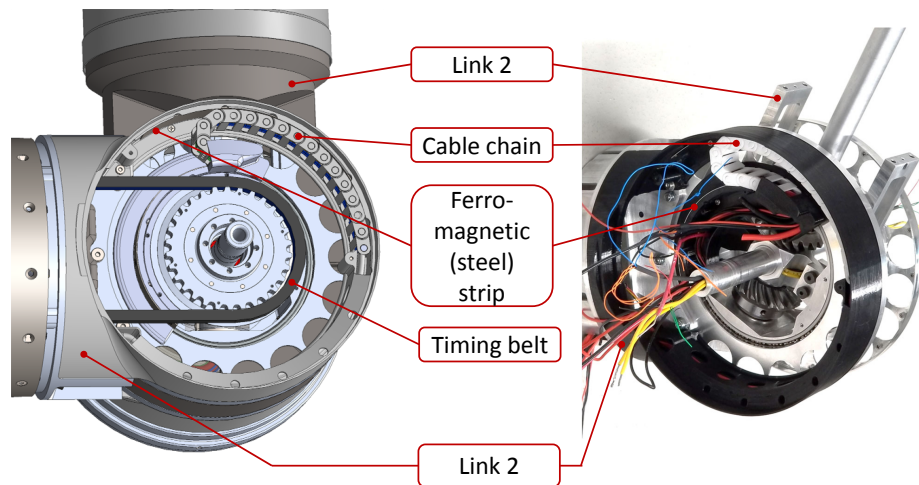
Figure 3.28: Cable chain for joint 3 rotation.

3.8.4 Joint 4 wiring

The wires running through the 4th joint are arranged differently due to the availability of space inside the long hollow shaft in the joint. Instead of bending, in chosen arrangement the wires experience $\pm 180°$ twisting deformation. The sufficient length (more than 400 mm) of the curling conductors allows avoiding plastic strain in the material. The arrangement is shown in Fig. 3.29.
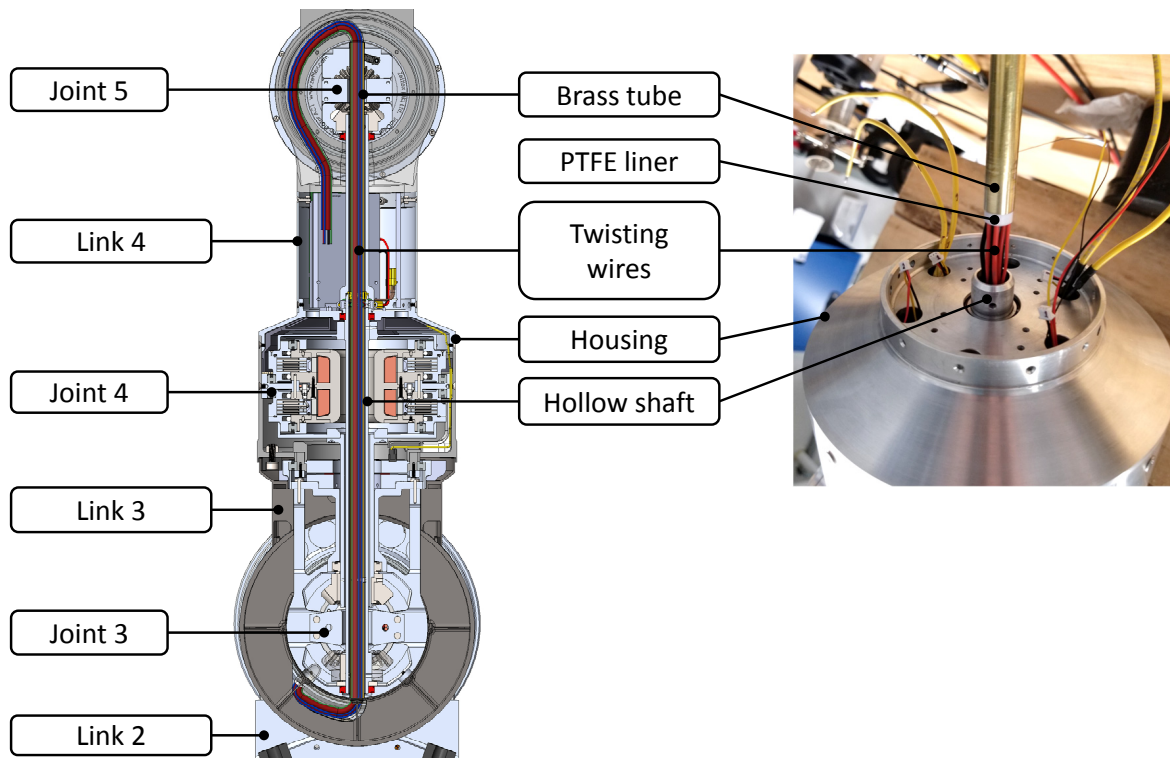
Figure 3.29: Cable twisting arrangement for joint 4 rotation.

The joint 4 twisting wiring consist of 6 power lines (six 20 AWG instead of two 14 AWG to improve distribution of the wires in the narrow channel), 2 wires for CAN bus (28 AWG), 2 wires for payload power (20 AWG), and 2 wires for payload data (28 AWG).

3.8.5 Joint 4 wiring

The 5th joint has limited space to accommodate a cable chain-type structure. Therefore, a spiral-shape flexible nylon cable guide is designed for reliable wiring as shown in Fig. 3.30.

The joint 5 cable guide runs 2 wires for payload power (20 AWG), 2 wires for payload data (28 AWG), 3 power wires for MR clutch coils (20 AWG, common ground, and 2 positive wires), and 6 wires for 2 pairs of Hall sensors (28 AWG, common ground, common +5 V, and 4 signal wires).
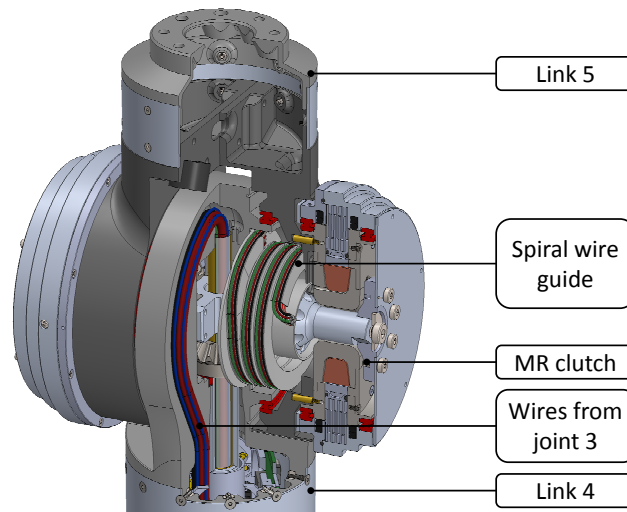
Figure 3.30: Spiral cable guide for joint 5 rotation.

3.9   Conclusion

An innovative design of a 5-DOF compliant manipulator with the distributive antagonistic magneto-rheological actuation is presented in this chapter. The assembled 5-DOF manipulator is shown in Fig. 3.31.
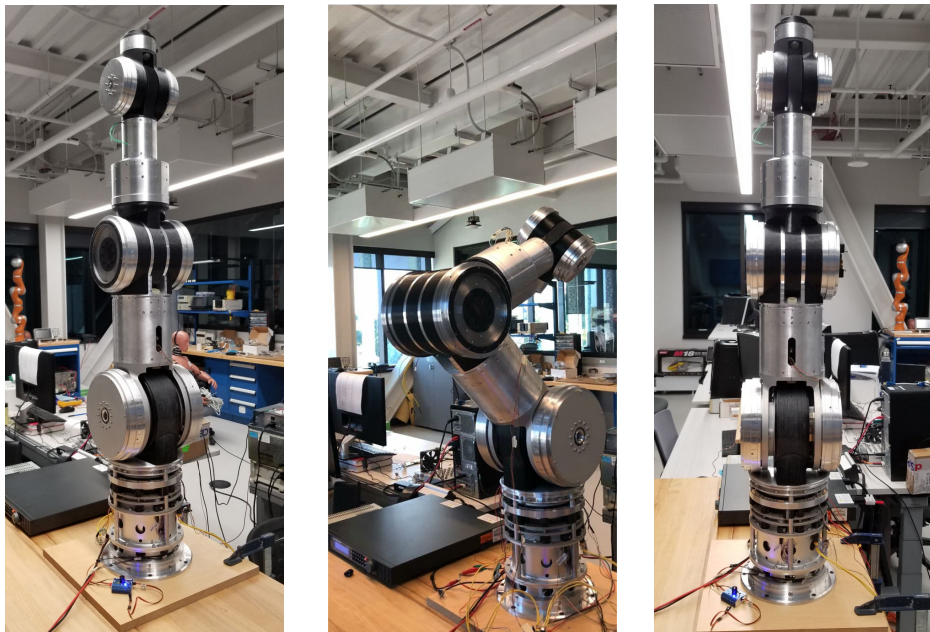
Figure 3.31: Assembled 5-DOF manipulator.

The compliant behavior of the manipulator is achieved by using a pair of MR clutches in each joint of the robot.

The transmission of the manipulator consists of a system of shafts, gears, and belts, and 5

pairs of antagonistic MR clutches. It delivers the rotation of a single brushless DC motor located at the base of the robot to the MR clutches at every joint. Multiple design concepts for the manipulator's drive train are presented and the advantages and disadvantages of each concept are described. For the selected most efficient drive train concept, the design of the entire manipulator including the mechanical structure of the links and joints, transmission mechanism, and motor power/data wiring is presented.

Table 3.1 shows specifications for the 5-DOF manipulator.

Table 3.1: 5-DOF manipulator specifications

Parameter	Value
Payload	10 kg
Reach	930 mm
Degrees of freedom	5 rotating joints
Height	1320 mm
Footprint	Diameter 240 mm
Weight	60 kg
Joint 1 range	$\pm 180°$
Joint 2 range	$\pm 100°$
Joint 3 range	$\pm 110°$
Joint 4 range	$\pm 175°$
Joint 5 range	$\pm 120°$

Bibliography

[1] S. Pisetskiy and M. R. Kermani, "Compliant 5-dof robot: Mechanical design," 2019. [Online]. Available: https://robot.gmc.ulaval.ca/en/events/icra2019-workshop-phri/

[2] "Universal robot ur3," Tech. Rep., 2021. [Online]. Available: https://www.universal-robots.com/products/ur3-robot/

[3] "Kinova jaco product page," Tech. Rep., 2021. [Online]. Available: https://www.kinovarobotics.com/en/products/assistive-technologies/kinova-jaco-assistive-robotic-arm

[4] V. Maheu, P. S. Archambault, J. Frappier, and F. Routhier, "Evaluation of the jaco robotic arm: Clinico-economic study for powered wheelchair users with upper-extremity disabilities," in *2011 IEEE International Conference on Rehabilitation Robotics*. IEEE, 2011, pp. 1–5.

[5] A. Campeau-Lecours, V. Maheu, S. Lepage, H. Lamontagne, S. Latour, L. Paquet, and N. Hardie, "Jaco assistive robotic device: Empowering people with disabilities through innovative algorithms," 2016.

[6] "Franka emika technical data," Tech. Rep., 2016. [Online]. Available: http://robotforum.ru/assets/files/Franka_Emika_pdf/FRANKA-EMIKA-technical-data_new.pdf

[7] "Irb 14050 single-arm yumi collaborative robot," Tech. Rep., 2021. [Online]. Available: https://new.abb.com/products/robotics/industrial-robots/irb-14050-single-arm-yumi

[8] R. Bischoff, J. Kurth, G. Schreiber, R. Koeppe, A. Albu-Schaeffer, A. Beyer, O. Eiberger, S. Haddadin, A. Stemmer, G. Grunwald, and G. Hirzinger, "The kuka-dlr lightweight robot arm - a new reference platform for robotics research and manufacturing," in *ISR 2010 (41st International Symposium on Robotics) and ROBOTIK 2010 (6th German Conference on Robotics)*, 2010, pp. 1–8.

[9] S. Shepherd and A. Buchstab, "Kuka robots on-site," in *Robotic Fabrication in Architecture, Art and Design 2014*. Springer, 2014, pp. 373–380.

[10] A. Shafer and M. R. Kermani, "Development of high performance intrinsically safe 3-dof robot," in *2014 IEEE International Conference on Robotics and Automation (ICRA)*. IEEE, 2014, pp. 619–624.

Chapter 4

5-DOF Manipulator: Simulation, control, and performance evaluation

This chapter presents kinematics and DH parameters for the 5-DOF robot, describes the simulation of the transmission, discusses in detail the behavior of the actuator based on antagonistically coupled magneto-rheological clutches. At the end of the chapter, the joint-level PID control described and performed experiments presented.

4.1   Introduction

The antagonistic MR actuation allows disengaging the active component from the load to reduce the reflected inertia and ensure full back-drivability. Additionally, this approach allows mounting the active element (i.e. motor) in a remote location while its mechanical power is transmitted to a group of actuators mounted at necessary locations.

Among other advantages, the antagonistic nature of the presented actuation offers the unique property of intrinsic passivity that makes the system an ideal candidate for applications such as teleoperation, rehabilitation, collaborative robotics, and many more. Such actuators can be used in applications requiring outstanding compliance, precise torque control, high bandwidth, and excellent stability.

Implementation of the unified transmission for the whole robotic system, however, may affect the performance of the joints due to the interdependence of all the components of the transmission. The relation between components depends on whether they are connected in series or parallel to the source of mechanical power. The influence of components on each other can be identified in advance based on the system architecture. Found relation should be included in the control system to ensure proper operation of the robotic system.

Below, the transmission system for the developed 5-DOF robot is analyzed and simulated to demonstrate the interdependence of the robot links and actuators.

4.2   Manipulator kinematics and transmission simulation

4.2.1   5-DOF Manipulator DH parameters

The 5-DOF manipulator is designed with only revolute joints and can be represented as a system of rigid objects (links) connected in series. The configuration and orientation of the joins allows to develop a simple kinematic model.

The position and orientation of the manipulator end-effector in Cartesian space relative to the base frame of reference can be determined with forward forward kinematics equations based on Denavit-Hartenberg (DH) parameters of the robot.
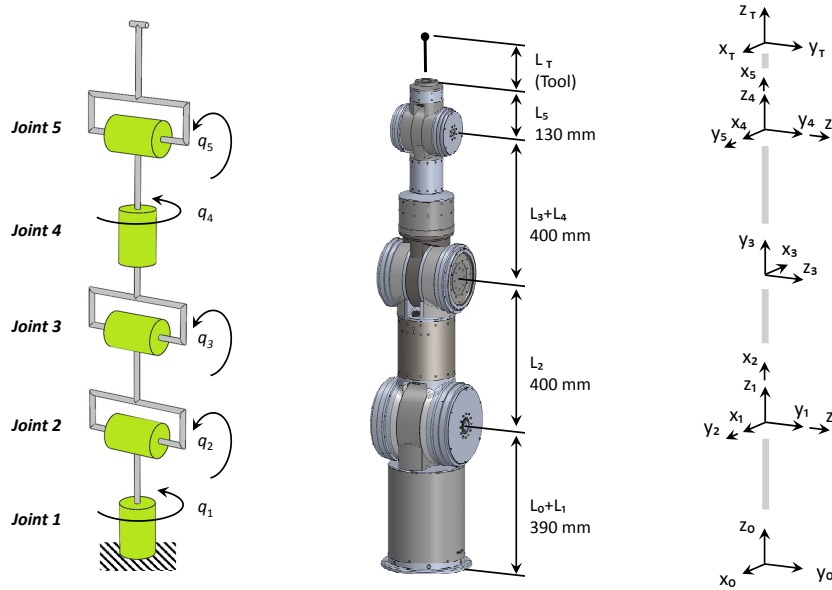
Figure 4.1: Manipulator kinematic arrangement and link coordinate frames assignment

Due to the fact that joint 1 and joint 2 are mutually orthogonal and share a common intersection point, the coordinate frames 0 and 1 could share the same origin. Similarly, because joint 4 and joint 5 share a common intersection point and mutually orthogonal, frames 4 and 5 could also share the origin. The frame assignment considered for 5-DOF manipulator is shown in Fig. 4.1.

Table 4.1: Link DH parameters for 5-DOF manipulator

Link i	α_{i-1}	a_{i-1}	d_i	q_i
1	0	0	$L_0 + L_1$	q_1
2	$-\pi/2$	0	0	$q_2 - \pi/2$
3	0	L_2	0	$q_3 - \pi/2$
4	$-\pi/2$	0	$L_3 + L_4$	$q_4 + \pi$
5	$-\pi/2$	0	0	$q_5 - \pi/2$

Table 4.1 summarizes DH parameters derived from the selected coordinate frames config-uration. In the table, α_{i-1} - is the angle from Z_{i-1} to Z_i measured about X_{i-1}, a_{i-1} is the distance from Z_{i-1} to Z_i measured along X_{i-1}, d_i is the distance from X_{i-1} to X_i measured along Z_i, and q_i is the joint angle from X_{i-1} to X_i measured about Z_i.

Refer to Appendix A for the transformation matrix equations.

4.2.2 5-DOF manipulator transmission simulation

As it is shown in Chapter 3, for the designed 5-DOF manipulator transmission system the angular velocity of MR clutch rotors relative to the corresponding stators can be calculated as follows,

$$\begin{bmatrix} \dot{\theta}_1^{\pm} \\ \dot{\theta}_2^{\pm} \\ \dot{\theta}_3^{\pm} \\ \dot{\theta}_4^{\pm} \\ \dot{\theta}_5^{\pm} \end{bmatrix} = \pm \begin{bmatrix} 0.01 \\ 0.005 \\ 0.005 \\ 0.005 \\ 0.005 \end{bmatrix} \dot{q}_m + \begin{bmatrix} -1 \\ 0 \\ 0 \\ 0 \\ 0 \end{bmatrix} \dot{q}_1 + \begin{bmatrix} 0 \\ -1 \\ -1 \\ -1 \\ -1 \end{bmatrix} \dot{q}_2 + \begin{bmatrix} 0 \\ 0 \\ -1 \\ -1 \\ -1 \end{bmatrix} \dot{q}_3 + \begin{bmatrix} 0 \\ 0 \\ 0 \\ -1 \\ +1 \end{bmatrix} \dot{q}_4 + \begin{bmatrix} 0 \\ 0 \\ 0 \\ 0 \\ -1 \end{bmatrix} \dot{q}_5 \qquad (4.1)$$

where $\dot{\theta}_i^+ = \dot{q}_i^- - \dot{q}_i$ and $\dot{\theta}_i^- = \dot{q}_i^- - \dot{q}_i$ are relative angular velocities between rotor ($\dot{q}_i^{\pm}$) and stator ($\dot{q}_i$) of a pair of clutches at joint i, $\dot{q}_m$ is motor output angular velocity, and $\dot{q}_i$ is the angular velocity of joint i (see Fig. 3.7).

To simulate the MR clutch relative velocities, a joint trajectory is used with angular posi-tion, velocity, and acceleration profile as shown in Fig. 4.2.
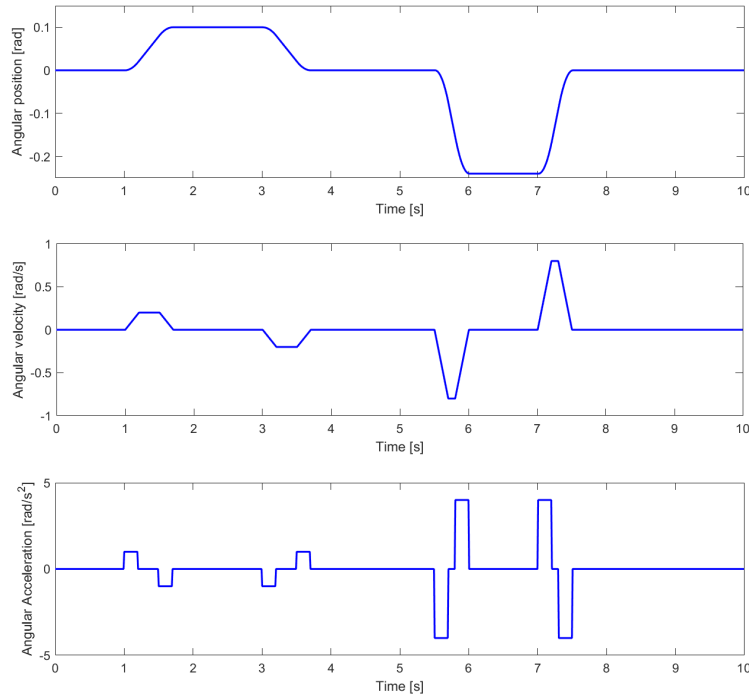

Figure 4.2: Joint trajectory parameters (angular position, velocity, and acceleration) used for MR clutch velocity in robot transmission simulation.

The joint starts to accelerate in the CCW direction at time $T = 1$ sec, reaches position 0.1 rad, and holds it for 1.3 sec. At the time $T = 3$ sec the joint moves back to the initial position 0 rad and holds it for 1.8 sec. At the time $T = 5.5$ sec the joint starts to accelerate in CW direction, moves to position -0.24 rad, and stays there for 1 sec. At the time $T = 7$ sec, the joint starts moving back to the initial position 0 rad. The motor in the simulation is set to a constant rotational speed of 50 rad/s (about 477 RPM).

During each separate simulation, the described trajectory profile (Fig. 4.2) is applied to only one joint in the 5-DOF manipulator.

Joint 1 actuated only

Fig. 4.3 shows the trajectories for all 5 joints for the case when only the 1st joint is active and follows the trajectory.

Figure 4.3: 5-DOF manipulator joints movement parameters for MR clutch velocity in serial transmission simulation: 1st joint active only.

As a result of the joint movements, the rotor-stator angular velocity of the clutches in the 1st joint changes. It can be observed in the top plot in Fig. 4.4 that the initial angular speed (0.5 rad/s) of the CCW clutch starts to fall down at the time $T = 1$ sec and drops to 0.3 rad/s. At the same time, the velocity of the CW clutch increases from 0.5 rad/s to 0.7 rad/s. Similarly, the velocity of the clutches starts to vary at the time $T = 3$ sec, $T = 5.5$, $T = 7$ sec when the joint starts to move.

However, the clutches at joints 2, 3, 4, and 5 do not change their rotor-stator relative velocity as can be seen in the bottom plots in Fig. 4.4 and Fig. 4.5. These clutches are not in series with the 1st joint actuation and their velocity is not affected by the movement of joint 1.

Figure 4.4: Simulation of the angular velocity for joint 1, 2, and 3 MR clutches.

Figure 4.5: Simulation of the angular velocity for joint 4 and 5 MR clutches.

Joint 2 actuated only

Fig. 4.6 shows the trajectories for the joints for the next simulation case when only the 2nd joint is active and follows the sample trajectory.
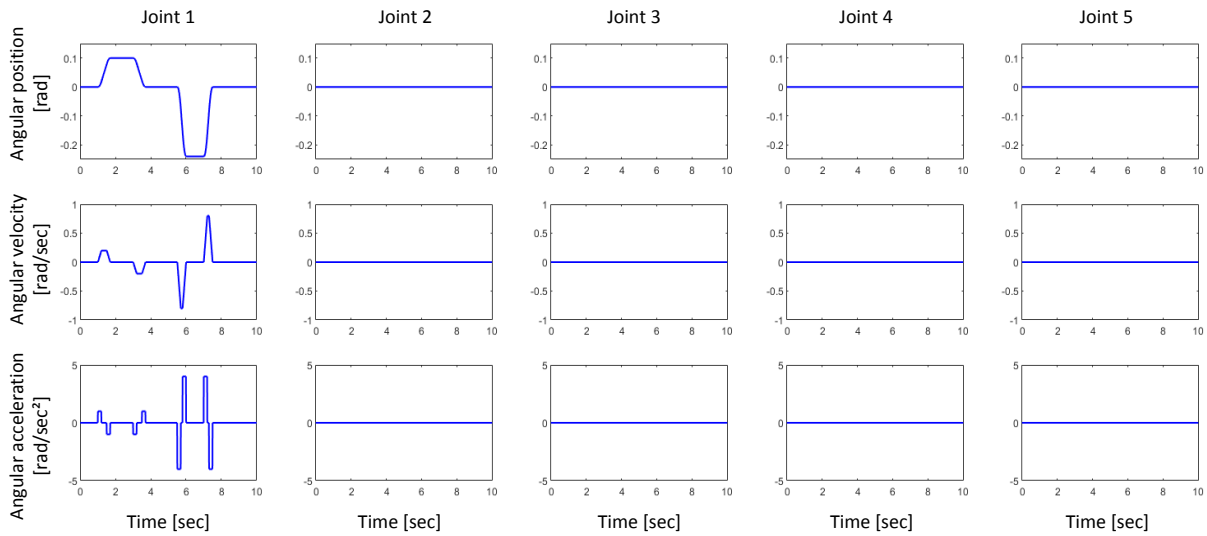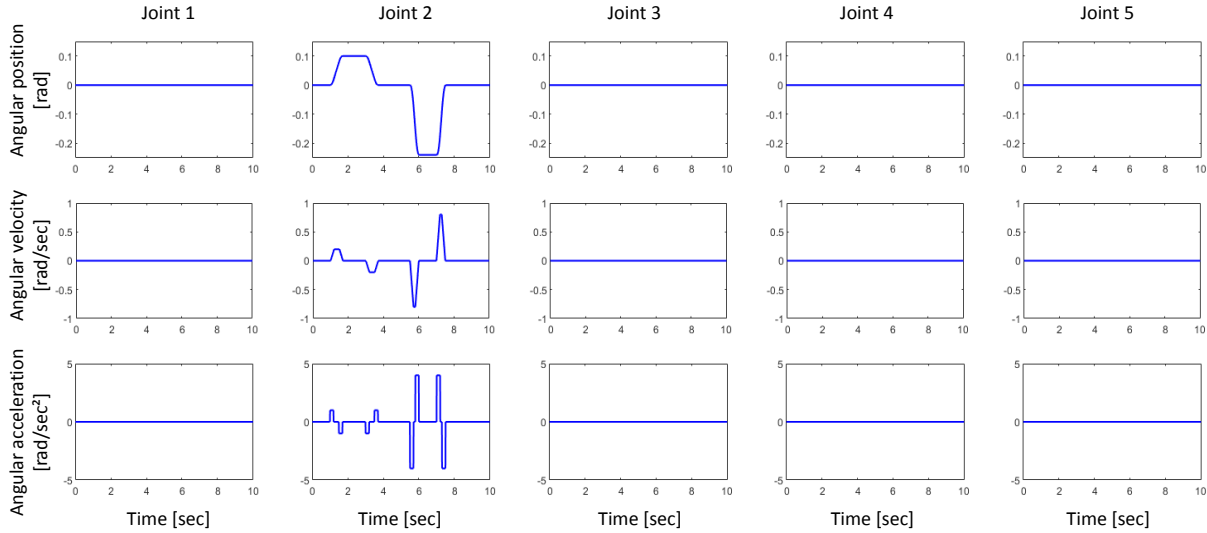

Figure 4.6: 5-DOF manipulator joints movement parameters for MR clutch velocity in serial transmission simulation: 2nd joint active only.

It can be observed in Fig. 4.7 and Fig. 4.8 that clutches in the joint 2, 3, 5, and 5 have varying rotor-stator velocities at the time $T = 3, 5.5,$ and 7 sec when the joint 2 starts to move. The MR clutches are interconnected in series with their respective joints and the change in joint 2 velocity affects their rotor-stator angular speed. The pair of clutches at the 1st joint are not affected by joint 2 movement as they are not in series with the 2nd joint.

Figure 4.7: Simulation of the angular velocity for joint 1, 2, and 3 MR clutches.

Figure 4.8: Simulation of the angular velocity for joint 4 and 5 MR clutches.

Joint 3 actuated only

Finally, Fig. 4.9 shows the trajectories for the joints for the simulation case when only the 3rd joint is active.

Figure 4.9: 5-DOF manipulator joints movement parameters for MR clutch velocity in serial transmission simulation: 3rd joint active only.

It can be observed in Fig. 4.10 and Fig. 4.11 that clutches in the joint 3, 4, and 5 have varying rotor-stator velocities at the time $T = 3, 5.5,$ and 7 sec when the joint 3 starts to move. The MR clutches are interconnected in series with their respective joints and the change in joint 3 velocity affects their rotor-stator angular speed. The clutches at the 2nd joint do not change their rotor-stator velocity because they are connected in series before the 3rd joint and are not altered by the joint 3 motion. Similar to the previous case, the pair of clutches at the 1st joint is not affected by joint 3 movement as they are not in series with the joint 2, 3, 4, and 5.
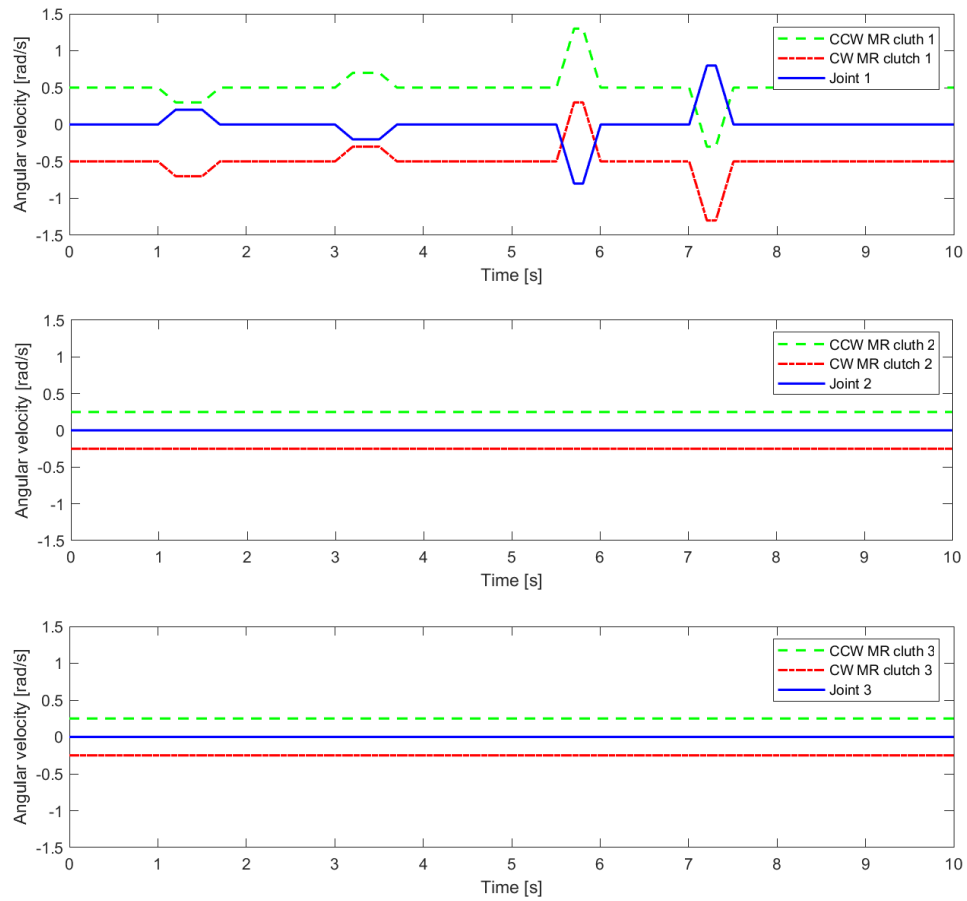
Figure 4.10: Simulation of the angular velocity for joint 1, 2, and 3 MR clutches.
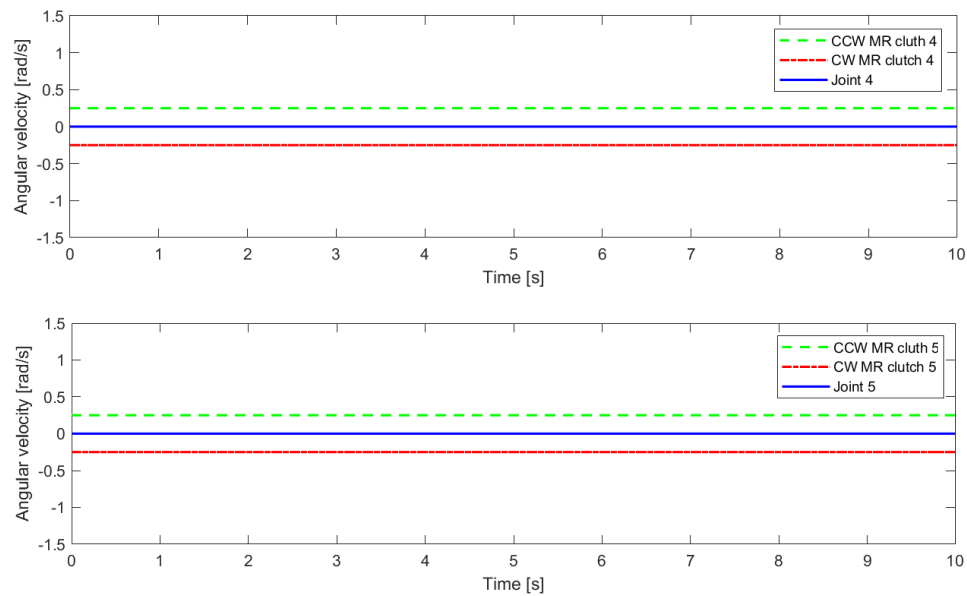

Figure 4.11: Simulation of the angular velocity for joint 4 and 5 MR clutches.

Joint 4 actuated only

Fig. 4.12 shows the trajectories for the joints for the simulation case when only the 4th joint is active.

Figure 4.12: 5-DOF manipulator joints movement parameters for MR clutch velocity in serial transmission simulation: 4th joint active only.

It can be observed in Fig. 4.13 and Fig. 4.14 that clutches in joint 4 and 5 have varying rotor-stator velocities at the time $T = 3, 5.5$, and 7 sec when the joint 4 starts to move. The MR clutches are interconnected in series with their respective joints and the change in joint 3 velocity affects their rotor-stator angular speed. The clutches at the 2nd and 3rd joints do not change their rotor-stator velocity because they are connected in series before the 4th joint and are not altered by the joint 4 motion. Similar to the previous cases, the antagonistic pair of clutches at the 1st joint are not affected by joint 4 movement as they are not in series with the joint 2, 3, 4, and 5.
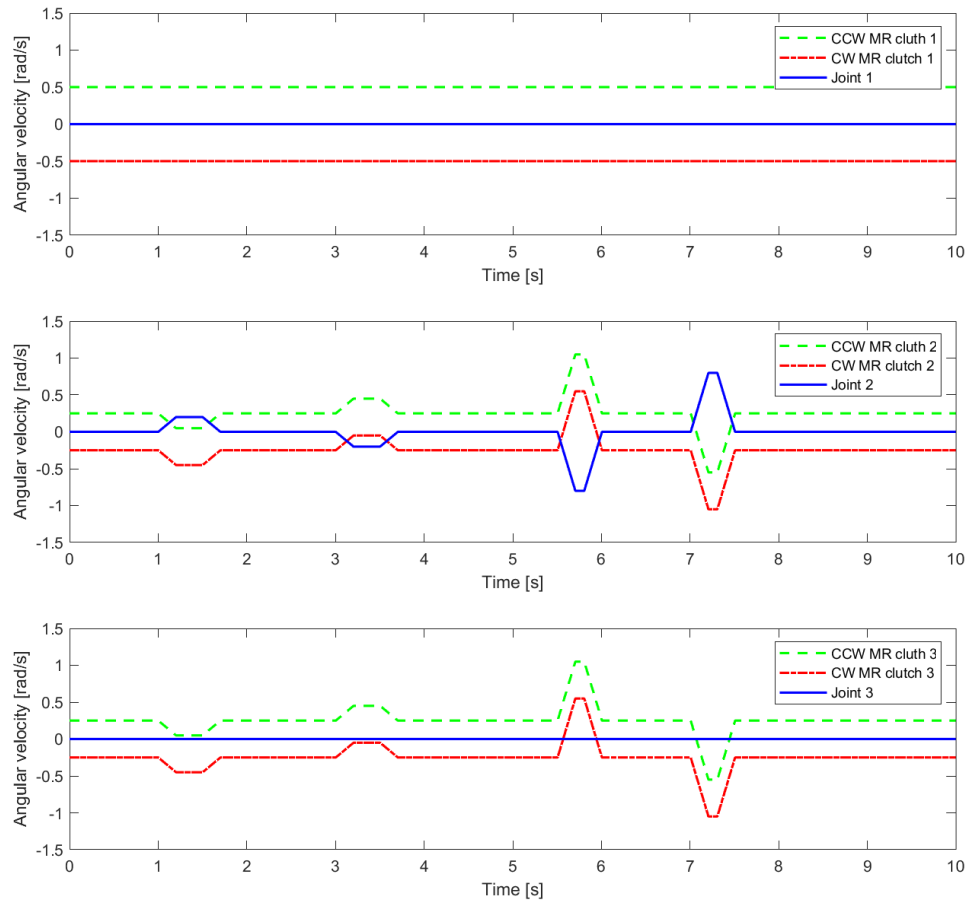
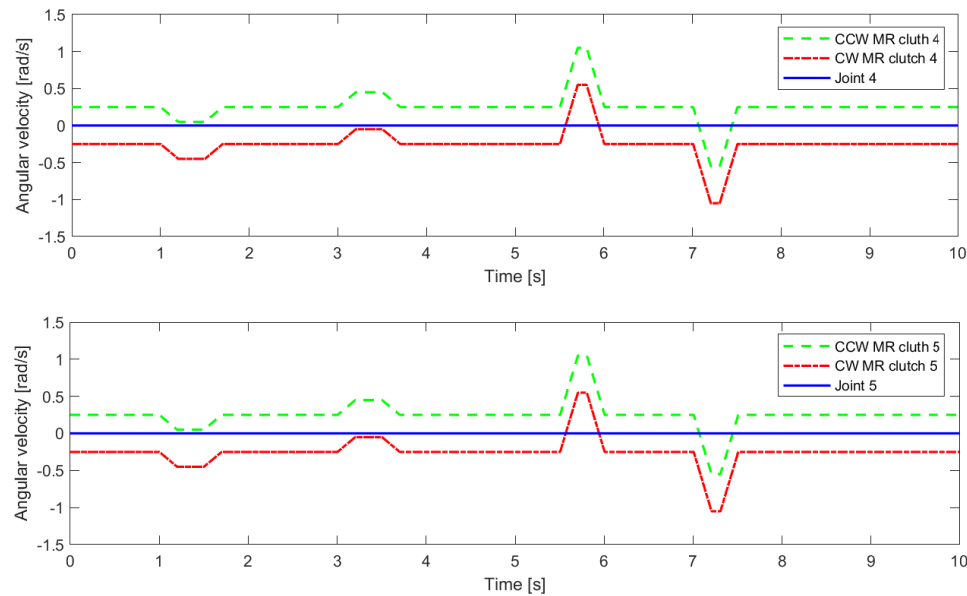Figure 4.13: Simulation of the angular velocity for joint 1, 2, and 3 MR clutches.

Figure 4.14: Simulation of the angular velocity for joint 4 and 5 MR clutches.

Joint 5 actuated only

Fig. 4.15 shows the trajectories for the joints for the simulation case when only the 5th joint is active.
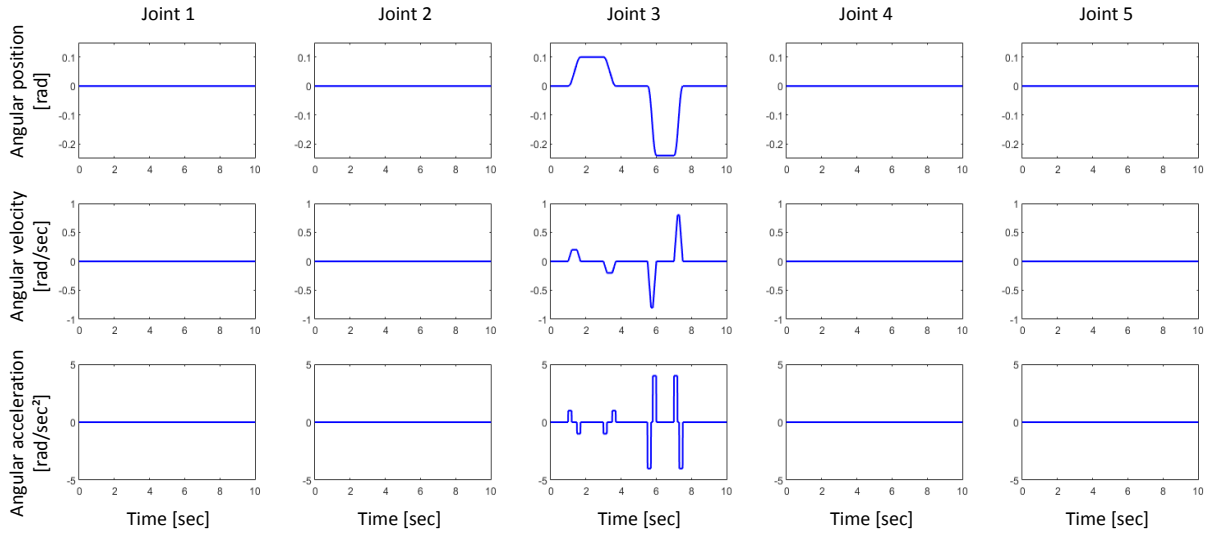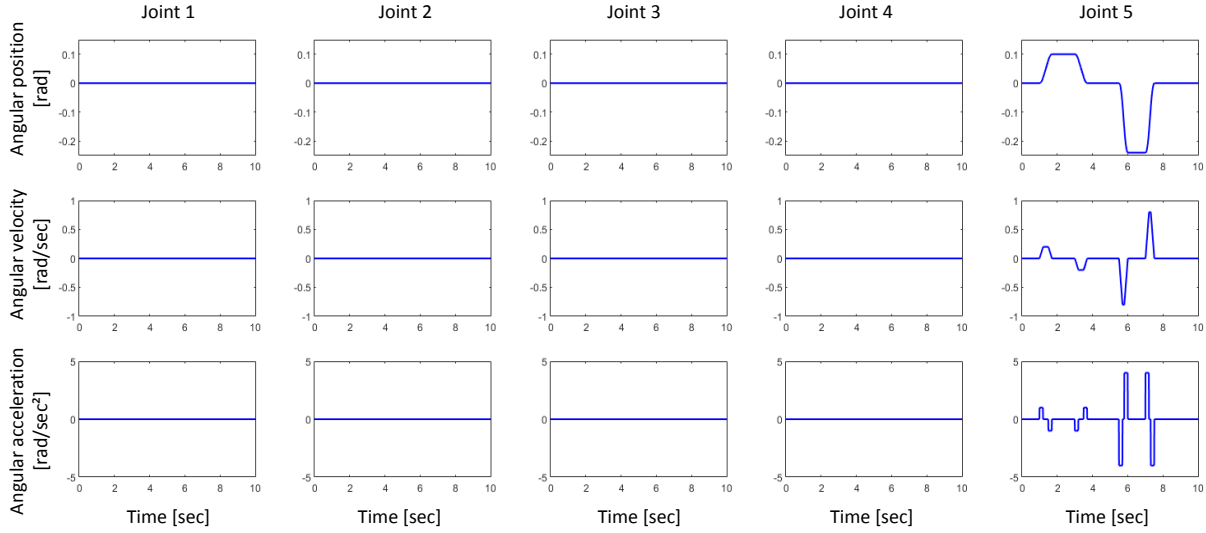

Figure 4.15: 5-DOF manipulator joints movement parameters for MR clutch velocity in serial transmission simulation: 5th joint active only.

It can be observed in Fig. 4.16 and Fig. 4.17 that clutches in joint 5 have varying rotor-stator velocities at the time $T = 3, 5.5,$ and 7 sec when the joint 5 starts to move. The MR clutches are interconnected in series with the joint and the change in joint 5 velocity affects their rotor-stator angular speed. The clutches at the 2nd, 3rd and 4th joints do not change their rotor-stator velocity because they are all connected in series before the 5th joint and are not altered by the joint 5 motion. Similar to the previous cases, the pair of clutches at the 1st joint is not affected by joint 5 movement as they are not in series with the joint 2, 3, 4, and 5.
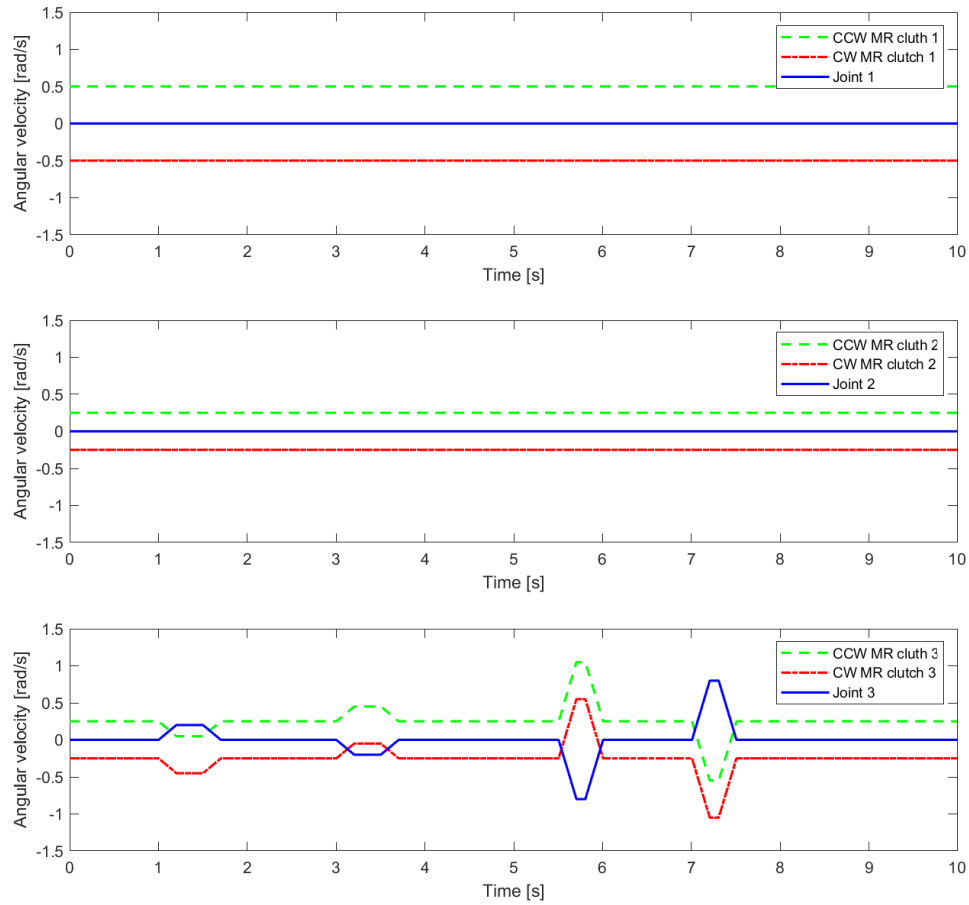
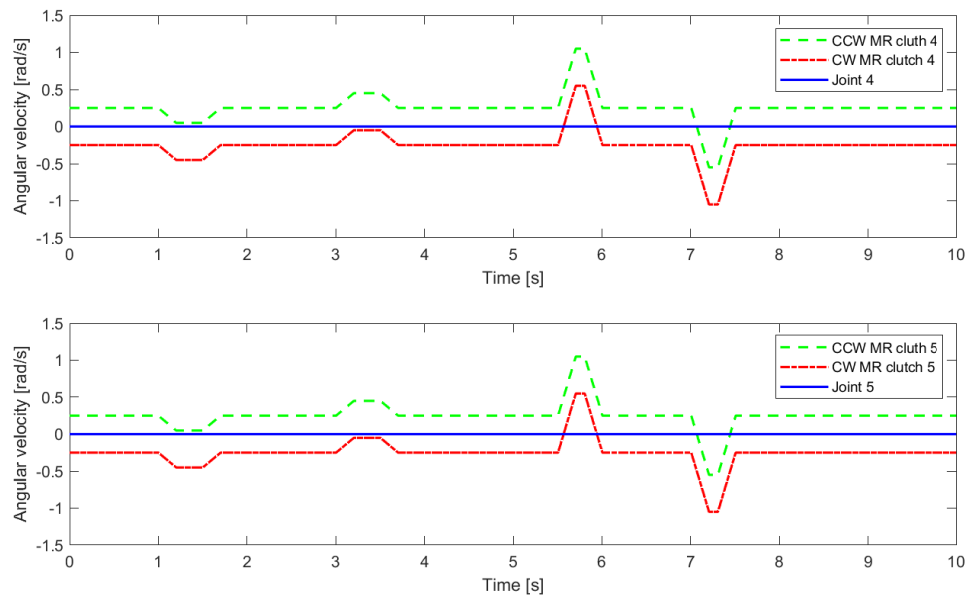Figure 4.16: Simulation of the angular velocity for joint 1, 2, and 3 MR clutches.
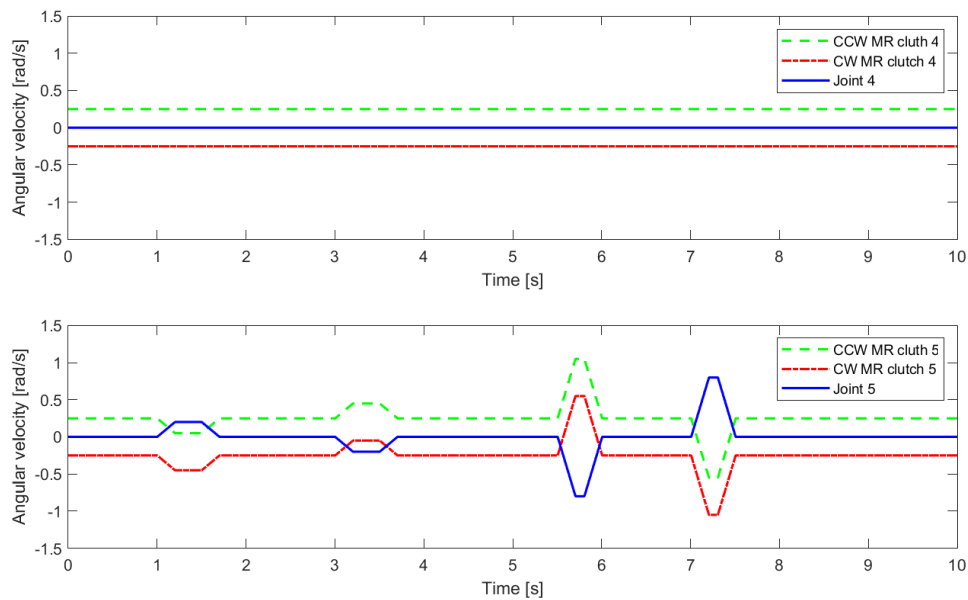
Figure 4.17: Simulation of the angular velocity for joint 4 and 5 MR clutches.

All 5 joints actuated

In the case when all 5 joints move at the same time, the resulting relative rotor-stator rotation of MR clutches includes the velocity components from all the joints in series that are located before the clutches in the transmission. To demonstrate the effect, the work of the transmission is simulated with the joints moving with similar trajectories. The starting points of the joints movement are shifted in time by 1 sec as shown in Fig. 4.18.
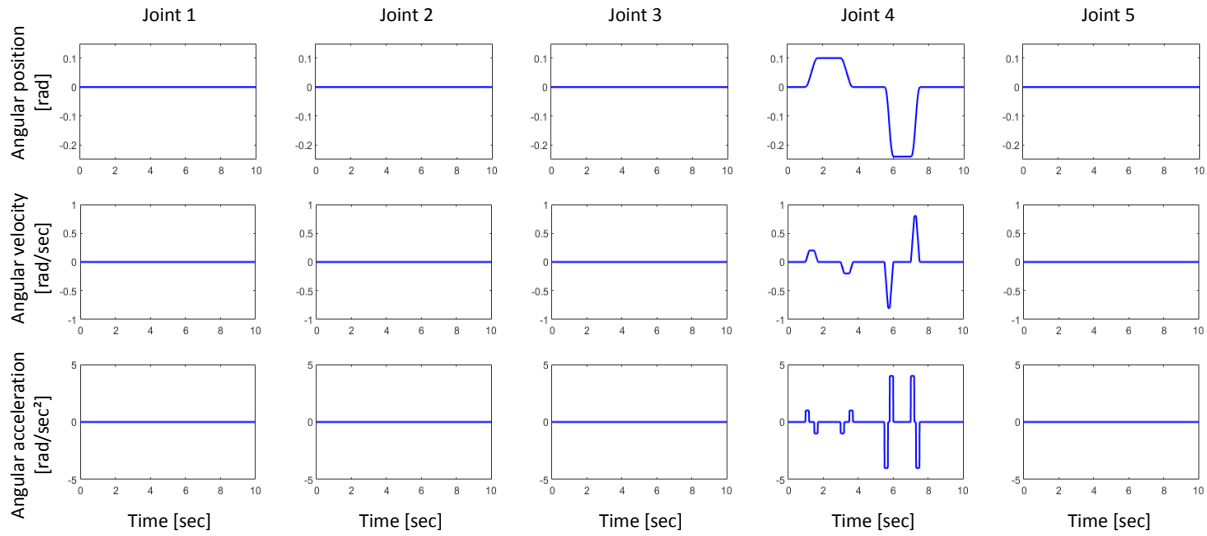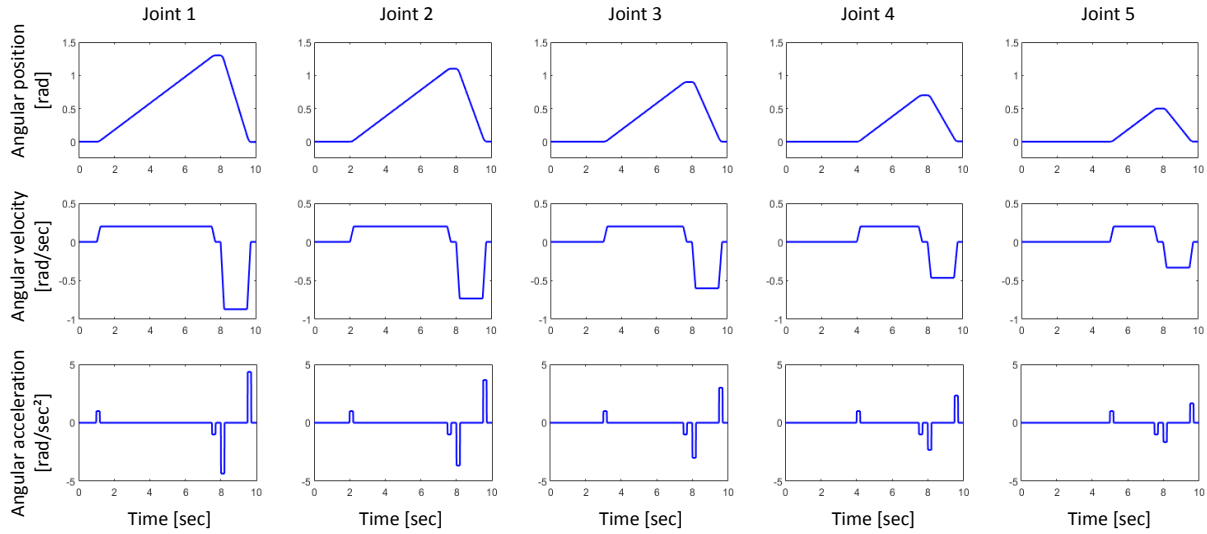

Figure 4.18: 5-DOF manipulator joints movement parameters for MR clutch velocity in serial transmission simulation: all 5 joints active.

On the 1st (top) plot in Fig. 4.19 the velocity of joint 1 clutches shows changes only when the speed of the 1st joint changes. It is seen that when joint 2, 3, 4, or 5 start to move, MR clutches in joint 1 do not change their rotor-stator velocity.

A similar situation is with the MR clutches in the 2nd joint, they do not change their velocity unless joint 2 starts to move. However, the MR clutches in 3rd, 4th, and 5th joints are clearly affected by the motion of the joints in series before them (Fig. 4.19, 4.20). The changes in the speed are represented by the steps in the plotted velocity curves. The curves of MR clutches in every subsequent joint have an additional step in the profile representing shifted in time beginning of the joint movement.
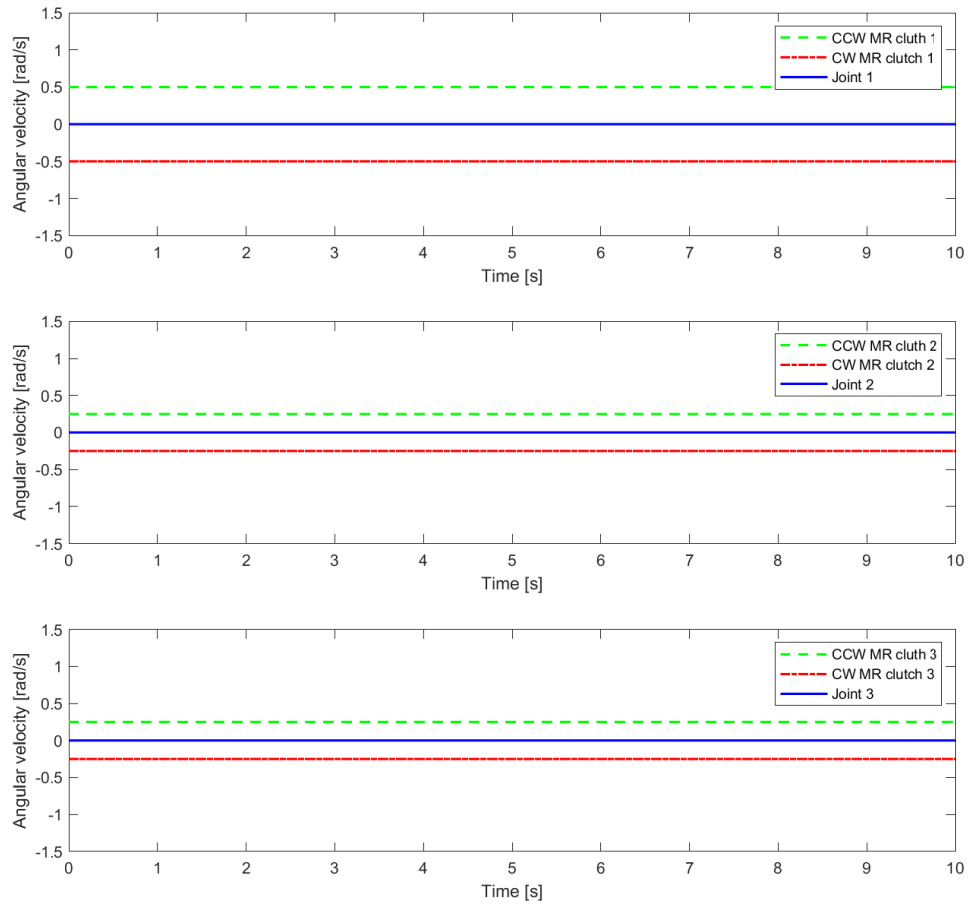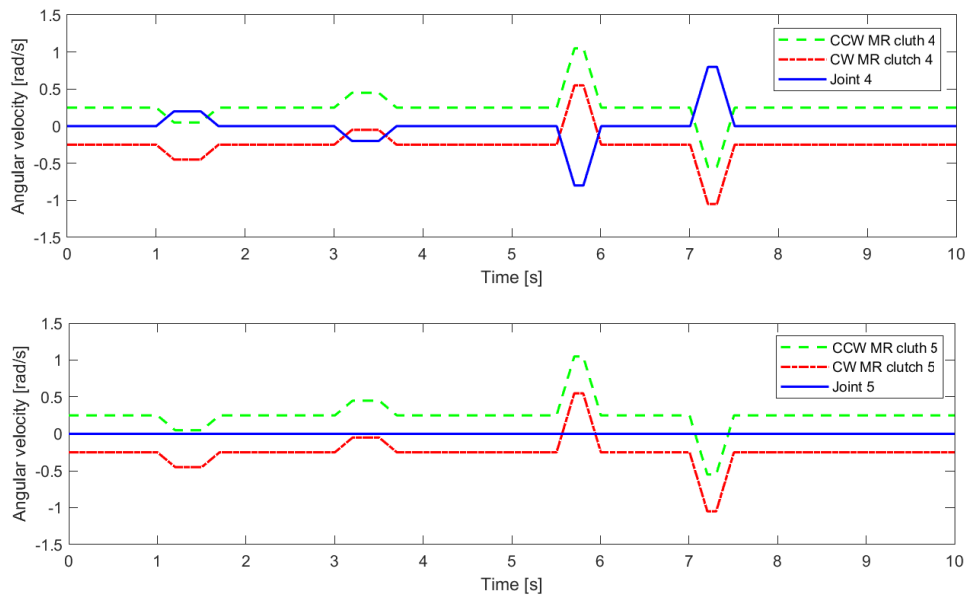
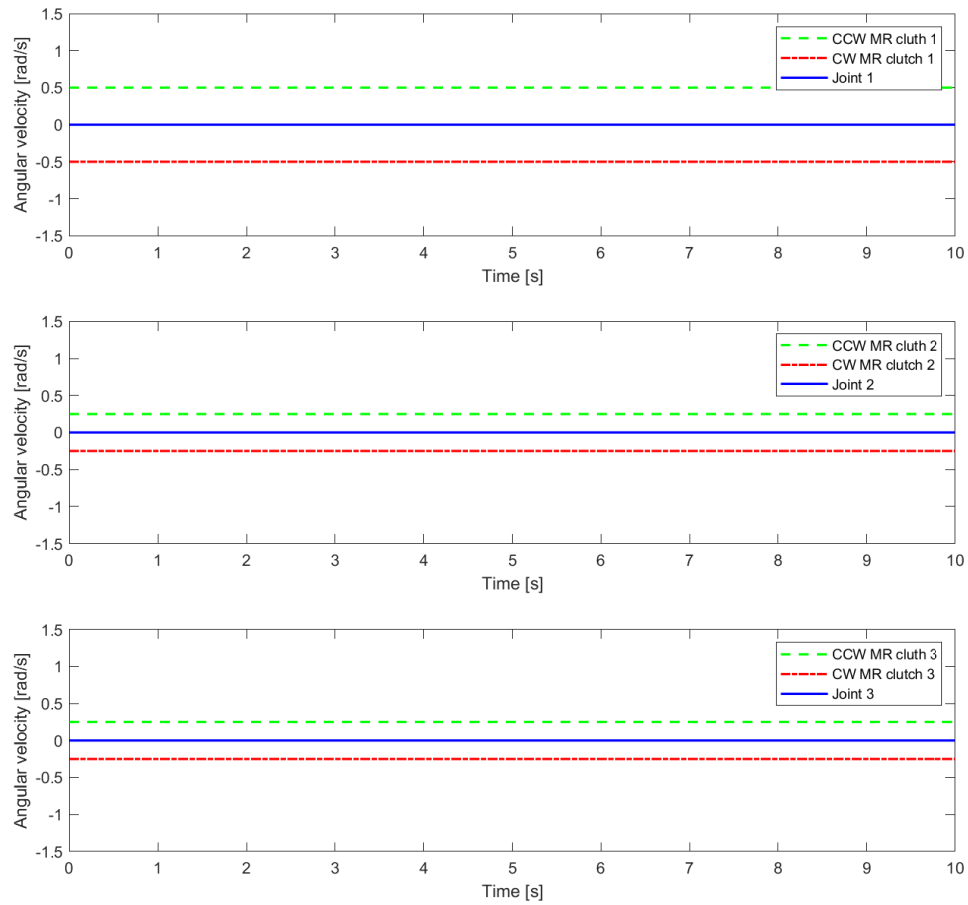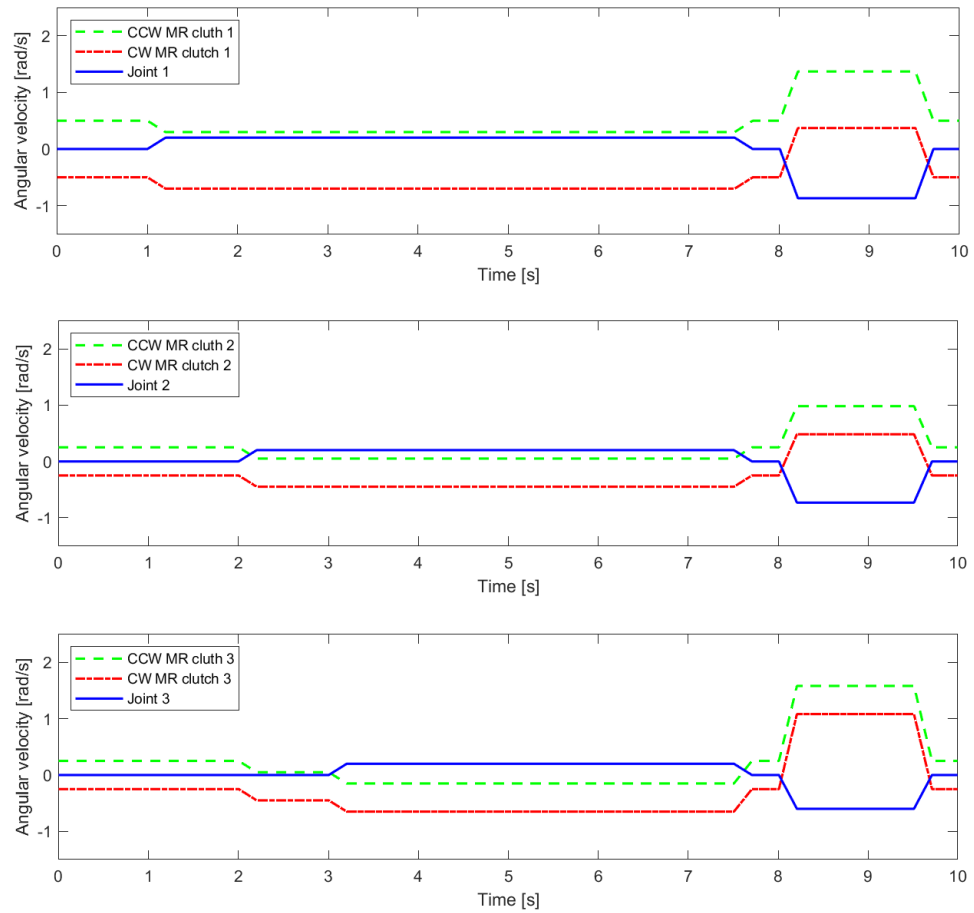Figure 4.19: Simulation of the angular velocity for joint 1, 2, and 3 MR clutches.
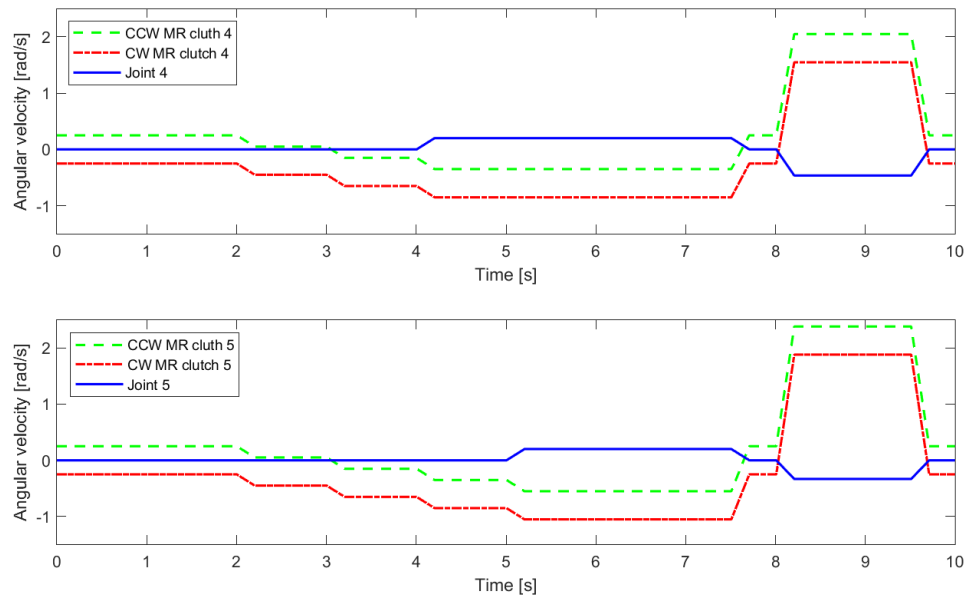
Figure 4.20: Simulation of the angular velocity for joint 4 and 5 MR clutches.

The direction of torque transmitted by the clutch depends on the direction of the rotor rotation relative to the stator. In case if the angular speed of joint movement exceeds the speed of the rotor, the rotor-stator relative rotation changes direction. Therefore, the transmitted torque changes the direction as well. This effect can be simulated using joint trajectory with velocity profile for a limited time exceeding the clutch rotor angular speed. In the second (middle) plot in Fig. 4.21 the angular velocity of the joint stays below 0.5 rad/s during counter-clockwise movement, but exceeds 0.5 rad/s during clockwise movement starting from $T = 7.2$ till $T = 8.2$ sec.
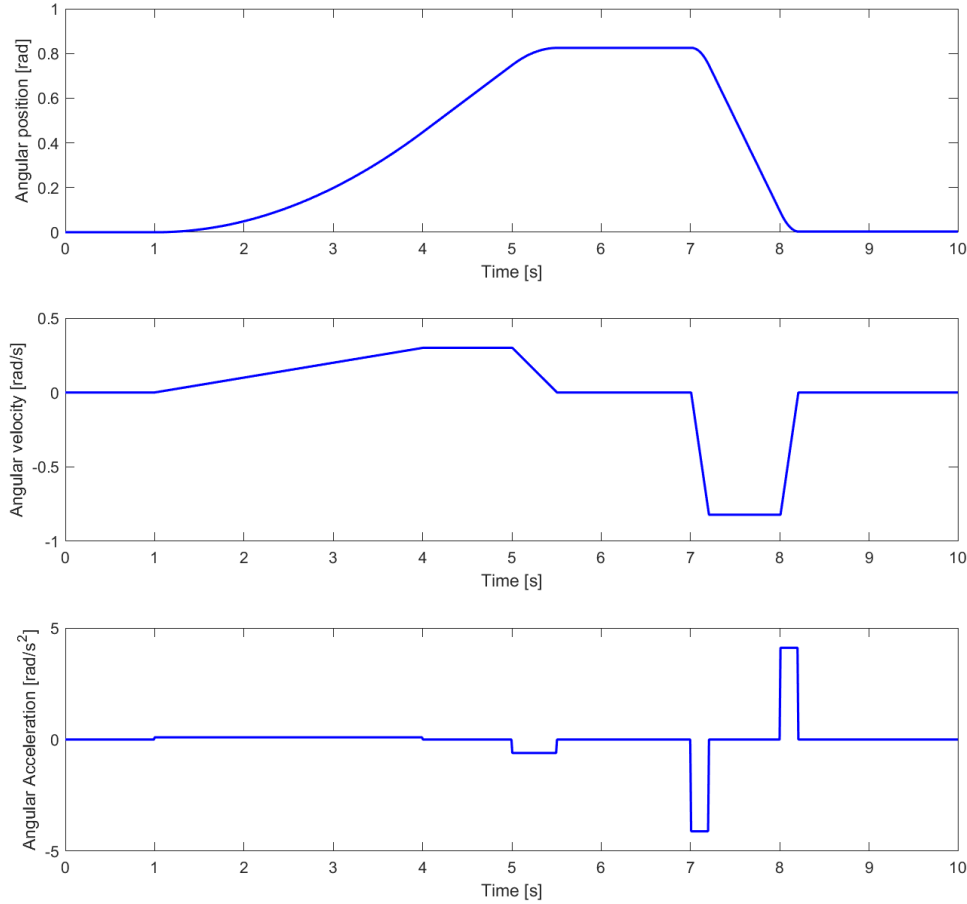
Figure 4.21: Joint trajectory parameters: Angular position, velocity, and acceleration

The first (top) plot in Fig. 4.22 represents the velocity curves for CCW and CW clutches at the joint spinning at 0.5 rad/s in opposite directions. It can be observed that the relative rotor-stator rotation of the MR clutches does not reverse the direction of rotation while the joint moves in the CCW direction with 0.3 rad/s. However, during CW joint movement, the speed of the CW clutch (red curve) changes direction at the time $T = 7.2$ sec as soon as the joint velocity exceeds 0.5 rad/s. The speed of the CW clutch achieves 0.3 rad/s in the CCW direction when the joint reaches 0.8 rad/s in CW. The velocity of the CCW clutch jumps up to 1.3 rad/s, but in the same CCW direction.

In the second (bottom) plot in Fig. 4.22, the curves of transmitted torques for CCW and CW clutches are presented. The simulated clutches transmit 10 N·m each due to yield stress.

Velocity-dependent viscous damping friction is simulated for both clutches with the Newtonian viscosity 5 N·m·s (2.1).
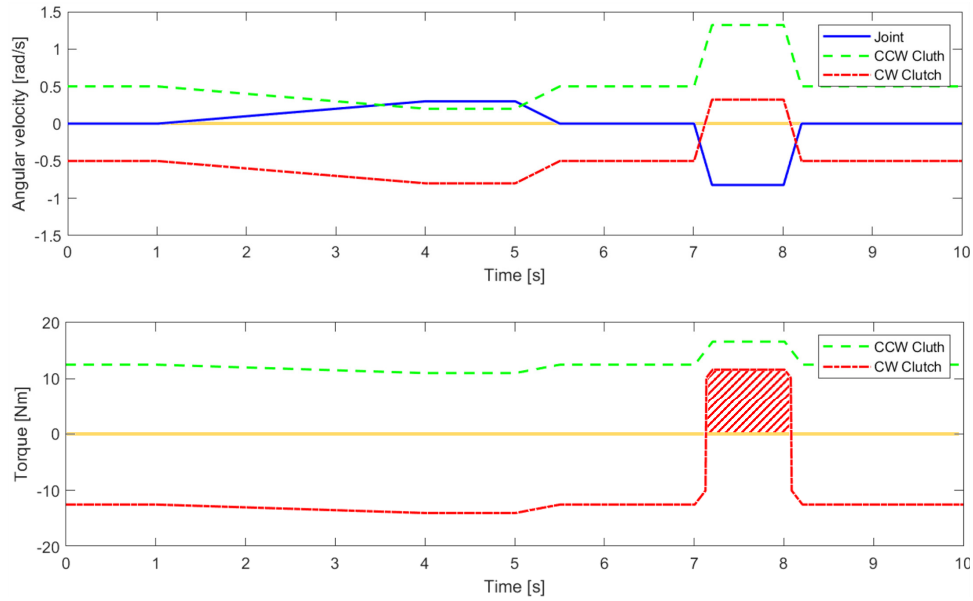
Figure 4.22: Joint velocity and MR clutch rotor-stator relative velocities (top) and MR clutch torques (bottom).

Therefore, in the bottom plot in Fig. 4.22, the torque of the CW clutch (represented by the red curve) changes direction to CCW at the time $T = 7.2$ s. It reaches a 10.2 N·m maximum value in the new (changed) direction as shown by cross-hatched area.

The torque of the other clutch (CCW) does not change the direction, however, it increases from 10.2 to 10.7 N·m due to increase viscose friction when the relative rotor-stator speed increases.

The effect of torque reversal when joint angular velocity exceeds MR clutch rotor-stator speed ensures inherently passive behavior of a joint built based on the antagonistic magneto-rheological clutch actuation approach. The passive behavior of such actuator is discussed in detail in the section 4.3 below.

4.3 Inherent passive behaviour of antagonistic MR actuator

Antagonistic actuation is a well-known and widely used approach in a variety of different fields. Regardless of the embodiment of the design, the majority of antagonistic implementations utilize compliant (backdrivable) actuators. The main feature of a compliant actuator is the ability to significantly reduce or completely disengage the reflected inertia of the actuator from the robot link when necessary.

In recent years, magnetorheological (MR) fluids have been extensively used in clutch-type devices for realizing compliant actuation [1], [2]. As described in Chapter 2, MR clutches possess good dynamic performance characteristics (i.e. high torque-to-inertia ratio, low nonlinearities, fast response time), and offer intrinsic compliance which are the crucial characteristics

required to build an antagonistic actuator.

The remarkable properties of MR clutch crucial for antagonistic implementation and control have already been explored in other high-performance magneto-rheological implementations such as haptic devices, rehabilitation equipment, vibration isolation, etc., [3, 4, 5, 6, 7]. The main focus in these studies is mainly the design, mechanical construction, and implementation issues of MR fluid-based devices.

In the section below, the analytical study of the MR clutch actuation in antagonistic configuration with the focus on passive behavior is presented. Using a pair of antagonistic MR clutches in the 2nd joint of the 5-DOF manipulator, experimental results are collected to support and validate the claims regarding the performance and safety of actuation.

4.3.1 Antagonistic actuation using a pair of MR clutches

In an antagonistic configuration, two MR clutches drive a single load (e.g., a robot joint). In this configuration, the rotors (inputs) of the MR clutches rotate in opposite directions. A single active drive such as an electric motor can be used to generate opposite rotational inputs using various transmission mechanisms (i.e. miter gears). Using this configuration, the MR clutches can provide torque to the load in both CW and CCW directions independently. As such, the direction and the magnitude of the delivered torque can be controlled. This configuration also allows controlling the stiffness of the joint.

One important feature of the antagonistic MR actuation is that it allows using the same active drive (e.g., motor) for other loads. This is because the active drive (motor) coupled to the input (rotor) of the MR clutch is not mechanically connected with the output (stator) of the clutch coupled to a load. The interaction between input and output is carried only through the layer of MR fluid. Thus the active drive can deliver power to other MR clutches whose output are at different states.

Fig. 4.23 shows the CAD model of a 5-DOF collaborative robot that is developed using this actuation concept. This is the first 5-DOF robot of its kind that has been developed using a single DC motor and 5 pairs of antagonistic MR clutches for driving the entire system. The figure highlights the assembly of the first two joints of the robot.

4.3.2 Formulating antagonistic actuation

As mentioned in Chapter 2, the transmission torque of a single MR clutch T_c is derived from the Bingham visco-plastic model as follows,

$$T_c = T_m \, \text{sgn}(\partial \omega) + k_b(\partial \omega) \tag{4.2}$$

where T_m is the magnetic field-dependent positive torque whose value is obtained after integrating (2.1) over the entire surface area of the disks in the MR clutch, $\partial \omega$ is the relative angular velocity between the input and output disks, and k_b is the damping coefficient that accounts for the viscosity of the MR fluid.

As shown, there are two independent input parameters in the MR clutch. One is the flux density of the applied magnetic field B often controlled using an input current in the electromagnetic coil. The changes in T_m depend on the value of this input, i.e., $T_m(B)$ (or the input
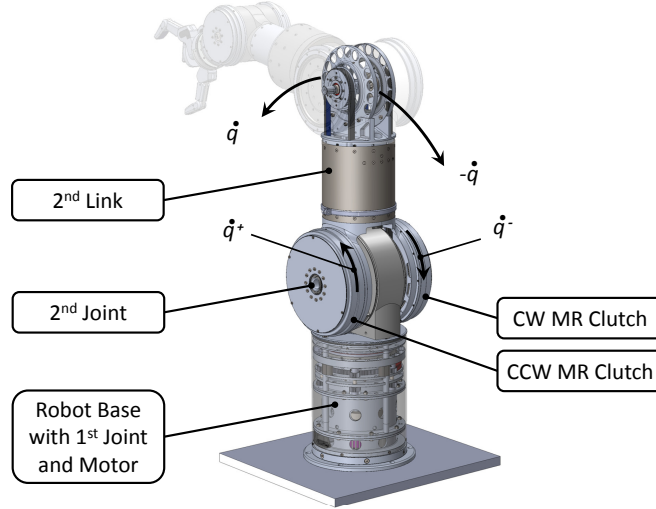
Figure 4.23: Assembled 1st and 2nd joints of the 5-DOF robotic arm with antagonistic MR actuators.

current to the electromagnetic coil $T_m(i)$). The second input parameter is the relative velocity, $\partial \omega$ (or the input velocity, ω_{in}) of the MR clutch. In most applications, the applied magnetic field, B (or the input coil current i) is used to control the transmission torque of an MR clutch while the input velocity ω_{in} is kept constant or quasi-constant.

(4.2) can be re-written using angular velocities of the joint and input velocity of the MR clutch, i.e.,

$$T_c = T_m \, \text{sgn}(\dot{q}_{in} - \dot{q}) + k_b(\dot{q}_{in} - \dot{q}) \tag{4.3}$$

where $\dot{q}$ represents the joint angular velocity which is the same as the MR clutch **output** velocity, and $\dot{q}_{in}$ is the **input** angular velocity of the MR clutch. The use of the sgn(.) function determines the direction of the MR clutch applied torque with respect to the direction of its input rotation. The applied torque will be in the direction of the input rotation as long as the MR clutch output (stator) rotates slower than its input (rotor) in the respective direction, i.e., $|\dot{q}| < |\dot{q}_{in}|$.

On the other hand, as soon as the MR clutch output shaft (stator) starts to rotate faster than its input shaft (rotor) due to some external forces, i.e., $|\dot{q}| > |\dot{q}_{in}|$, then the direction of the MR clutch applied torque is reversed. This switching happens automatically and is inherent in MR clutch behavior. This behavior is similar to the generative mode of a DC motor or the break mode of a car engine when it is downshifted. This so-called "brake" behavior of an MR clutch combined with its compliance results in unique characteristics that are ideal for safe and intuitive robotic manipulation.

If the output (stator) of the MR clutch shaft rotates at the same speed as the input shaft (rotor), i.e., $|\dot{q}| = |\dot{q}_{in}|$, the transmission torque of the MR clutch can any value within $[-T_m, T_m]$ interval.

In an antagonistic configuration, the torque applied to the load, T_a is the summation of the transmission torques of each MR clutch in the pair, i.e.,

$$T_a = T_c^+(B^+, \dot{q}_{in}^+) + T_c^-(B^-, \dot{q}_{in}^-) \tag{4.4}$$

where the $+$ and $-$ superscripts are used, in general, for referring to all variables associated with the positive (CCW) and negative (CW) directions, respectively, as such, T_c^+ and T_c^- are the transmission torques, $\dot{q}_{in}^+$ and $\dot{q}_{in}^-$ are the input velocities, and B^+ and B^- are the flux densities of the applied magnetic field in the positive (CCW) and negative (CW) MR clutch, respectively. Since a single motor is used to produce the positive and negative rotations, the input velocity $\dot{q}_{in} = \dot{q}_{in}^+ = -\dot{q}_{in}^-$ where $\dot{q}_{in} > 0$. It is also assumed that the MR clutches have matched viscous coefficients. Thus, the torque of an antagonistic pair acting on the joint can be represented as follows,

$$
\begin{aligned}
T_a &= T_m^+ \operatorname{sgn}(\dot{q}_{in}^+ - \dot{q}) + T_m^- \operatorname{sgn}(\dot{q}_{in}^- - \dot{q}) \\
&\quad + k_b(\dot{q}_{in}^+ - \dot{q}) + k_b(\dot{q}_{in}^- - \dot{q}) \\
&= T_m^+ \operatorname{sgn}(\dot{q}_{in} - \dot{q}) + T_m^- \operatorname{sgn}(-\dot{q}_{in} - \dot{q}) - 2k_b\dot{q}
\end{aligned}
\tag{4.5}
$$

The standard ISO 10218-1:2011 defines the requirement for industrial robots to guarantee safe operation by limiting the maximum speed of the system [8]. And, as mentioned earlier, the inherent behavior of an MR clutch that ensures automatic changing of the applied torque direction is a remarkable and very important feature in limiting the actuation velocity. To show this the dynamics of a single joint mechanism driven using an antagonistic pair of MR clutches is analyzed in the next Section and uniform boundedness of the speed is shown. The results from this section can be expanded to multiple degrees of freedom devices such as robotic manipulators.

4.3.3 Uniform velocity boundedness: Lyapunov Analysis

In this section, the behavior of the antagonistic MR actuation approach is explained and shown why it is well suited for safe and intuitive manipulation. The experimental results supporting the claims regarding inherent safe actuation are provided afterward.

Consider the dynamics of the single joint, robot as follows,

$$
J\ddot{q} + k_d\dot{q} + g(q) = T_a
\tag{4.6}
$$

where J is the inertia of the joint, k_d is the damping coefficient of the joint, $g(q)$ is the gravity term, and T_a is the torque of the antagonistic MR clutch pair given in (4.5). The proof is provided that the velocity of this mechanism remains bounded in the entire operation mode.

The operating space of the MR clutches is divided into two regions namely, active region where $|\dot{q}| < \dot{q}_{in}$, and the braking region where $|\dot{q}| > \dot{q}_{in}$. Without losing generality, it can be assumed that gravity is compensated through the control action. The goal is to show that the joint velocity is uniformly ultimately bounded by $\dot{q}_{in}$.

To show this, the dynamics given in (4.6) is used to define the Lyapunov storage function,

$$
V(q, \dot{q}) = \frac{1}{2}J\dot{q}^2
\tag{4.7}
$$

where $V(q, \dot{q})$ is positive definite. The time derivative of the storage function evaluated along the trajectory of (4.6) is given by,

$$
\dot{V} = J\dot{q}\ddot{q}
\tag{4.8}
$$

Substituting (4.5) and (4.6) in (4.8), one can obtain,

$$\dot{V} = (T_a - k_d \dot{q})\dot{q} \qquad (4.9)$$
$$= T_m^+ \operatorname{sgn}(\dot{q}_{in} - \dot{q})\dot{q} + T_m^- \operatorname{sgn}(-\dot{q}_{in} - \dot{q})\dot{q}$$
$$- 2k_b \dot{q}^2 - k_d \dot{q}^2$$

It can be shown that as soon as one of the MR clutches enters the braking mode where $|\dot{q}| > \dot{q}_{in}$, then $\dot{V}$ becomes negative definite, i.e.,

$$\dot{V} = -(T_m^+ \operatorname{sgn}(\dot{q}) + T_m^- \operatorname{sgn}(\dot{q}))\dot{q} - 2k_b \dot{q}^2 - k_d \dot{q}^2$$
$$= -(T_m^+ + T_m^-)|\dot{q}| - 2k_b \dot{q}^2 - k_d \dot{q}^2 < 0 \qquad (4.10)$$

In deriving (4.10) the fact that $\operatorname{sgn}(\dot{q}_{in} - \dot{q}) = -\operatorname{sgn}(\dot{q})$ (and similarly $\operatorname{sgn}(-\dot{q}_{in} - \dot{q}) = -\operatorname{sgn}(\dot{q})$) when $|\dot{q}| > \dot{q}_{in}$ is used. This shows that as soon as one of the MR clutches enters the braking region (i.e., $\dot{q} > \dot{q}_{in}$ or $\dot{q} < -\dot{q}_{in}$), the derivative of the storage function becomes negative and forces the corresponding MR clutch to return back to the active region where it behaves with bounded output velocity as expected.

When $|\dot{q}| = \dot{q}_{in}$, one can use the same storage function (4.7) to analyze the behaviour of the system. To this end, let us consider the case when $\dot{q} = \dot{q}_{in}$, in which the positive (CCW) MR clutch produces a variable torque $T_c^+ \in [-T_m^+, T_m^+]$. It is easy to show that,

$$\dot{V} = (T_c^+ - T_m^-)\dot{q}_{in} - (2k_b + k_d)\dot{q}_{in}^2 \qquad (4.11)$$

The derivative of the storage function is negative define (i.e., $\dot{V} < 0$) for any value of $T_c^+ \leqslant 0$, forcing the positive (CCW) MR to return back to the active region. A similar argument can be made when $\dot{q} = -\dot{q}_{in}$ for the negative (CW) MR clutch, which will complete the proof.

∎

In summary, the natural behavior of antagonistic MR actuators forces the joint angular velocity to remain uniformly ultimately bounded.

4.3.4   Safe control design example

It is known that the severity of an accident (e.g. collision) with a robot manipulator directly relates to the energy transferred from the robot to the human [8]. Thus, one common strategy in designing a human-safe robot is to limit the total kinetic energy of the system to a safe limit. It can be shown that the proposed actuator provides a simple and intuitive means of achieving this requirement without using any additional sensors and/or complex control algorithms.

Let's assume an upper bound for the total kinetic energy of the system, λ_{max} for which the safety of the human in case of an accident can be guaranteed. Considering the total kinetic energy of the system defined in (4.6) along all system's trajectories as

$$E_k(\dot{q}) = \frac{1}{2}J\dot{q}^2 \qquad (4.12)$$

then the objective of the safe control design is to limit the total kinetic energy of the system, i.e.,

$$E_k(\dot{q}) \leqslant \lambda_{\max}, \qquad \forall \; \dot{q} \in \mathbb{R} \tag{4.13}$$

A gear ratio of β between the motor and the input (rotor) of the MR clutches considered, i.e.,

$$\dot{q}_{\text{in}} = \beta \dot{q}_{\text{mot}} \tag{4.14}$$

where $\dot{q}_{\text{mot}}$ is the velocity of the motor. Previously it was shown that the joint velocity of the system was uniformly ultimately bounded to $|\dot{q}_{\text{in}}|$. Using these results, it can be shown that,

$$\frac{1}{2}J\dot{q}^2 \leqslant \frac{1}{2}J\dot{q}_{\text{in}}^2 \leqslant \frac{1}{2}J(\beta\dot{q}_{\text{mot}})^2 \tag{4.15}$$

To satisfy the safe control design requirement defined in (4.13), there exists an explicit solution for the motor velocity that guarantees total kinetic energy along all system's trajectories, i.e.,

$$\dot{q}_{\text{mot}} \leqslant \left(\frac{2\lambda_{\max}}{J\beta^2}\right)^{\frac{1}{2}} \tag{4.16}$$

Since the motor is mechanically decoupled from the load, one can guarantee that the antagonistic MR actuation cannot deliver kinetic energy to the system beyond the safe level. This statement is true even when the load is driven externally such that the total kinetic energy of the system exceeds the safe level, in which case the automatic switching of the actuator to braking mode forces the joint velocity to reduce until the kinetic energy of the system is reduced below the safe level. One should note that this behavior is inherent to the actuator and does not depend on any sensor measurements nor any specific control algorithm.

Similar control strategies based on deliverable torque or stiffness control can be achieved using antagonistic MR actuators with the same level of simplicity and intuitiveness.

In the next section, the experimental results are provided to validate the theories discussed in this section.

4.3.5 Relationship between the actuator torque and joint velocity

To visualize the active and braking regions of the operation, the relationship between the joint velocity and the actuator torque is presented here. As in the previous section, it is assumed $\dot{q}_{\text{in}} = \dot{q}_{\text{in}}^+ = -\dot{q}_{\text{in}}^-$.

Moreover, the output joint velocity in both active (i.e., $|\dot{q}| < \dot{q}_{\text{in}}$) and braking (i.e., $|\dot{q}| > \dot{q}_{\text{in}}$) regions should be considered to capture the complete torque-velocity curve. Since the inherent behavior of an MR clutch bounds the joint velocity to within the active region, it is assumed that an external force acts on the joint. The specific experimental setup that enables realizing such conditions is explained in the next section.

For simplicity, one can start with an ideal torque-velocity relationship considering only the sheer stress of the MR fluid (as in Bingham plastic and Herschel-Buckley models) and ignoring the effects of MR fluid viscosity (i.e., $k_{\text{b}} = 0$) and backlash in torque transmission. Fig. 4.24 depicts the torque-velocity relationship. The figure shows the torque-velocity curves

(a) CCW MR clutch   +   (b) CW MR clutch   =   (c) Both MR clutches
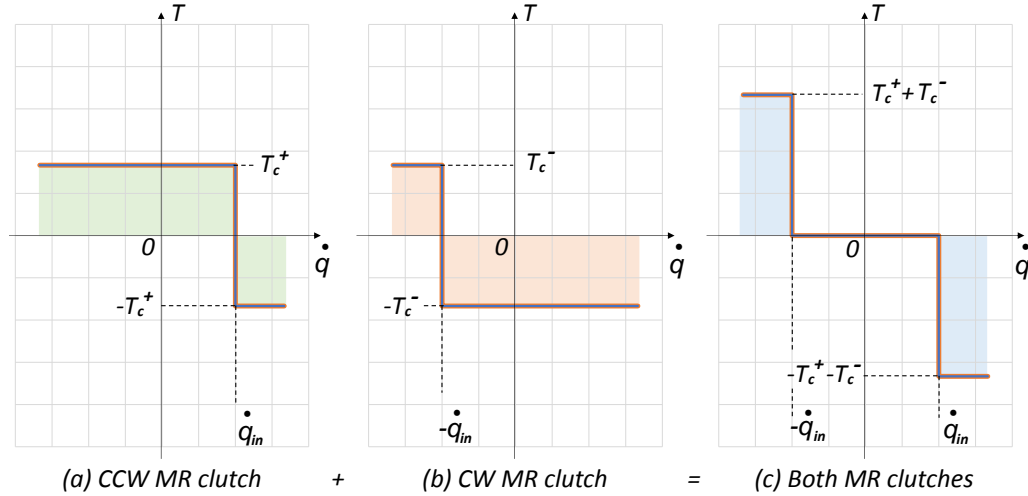
Figure 4.24: The relation between transmitted torque and joint angular velocity for the ideal case: $T_c^+ = T_c^-$, no viscosity, no backlash in the transmission.

for the positive (CCW) and negative (CW) MR clutches, separately, as well as the antagonistic combination of both MR clutches.

Fig. 4.24 (a) shows the torque-velocity curve for the positive (CCW) MR clutch exerting a positive toque T_c^+ within the active region. The torque becomes negative (i.e., $-T_c^+$) when the velocity surpasses $\dot{q}_{in}$ in CCW direction. Similar curve for the negative (CW) MR clutch is shown Fig. 4.24 (b) exerting a torque in CW direction ($-T_c^-$) within the active region and switching the torque in CCW direction (positive T_c^-) as soon as the velocities surpasses $-\dot{q}_{in}$ in CW direction.

In this figure, $T_c^+ = T_c^-$, consequently the antagonistic combination of two torques within the active region will be zero as shown in Fig. 4.24 (c). Outside the active region, the actuator resists twice as hard to exit the braking region.

Normally, not both MR clutches in the pair are activated with equal torque simultaneously yet only one MR clutch is activated for the corresponding direction. Opposing clutch in the pair, either (ideally) exerts zero torque or a small torque due to friction and residual magnetism.

Fig. 4.25 depicts the torque-velocity relation for a case where only the positive (CCW) MR clutch is used for actuating the load with a torque T_c^+. In this case, the negative (CW) MR clutch acts as a disturbance during actuation in the active region with torque $-T_c^-$ where it is assumed $T_c^- \ll T_c^+$.

If the effect of MR fluid viscosity, as well as small variations in the yield stress [9], is included in the torque-velocity curve of the actuator, the results will be as shown in Fig. 4.26.

As observed, the torque-velocity curve has a slope reflecting the torque increase with respect to the velocity due to the viscosity of the fluid. Moreover, the smooth transition of torque (i.e., rounded corners in the graph) is the direct result of yield stress variations [9]. In obtaining these results, it was assumed that only the positive (CCW) MR clutch was energized while the other MR clutch exerted a small torque due to the remnant magnetic field and the Coulomb friction in the rotary seals.

Finally, adding the effect of backlash within the mechanical transmission of the MR clutch

(a) CCW MR clutch   +   (b) CW MR clutch   =   (c) Both MR clutches
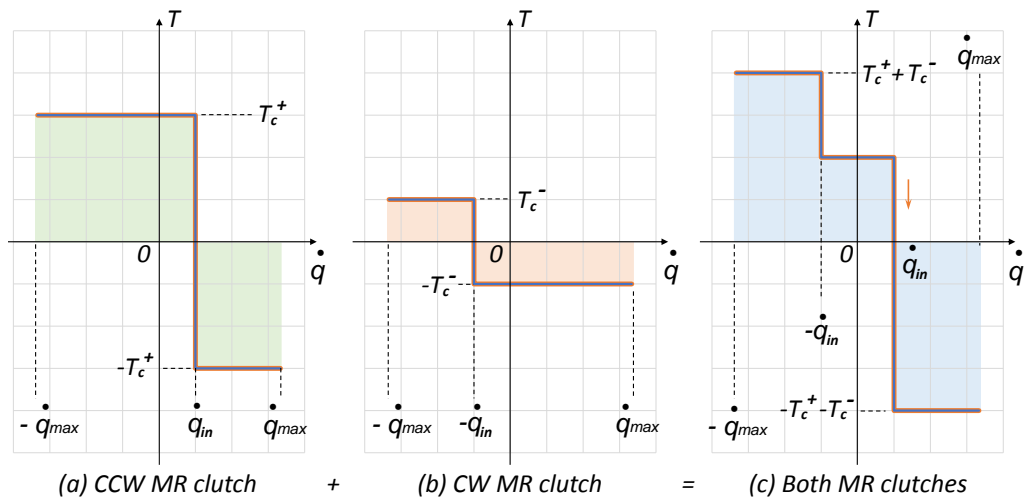
Figure 4.25: The relation between transmitted torque and joint angular velocity for the ideal case: $T_c^+ \gg T_c^-$, no viscosity, no backlash in the transmission.
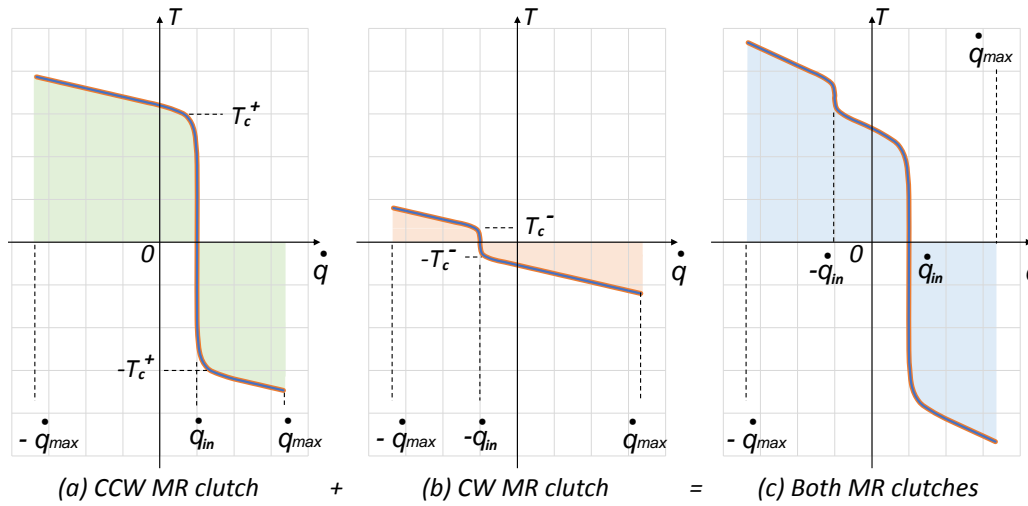

(a) CCW MR clutch   +   (b) CW MR clutch   =   (c) Both MR clutches

Figure 4.26: The relation between transmitted torque and joint angular velocity for the case when MR fluid viscosity is taken into account.

will lead to the torque-velocity curve shown in Fig. 4.27.
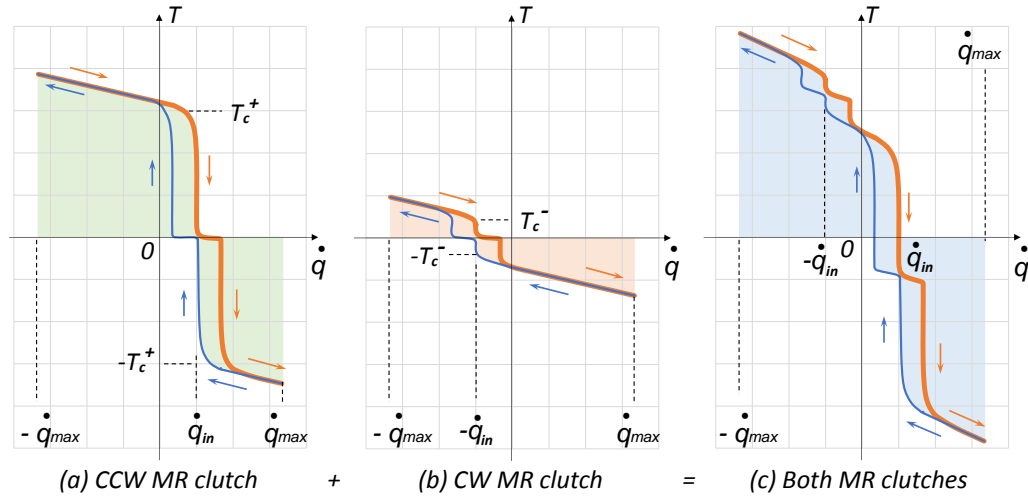
Figure 4.27: The relation between transmitted torque and joint angular velocity for the case when viscous MR fluid and backlash in the transmission are taken into account.

As observed, the effect of backlash only appears in the results when the joint velocity (output velocity of the MR clutch $\dot{q}$) reaches the clutch input velocity $\dot{q}_{\text{in}}$. The backlash is due to the imperfect coupling of mechanical parts such as spur gears as they change transmitting torque direction. For example, in the case of spur gear transmission, at this moment the tooth of the driving gear separates from the tooth of the driven gear and starts to move across the gap towards the second adjacent tooth. During this backlash movement, the separation or decoupling of the components inhibits the MR clutch from transmitting torque as seen in Fig. 4.27 (c). Therefore, no torque is transmitted until the gap is crossed and the parts regain proper engagement.

4.3.6 Experimental verification of intrinsic passivity

In this section, experimental results are provided to validate the previous analysis. The tests are performed using the 2$^{\text{nd}}$ joint of the 5-DOF manipulator. The higher joints of the robot are removed as shown Fig. 4.23 in order to eliminate the effect of their inertia on the results. Similar results can be obtained for other joints which are not included here for the sake of brevity.

To perform the experiments, the positive (CCW) and negative (CW) MR clutches in joint 2 are activated in sequence so that the 2$^{\text{nd}}$ link would rotate in clockwise and counter-clockwise directions in a reciprocated manner. A sequence of robot poses representing its reciprocal motion is as shown in Fig. 4.28.

The first figure, labeled Pos. 1 in Fig. 4.28 shows link 2 of the robot as it passes through the upright position in the CW direction. The joint velocity is maximum in this position ($\dot{q} = \dot{q}_{\text{max}}$). Pos. 2 shows link 2 after decelerating and reaching a zero velocity in the CW direction. At this position, the direction of the motion is switched to the CCW direction using the appropriate MR clutch. Pos. 3 shows link 2 as it accelerates in the CCW direction. Pos .4, Pos. 3' and
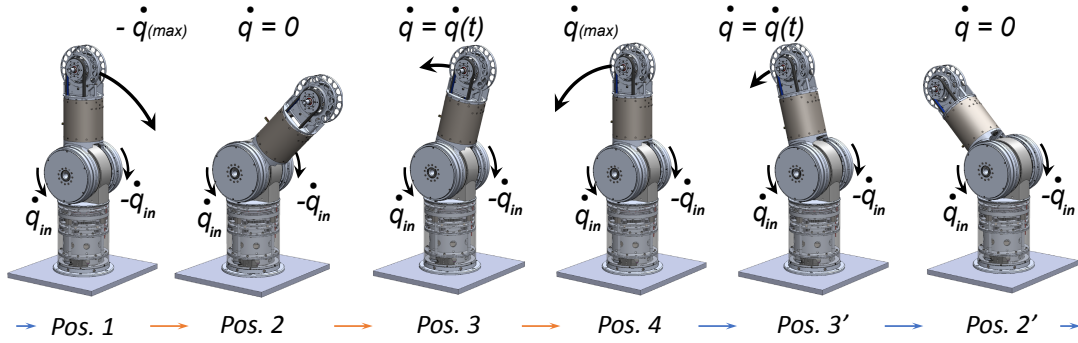
Figure 4.28: Robot positions.

Pos. 2' are identical to Pos. 1 Pos. 3 and Pos. 2, respectively, but in the CCW direction. This motion cycle will repeat as the link starts to accelerate in a CW direction towards Pos. 1 again.

To achieve this motion cycle, the MR clutches are activated in sequence with the desired torque value. For example, one clutch in the pair is energized with a constant current of 0.2 A, while the opposing clutch is in an "off" state. The input (rotor) velocities of both MR clutches are set to 6 deg/s in opposite directions.

Joint 2 is moved within the ±20 degree range from its upright position. To force the joint velocity outside the active region of the MR clutches, joint 2 of the robot is attached to a KUKA Light-Weight Robot (LWR) 4+. The KUKA robot is programmed to pull or push the joint depending on the direction of the joint actuation. This combination forces the velocity of the joint to periodically surpass the input velocity of MR clutches and temporarily moves the joint into the braking region of actuation. In the experiment, the maximum angular velocity of joint 2 reached to 54 deg/s in either directions. The test setup used for these experiments is shown in Fig. 4.29.
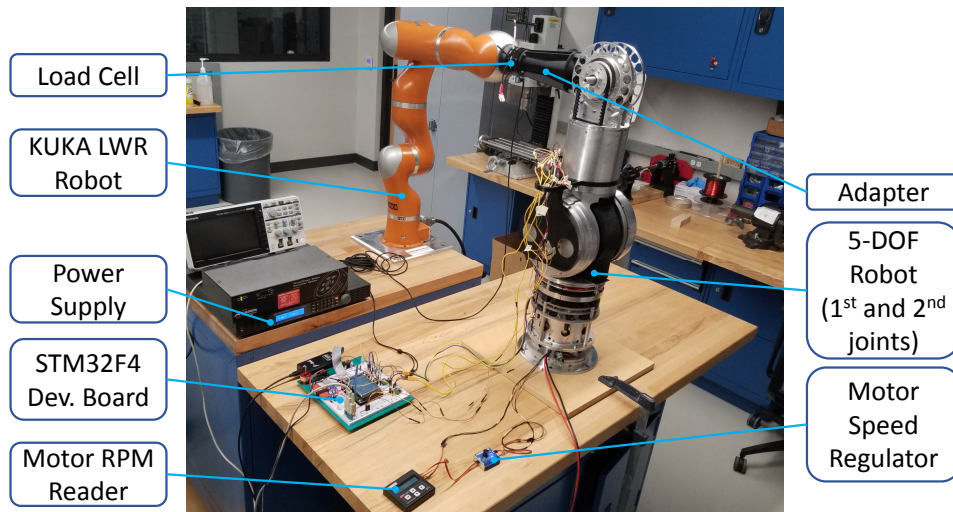

Figure 4.29: Experimental set-up consisting of the lower part of the MR actuated 5-DOF robot and a KUKA LWR 4+ robot.

A force/torque sensor (ATI Gamma US-15-50) is used at the coupling point between the

two robots. The force/torque sensor measures the total torque applied to joint 2 at the coupling point. STM32F407VET6 microcontroller is used to acquire the data at a sampling frequency of 1 kHz. The microcontroller is also responsible for generating suitable control signals for each MR clutch through motor drivers TI DRV8874 that provide the necessary current to energize the MR clutches. Each joint of the robot including joint 2 is equipped with an Absolute Zettlex encoder (17-bit for joint 2) from IncOder[TM] to measure the angular position at 10 kHz frequency. A single brushless DC motor (Hacker, model Q80-13XS F3A) with a harmonic gearbox (SHD-25-100-2SH) provides power to all 5 joints of the robot. The motor and the gearbox are located at the base of the robot to minimize the robot's inertia.

4.3.7 Experimental results

Using the force/torque sensor and encoder measurements the relationship between the actuator torque and the output angular velocity obtained for cases when either positive (CCW) or negative (CW) MR clutch in the 2nd joint antagonistic actuator energised. The results for cases when MR clutches are subject to 0.2 A current are shown in Fig. 4.30.

(a) Measured Torque
for CCW MR clutch energized

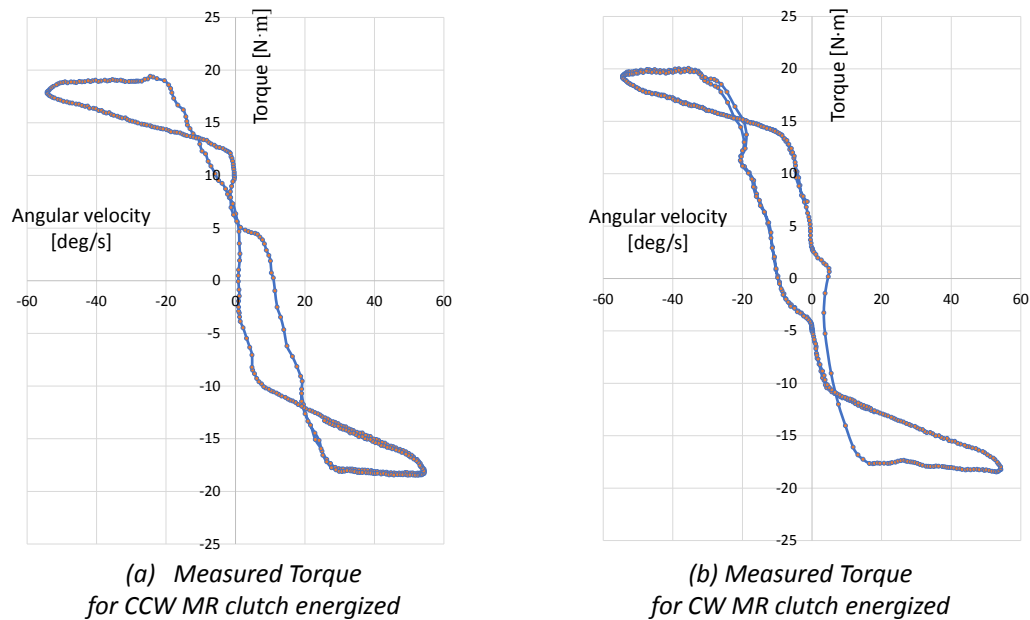*(b) Measured Torque*
for CW MR clutch energized

Figure 4.30: The torque-velocity relationship in the antagonistic MR actuator in the 2nd robot joint for cases when either CCW (a) or CW (b) MR clutch is subjected to 0.2 A current.

Since the force/torque sensor reading is performed using the attached robot link and not at the robot's join, one can see the undesired effects of other parameters such as gravity, friction, joint and link flexibility, etc. on the results [10, 11, 12]. As such, the torque-velocity curve appears with a visible hysteresis in both high and low angular velocity regions. The hysteresis in the low-velocity region is mostly due to the limited rigidity of the structure and due to the backlash in the mechanical transmission. This behavior is previously predicted in Fig. 4.27. On the other hand, the hysteresis in the high-velocity region is mostly due to the inertial and gravitational forces. Using the joint angle measurements and the known value of the robot

mass, the effect of the gravity and inertial forces can be removed from the results as shown in Fig. 4.31.
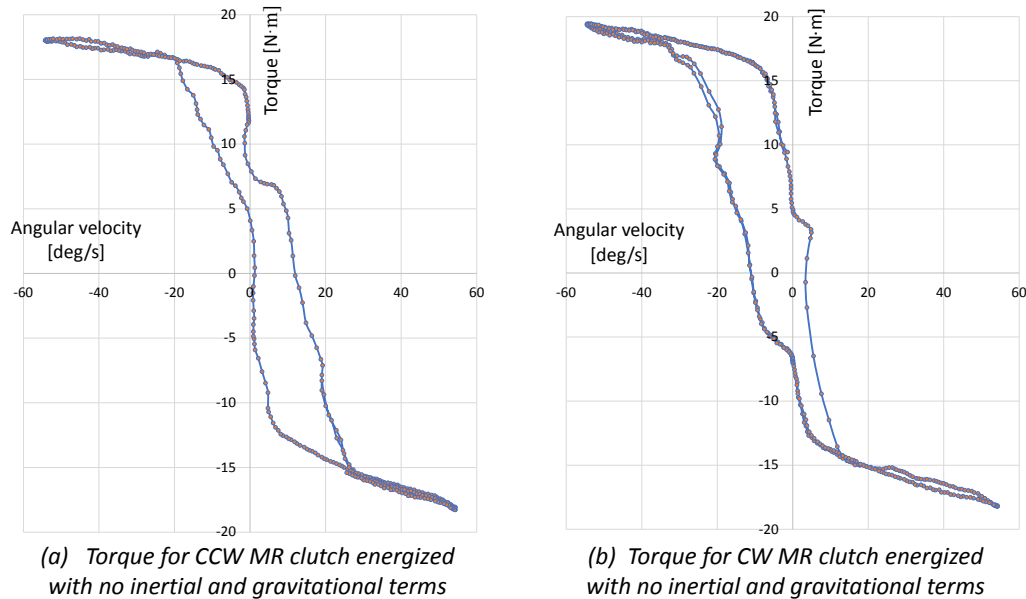

(a) Torque for CCW MR clutch energized with no inertial and gravitational terms

(b) Torque for CW MR clutch energized with no inertial and gravitational terms

Figure 4.31: The torque-velocity relationship in the antagonistic MR actuator in the 2nd robot joint for cases when either CCW (a) or CW (b) MR clutch is subjected to 0.2 A current, with no inertial and gravitational terms.

The figure includes the torque-velocity curves for the same cases when either positive (CCW) or negative(CW) MR clutch energized with 0.5 A coil current. As observed, the torque-velocity curve of the actuator with positive (CCW) clutch energized shown in Fig. 4.31 (a) matches very well with the one depicted in Fig. 4.27 (c) which was obtained using the theories of MR actuation and the assumption of backlash within the mechanical transmission.

To evaluate the stability behavior of the antagonistic MR actuator bounding the output velocity under large external disturbances, additional experiments were performed using the same set-up shown in Fig. 4.29.

In this experiment, the MR clutches in the 2nd joint were energized alternately in order to move the link between ±20 degrees in the same pattern like the one shown in Fig. 4.28. The link was moved at a constant angular velocity of ±3.5 deg/s and the input (rotor) velocity of MR clutches in the pair was set to ±6 deg/sec. The KUKA LWR 4+ robot was used to introduce disturbance by exerting short periodic perturbations that forced the 2nd joint to move temporarily at a speed above the MR clutch input velocity. This would allow us to observe and study the behavior of the MR clutch when in braking mode. The results are shown in Fig. 4.32 which includes the angular position and angular velocity of the 2nd joint, as well as the antagonistic actuation torque.

On the plot in Fig. 4.32, there are 3 perturbations presented, two during clockwise rotation that forces the angular velocity to 24 deg/s in that direction and one perturbation during the counter-clockwise direction that forces the velocity to about 39 deg/s in the corresponding direction. The effect of these velocity increases is clearly seen in the angular position of the joint.
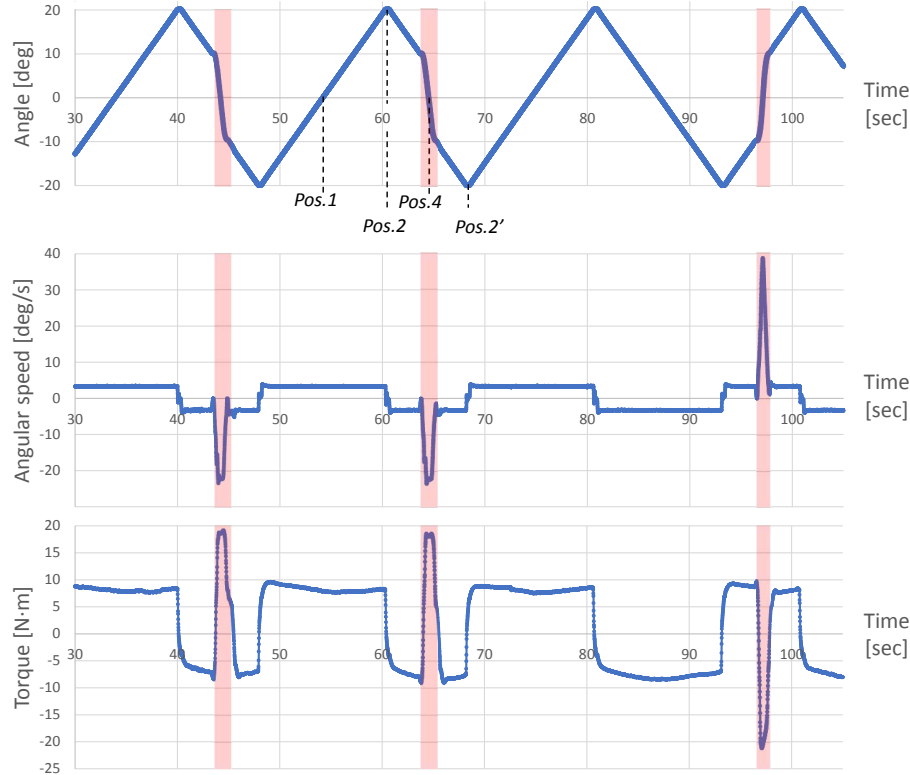
Figure 4.32: Closed-loop position control using antagonistic MR actuator

Looking at the torque graph (the bottom graph) in Fig. 4.32 one can see that at the velocity surges, the MR actuator immediately reverses the torque direction forcing the system to return to the active region and reduces the output velocity. The barking regions are highlighted in the graphs with the red color. The observed behavior occurs instantaneously and inherently without relying on sensor information or a control system. The behavior is triggered as soon as the velocity of the joint (link) exceeds the input (rotor) velocity of the MR clutches. Starting this instant, the MR clutch acts as a brake with the torque opposing the high-velocity motion. The results clearly validate the theoretical results in terms of the uniform boundedness nature of the MR actuation. On a broader point, these results underpin the earlier claims regarding the suitability of MR actuation for safe, intuitive, and dependable actuation without the complexities and high cost of alternative approaches.

4.4 Joint level control for antagonistic MR actuator

4.4.1 Antagonistic MR actuator position control

The simplest control design for 5-DOF manipulator can be developed based on building a separate proportional-integral-derivative (PID) compensator at the level of each joint. For every pair of antagonistically arranged MR clutches, an identical PID control algorithm is implemented in the respective controller board (Fig. 4.33). However, the proportional, integral, and derivative gains are selected and tuned separately for every joint.
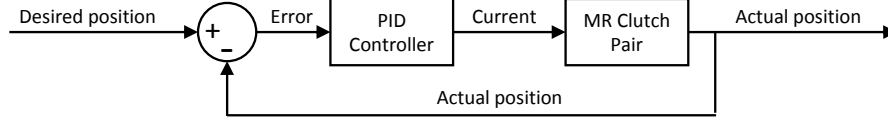
Figure 4.33: Joint level position control diagram for the 5-DOF.

In the joint level position control, the angular position data from the joint encoder is used as a feedback response signal to calculate the input current for each MR clutches in a pair. The PID regulation controller can be written in the following form

$$u(t) = K_{\mathrm{p}}e(t) + K_{\mathrm{i}} \int_0^t e(\tau)\,d\tau + K_{\mathrm{d}}\frac{de(t)}{dt}, \tag{4.17}$$

where K_p is the proportional gain, K_i is the integral gain, K_d is the derivative gain, $e(t) = (q_d(t) - q(t))$ is the error between the desired value of the joint position $q_d(t)$ and the actual position of the joint $q(t)$. To implement the PID controller on the STM32-based digital controller board, the discretization is performed as follows,

$$\int_0^t e(\tau)\,d\tau \approx T \sum_{n=1}^{k} e_n, \tag{4.18}$$

$$\frac{de(t)}{dt} \approx \frac{e_k - e_{k-1}}{T}, \tag{4.19}$$

where T is the sampling period, e_k is the error of the k-th sample. The PID regulation controller can be re-written as follows,

$$u_k = K_p \cdot e_k + K_i \cdot T \sum_{n=1}^{k} e_n + \frac{K_d \cdot (e_k - e_{k-1})}{T}. \tag{4.20}$$

Position control: sinusoidal reference signal tracking

The work presented in this section was prepared in collaboration with Ziqi Yang.

The sinusoidal input tracking control experiment is performed with the 2nd joint of the 5-DOF manipulator. The amplitude of the input signal is set to 20°, with the minimum angular position of the joint 153°, maximum 173°. Manual tuning of PID gains is performed during multiple runs. The experimental tracking is performed with 0.25 Hz, 0.5 Hz, and 1 Hz frequency of the sine wave. The motor speed is kept constant (250 RPM) to ensure constant angular velocity of the MR clutch rotors.

Fig. 4.34 shows the angular position (top plot) and positional error (bottom plot) for the 0.25 Hz sine wave tracking experiment. Small error less than 0.2 ° demonstrates good performance of the joint controller.
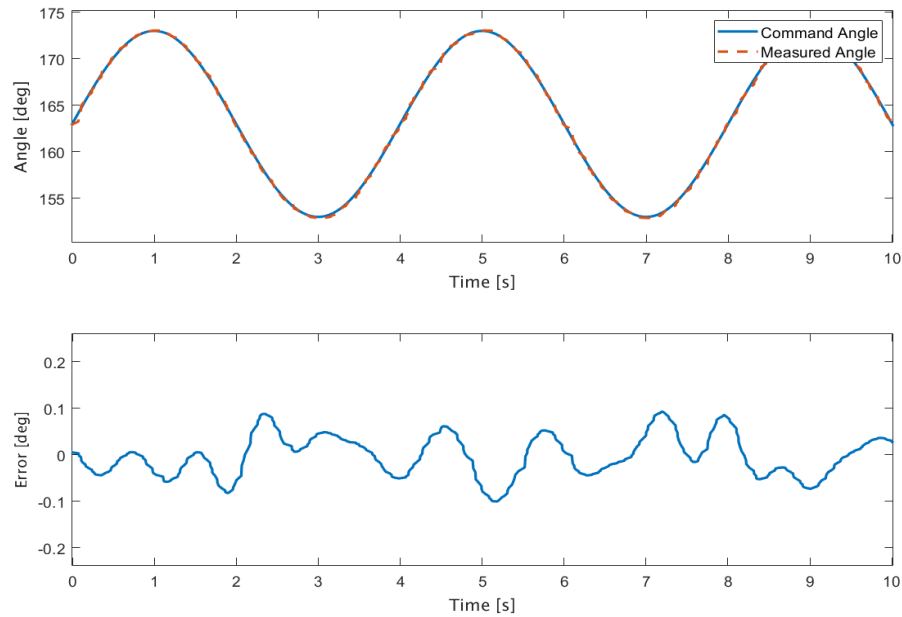
Figure 4.34: Joint 2 position tracking a 0.25Hz sinusoidal reference signal.

Fig. 4.35 shows the angular position (top plot) and positional error (bottom plot) for the 0.5 Hz sine wave tracking experiment. Greater error with the amplitude $0.2°$ can be observed. The test results show deterioration of tracking performance at the higher frequency of sine wave input signal.

Fig. 4.36 shows the angular position (top plot) and error (bottom plot) for the 1.0 Hz sine wave tracking experiment. Even bigger error with the amplitude $0.6°$ can be observed. Oscillation with amplitude $0.15°$ can be observed on the plot. The test results show further deterioration of tracking performance at 1 Hz frequency of sine wave input signal.

Based on the experimental results, good tracking performance of the PID control is observed for a frequency lower than 0.5 Hz. However, the higher frequency input signal produces a larger error and unwanted oscillations of the joint.
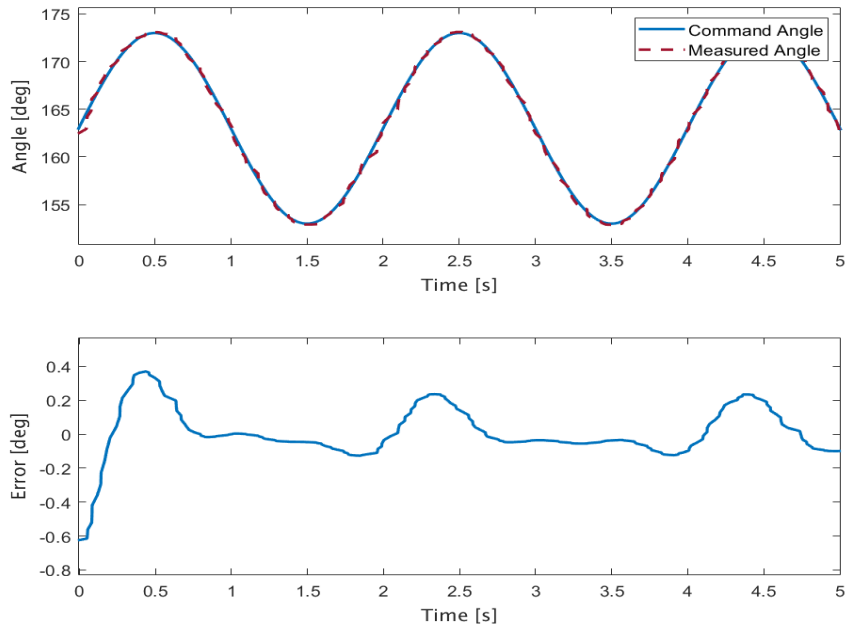
Figure 4.35: Joint 2 position tracking a 0.5Hz sinusoidal reference signal.
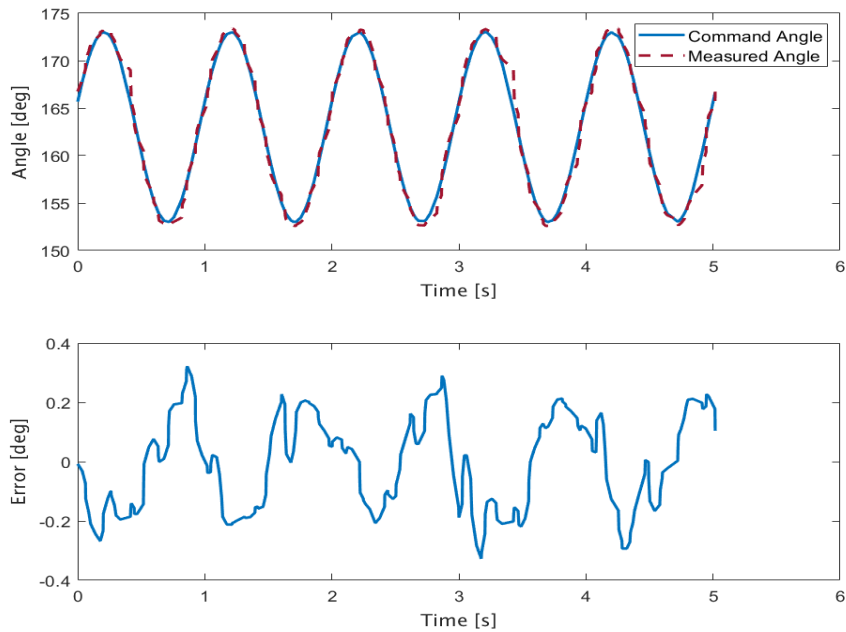
Figure 4.36: Joint 2 position tracking a 1Hz sinusoidal reference signal.

Position control: trapezoidal shape input tracking

The trapezoidal shape trajectory tracking control experiment is performed with the position input profile shown in Fig. 4.37. For the first step, the input signal is applied to the 1st joint of the 5-DOF manipulator. The amplitude of the input signal is set to 40°, with the minimum angular position of the joint 178°, maximum 128°. Manual tuning of PID gains is performed during multiple consecutive runs.

Fig. 4.37 shows the angular position (top plot) and error (bottom plot) for the trapezoidal shape trajectory tracking experiment. A positional error with the amplitude 1° can be observed on the bottom plot during joint movements. The oscillation with amplitude 0.15° can be also observed on the error plot. However, during stationary periods the positional error is less than 0.1°.
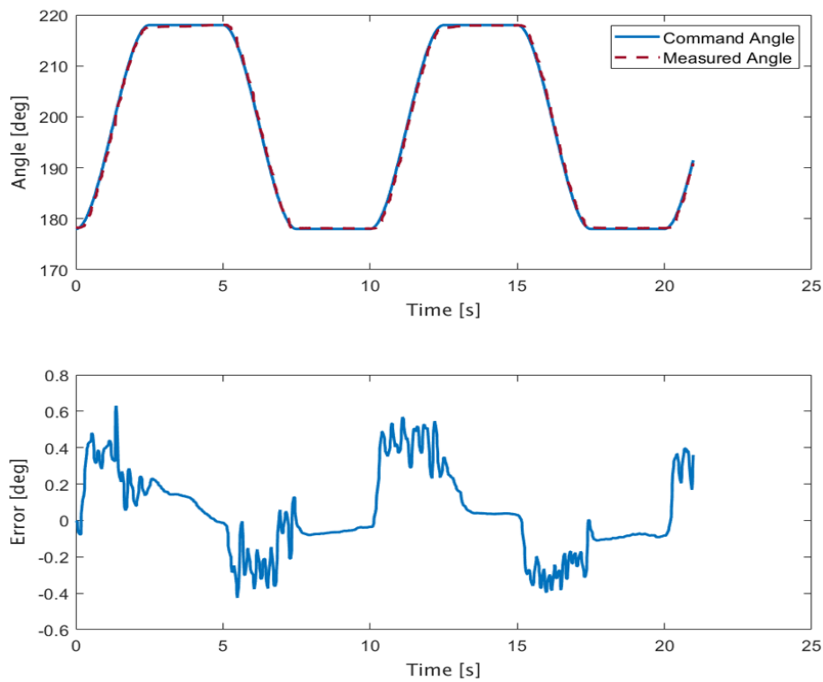
Figure 4.37: Joint 1 trajectory tracking.

For the second step, similar trapezoidal shape input signal is applied to the 2nd joint of the 5-DOF manipulator. The amplitude of the input signal is set to 40°, with the minimum angular position of the joint 178°, maximum 128°. Manual tuning of PID gains is performed during multiple consecutive runs.

Fig. 4.38 shows the angular position (top plot) and error (bottom plot) for the trapezoidal shape trajectory tracking experiment. A positional error with the amplitude 0.9° can be observed on the bottom plot during periods of joint movements. The oscillations with amplitude 0.2° can be also observed on the error plot. During stationary periods the positional error is around 0.2°.

For the final step, the trapezoidal shape input signals are applied to both 1st and 2nd joints of the 5-DOF manipulator at the same time. The amplitude of the input signal is set to 40°
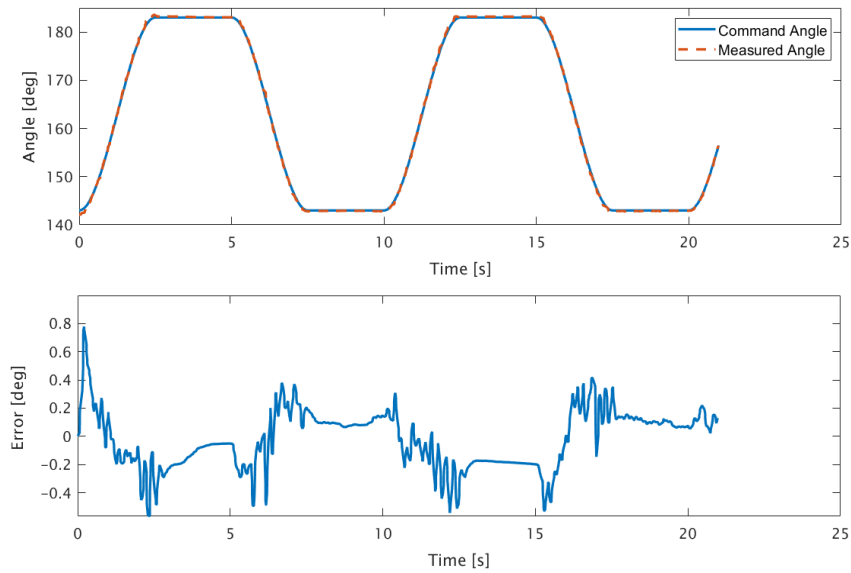
Figure 4.38: Joint 2 trajectory tracking.

for both joints. The minimum angular position of the joint 1 is set to 178°, maximum to 128°. The minimum angular position for the joint 2 is set to 178°, maximum to 128°. The PID gains developed for the first two experimental steps are used. The controller board for the 1st joint is used as a master unit, sending required position input signals to the 2nd joint board for proper movement synchronization.

Fig. 4.39 shows the angular positions of the 1st and 2nd joints for the trapezoidal shape trajectory tracking experiment. A positional error with the amplitude 0.9° can be observed on the bottom plot during periods of joint movements.

Fig. 4.40 shows the errors of the 1st and 2nd joints for the trapezoidal shape trajectory tracking experiment. A positional error with the amplitude 1.4° can be observed on the top plot for the 1st joint. The smaller positional error with the amplitude 0.6° is seen on bottom plot the 2nd joint. The oscillations with amplitude 0.3° can be also observed on both error plots. During stationary periods the positional error of the 1st is around 0.1°, while the similar error for the 2nd joint is exceeds 0.2°.

Based on the experimental results, the feasibility of tracking based on PID control is evaluated. It is observed that the precision of tracking is less than 1.4° for the 1st joint and around 0.6° for the 2nd joint.

The main factors contributing to the precision deterioration identified as uneven friction in the MR clutches and low sampling frequency used to read encoders angular position. For a frequency lower than 0.5 Hz. However, the higher frequency input signal produces a larger error and unwanted oscillations of the joint. Overall the PID joint level control approach is capable to perform predictable and stable control of 5-DOF manipulator joints movement.
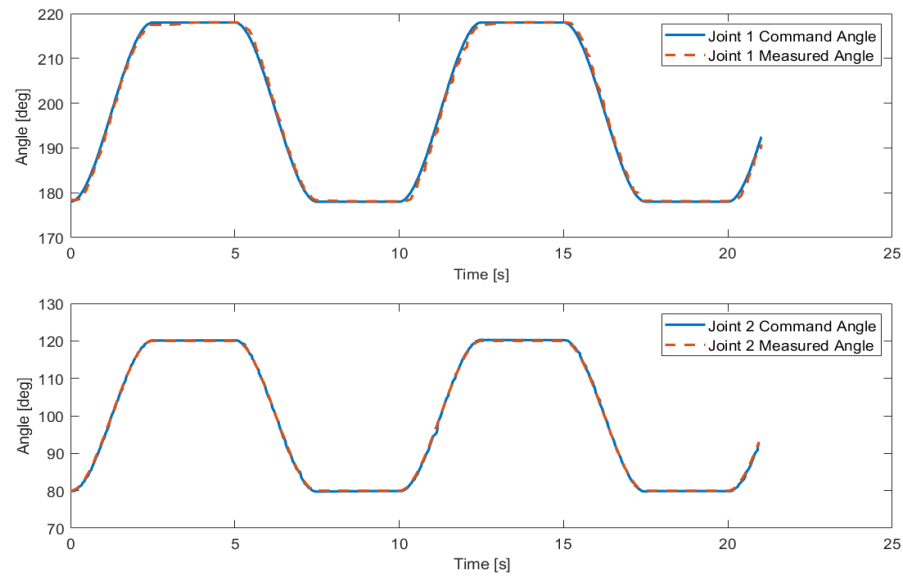
Figure 4.39: Joint 1 and joint 2 simultaneous trajectory tracking.
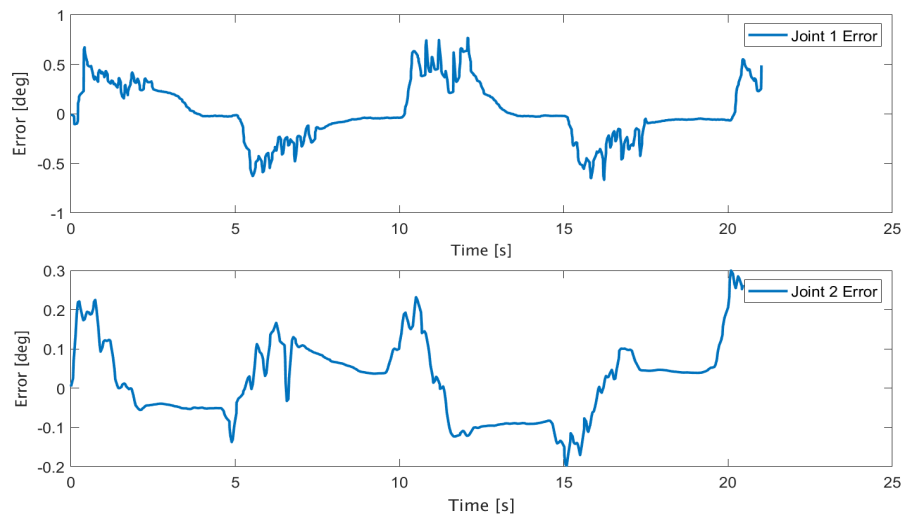
Figure 4.40: Position error for Joint 1 and joint 2 simultaneous trajectory tracking.

4.5   Conclusion

In this chapter, the simulation of the transmission system validates the feasibility of controllable actuation of all 5 joints of the robot. The influence of components on each other is simulated

based on the system architecture. Found relationships are ready to be embedded in the control system to ensure proper operation of the robotic system.

Additionally, the compliant and passive behavior of magneto-rheological clutches used in an antagonistic configuration was theoretically and experimentally studied. The effects of mechanical backlash in a transmission, MR fluid viscosity, and yield stress variations on the transmitted torque of the actuator were analyzed.

The theoretical results were validated using an experimental setup consisting of a pair of antagonistic MR clutches in the 2nd joint of a 5-DOF compliant robot and a KUKA LWR 4+ robot. It was experimentally shown that antagonistic MR actuators provide excellent dynamic characteristics within the nominal (active) region of the actuators. Outside this region, the actuator exhibits an intrinsic tendency to return to the nominal (active) region by bounding the actuator's output velocity.

The results show the suitability of MR actuators and demonstrate the possibility for designing systems with safe and dependable behavior within the entire control region and without compromising the performance of the actuation and/or incurring excessive design costs.

Finally, the joint-level PID control is presented and several performed experiments described. The test results validate the capability of the PID joint level control to achieve predictable and stable control of 5-DOF manipulator joints movement.

Bibliography

[1] W. Li, P. Yadmellat, and M. R. Kermani, "Linearized torque actuation using fpga-controlled magnetorheological actuators," *IEEE/ASME Transactions on Mechatronics*, vol. 20, no. 2, pp. 696–704, 2015.

[2] P. Yadmellat and M. R. Kermani, "Study of limit cycle in antagonistically coupled magneto-rheological actuators," *Control Engineering Practice*, vol. 35, pp. 92–101, 2015.

[3] P. Fauteux, M. Lauria, B. Heintz, and F. Michaud, "Dual-differential rheological actuator for high-performance physical robotic interaction," *IEEE Transactions on Robotics*, vol. 26, no. 4, pp. 607–618, 2010.

[4] C. Véronneau, J. Denis, L.-P. Lebel, M. Denninger, V. Blanchard, A. Girard, and J.-S. Plante, "Multifunctional remotely actuated 3-dof supernumerary robotic arm based on magnetorheological clutches and hydrostatic transmission lines," *IEEE Robotics and Automation Letters*, vol. 5, no. 2, pp. 2546–2553, 2020.

[5] M.-A. Bégin, M. Denninger, and J.-S. Plante, "Design and experimental validation of a 2dof sidestick powered by hyper-redundant magnetorheological actuators providing active feedback," in *2019 International Conference on Robotics and Automation (ICRA)*. IEEE, 2019, pp. 4011–4017.

[6] J. Wu, H. Li, X. Jiang, and J. Yao, "Design, simulation and testing of a novel radial multi-pole multi-layer magnetorheological brake," *Smart Material and Structures*, vol. 27, no. 2, pp. 1–12, 2018.

[7] X. Wu, C. Huang, Z. Tian, and J. Ji, "Development of a novel magnetorheological fluids transmission device for high-power applications," *Smart Material and Structures*, vol. 28, no. 5, pp. 1–13, 2019.

[8] "Iso 10218-1:2011 robots and robotic devices — safety requirements for industrial robots," https://www.iso.org/obp/ui/#iso:std:iso:10218:-1:en, accessed: 2021-01-01.

[9] F. Ahmadkhanlou, M. Mahboob, S. Bechtel, and G. Washington, "An improved model for magnetorheological fluid-based actuators and sensors," *Journal of Intelligent Material Systems and Structures*, vol. 21, no. 1, pp. 3–18, 2010.

[10] M. R. Kermani, R. V. Patel, and M. Moallem, "Friction identification and compensation in robotic manipulators," *IEEE Transactions on Instrumentation and Measurement*, vol. 56, no. 6, pp. 2346–2353, 2007.

[11] M. R. Kermani, R. Patel, and M. Moallem, "Multimode control of a large-scale robotic manipulator," *IEEE Transactions on Robotics*, vol. 23, no. 6, pp. 1264–1270, 2007.

[12] M. R. Kermani, M. Moallem, and R. Patel, "Study of system parameters and control design for a flexible manipulator using piezoelectric transducers," *Smart Materials and Structures*, vol. 14, no. 4, pp. 843–849, 2005.

Chapter 5

5-DOF Manipulator: Compliant Gripper with Miniaturized MR Clutches

Parts of the material in this chapter are published in "The 2020 IEEE/RSJ International Conference on Intelligent Robots and Systems (IROS)", 2020, Paris, France [1].

This chapter presents a novel design of a miniaturized magneto-rheological clutch and a design concept of a compliant gripper where miniaturized clutches are used for actuation.

After a brief description of the MR fluid operation modes used in MR clutch actuators, the details of the squeeze mode use approach are explained. After describing the early versions of the innovative clutch and results of preliminary testing, the mechanical design of the miniaturized "Planetary" MR clutch are discussed. The distribution of the magnetic flux inside the MR clutch is studied using finite element analysis in COMSOL Multiphysics software. Preliminary experimental results using a prototype MR clutch that validates the new concept and the results therein will be presented next. To clearly show the performance of the proposed design, we compared the torque capacity of our MR clutch obtained experimentally with that of a simulated disk-type MR clutch of a similar size.

At the end of the chapter, the possible implementation of the miniaturized clutch in the compliant end-effector is presented in the form of a 7-DOF gripper design concept.

5.1 Introduction

The use of magneto-rheological clutches and brakes is increasingly receiving attention for their distinctive characteristics such as fast response, low power consumption, high torque to weight ratio, precision in torque control, and intrinsic compliance of such devices. In robotics, MR clutches often used to achieve safety and the intrinsic compliance of the robot joints [2], [3], [4], [5], [6]. However, miniature clutches have rarely been implemented due to difficulties in manufacturing and small torque they capable of transmitting.

Development of small size MR clutch opens up a new possibility for the creation of compliant grippers similar to a concept shown in Fig. 5.1. Such end-effectors will be extremely desirable devices in agriculture, medicine, and haptic applications [7, 8, 9, 10]. The compliant-joint devices allow addressing some of the issues encountered in dealing with soft tissues and

objects such as fruits, live organs, food, etc. [11].

To this effect, conventional MR clutches with disk or drum configurations cannot be efficiently used in the design of compliant-joint end-effectors or robotic hands, because the delivered torque of these types of clutches reduces significantly as the diameter of the clutch becomes smaller.
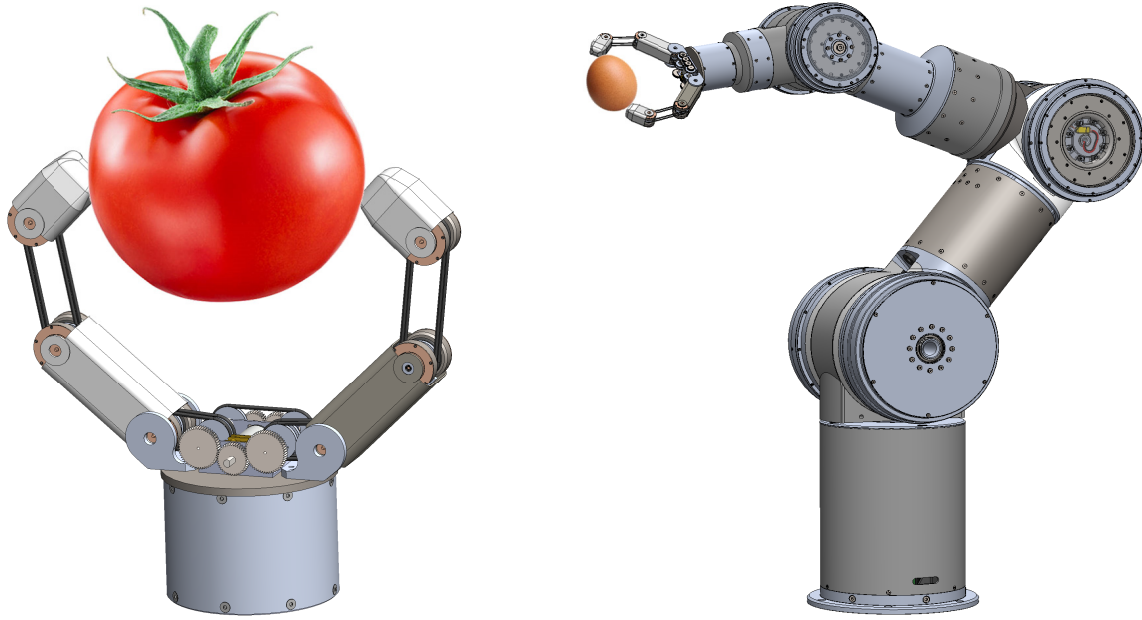
Figure 5.1: Design concept of a compliant robotic gripper with the miniaturized MR clutches used for the actuation of the joints.

The goal of this research is to evaluate the feasibility of an innovative design of an MR clutch based on a planetary gear mechanism allowing the miniaturization of an MR clutch for a given torque value and integrating the clutch in the robotic end-effector. The details of the design and description of the assembled prototype presented in this chapter show the feasibility of miniaturizing MR clutches. The details of the end-effector concept designed based on small-sized clutches presented at the end of the chapter.

The contributions of this work are as follows:

- An innovative design concept of an MR clutch using squeeze mode of MR fluid is described.

- The distribution of the magnetic flux inside the MR clutch is simulated and analyzed.

- A prototype of a miniaturized MR clutch is developed and preliminary experimental results that validate the proposed design are presented.

- A concept of 7-DOF end-effector utilizing 2 small-size disk-type and 12 miniature-size planetary-type MR clutches is developed and presented.

5.1.1   MR fluid operation modes used in actuators

As it is described in chapter 2, the functional principle of an MR clutch (MR brake) is based on variable viscosity of magneto-rheological fluids. The MR fluid is a two-phase fluid, containing micron-sized spherical iron particles floating in a carrier fluid. Due to the ferromagnetic properties of iron, the particles can be easily magnetized with an external magnetic field. The tiny magnetized particles attract each other and form chains along the magnetic field lines. The direction of the chains determines the anisotropic properties of the fluid. The strength of these chains depends on the strength of the magnetic field. The viscosity of the MR fluid depends on the number of created chains and their strength. As a result, the viscosity of MR fluid can be precisely controlled by varying the magnetic field with a response time of less than 1 ms.

There are four known MR fluid operation modes that can be used in MR-based devices: Valve mode [12], shear mode [13, 14], squeeze mode [15, 16], and pinch mode [17]. Most types of MR clutches use MR fluids in shear mode [18, 19].

Due to the limited achievable yield stress of the MR fluid (around 100 kPa [20]), the torque-to-weight ratio of an MR clutch cannot be improved indefinitely. In practical applications, the highest ratio achieved is close to 60 Nm/kg [21].

There are several designs developed in an attempt to overcome the limitations of achievable MR fluid yield stress. These designs utilize innovative approaches such as the use of compression plus shear mode [22], the use of small steel rollers as large size magnetic particles [23], and the use of arc form shape of the clutch rotor [24].

The new design of the MR clutch presented in this chapter uses the MR fluid in squeeze mode. This mode is expected to generate higher torque than a similar size conventional MR clutch.

5.2   Design of miniaturized MR clutch

5.2.1   Design objectives

This study was motivated by the need for a miniaturized MR clutch with sufficient torque characteristics that could fit into the fingers of a prospective compliant gripper, such as the concept shown in Fig. 5.1. The outer diameter and the width of the desirable MR clutch are set to be not more than 20 mm and 10 mm respectively. Chosen dimensions allow to incorporate a pair of antagonistically actuated clutches into a joint of a reasonably small finger that is comparable in size with a human finger.

The "classical" disc-type clutch design is used as a starting point to estimate the value of the torque that can be transmitted by such a small device.

5.2.2   Disk-type MR clutch

In this section, the design of a disk-type MR clutch and its torque characteristics explored for the given size requirements. A previously verified model of MR clutch [25] based on Finite Element Analysis in COMSOL Multiphysics software is used to evaluate the design.

Fig. 5.2 shows a disk-type MR clutch with the outer diameter of (OD) 19 mm and width of 9 mm. It is assumed that the construction of such a clutch poses no extreme requirements for the precision of the manufactured parts.
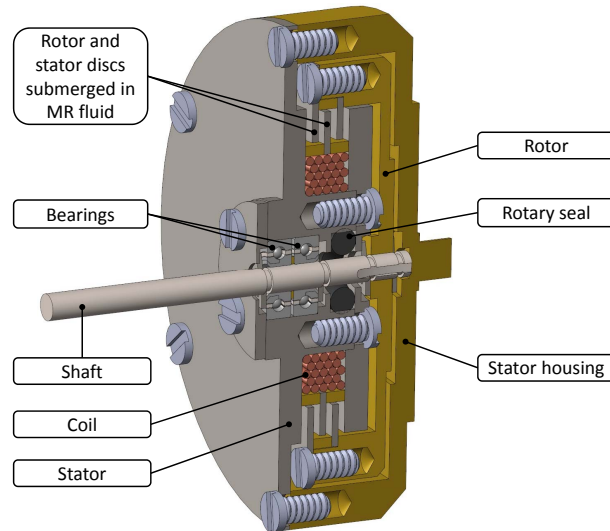
Figure 5.2: Construction of the miniaturized "Disk" MR clutch.

The clutch is comprised of two carbon steel rotor disks and one stator disk with a thickness of 0.25 mm each. The gaps between the disks are 0.25 mm. The electromagnetic coil is wound on the carbon steel stator and has 25 turns of AWG 28 wire. The rotor is made of brass and mounted on the stainless steel shaft. The shaft is 1 mm in diameter and is mounted on two ball bearings with 3 mm OD. The rotary seal is used to isolate the volume containing MR fluid inside the clutch. The brass stator housing is tightly attached to the carbon steel stator. Miniature screws used for the assembly are 2 mm long with M1 thread each.

The geometry of the magnetic core was optimized to avoid saturation in the local areas as it was reasonable taking into account the small size of the device and manufacturability of the parts. Fig. 5.3 shows the magnetic flux density of the described MR clutch for input current of 3.6 A.

Using this model, the maximum torque capacity of the clutch for the maximum input current of 3.6 A was calculated to be 20.3 N·mm. The transmitted torque could be further improved by increasing the number of disks and reducing the size of the gaps between them. However, this could be difficult to achieve due to the high tolerance required, the complexity, and miniature of the parts. Further optimization of the core shape cannot substantially increase the torque.

5.2.3 "Planetary" MR clutch

In order to improve the torque capacity of an MR clutch, an alternative design is proposed for the miniaturized clutch. Rather than utilizing a pure shear mode, as is done in conventional disk-type and drum-type clutches, the idea is to make use of more effective squeeze mode. While the behavior of the MR fluid in this mode is still not fully understood, the forces gener-
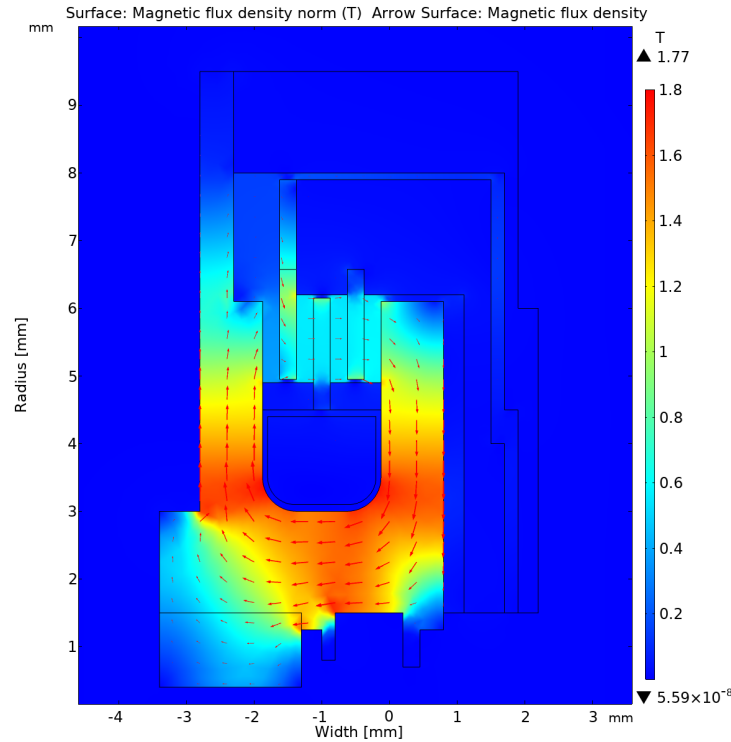
Figure 5.3: Magnetic flux density contour map in the miniaturized disk-type MR clutch (coil wire current 3.6 A, total coil current 90 A for 25 turns of wire).

ated within small displacement at squeeze mode are grossly larger than that in pure shear mode [16]. It is therefore hypothesized that an MR clutch operating in squeeze mode can have larger torque capacity than other similar designs working in shear mode.

To this end, it is proposed to use the rotating cogwheels (gears) in mesh to squeeze the MR fluid from the space between the teeth. An example of a configuration with two cogwheels is shown in Fig. 5.4.

The top cogwheel is assumed to rotate counter-clockwise and driving the bottom cogwheel clockwise, or vice versa. As the teeth of the two gears approach and come in contact, the MR fluid is trapped and then forcefully squeezed out from the space between them. As the rotation progresses, the contacting teeth of the cogwheels start to depart and the fluid is pulled into the opening void with low pressure that is left behind the separating teeth.

To implement this squeezing method in the construction of the MR clutch, it is proposed to use a mechanism similar to a planetary (epicyclic) gear train with free-running planet gears.

To test the idea a very simple planetary mechanism is designed as shown in Fig. 5.5 (a). It consists of an 80 mm diameter base that combines an inner gear (1 mm gear module) and a volume for the MR fluid. The sun gear of the mechanism acts as the input (or rotor) and the ring gear acts as the output (or stator). The sun gear has a handle to manually rotate it and drive 10 planet gears in mesh.

MR fluid MRF-140CG [26] was poured into the base volume (Fig. 5.5 (b)) and sun gear rotation was checked manually by turning the handle. It was found that a very small effort required to move the sun gear and planet gears immersed in MR fluid.
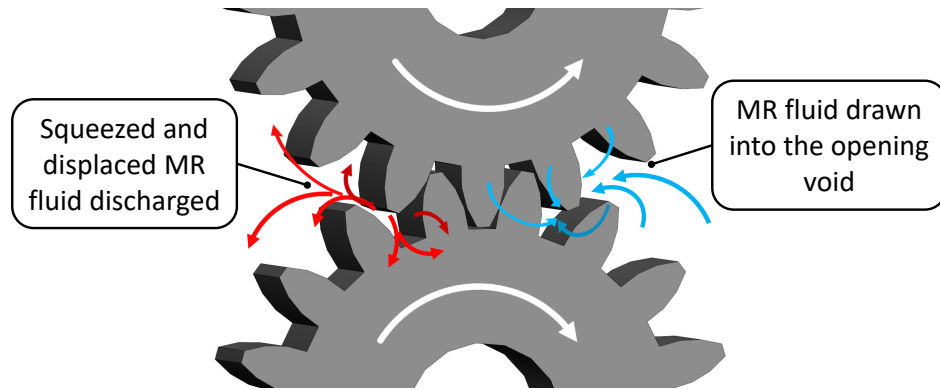
Figure 5.4: Process of squeezing MR fluid between the teeth of rotating spur gears in mesh.

For the next step, a permanent magnet was placed under the base of the mechanism to increase the MR fluid viscosity. It can be seen in Fig. 5.5 (c) that some spikes of fluid riding the magnetic field lines appear on the surface of the MR fluid affected by the magnet. Attempts to rotate the sun gear revealed that it was well locked in position due to the hardened fluid between the teeth.

(a)   (b)   (c)
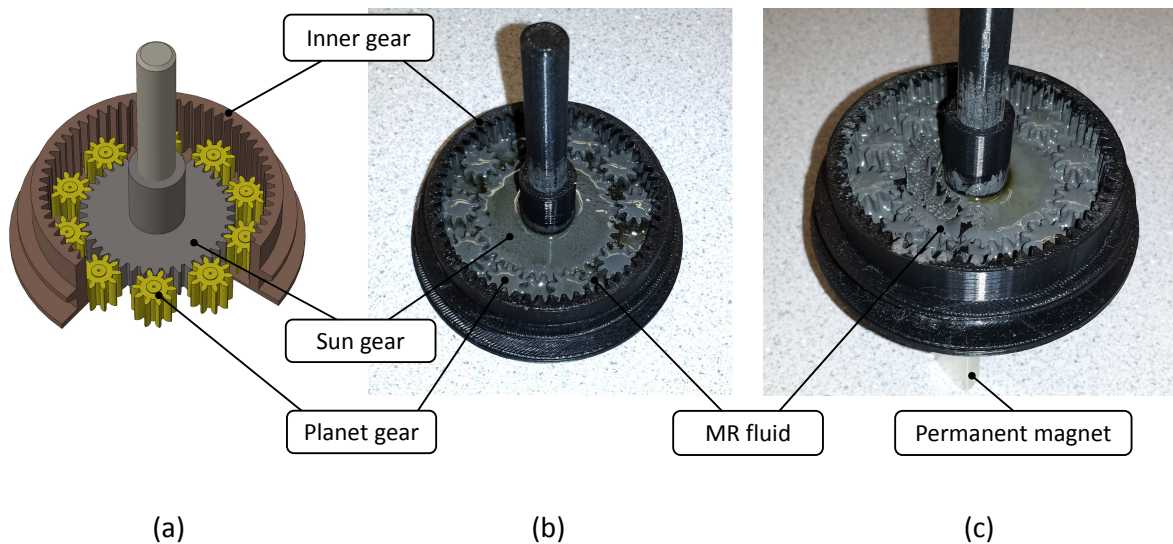
Figure 5.5: Planetary gear mechanism to test feasibility of building a "Planetary" MR clutch: (a) - CAD model, (b) - 3-D printed prototype filled with MR fluid, (c) - prototype with MR fluid placed on top of the permanent magnet.

To further develop the idea, a full-functioning clutch with electromagnetic coil is designed based on the planetary mechanism (Fig. 5.6 (a)). It has same size inner, sun, and planet gears (1 mm module), however, the volume for MR fluid is enclosed with the housing and sealed with the O-rings and rotary seal. The ball bearings are installed to support stainless steel shaft, the coil is wound with 80 turns of 21 AWG wire, two Hall sensors are embedded to measure the magnetic flux density. The clutch is filled with MR fluid MRF-140CG [26].
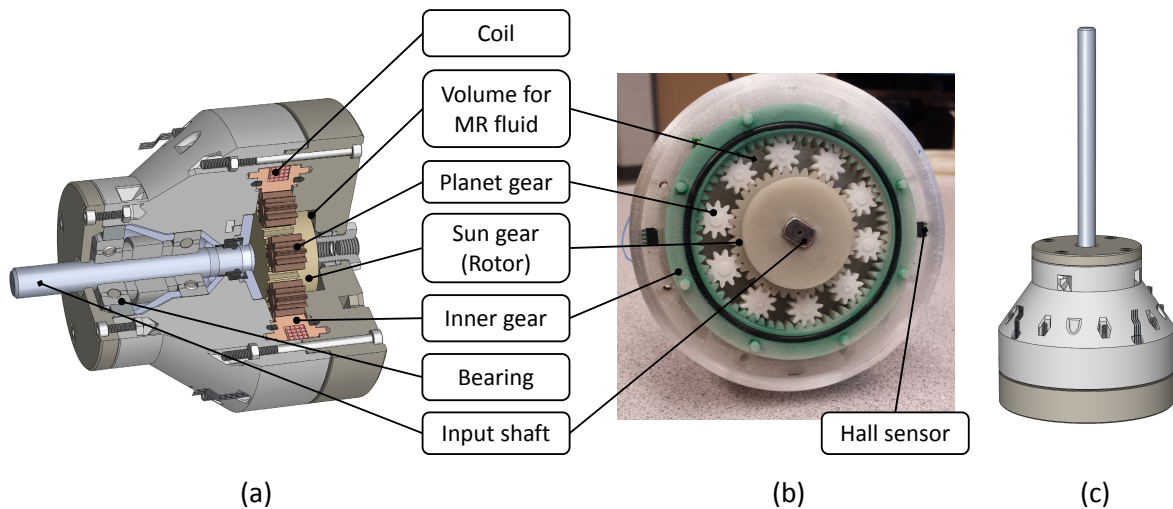
Figure 5.6: First prototype of the "Planetary" MR clutch: (a) - CAD model, (b) - Assembled planetary mechanism of the MR clutch prototype, (c) - overview of the assembled prototype.

For the test, 5 A current was applied to the coil while the shaft was rotated with the milling machine Craftex CX-600 at constant speed 50 rpm. The measurements performed using load cell CZL616C connected to an acquisition board Phidgets PhidgetBridge RB-Phi-107 registered small torque less than 0.1 N·m. It was concluded that the reason behind such a small transmitted torque was due to low magnetic flux density in absence of ferromagnetic materials in the magnetic circuit as well as ineffective direction of magnetic field lines in the systems. The lines of the magnetic field distributed parallel to the surface of the engaging teeth as shown in Fig. 5.7. The chains of MR fluid particles build along the field lines easily slide over each other without braking while fluid is being squeezed between the teeth. This sliding does not pose significant resistance to the moving surfaces.
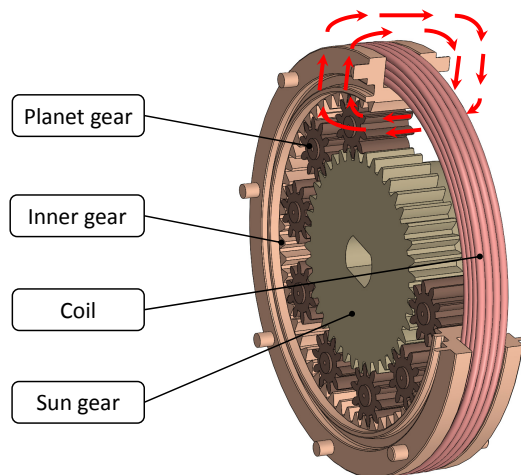
Figure 5.7: Direction of magnetic field lines in the "Planetary" MR clutch prototype.

To improve the magnetic circuit and change the orientation of magnetic field lines to perpendicular relative to the teeth surface, the new improved design of the "Planetary" MR clutch

was developed. The details of the proposed clutch are shown in Fig. 5.8. Similar to the previous design, the sun gear of the planetary mechanism acts as the input (or rotor) and the ring gear acts as the output (or stator). However, the stator for the electromagnetic coil, the inner gear, the sun, and the planet gears are all made of carbon steel. Additionally, the coil was relocated to the side of the clutch to orient the magnetic field lines perpendicular to the teeth surface.
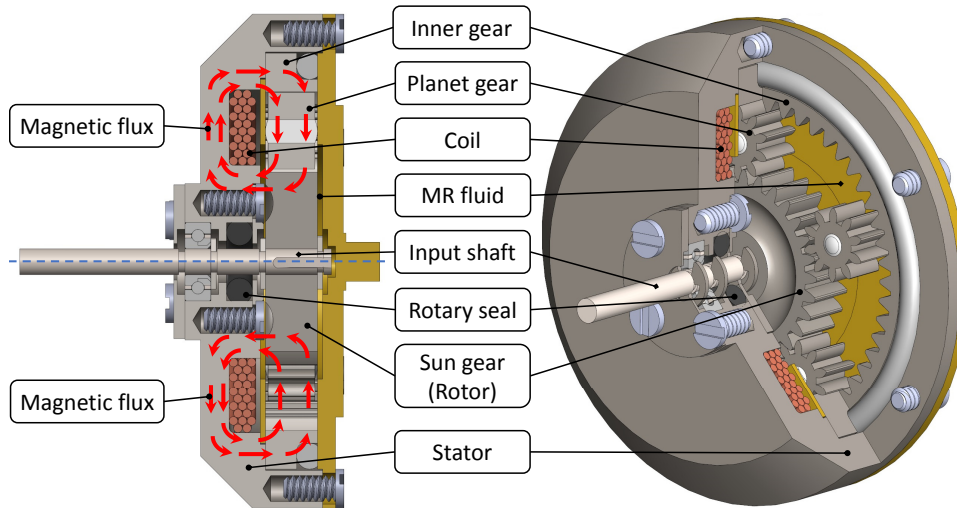
Figure 5.8: Design of the improved miniature "Planetary" MR clutch.

The proposed improved "Planetary" clutch has similar size as well as a number of parts as its disk-type counterpart described in subsection 5.2.2. In this design, the stator carries the similar size electromagnetic coil. The ferromagnetic inner gear (the so-called ring gear in a planetary mechanism) is also included in the magnetic circuit. The inner gear is stationary and is fixed inside the stator cutout. A number of planet gears are in mesh with the inner gear and with the sun gear in the center of the mechanism. The sun gear plays the role of a rotor and it is fixed to the input shaft using snap rings and a key. The input shaft is mounted on one bearing only (1st shaft support). The function of the 2nd shaft support is performed by the planet gear mechanism working as a "roller" bearing. A rotary shaft seal isolates the volume containing MR fluid inside the clutch. The brass stator lid covers the planetary mechanism and prevents the rotation of the inner gear inside the stator. Miniature M1 screws are used as fasteners for the clutch assembly.

5.3 Magnetic flux distribution

The distribution of the magnetic field density was simulated for the proposed MR clutch design using the Finite Element Method in COMSOL Multiphysics software. Several cases were studied with 1, 2, 3, 4, and 5 planet gears in the planetary gear mechanism. Fig. 5.9 and 5.10 show the map of the magnetic flux density for the cases with 2 and 5 planet gears.

As seen in figures 5.9 and 5.10, the density of the magnetic flux is the highest in the regions where the ferromagnetic planet gears are currently located. This is the intended region for the MR fluid to undergo the squeeze mode. One can expect that increasing the number of planet

Surface: Magnetic flux density norm (T); Arrow Surface: Magnetic flux density
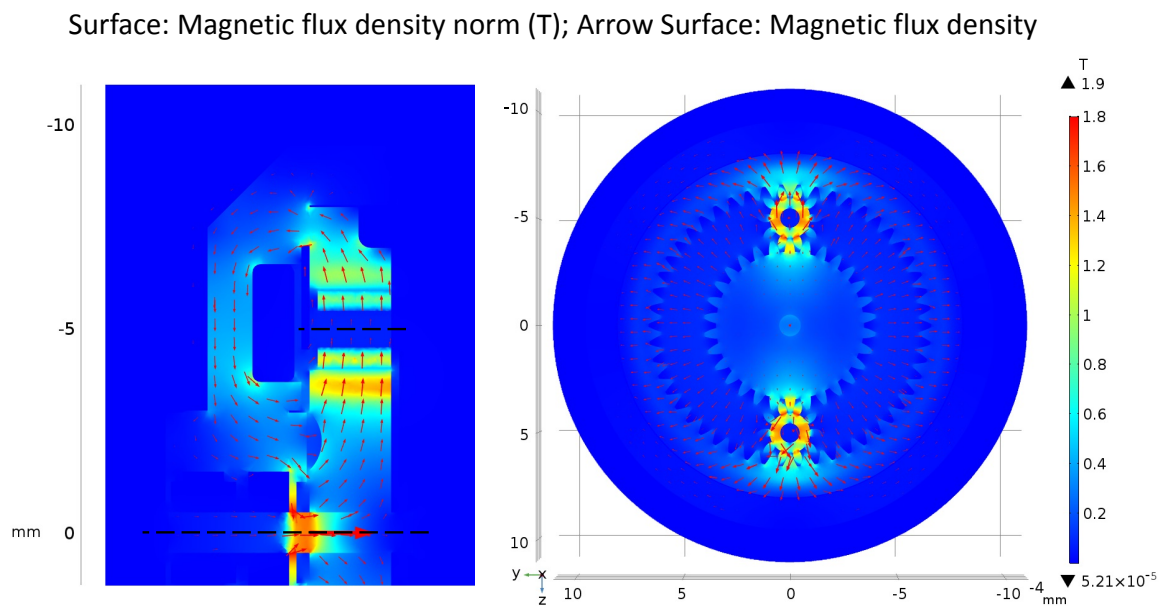
Figure 5.9: Magnetic flux density contour map in the miniaturized "Planetary" MR clutch with 2 planet gears (coil wire current 3.6 A, the total coil current 90 A for 25 turns of wire).

Surface: Magnetic flux density norm (T); Arrow Surface: Magnetic flux density
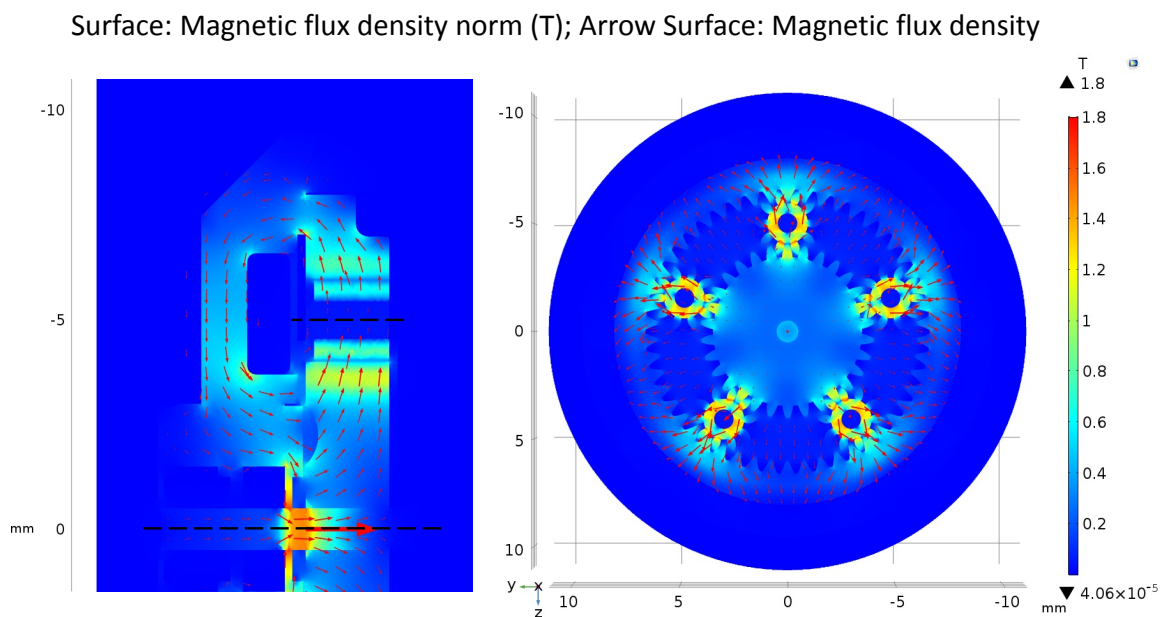
Figure 5.10: Magnetic flux density contour map in the miniaturized "Planetary" MR clutch with 5 planet gears (coil wire current 3.6 A, the total coil current 90 A for 25 turns of wire).

gears will increase the number of fluid squeeze regions and result in larger torque capacity of the clutch. On the other hand, a higher number of planet gears can reduce the flux density by providing multiple parallel paths for the magnetic flux. There is clearly a trade-off between the number of planet gears and the magnetic flux density. However, it is difficult to mathematically calculate the exact relationship between the value of the magnetic flux passing through each gear and the number of gears in the system. In order to evaluate this relationship more precisely, a set of 12 virtual Domain Point Probes are used in COMSOL Multiphysics as shown in Fig. 5.11.
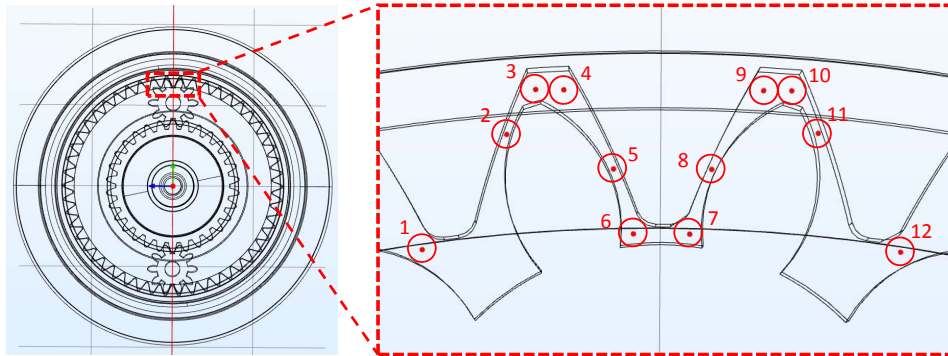
Figure 5.11: Location of the Domain Point Probes in the MR fluid between the teeth in the COMSOL model.

The probes are positioned between the teeth of the sun gear and one of the planet gears for all simulation cases (i.e. with 1, 2, ..., 5 planet gears).

The results of the magnetic flux density norm measurements at each probe are tabulated in Fig. 5.12. The average flux density norm for each simulated case is also calculated in the rightmost column.

Number of Planet gears	Magnetic flux density norm at the probe (T)												Average flux density norm (T)
	Probe 1	Probe 2	Probe 3	Probe 4	Probe 5	Probe 6	Probe 7	Probe 8	Probe 9	Probe 10	Probe 11	Probe 12	
1	0.277	0.552	0.217	0.193	0.480	0.244	0.263	0.576	0.197	0.240	0.471	0.288	0.333
2	0.269	0.540	0.212	0.188	0.471	0.238	0.256	0.563	0.193	0.243	0.461	0.281	0.326
3	0.258	0.524	0.206	0.182	0.458	0.227	0.247	0.546	0.186	0.234	0.448	0.270	0.315
4	0.246	0.506	0.198	0.175	0.444	0.219	0.237	0.529	0.180	0.226	0.435	0.259	0.304
5	0.234	0.489	0.190	0.168	0.426	0.207	0.225	0.511	0.173	0.216	0.416	0.245	0.292

Figure 5.12: Magnetic Flux Density measurements at Domain Point Probes.

Based on average flux density, the approximate magnetic flux passing through a part of the planet gear surface (8.61 mm^2) is calculated. For each simulated case the magnetic flux through a single planet gear and through all planet gears in the clutch are plotted in Fig.5.13. The results show a slight reduction of the magnetic flux through each gear (orange) as the

number of planet gears in the system increases. However, the total magnetic flux through all planet gears (blue) increases almost proportionally to the total number of the planet gears.
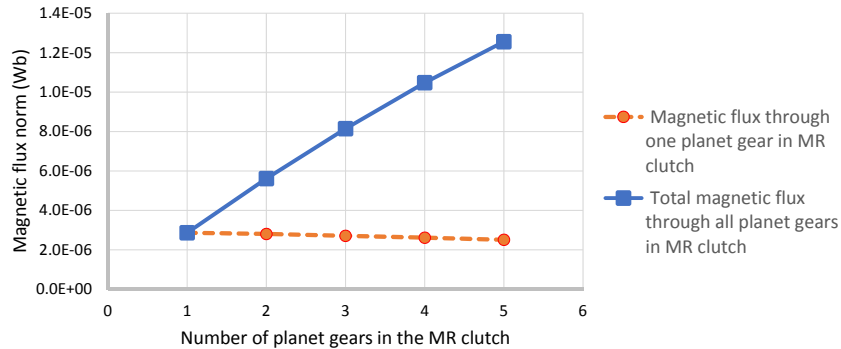
Figure 5.13: A plot of the relation between the number of planet gears in the clutch and the magnetic flux passing through the gears.

The small reduction observed in the magnetic flux despite increasing the number of planet gears can be described as follows. Increasing the number of planet gears reduces the flux density in each gear. On the other hand, increasing the number of planet gears decreases the total reluctance of the magnetic circuit which in turn results in larger total flux in the clutch. As such, the magnetic flux through a single gear is only slightly reduced, while the total magnetic flux through the circuit increases almost proportionally to the number of gears.

5.4 Preliminary experimental results

In order to prove the feasibility and to evaluate the performance of the proposed "Planetary" MR clutch design, a prototype of the device was built as shown in Fig. 5.14.
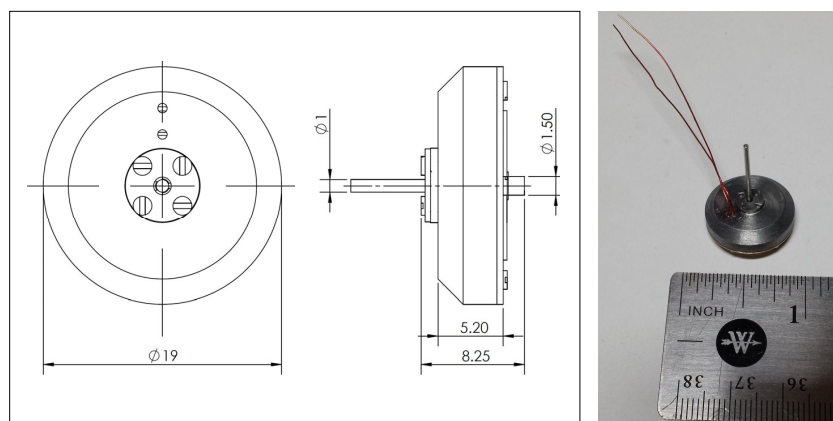
Figure 5.14: An assembled prototype of the "Planetary" MR clutch and its basic dimensions.

The dimensions of the prototype MR clutch were based on the design requirements described in Section III. The total weight of the prototype clutch filled with MR fluid MRF-140CG [26] was measured to be 10 g.

The prototype was first tested with a set of 2 planet gears (Fig. 5.15 a), and then with a set of 3 planet gears (Fig. 5.15 b).

(a) MR clutch with 2 planet gears   (b) MR clutch with 3 planet gears
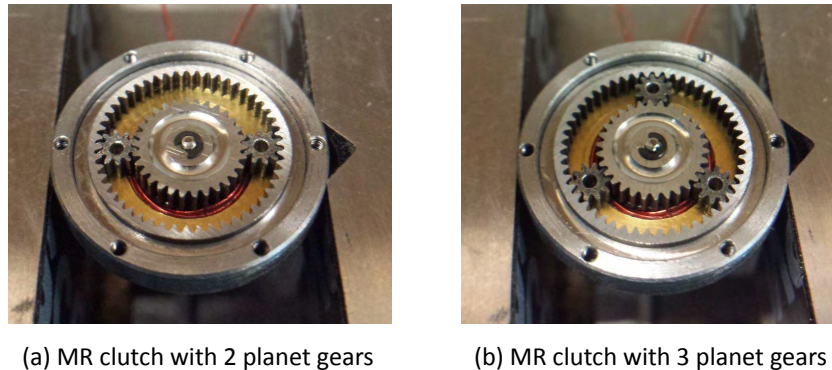
Figure 5.15: Pictures of the "Planetary" clutch prototype with the 2 and 3 planet gears installed.

For the experiments, a milling machine Craftex CX-600 was used to rotate the MR clutch at a constant speed of 50 rpm. A power supply TTi EX752M was used to supply current to the electromagnetic coil. A 50 mm 3D-printed shoulder was attached to the clutch. The torque was measured using a micro load cell CZL616C connected to an acquisition board Phidgets PhidgetBridge RB-Phi-107. The test setup is shown in Fig. 5.16.
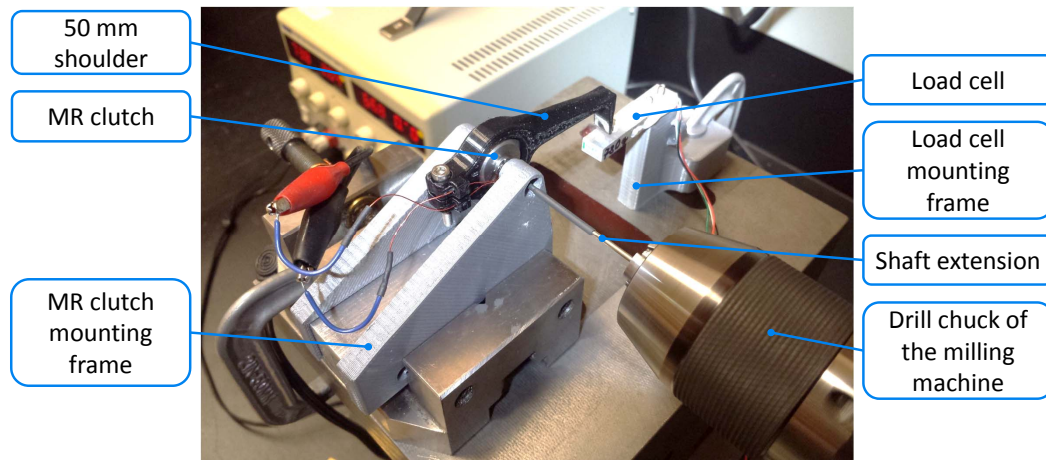
Figure 5.16: Experimental setup with the MR clutch installed.

During the tests, a constant current of up to 3.6 A with an incremental step of 0.2 A was applied to each prototype MR clutch. For each value of the current, the transmitted torque was recorded during 4 seconds at 0.1 seconds intervals and then averaged. The results of the tests are shown in Fig. 5.17 in blue and green solid lines.

The graphs illustrate the actually transmitted torque for two "Planetary" MR clutch configurations with 2 and 3 planet gears respectively. It can be observed that the torque capacity of the "Planetary" MR clutch increases nearly proportionally to the number of planet gears used. Therefore, the torque of the planetary clutch with multiple planet gears can be calculated as the multiplication of the one-gear clutch torque by the number of gears. Based on the obtained test
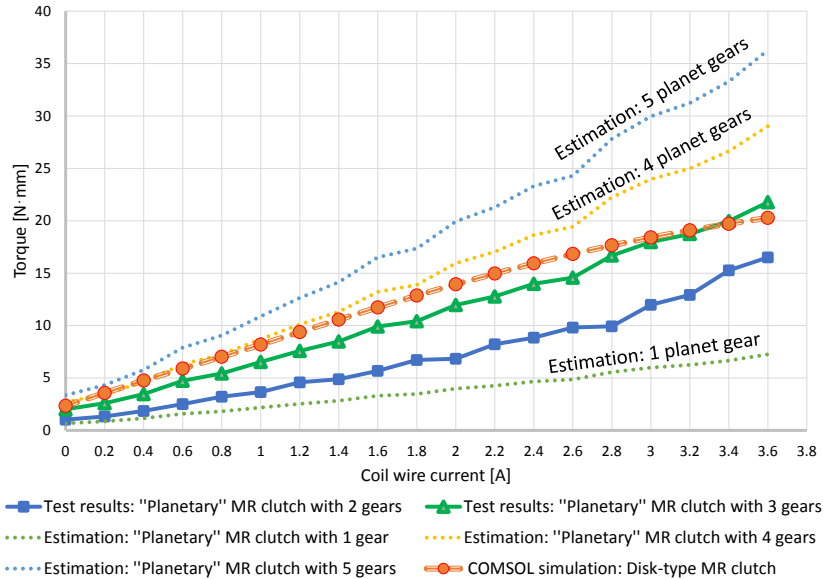
Figure 5.17: Comparison of the experimental results for the "Planetary" MR clutch and disk-type MR clutch.

results, the torque values for the "Planetary" clutch with 1, 4, and 5 planet gears are estimated and included in Fig. 5.17 in dotted lines.

In addition, the torque results for the disk-type MR clutch described in chapter III-B are also included in the plot in Fig. 5.17. The results were obtained through the simulation using the developed COMSOL Multiphysics model. It can be observed that the performance of the "Planetary" clutch with 3 planet gears is close to the torque capabilities of a disk-type clutch with 3 disks.

As conjectured, increasing the number of planet gears in the proposed design will lead to higher torque capabilities of the "Planetary" clutch. For the current MR clutch configuration, the maximum of 10 planet gears can be installed as shown in Fig. 5.18.
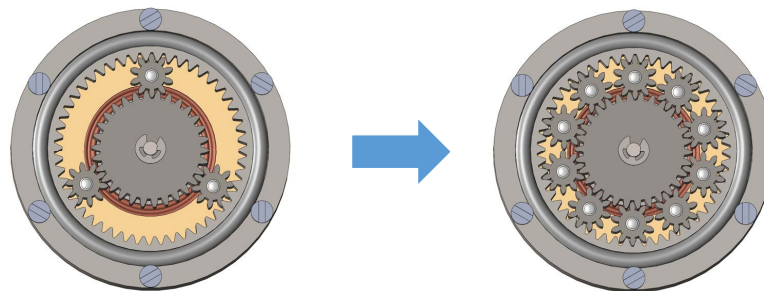
Figure 5.18: "Planetary" clutch with 3 and 10 (the maximum possible number for current design) planet gears installed.

At 8 A/mm^2 current density (0.64 A wire current for 28 AWG) the clutch with 10 planet gears has torque-to-weight ratio approximated as 1.6. While the clutch with 3 planet gears has torque-to-weight ratio calculated as 0.5 for the same current density.

Similarly, increasing the number of disks will lead to improved torque capabilities of the disk-type clutch. However, while the planetary clutch can be easily improved just by inserting the additional planet gears, the disk-type clutch requires changes in the thickness of the disks and spacers.

Additionally, it is believed that the performance of the "Planetary" clutch can be further improved through optimization of the gear parameters such as the number of teeth, pitch diameter, modulus, pressure angle, tooth profile, and others.

5.5 Compliant 7-DOF Gripper Concept

Based on the dimensions of the innovative "planetary" clutch described in the previous section, the concept of the compliant gripper is developed as the next logical step forward.

The concept of the compliant 7-DOF gripper is developed based on kinematics shown in Fig. 5.19 (a). It has two fingers with 3 joints each and one additional wrist joint at the gripper base.

The joint at the base is located and oriented in such a way that if the gripper is mounted on the 5-DOF robot (Fig. 5.1), the wrist joint axis intersects the axes of the manipulator's last two joints (joint 4 and joint 5) at the same point. Three joint axes intersecting at the same point ensure the existence of a closed-form inverse kinematics solution for the 6-DOF (5-DOF robot plus 1 wrist joint) system.

(a)   (b)
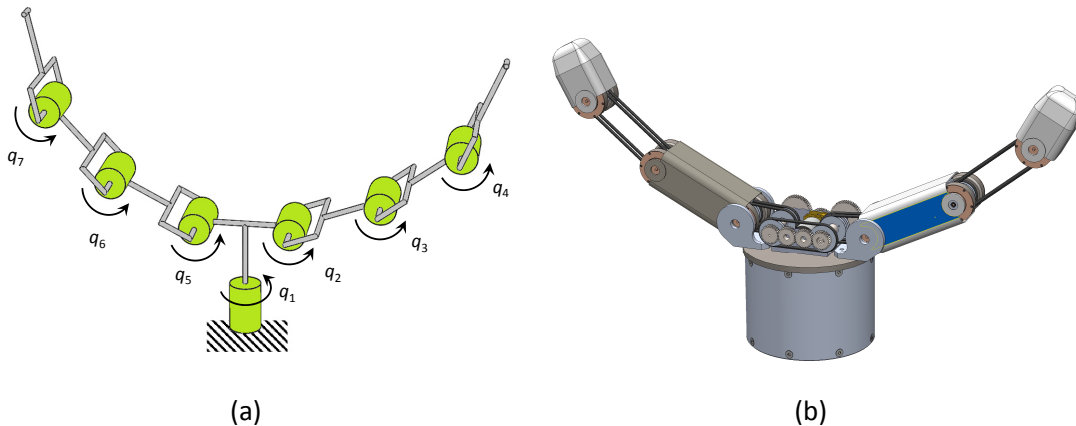
Figure 5.19: Symbolic representation of the kinematics (a) and CAD model (b) of a compliant robotic gripper design concept.

The joints of the fingers are actuated using a single brushed Premium N20 motor with a gearbox. The axes of all finger joints are parallel to each other, so a simple belt transmission can be used to actuation each joint.

Each joint of a finger uses two MR clutches spinning in opposite directions. The clutches rotating in one direction are located in the same plane, therefore, a simple serial belt transmission is used to transmit rotation from one clutch to the next as shown in Fig. 5.20. Each clutch rotor is attached to 2 pulleys, one pulley receives rotation from the driving belt, another pulley moves the driven belt to actuate the next clutch in series.
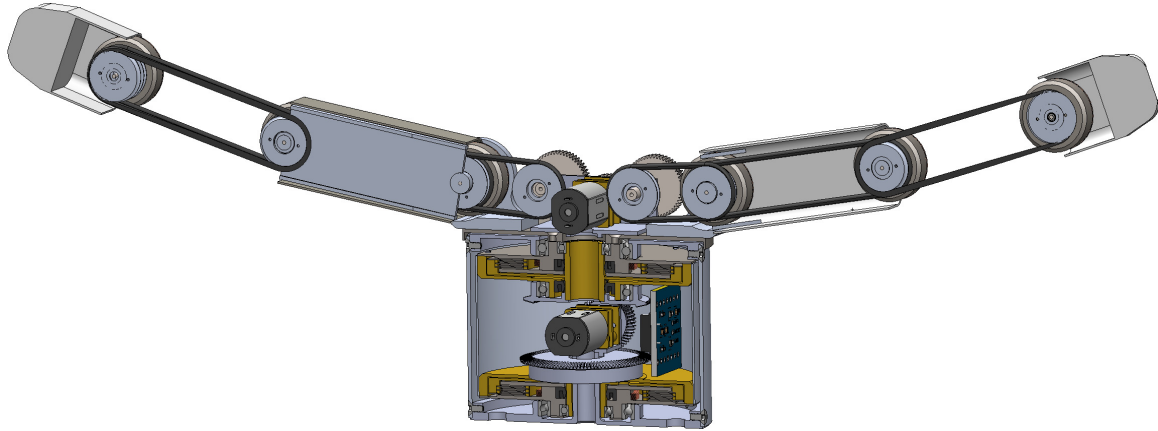
Figure 5.20: Design concept of a compliant robotic gripper with belt transmission actuating clutches rotating in the same direction (cross section view)

To obtain the opposite rotation of the pulleys, a set of spur gears is used as shown in Fig. 5.21. The motor rotates two spur gears "1" and "3" in mesh that are attached to the driving belt pulley for each finger ("A" and "B" respectively). The spur gear "3" is also attached to the spur gear "4" on the other side of the gripper (on of the bottom gears in Fig. 5.21). The spur gear train "4 - 5 - 6 - 7" drives the belt pulley "D" in opposite direction to the pulley "A". Spur gear "7" is also attached to the belt pulley "E" that transmits the motion to the pulley "F". Belt pulley "F" rotates pulley "C" via hollow shaft mounted coaxially with the shaft connecting spur gears "3" and "4". As a result, the pulley "C" rotates in the opposite direction to the pulley "B".
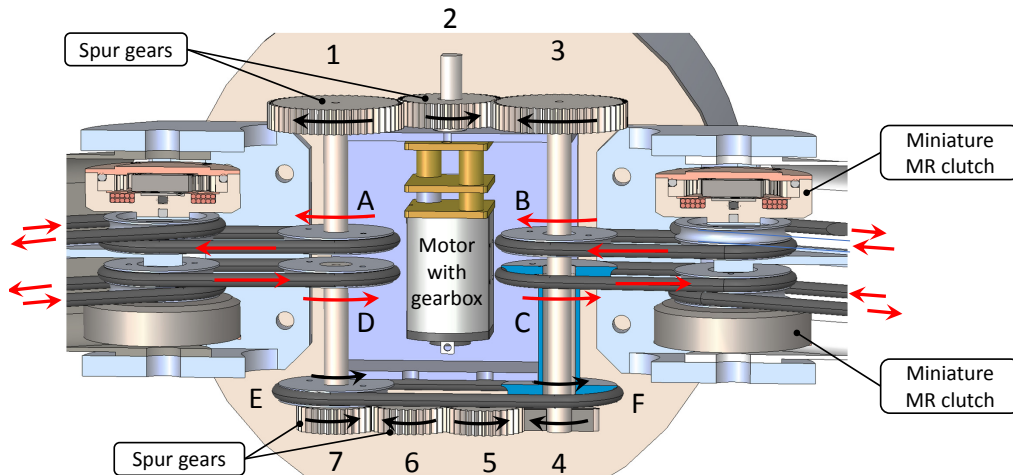
Figure 5.21: Design concept of the finger spur gear transmission used to obtain belt pulleys rotation in opposite directions.

To actuate the wrist joint, a similar Premium N20 motor is used. The motor is located in the gripper base between two antagonistic MR clutches as shown in Fig. 5.22. The bevel pinion on the output of the motor gearbox is in mesh with two bevel gears driving top and bottom MR

clutch rotors in opposite directions perpendicular to the motor shaft rotation.

For the wrist joint, the disk-type MR clutches are depicted in the design concept. However, "Planetary" clutches with the same external dimensions could be used instead.
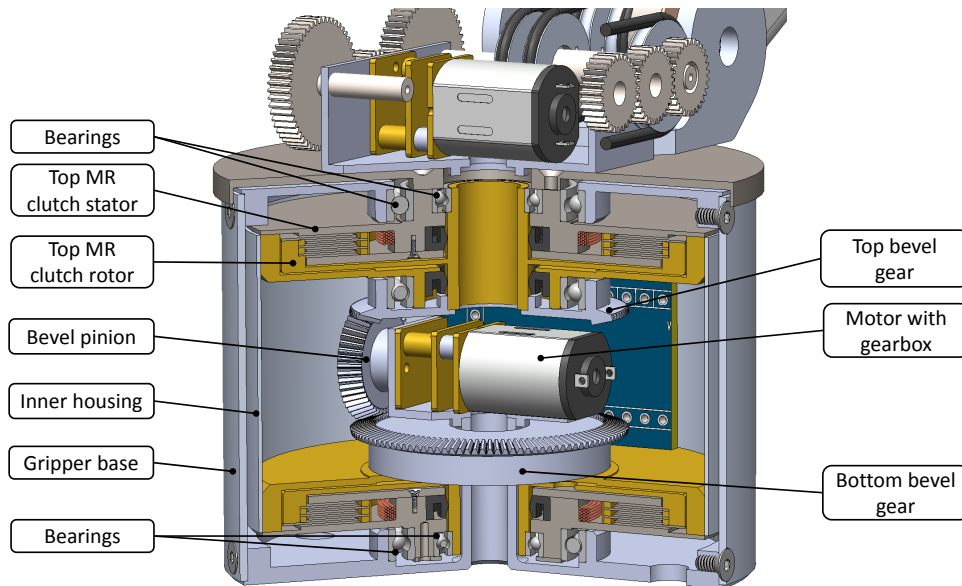
Figure 5.22: Design of the base of the compliant robotic gripper.

Building a compliant gripper similar to the presented concept could be very beneficial to address difficulties in manipulating soft tissues, live organs, and agricultural objects. However, further research is necessary to increase the torque transmitted by miniature MR clutches, to reduce the size of finger actuators, and to optimize the transmission system of the end-effector.

5.6   Conclusion

An innovative design of a magneto-rheological clutch based on planetary gear mechanism and using MR fluid in squeeze mode was presented and experimentally validated in this chapter. The results ascertained the possibility of building a miniaturized MR clutch with similar or even better torque performance when compared with conventional disk-type MR clutch of similar size.

It is observed that the value of the transmitted torque nearly proportionally depends on the number of planet gears installed. At the same time, according to the simulation in COMSOL Multiphysics, the magnetic flux passing through each planet gear decreases slightly with each additional gear introduced in the system.

The design of the "Planetary" clutch allows the improvement of the torque capabilities through the simple installation of the additional planet gears up to the maximum number allowed by the clutch configuration.

Based on the miniature MR clutch design, the concept of a compliant end-effector with 7 degrees of freedom and 2 motors is developed. The transmission system of the gripper is based on belts introduced between the finger joints. A system of spur gears is used to obtain antagonistic rotation of the driving pulleys.

Bibliography

[1] S. Pisetskiy and M. R. Kermani, "A concept of a miniaturized mr clutch utilizing mr fluid in squeeze mode," in *2020 IEEE/RSJ International Conference on Intelligent Robots and Systems (IROS)*. IEEE, 2020, pp. 6347–6352.

[2] P. Fauteux, M. Lauria, B. Heintz, and F. Michaud, "Dual-differential rheological actuator for high-performance physical robotic interaction," *IEEE Transactions on Robotics*, vol. 26, no. 4, pp. 607–618, 2010.

[3] J. Viau, P. Chouinard, J.-P. L. Bigue, G. Julió, F. Michaud, and J.-S. Plante, "Tendon-driven manipulator actuated by magnetorheological clutches exhibiting both high-power and soft motion capabilities," *IEEE/ASME Transactions on Mechatronics*, vol. 22, no. 1, pp. 561–571, 2017.

[4] T. Kikuchi, K. Otsuki, J. Furusho, H. Abe, J. Noma, M. Naito, and N. Lauzier, "Development of a compact magnetorheological fluid clutch for human-friendly actuator," *Advanced Robotics*, vol. 24, no. 10, pp. 1489–1502, 2010.

[5] A. S. Shafer and M. R. Kermani, "On the feasibility and suitability of mr fluid clutches in human-friendly manipulators," *IEEE/ASME Transactions on Mechatronics*, vol. 16, no. 6, pp. 1073–1082, 2010.

[6] A. Shafer and M. R. Kermani, "Development of high performance intrinsically safe 3-dof robot," in *2014 IEEE International Conference on Robotics and Automation (ICRA)*. IEEE, 2014, pp. 619–624.

[7] M. Abdeetedal and M. R. Kermani, "Grasp synthesis for purposeful fracturing of object," *Robotics and Autonomous Systems*, vol. 105, pp. 47–58, 2018.

[8] N. Najmaei, A. Asadian, M. R. Kermani, and R. V. Patel, "Design and performance evaluation of a prototype mrf-based haptic interface for medical applications," *IEEE/ASME Transactions on Mechatronics*, vol. 21, no. 1, pp. 110–121, 2015.

[9] N. Najmaei, A. Asadian, M. R. Kermani, and R. Patel, "Magneto-rheological actuators for haptic devices: Design, modeling, control, and validation of a prototype clutch," in *2015 International Conference on Robotics and Automation (ICRA)*. IEEE, 2015, pp. 207–2012.

[10] N. Najmaei, P. Yadmellat, M. R. Kermani, and R. V. Patel, "Application of magneto-rheological fluid based clutches for improved performance in haptic interfaces," in *2014 International Conference on Robotics and Automation (ICRA)*. IEEE, 2014, pp. 832–837.

[11] M. Abdeetedal and M. R. Kermani, "Development and grasp analysis of a sensorized underactuated finger," in *2017 IEEE/RSJ International Conference on Intelligent Robots and Systems (IROS)*. IEEE, 2017, pp. 6331–6336.

[12] N. M. Wereley, "Nondimensional herschel—bulkley analysis of magnetorheological and electrorheological dampers," *Journal of Intelligent Material Systems and Structures*, vol. 19, no. 3, pp. 257–268, 2008.

[13] N. Wereley, J. Cho, Y. Choi, and S. Choi, "Magnetorheological dampers in shear mode," *Smart Materials and Structures*, vol. 17, no. 1, p. 015022, 2007.

[14] V. A. Neelakantan and G. N. Washington, "Modeling and reduction of centrifuging in magnetorheological (mr) transmission clutches for automotive applications," *Journal of Intelligent Material Systems and Structures*, vol. 16, no. 9, pp. 703–711, 2005.

[15] R. Stanway, J. Sproston, M. Prendergast, J. Case, and C. Wilne, "Er fluids in the squeeze-flow mode: an application to vibration isolation," *Journal of Electrostatics*, vol. 28, no. 1, pp. 89–94, 1992.

[16] A. Farjoud, R. Cavey, M. Ahmadian, and M. Craft, "Magneto-rheological fluid behavior in squeeze mode," *Smart Materials and Structures*, vol. 18, no. 9, p. 095001, 2009.

[17] F. Goncalves and J. Carlson, "An alternate operation mode for mr fluids—magnetic gradient pinch," in *Journal of Physics: Conference Series*, vol. 149, no. 1. IOP Publishing, 2009, p. 012050.

[18] R. Andrade, A. Bento Filho, C. Vimieiro, and M. Pinotti, "Optimal design and torque control of an active magnetorheological prosthetic knee," *Smart Materials and Structures*, vol. 27, no. 10, p. 105031, 2018.

[19] H. Qin, A. Song, and Y. Mo, "Performance evaluation of a hollowed multi-drum magne-torheological brake based on finite element analysis considering hollow casing radius," *IEEE Access*, vol. 7, pp. 96 070–96 078, 2019.

[20] J. D. Carlson and M. R. Jolly, "Mr fluid, foam and elastomer devices," *mechatronics*, vol. 10, no. 4-5, pp. 555–569, 2000.

[21] C. Kieburg, G. Oetter, R. Lochtman, C. Gabriel, H. Laun, J. Pfister, G. Schober, and H. Steinwender, "High performance magnetorheological fluids tailored for a 700 nm au-tomotive 4-wheel-drive clutch," in *Electrorheological Fluids And Magnetorheological Suspensions*. World Scientific, 2007, pp. 101–107.

[22] C. Sarkar and H. Hirani, "Theoretical and experimental studies on a magnetorheological brake operating under compression plus shear mode," *Smart Materials and Structures*, vol. 22, no. 11, p. 115032, 2013.

[23] A. K. Kwan, T. H. Nam, and Y. Y. Il, "New approach to design mr brake using a small steel roller as a large size magnetic particle," in *2008 International Conference on Control, Automation and Systems*.   IEEE, 2008, pp. 2640–2644.

[24] S. H. Mousavi and H. Sayyaadi, "Optimization and testing of a new prototype hybrid mr brake with arc form surface as a prosthetic knee," *IEEE/ASME Transactions on Mechatronics*, vol. 23, no. 3, pp. 1204–1214, 2018.

[25] W. Li, P. Yadmellat, and M. R. Kermani, "Design optimization and comparison of magneto-rheological actuators," in *2014 IEEE International Conference on Robotics and Automation (ICRA)*.   IEEE, 2014, pp. 5050–5055.

[26] "Mrf-140cg magneto-rheological fluid," Lord Technical Data, 2008. [Online]. Available: http://www.lordmrstore.com

Chapter 6

Conclusion and Future Work

In this chapter, the review of the main thesis contributions is presented and possible directions for future research activity are proposed.

6.1 Summary of contributions

Safety and compliance, robustness, and ability to work in a rapidly changing environment are the crucial characteristics for the robotic systems of the future, urgently needed to support the quality of life of the rapidly aging world population. Future robots should be capable of replacing people in many areas starting from industry and agriculture to health support and helping people with chores in their own homes.

The innovative design of the 5-DOF manipulator, presented in this work, demonstrates the possibility of building inherently compliant complex robots. The remarkable properties of the antagonistic MR actuation approach used in the robot allow the development of a low-cost system capable to perform sophisticated tasks that require low impedance and variable stiffness of the joints.

The feasibility of integrating antagonistic MR actuators in all 5 joints of the robot driven by a single motor is the main outcome of this study. In addition, the design, simulation, prototyping, and testing of the innovative disk-type MR clutch with a high torque-to-mass ratio demonstrated the possibility to significantly reduce the weight and to improve the performance of the manipulator.

The 5-DOF manipulator transmission system is simulated to demonstrate the influence of transmission components on each other performance during operation.

Additionally, the inherent passivity of the antagonistic MR actuation is analytically studied and experimentally validated using the 2nd joint of the manipulator prototype.

Furthermore, the position control experiments demonstrated the possibility of the development of a simple and effective joint level PID control system.

Finally, an innovative design of a miniature magneto-rheological clutch based on planetary gear mechanism and using MR fluid in squeeze mode is developed, assembled, and tested. Based on the miniature MR clutch design, the concept of a compliant end-effector with 7 degrees of freedom and only 2 motors is developed.

All in all, the research demonstrated that the use of antagonistic MR actuators in the robot

joints brings compliance, power, safety, and control simplicity to the multi-DOF robotic systems of the future.

6.2   Future work

Further work is planned to improve the FEM model of the MR clutch to better correlate with the results of the experiments with the actual hardware.

Future steps include improving joint-level control and the development of the task-space robot-level control system for the 5-DOF manipulator.

The inherent passivity of multi-DOF systems is to be investigated and tested based on the developed 5-DOF manipulator.

Further research is planned to evaluate alternative designs of the MR clutch with cogwheels based on planetary gear train without inner gear and planetary gear train without sun gear.

The detailed mathematical modeling planned for development to benefit in the optimization of the "planetary" clutch as well as in determining the achievable limits of the proposed design.

Based on the presented 7-DOF gripper concept, further work is planned to design, prototype, and test a compliant end-effector using an antagonistic MR clutch actuation approach.

Appendices

Appendix A

5-DOF Manipulator DH parameters and transformations
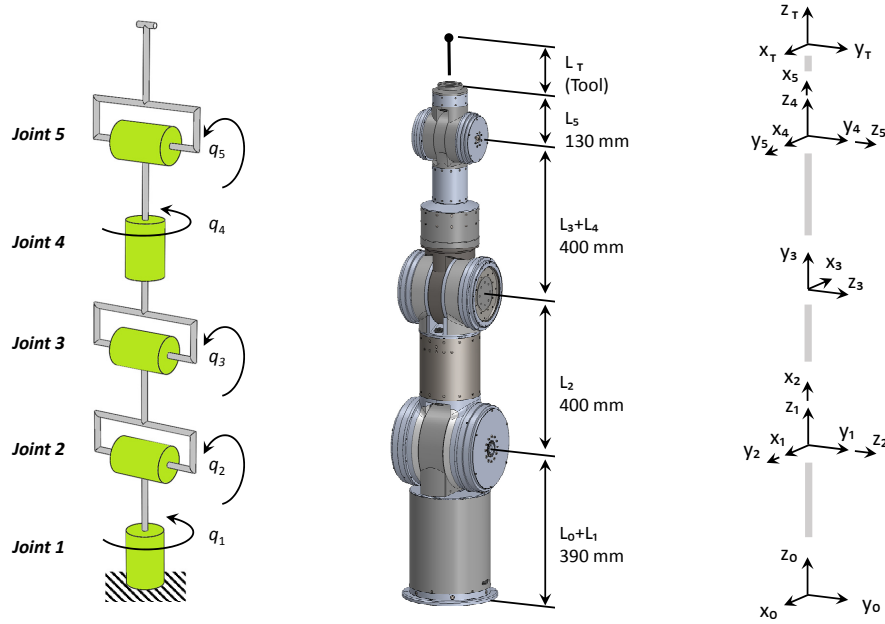
Figure A.1: Manipulator kinematic arrangement and link coordinate frames assignment

Using general form of transformation,

$$
{}^{i-1}_{i}T = \begin{bmatrix} cq_i & -sq_i & 0 & a_{i-1} \\ sq_i c\alpha_{i-1} & cq_i c\alpha_{i-1} & -s\alpha_{i-1} & -s\alpha_{i-1}d_i \\ sq_i s\alpha_{i-1} & cq_i s\alpha_{i-1} & c\alpha_{i-1} & c\alpha_{i-1}d_i \\ 0 & 0 & 0 & 1 \end{bmatrix},
$$

the transformation for each link can be written as follows,

Table A.1: 5-DOF manipulator DH parameters

Link i	α_{i-1}	a_{i-1}	d_i	q_i
1	0	0	$L_0 + L_1$	q_1
2	$-\pi/2$	0	0	$q_2 - \pi/2$
3	0	L_2	0	$q_3 - \pi/2$
4	$-\pi/2$	0	$L_3 + L_4$	$q_4 + \pi$
5	$-\pi/2$	0	0	$q_5 - \pi/2$

$$
{}^0_1T = \begin{bmatrix} cq_1 & -sq_1 & 0 & 0 \\ sq_1 & cq_1 & 0 & 0 \\ 0 & 0 & 1 & L_0 + L_1 \\ 0 & 0 & 0 & 1 \end{bmatrix},\
{}^1_2T = \begin{bmatrix} sq_2 & cq_2 & 0 & 0 \\ 0 & 0 & 1 & 0 \\ cq_2 & -sq_2 & 0 & 0 \\ 0 & 0 & 0 & 1 \end{bmatrix},\
{}^2_3T = \begin{bmatrix} sq_3 & cq_3 & 0 & L_2 \\ -cq_3 & sq_3 & 0 & 0 \\ 0 & 0 & 1 & 0 \\ 0 & 0 & 0 & 1 \end{bmatrix},
$$

$$
{}^3_4T = \begin{bmatrix} -cq_4 & sq_4 & 0 & 0 \\ 0 & 0 & 1 & L_3 + L_4 \\ sq_4 & cq_4 & 0 & 0 \\ 0 & 0 & 0 & 1 \end{bmatrix},\
{}^4_5T = \begin{bmatrix} sq_5 & cq_5 & 0 & 0 \\ 0 & 0 & 1 & 0 \\ cq_5 & -sq_5 & 0 & 0 \\ 0 & 0 & 0 & 1 \end{bmatrix}.
$$

Transformation for the tool frame could be added as

$$
{}^5_TT = \begin{bmatrix} 0 & 0 & 1 & L_5 + L_T \\ 1 & 0 & 0 & 0 \\ 0 & 1 & 0 & 0 \\ 0 & 0 & 0 & 1 \end{bmatrix}.
$$

The full forward transformation is

$$
{}^0_TT = {}^0_1T\,{}^1_2T\,{}^2_3T\,{}^3_4T\,{}^4_5T\,{}^5_TT = \begin{bmatrix} r_{11} & r_{12} & r_{13} & p_x \\ r_{21} & r_{22} & r_{23} & p_y \\ r_{31} & r_{32} & r_{33} & p_z \\ 0 & 0 & 0 & 1 \end{bmatrix},
$$

where
$r_{11} = -sq_5\,cq_1\,s(q_2 + q_3) - cq_5\,(sq_1\,sq_4 - cq_4\,cq_1\,c(q_2 + q_3))$,
$r_{21} = cq_5\,(cq_1\,sq_4 + cq_4\,sq_1\,c(q_2 + q_3)) - sq_5\,sq_1\,s(q_2 + q_3)$,
$r_{31} = -sq_5\,c(q_2 + q_3) - cq_4\,cq_5\,s(q_2 + q_3)$,

$r_{12} = -cq_4\,sq_1 - sq_4\,cq_1\,c(q_2 + q_3)$,
$r_{22} = cq_1\,cq_4 - sq_4\,sq_1\,c(q_2 + q_3)$,
$r_{32} = sq_4\,s(q_2 + q_3)$,

$r_{13} = cq_5\,cq_1\,s(q_2 + q_3) - sq_5\,(sq_1\,sq_4 - cq_4\,cq_1\,c(q_2 + q_3))$,
$r_{23} = cq_5\,sq_1\,s(q_2 + q_3) + sq_5\,(cq_1\,sq_4 + cq_4\,sq_1\,c(q_2 + q_3))$,

$r_{33} = cq_5 \, c(q_2 + q_3) - cq_4 \, sq_5 \, s(q_2 + q_3),$

$p_x = (L_3 + L_4)(cq_1 \, cq_2 \, sq_3 + cq_1 \, cq_3 \, sq_2) - L_5 \, (sq_5 \, (sq_1 \, sq_4 - cq_4 \, (cq_1 \, cq_2 \, cq_3 - cq_1 \, sq_2 \, sq_3)) - cq_5 \, (cq_1 \, cq_2 \, sq_3 + cq_1 \, cq_3 \, sq_2)) + L_2 \, cq_1 \, sq_2,$

$p_y = L_34s(q_2+q_3)sq_1 + L_2 \, sq_1 \, sq_2 + L_5 \, s(q_2+q_3)cq_5 \, sq_1 + L_5 cq_1 \, sq_4 \, sq_5 - L_5 cq_4 \, sq_1 \, sq_2 \, sq_3 \, sq_5 + L_5 \, cq_2 \, cq_3 \, cq_4 \, sq_1 \, sq_5,$

$p_z = L_0 + L_1 + (L_3 + L_4) \, c(q_2 + q_3) + L_2 \, cq_2 - (L_5 \, s(q_2 + q_3) \, s(q_4 + q_5))/2 + L_5 \, c(q_2 + q_3) \, cq_5 + (L_5 \, s(q_4 - q_5) \, s(q_2 + q_3))/2.$

Appendix B

5-DOF Manipulator Mechanical Design
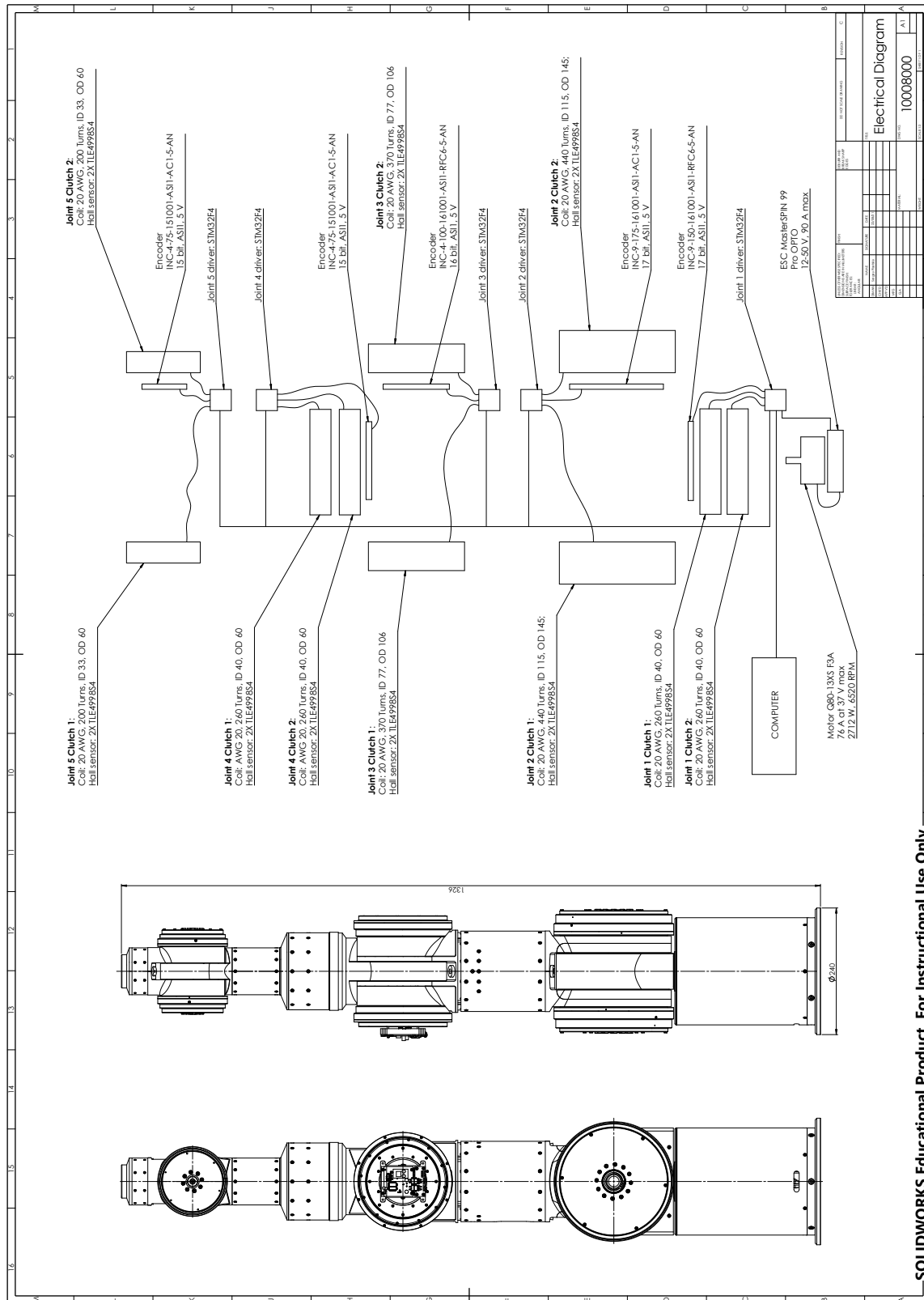
Figure B.1: Drawing: 5-DOF manipulator electrical scheme.

Item	Part Number	Description	Quantity
1	10000401	Gear KKSP119002GFG	1
2	10000076	Pulley	1
3	90327A115	Screw M4 x 16	8
4	10000073	Axis2 Transmission Cylinder	1
5	10000071	Axis2 Transmission Flange	1
6	10000072	Axis2 Transmission Disk	1
7	96717A120	Key 4 x 4 x 12 mm	3
8	90666A112	Screw M4 x 6	12
9	71806C	Bearing Angular 71806C	1
10	71809C	Bearing Angular 71809C	1
11	92906A087	Set Screw M4 x 8	3

Axis2 Transmission Assembly

10004000

SECTION A-A

Figure B.2: Drawing: Joint 2 bevel gear and pulley assembly.
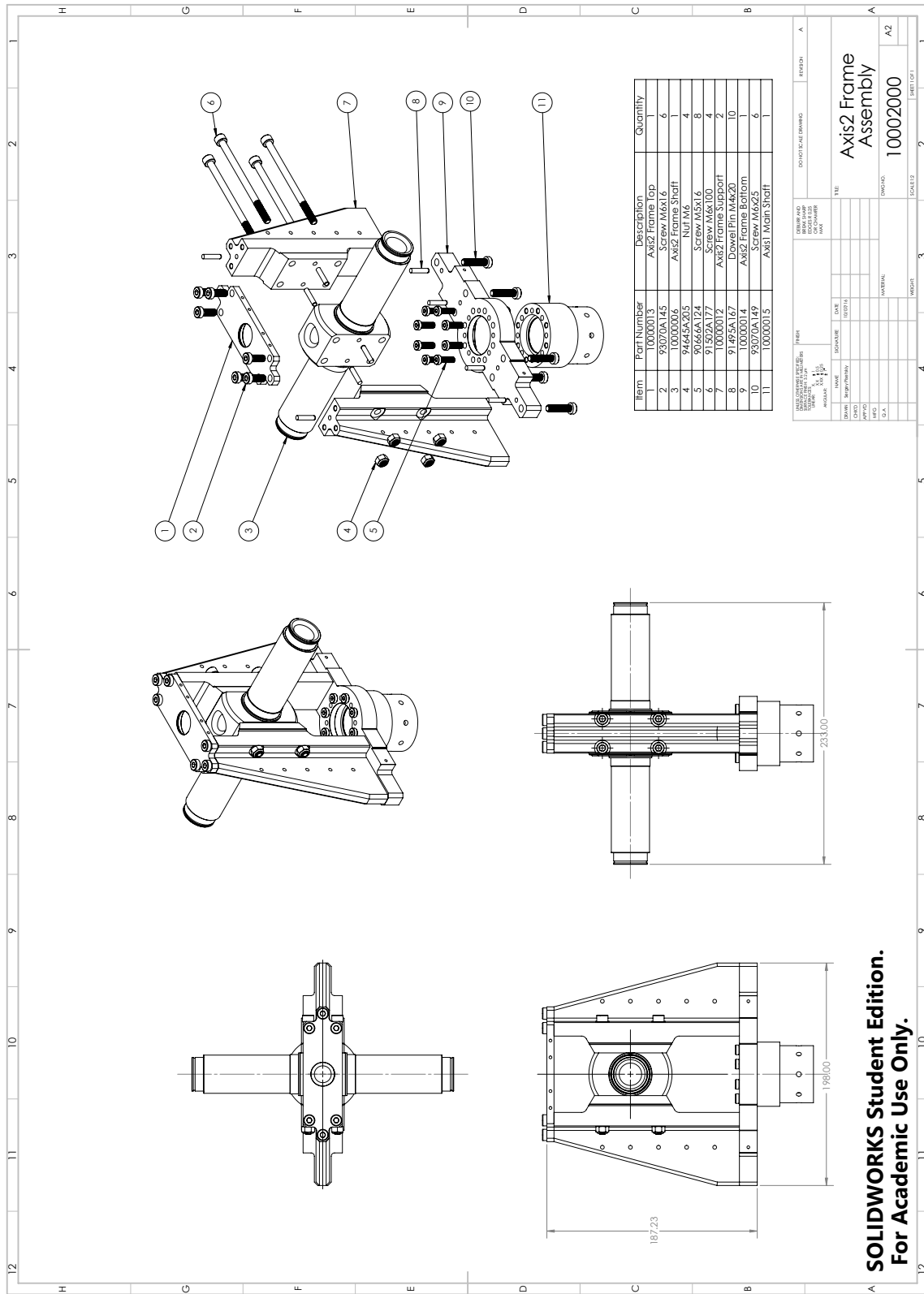
Figure B.3: Drawing: Link 1 joint 2 frame assembly.

Figure B.4: Drawing: Link 1 housing.

2X ⌀ 6.80 ▽ 17.75
M8X1.25 - 6H ▽ 14.00
⌵ ⌀ 8.05 X 90°, NEAR SIDE

⌀ 6.60

⌀ 12.70

197.00±0.05

22

2X ⌀ 12.00 h6 $^{0.00}_{-0.01}$

SECTION A-A

UNLESS OTHERWISE SPECIFIED:
DIMENSIONS ARE IN MILLIMETERS
SURFACE FINISH: 3.2 μm
TOLERANCES:
LINEAR: X.   ± 1
               X.X   ± 0.5
               X.XX ± 0.25
ANGULAR: ± 1°

FINISH:

DEBURR AND
BREAK SHARP
EDGES R 0.25
OR CHAMFER
MAX

DO NOT SCALE DRAWING   REVISION   B

	NAME	SIGNATURE	DATE				TITLE:
DRAWN	Sergey Pisetskiy		23/08/16				
CHK'D							
APPV'D							
MFG							
Q.A							

TITLE:
Link 01 Standoff

SOLIDWORKS Student Edition
For Academic Use Only

MATERIAL:
AL 2024 T3
McMaster-Carr 1968T23

DWG NO.
10000002

A4

WEIGHT: SCALE:2:1   SHEET 1 OF 1

Figure B.5: Drawing: Link 1 standoff.

Figure B.6: Drawing: Link 1 top flange.
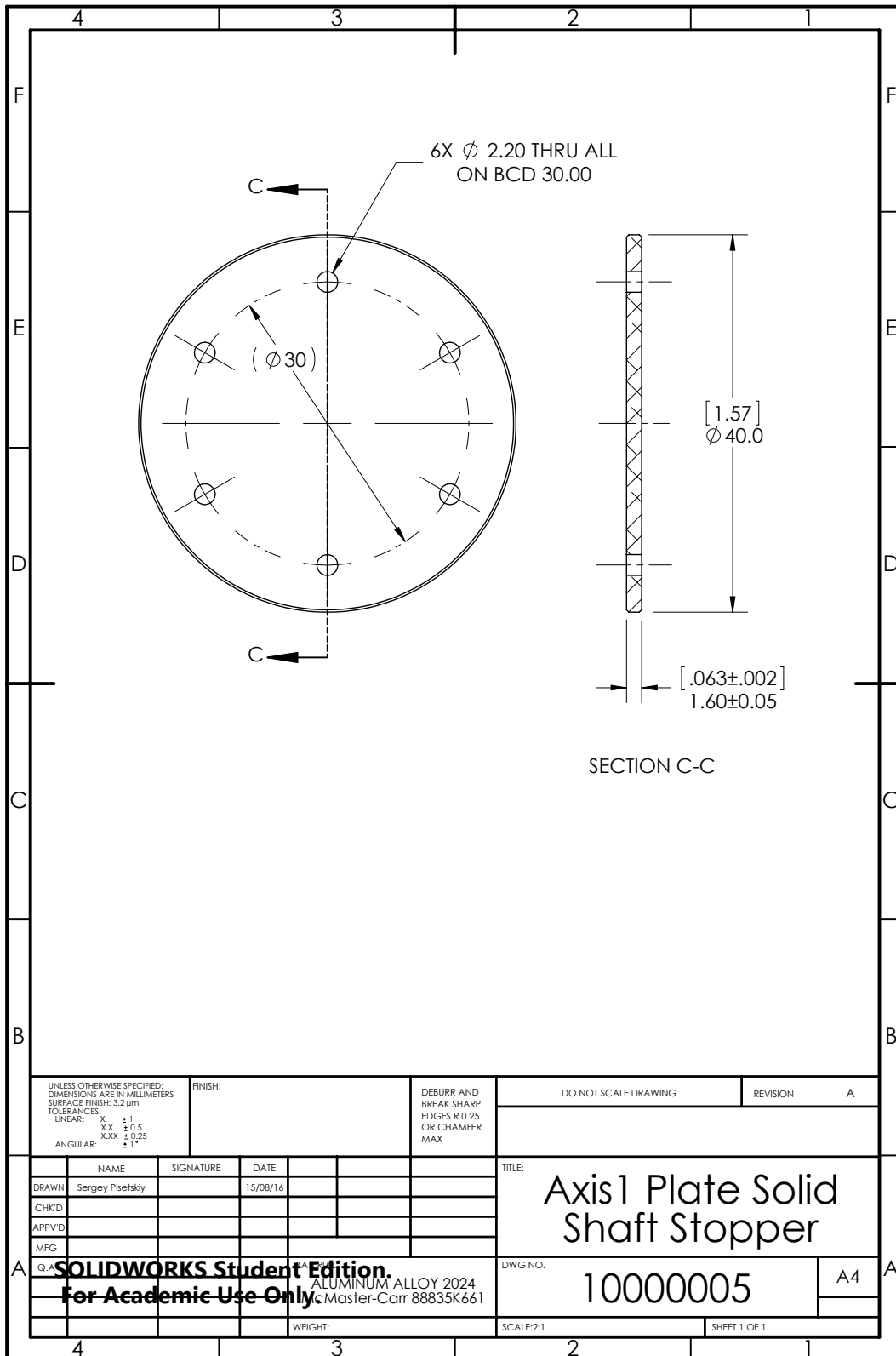
Figure B.7: Drawing: Joint 1 solid shaft stopper.
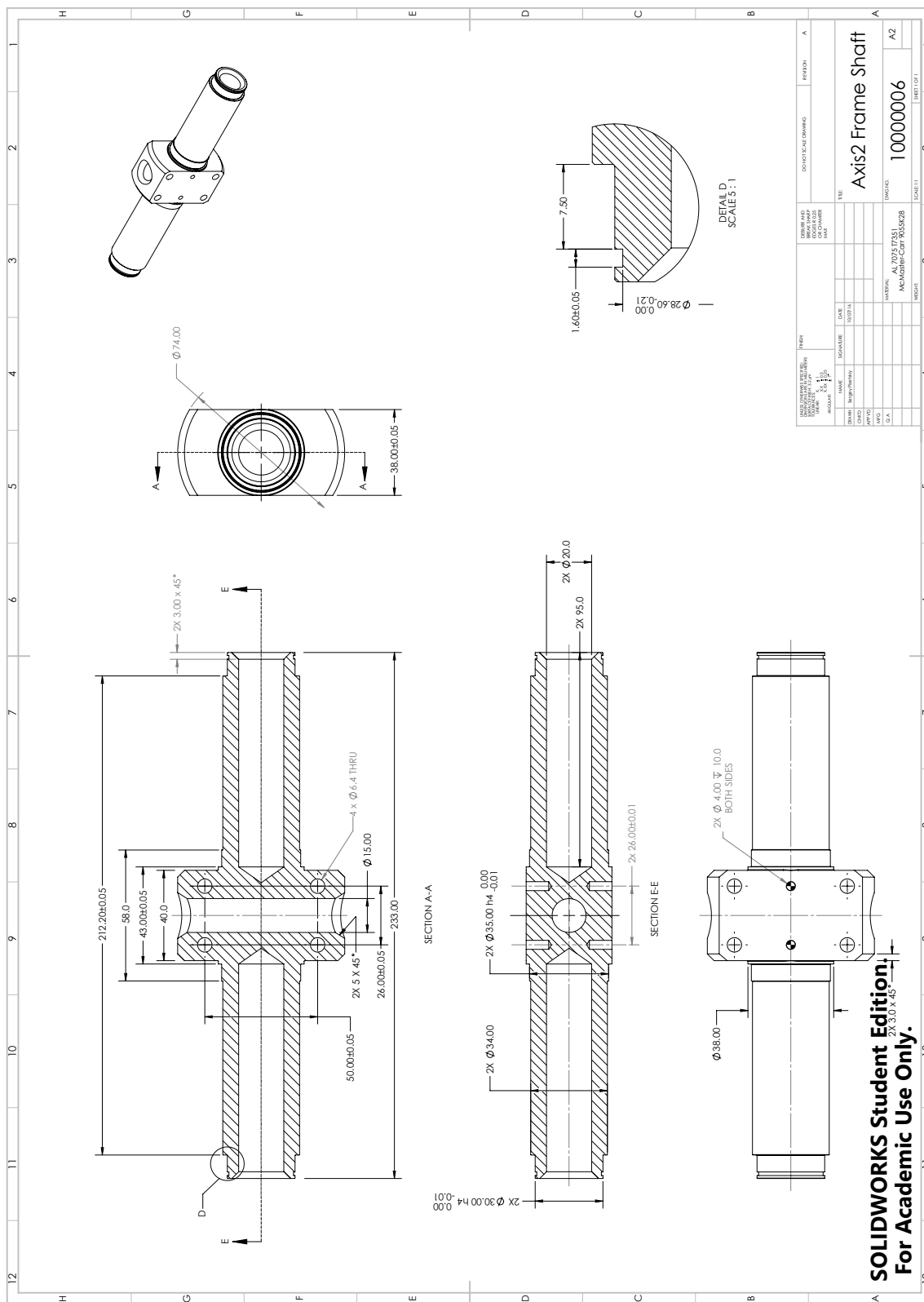
Figure B.8: Drawing: Joint 2 frame shaft.
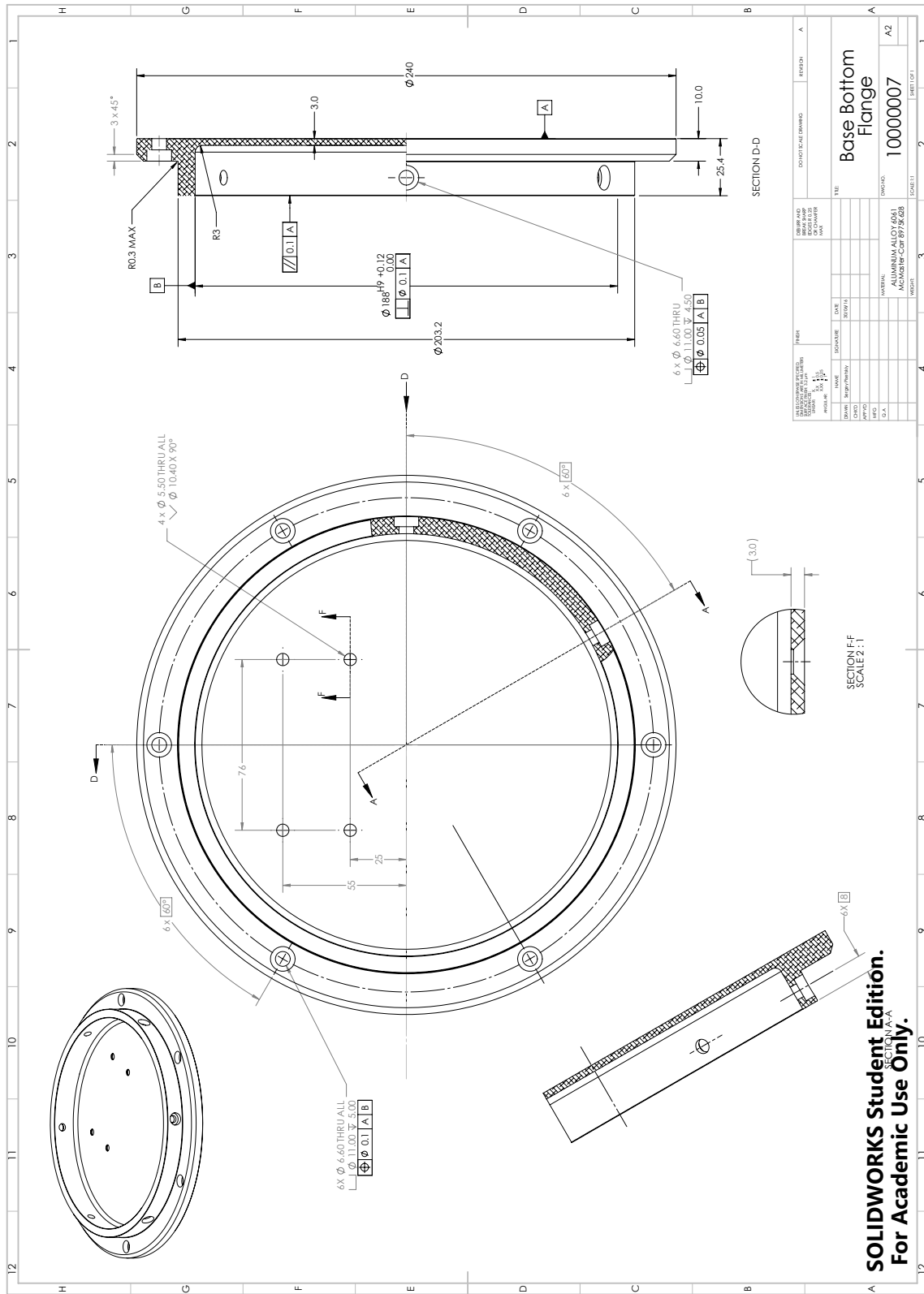
Figure B.9: Drawing: Link 1 bottom flange.

Figure B.10: Drawing: Link 1 bottom ring.
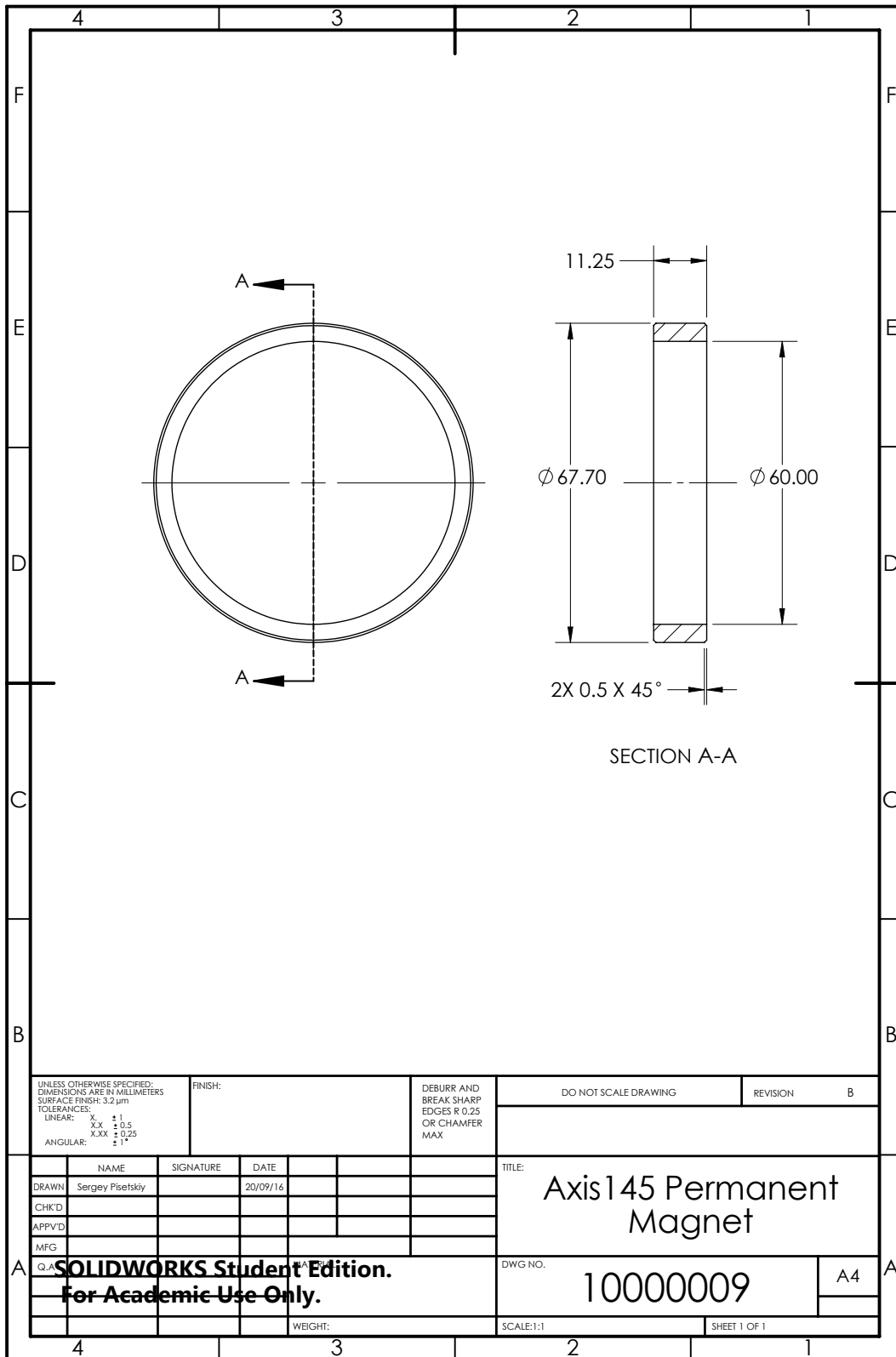
Figure B.11: Drawing: Joint 1, 4, 5 permanent magnet.

23.00

$\emptyset$155.00 $\emptyset$146.00

A

A

SECTION A-A

	NAME	SIGNATURE	DATE				TITLE:
DRAWN	Sergey Pisetskiy		24/06/16				
CHK'D							
APPV'D							
MFG							
Q.A							

UNLESS OTHERWISE SPECIFIED:
DIMENSIONS ARE IN MILLIMETERS
SURFACE FINISH: 3.2 μm
TOLERANCES:
LINEAR: X.   ± 1
             X.X   ± 0.5
             X.XX ± 0.25
ANGULAR: ± 1°

FINISH:

DEBURR AND
BREAK SHARP
EDGES R 0.25
OR CHAMFER
MAX

DO NOT SCALE DRAWING   REVISION   A

TITLE: Axis2 Permanent Magnet

DWG NO. 10000010   A4

WEIGHT: SCALE:1:2   SHEET 1 OF 1

Figure B.12: Drawing: Joint 2 permanent magnet.
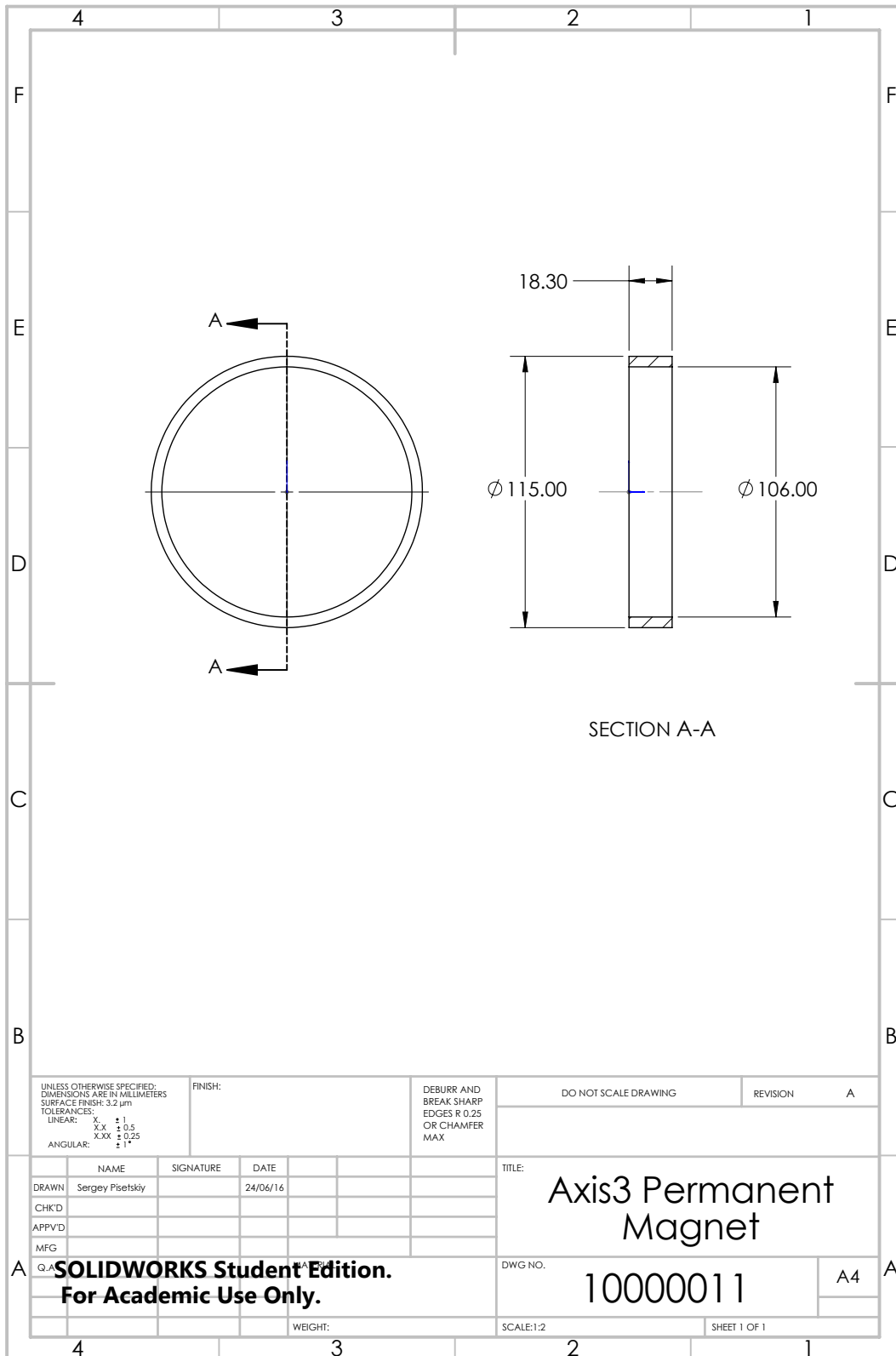
Figure B.13: Drawing: Joint 3 permanent magnet.

Figure B.14: Drawing: Joint 2 frame support.
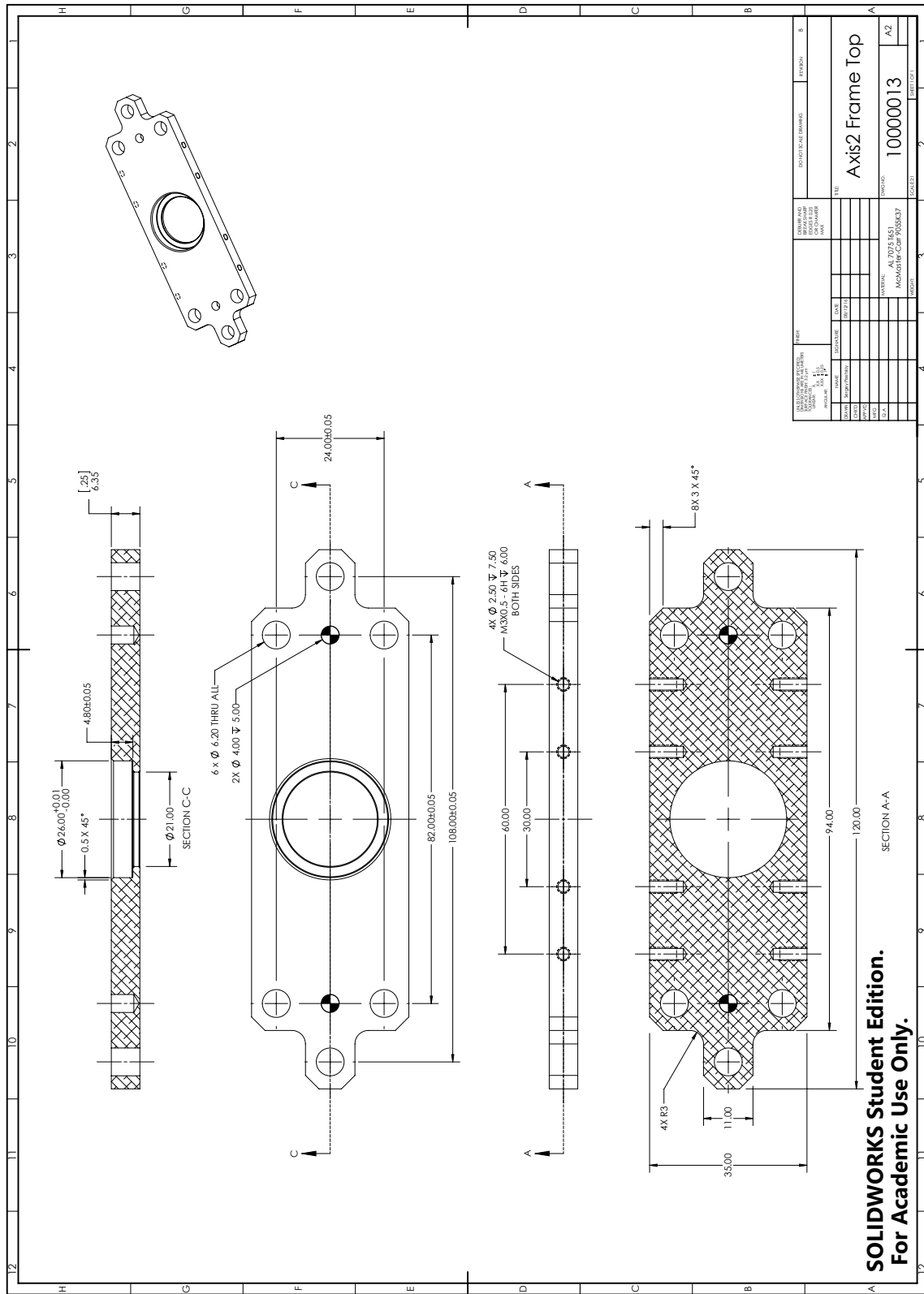
Figure B.15: Drawing: Joint 2 frame top.
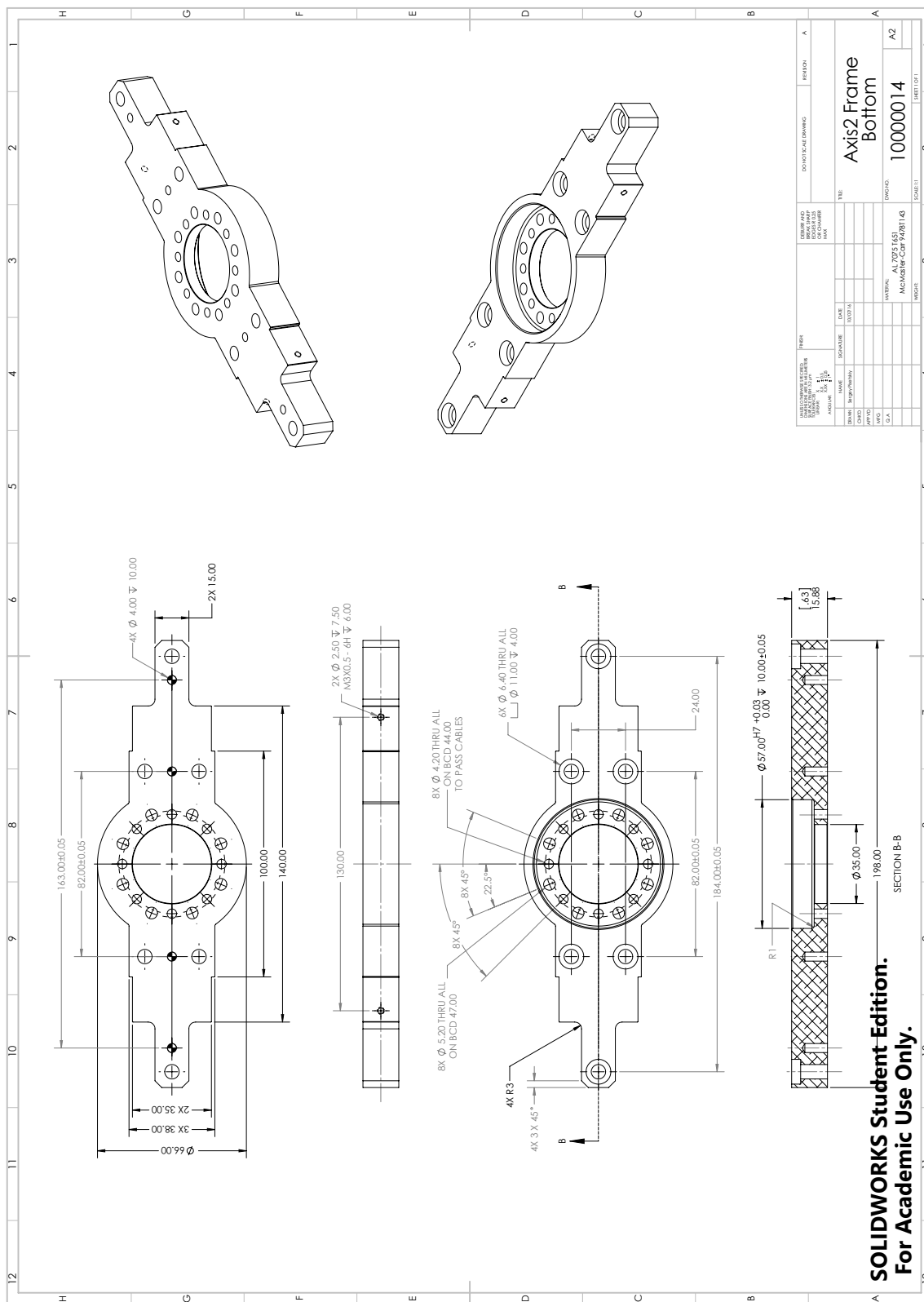
Figure B.16: Drawing: Joint 2 frame bottom.
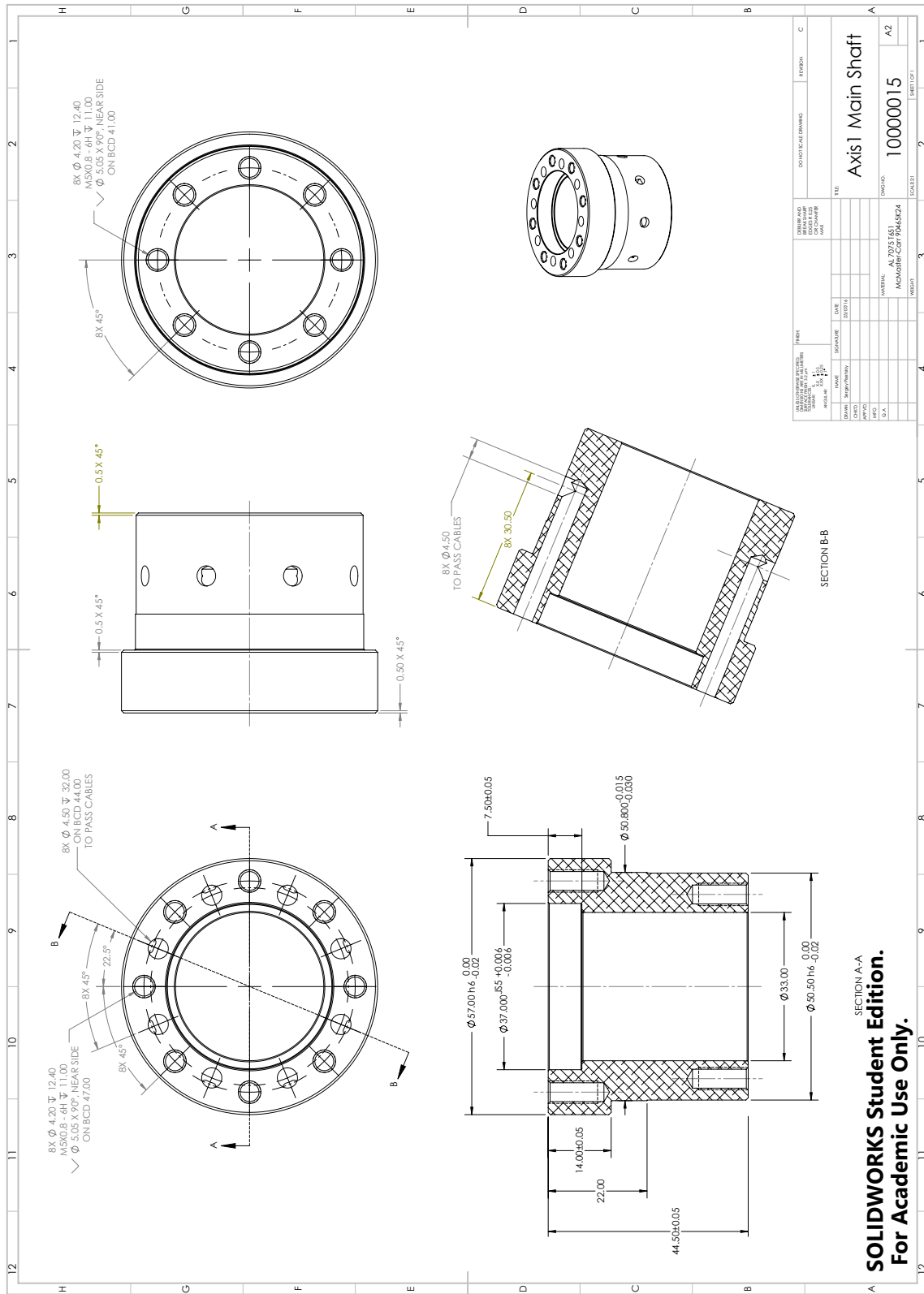
Figure B.17: Drawing: Joint 1 main shaft.
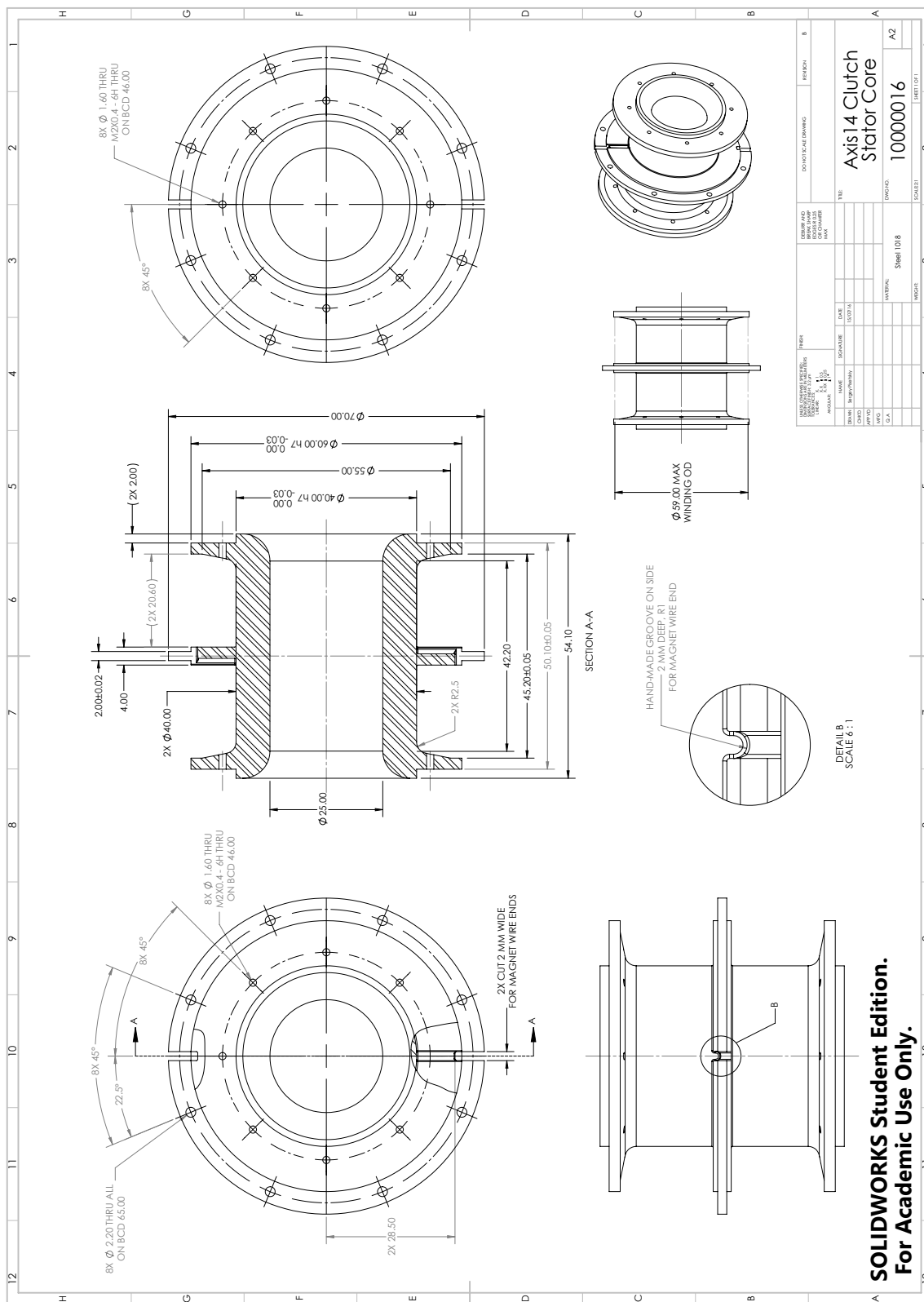
Figure B.18: Drawing: Joint 1, 4 clutch stator core.
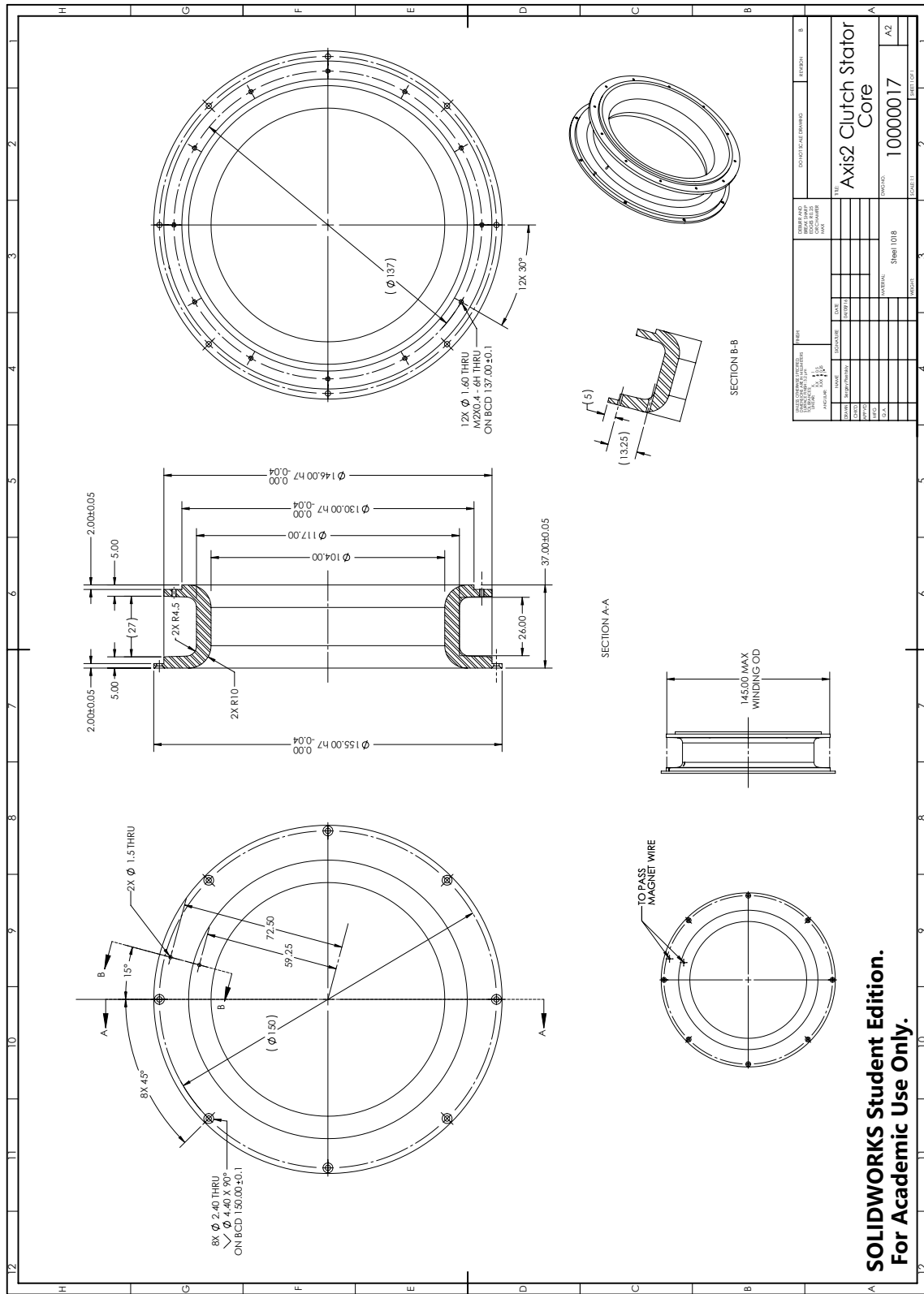
Figure B.19: Drawing: Joint 2 clutch stator core.

Figure B.20: Drawing: Joint 3 clutch stator core.
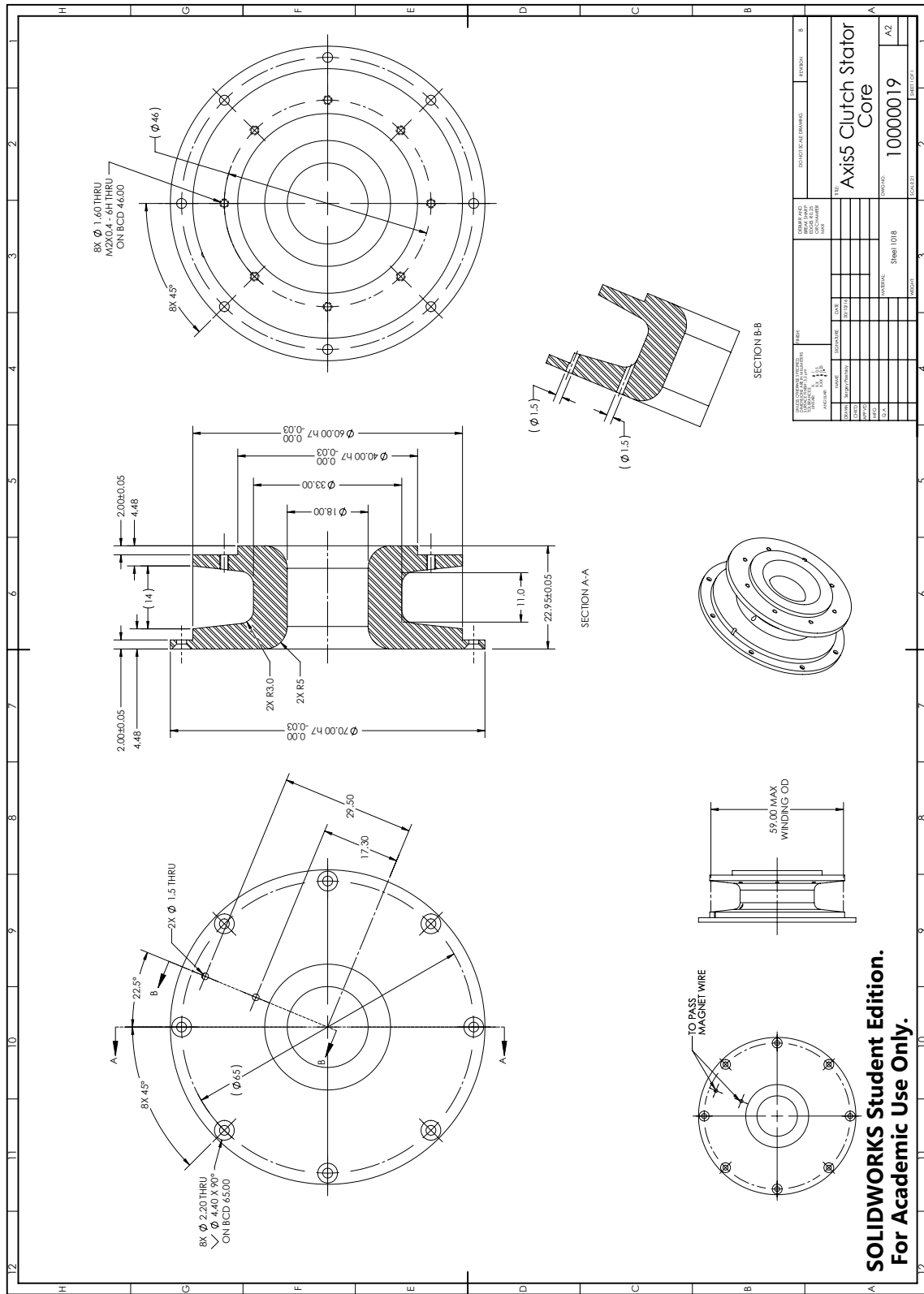
Figure B.21: Drawing: Joint 5 clutch stator core.

Figure B.22: Drawing: Joint 1, 4, 5 clutch stator disk.
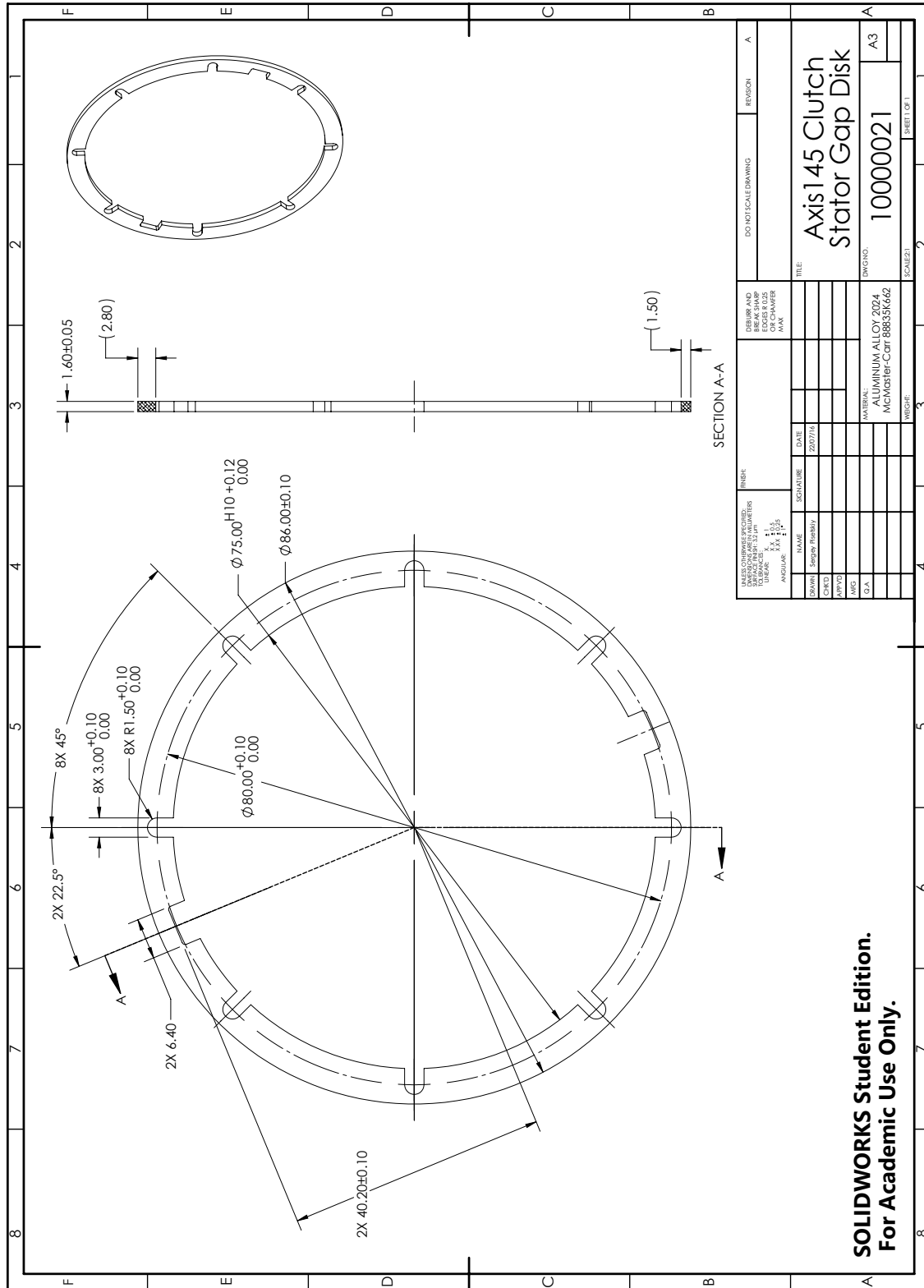
Figure B.23: Drawing: Joint 1, 4, 5 clutch stator spacer.
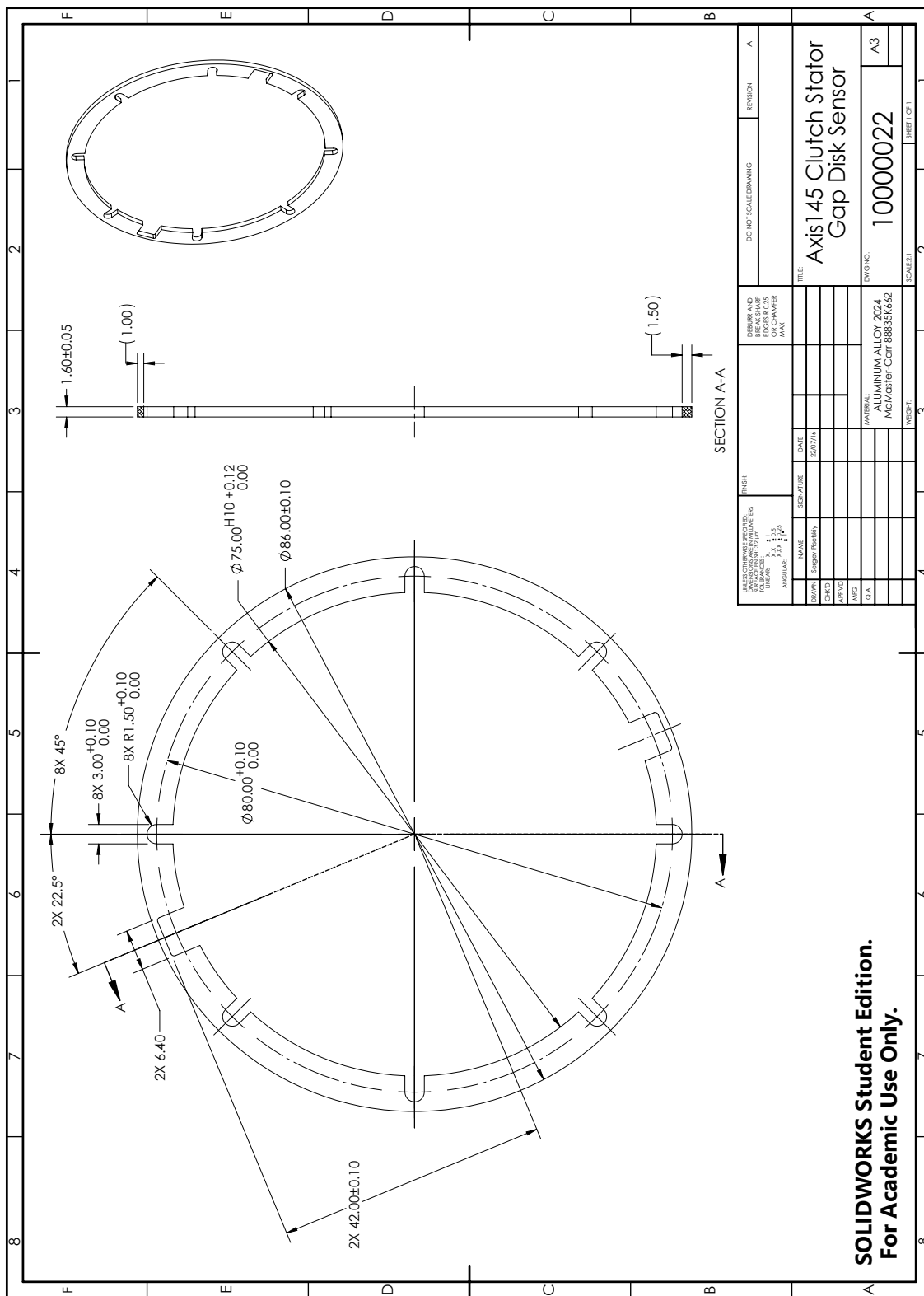
Figure B.24: Drawing: Joint 1, 4, 5 clutch stator sensor spacer.

Figure B.25: Drawing: Joint 1, 4, 5 clutch stator seling spacer.
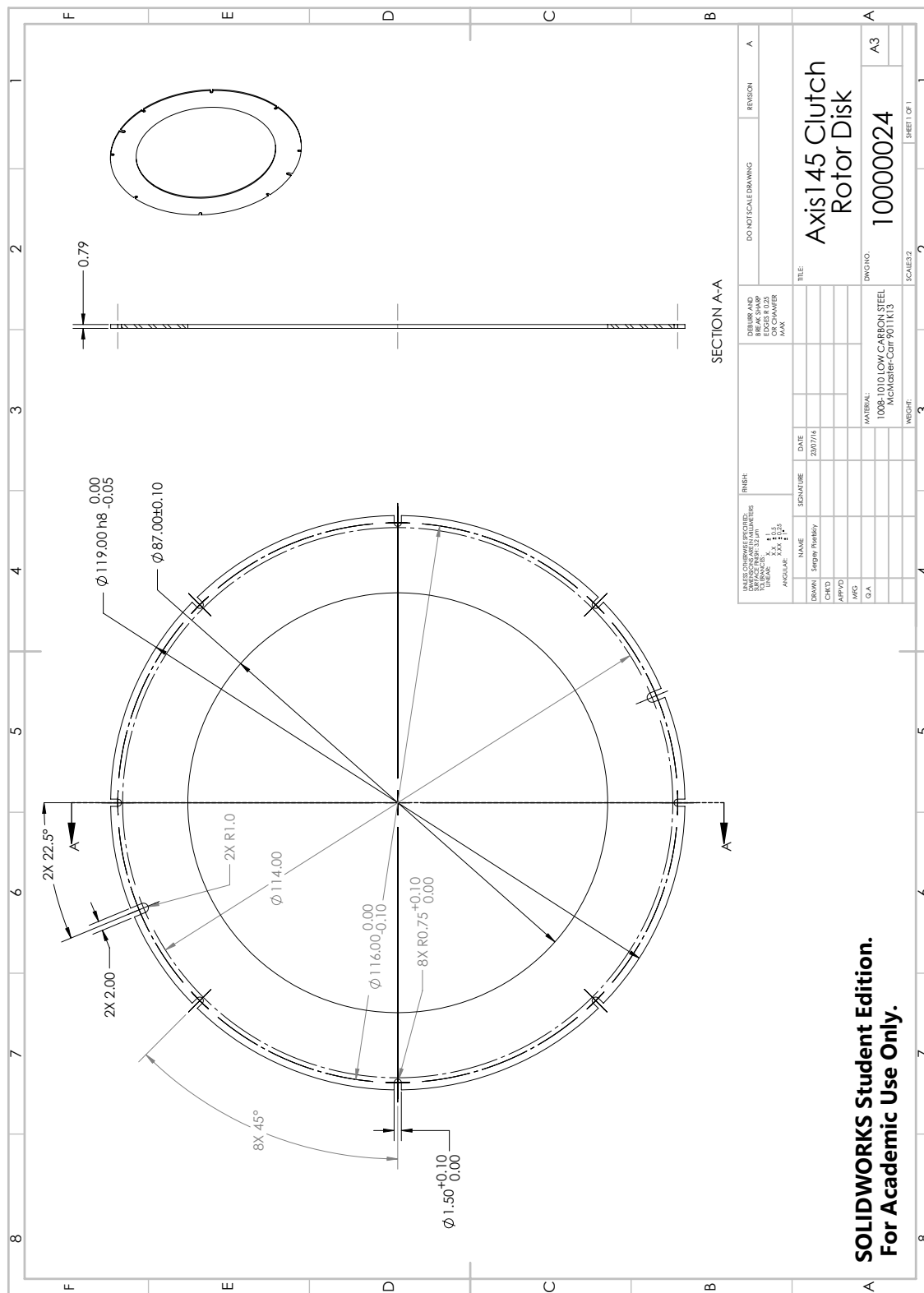
Figure B.26: Drawing: Joint 1, 4, 5 clutch rotor disk.

Figure B.27: Drawing: Joint 1, 4, 5 clutch rotor spacer.

Figure B.28: Drawing: Joint 2 clutch stator disk.
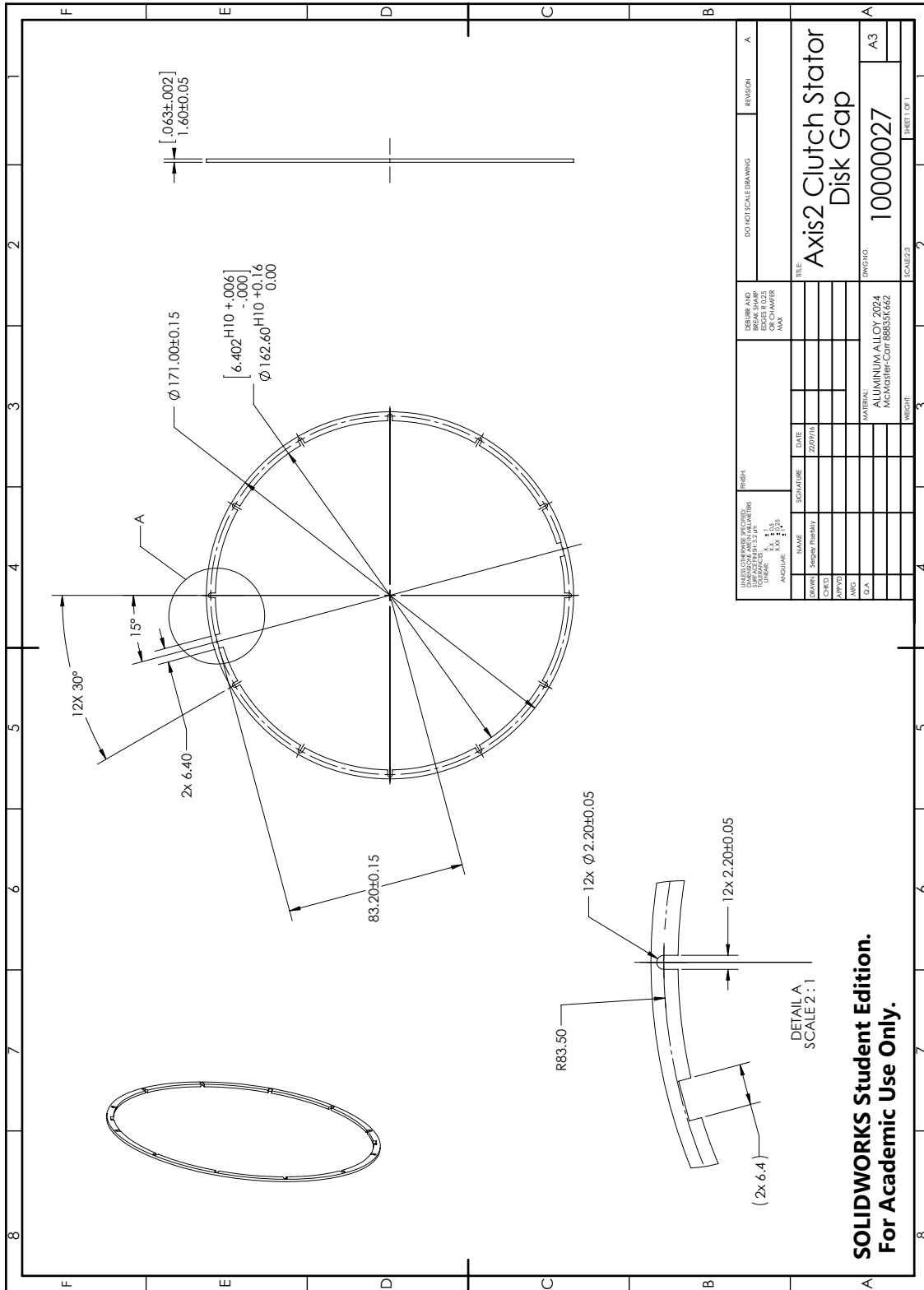
Figure B.29: Drawing: Joint 2 clutch stator spacer.

Figure B.30: Drawing: Joint 2 clutch stator sensor spacer.
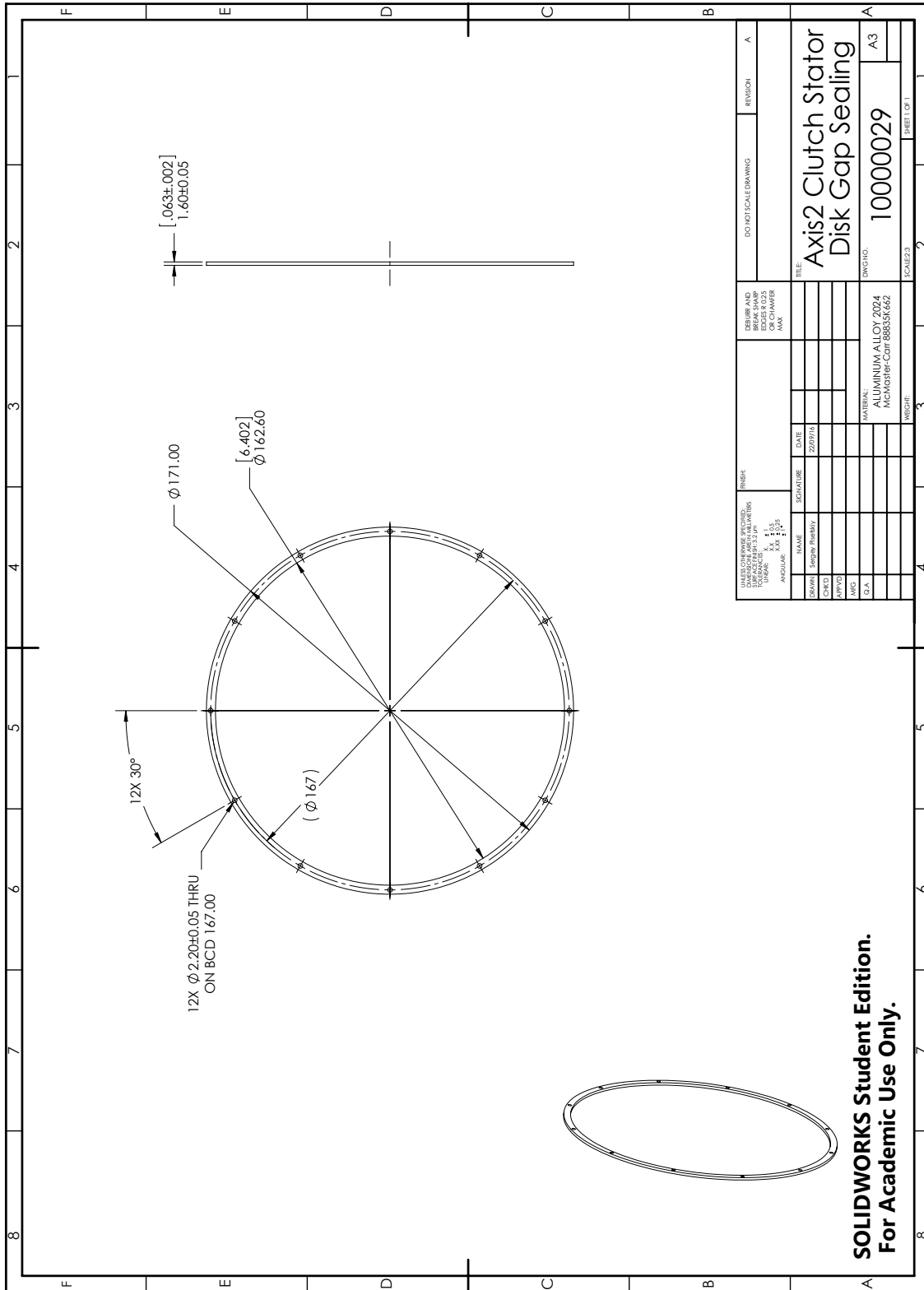
Figure B.31: Drawing: Joint 2 clutch stator sealing spacer.

Figure B.32: Drawing: Joint 2 clutch rotor disk.
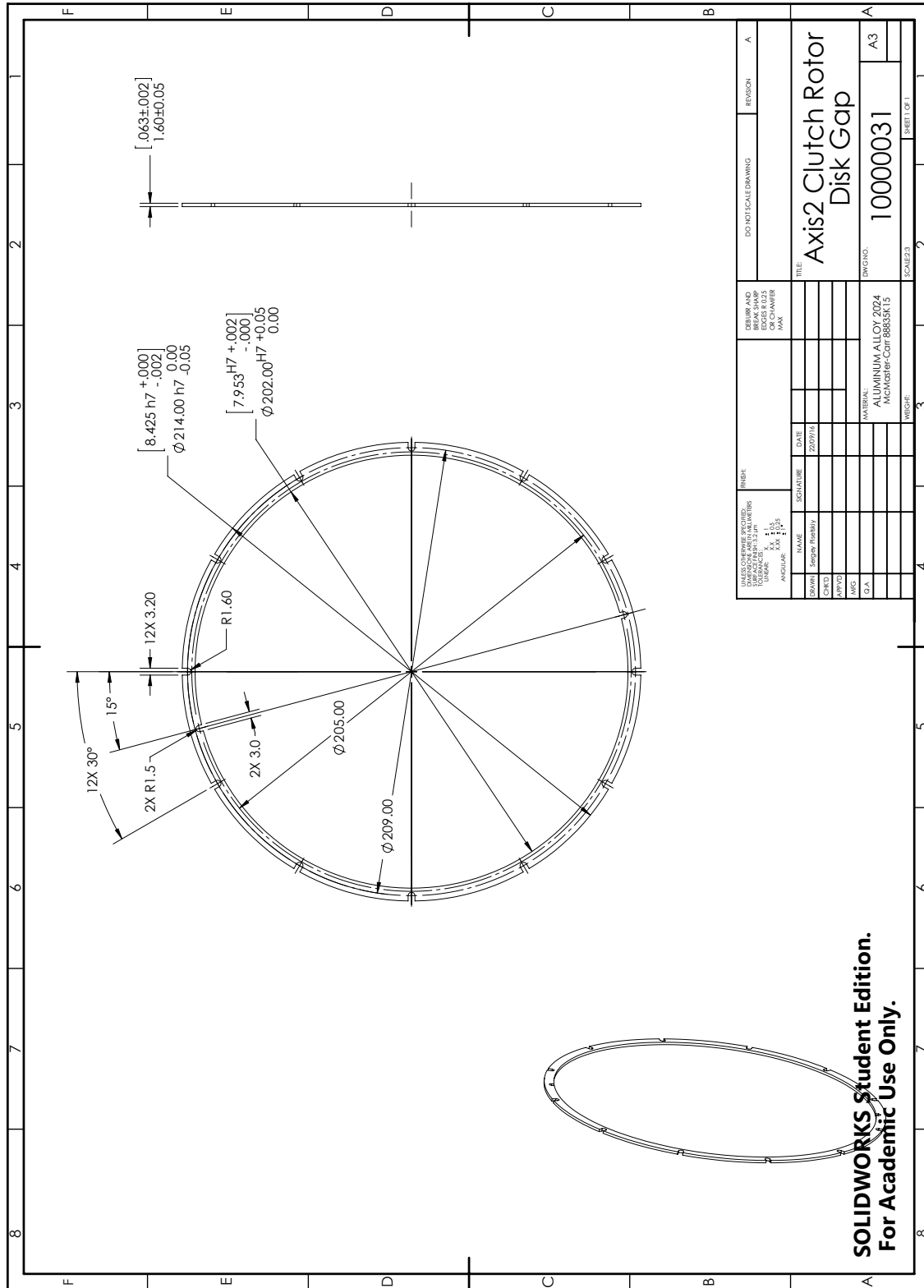
Figure B.33: Drawing: Joint 2 clutch rotor spacer.

SECTION A-A

SOLIDWORKS Student Edition.
For Academic Use Only.
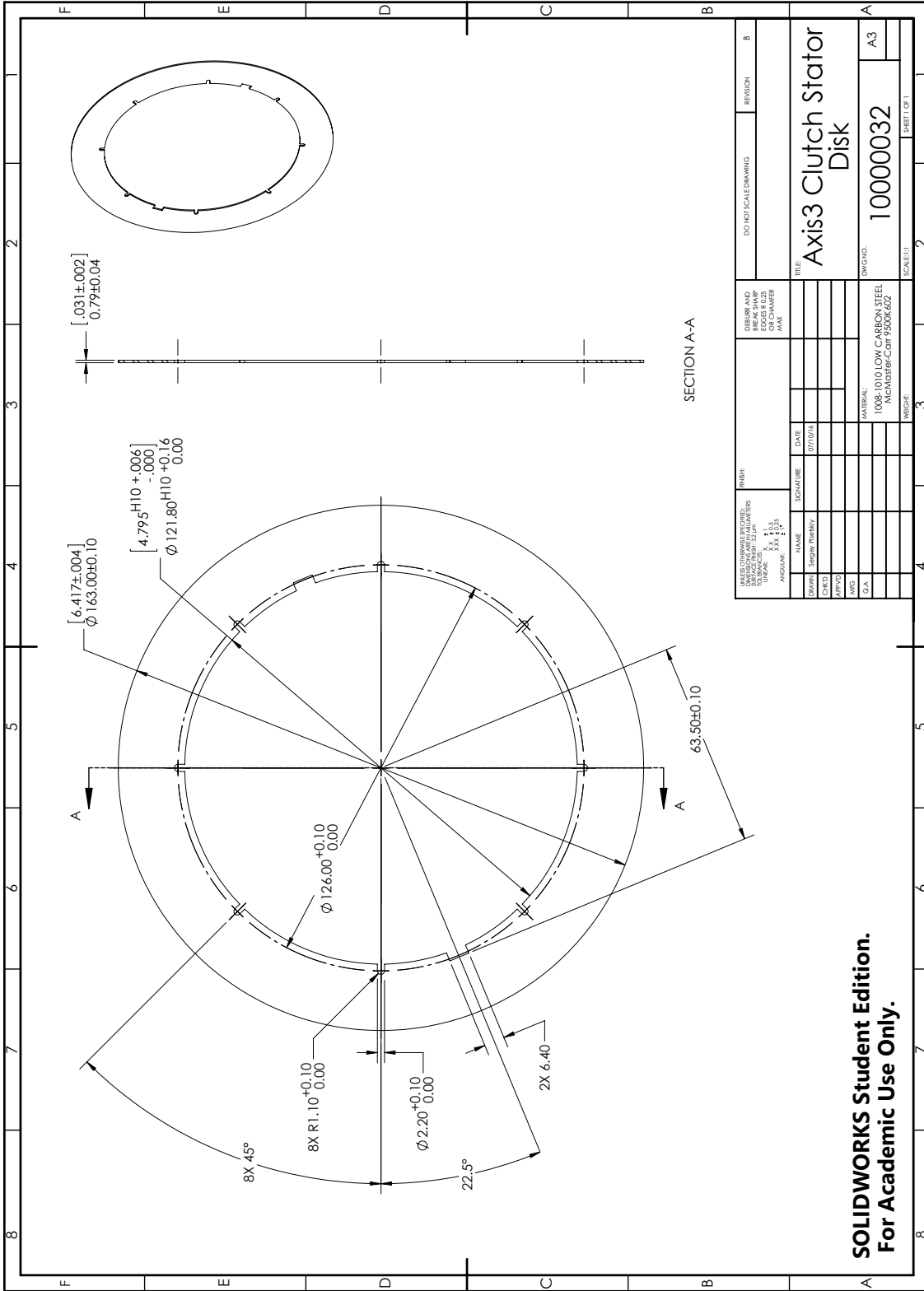
Figure B.34: Drawing: Joint 3 clutch stator disk.
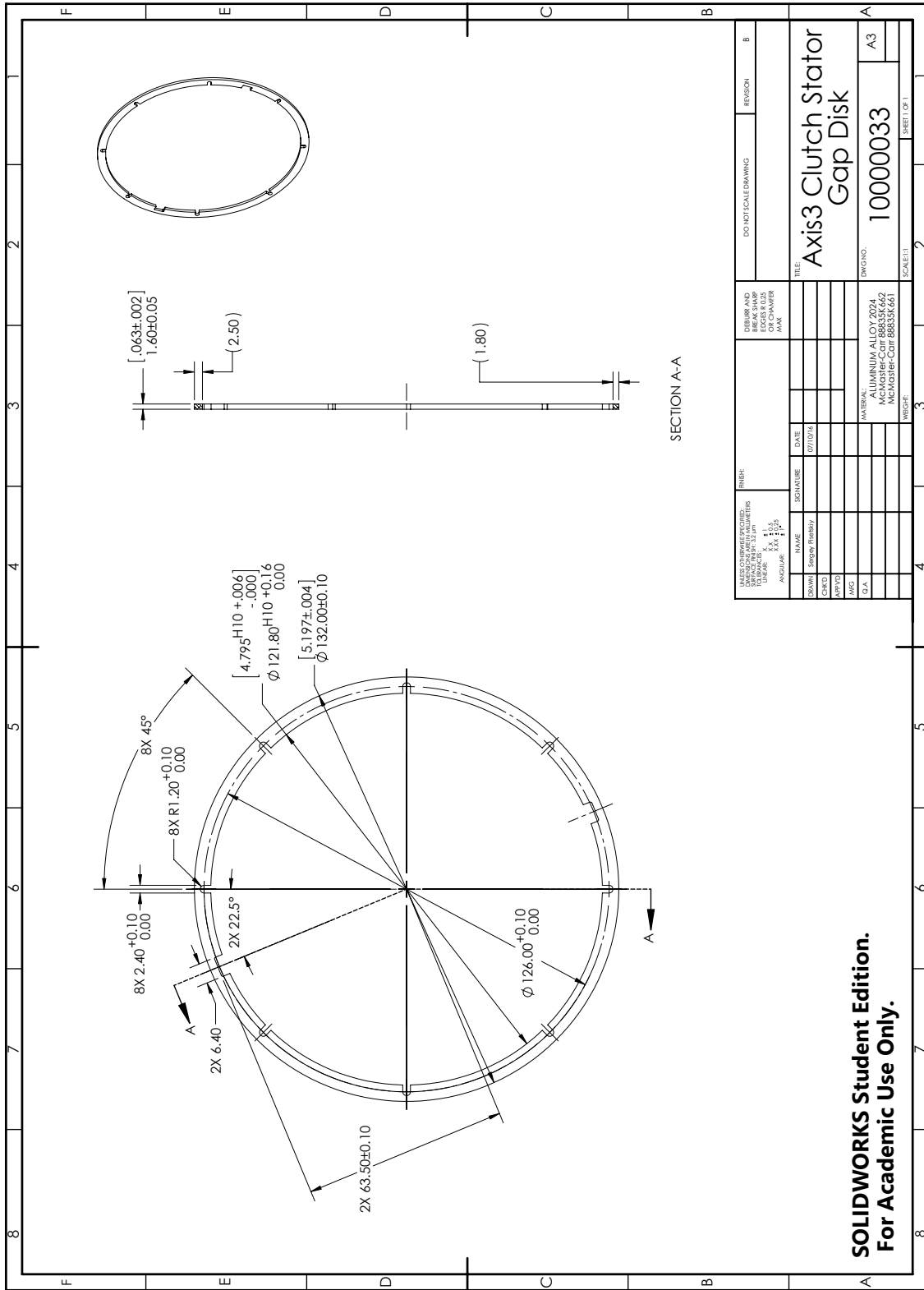
Figure B.35: Drawing: Joint 3 clutch stator spacer.

Figure B.36: Drawing: Joint 3 clutch stator sensor spacer.
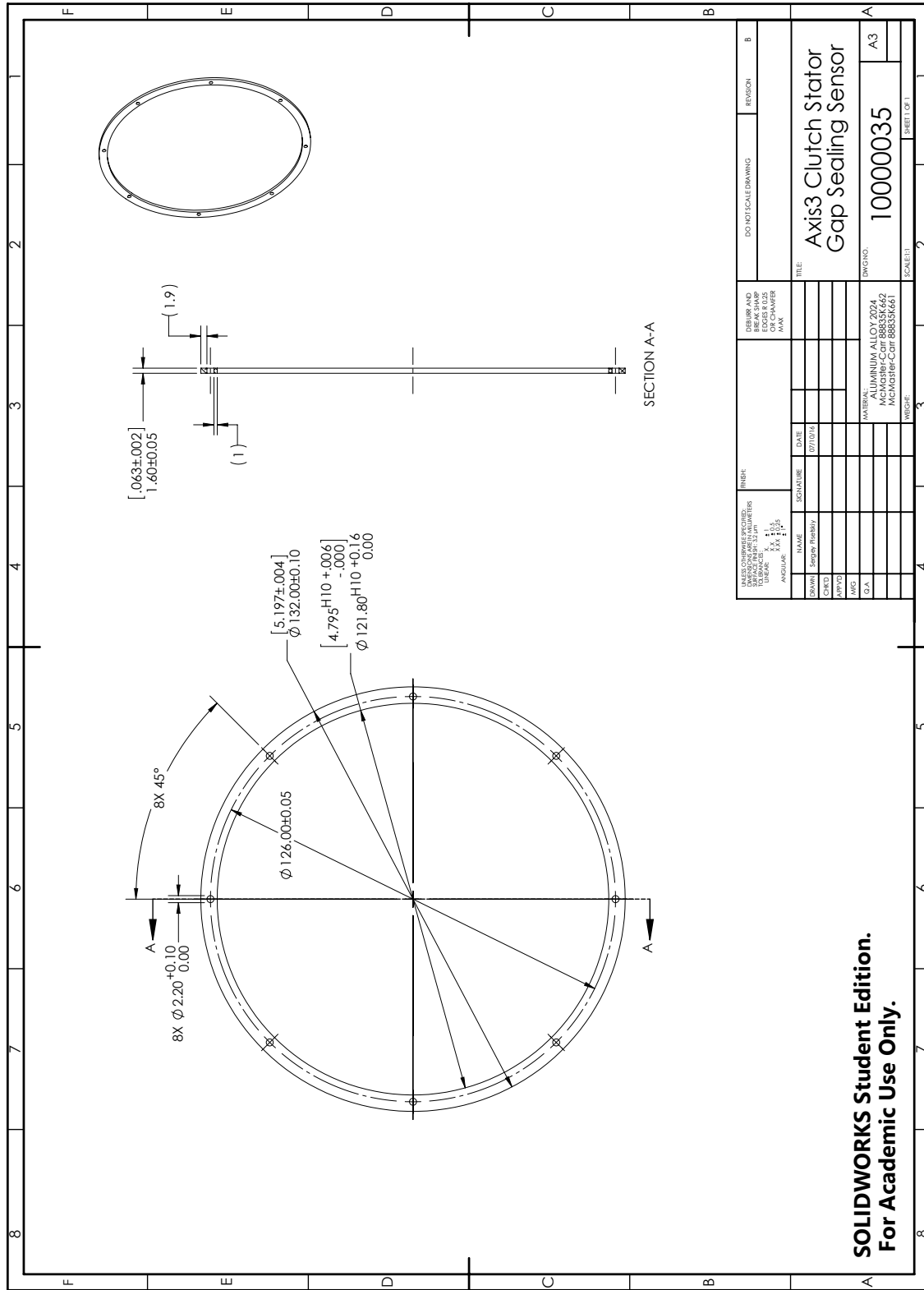
Figure B.37: Drawing: Joint 3 clutch stator sealing spacer.

Figure B.38: Drawing: Joint 3 clutch rotor disk.
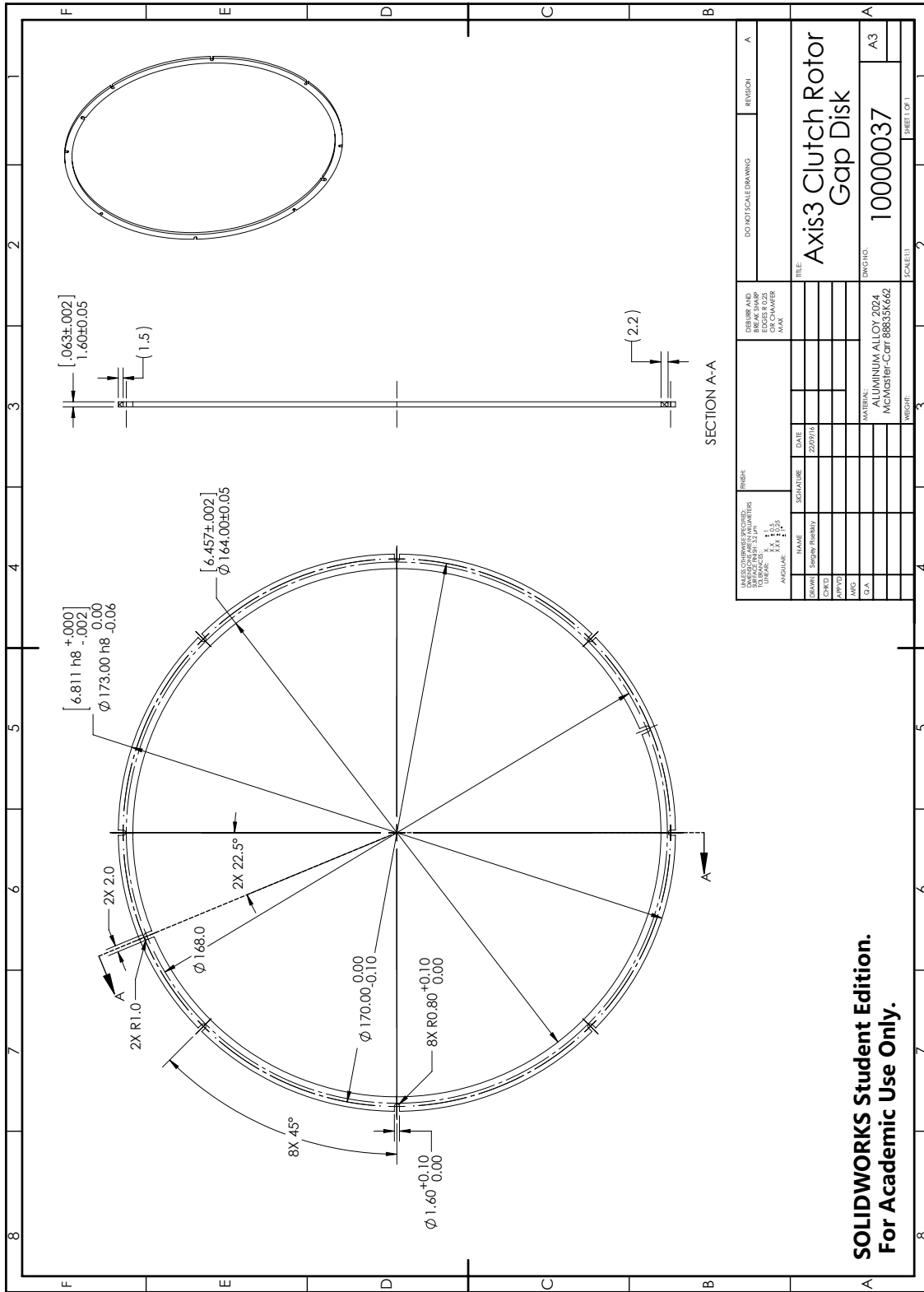
Figure B.39: Drawing: Joint 3 clutch rotor spacer.

Figure B.40: Drawing: Joint 1, 4 clutch stator flange.

Figure B.41: Drawing: Joint 1, 4, 5 clutch stator side.
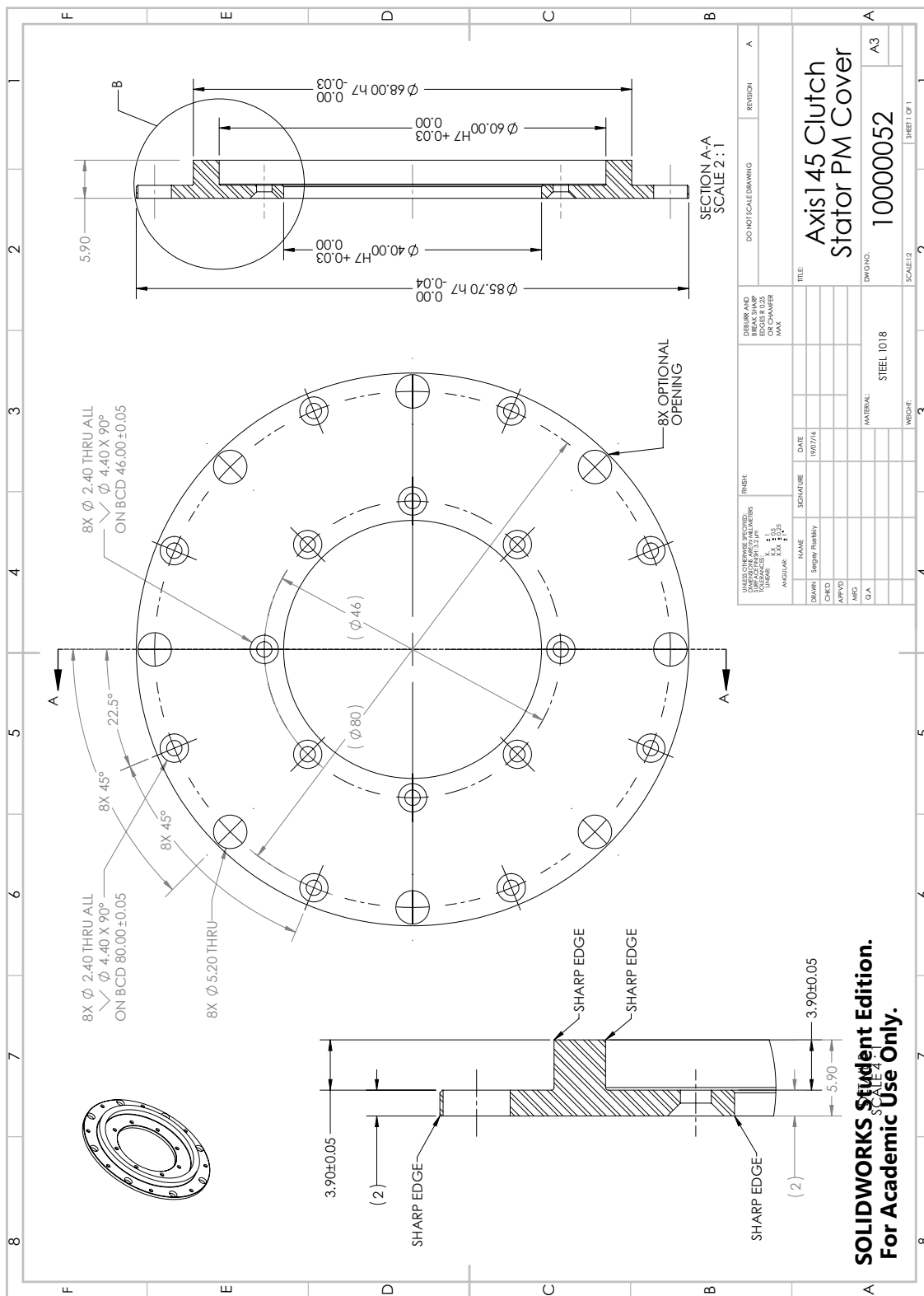
Figure B.42: Drawing: Joint 1, 4, 5 clutch stator permanent magnet cover.
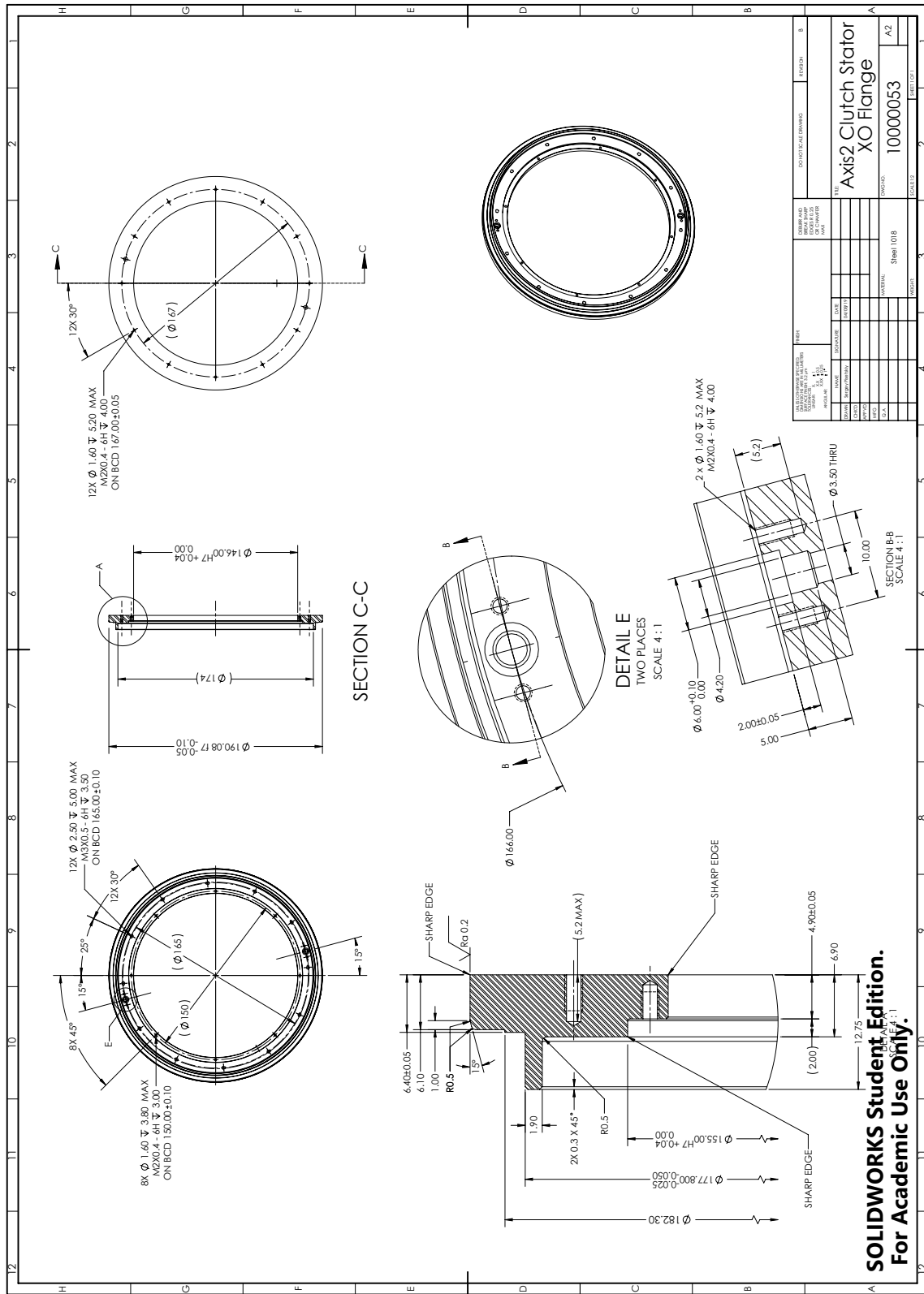
Figure B.43: Drawing: Joint 2 clutch stator flange.

Figure B.44: Drawing: Joint 2 clutch stator side.
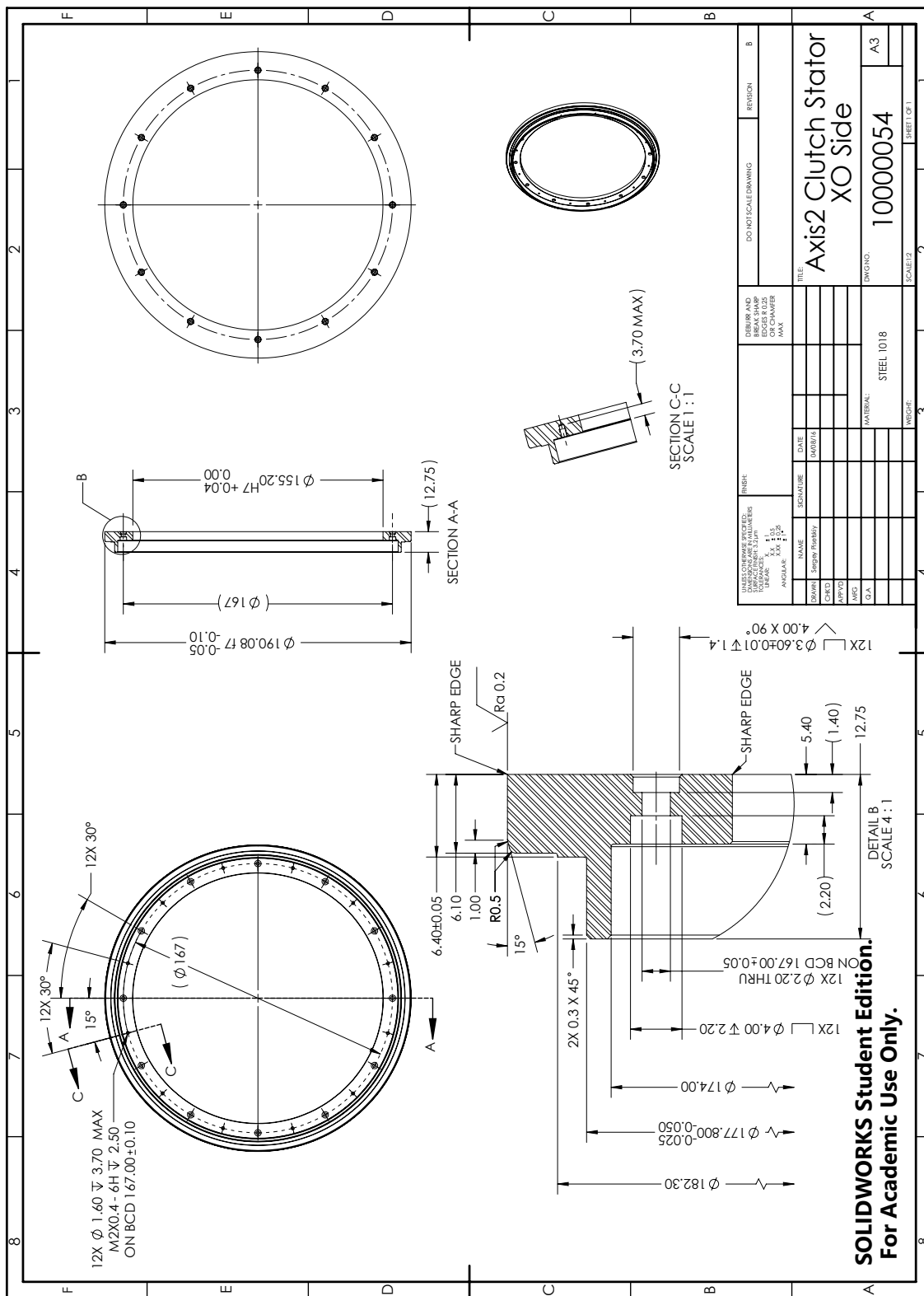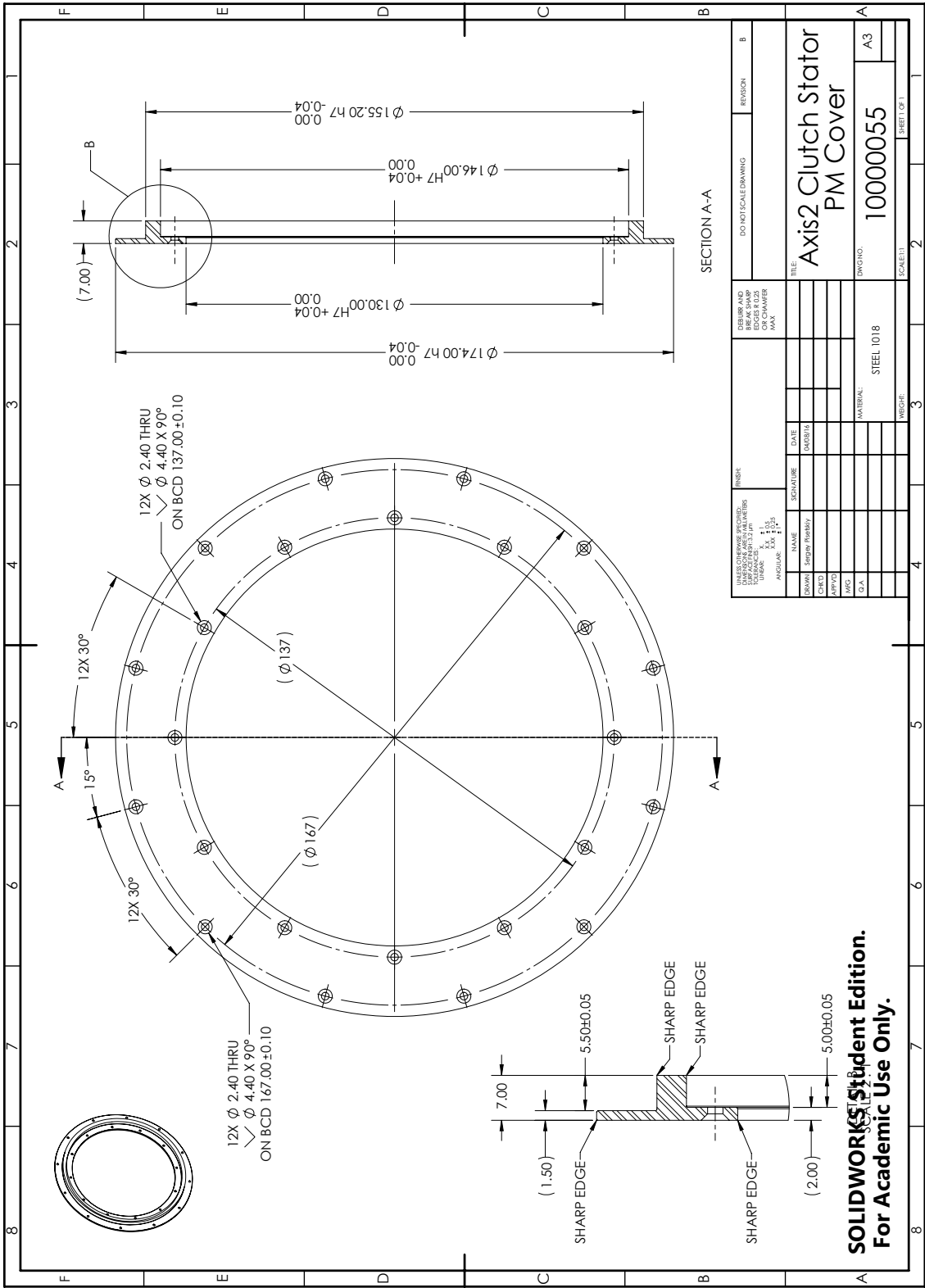
Figure B.45: Drawing: Joint 2 clutch stator permanent magnet cover.
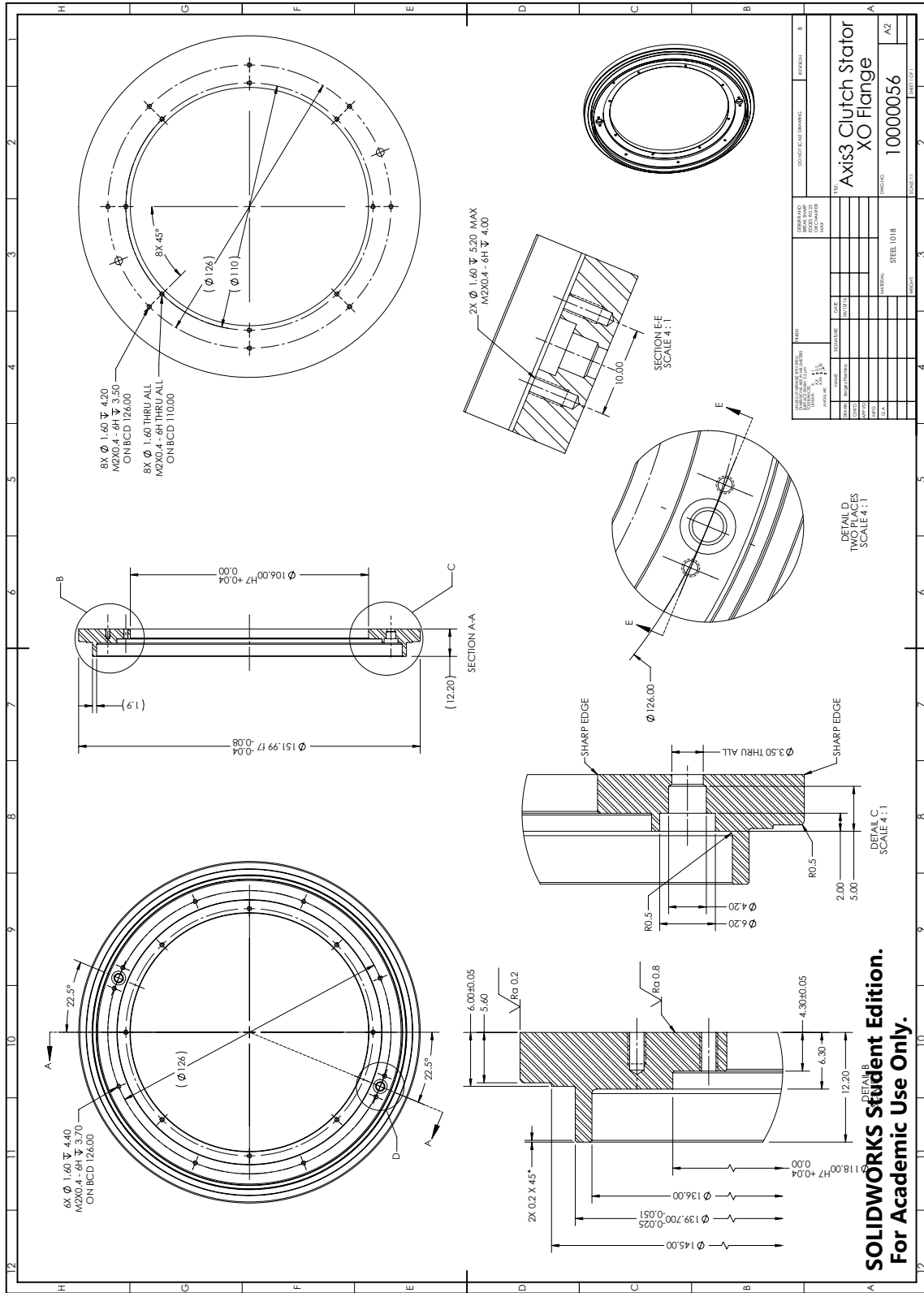
Figure B.46: Drawing: Joint 3 clutch stator flange.

Figure B.47: Drawing: Joint 3 clutch stator side.
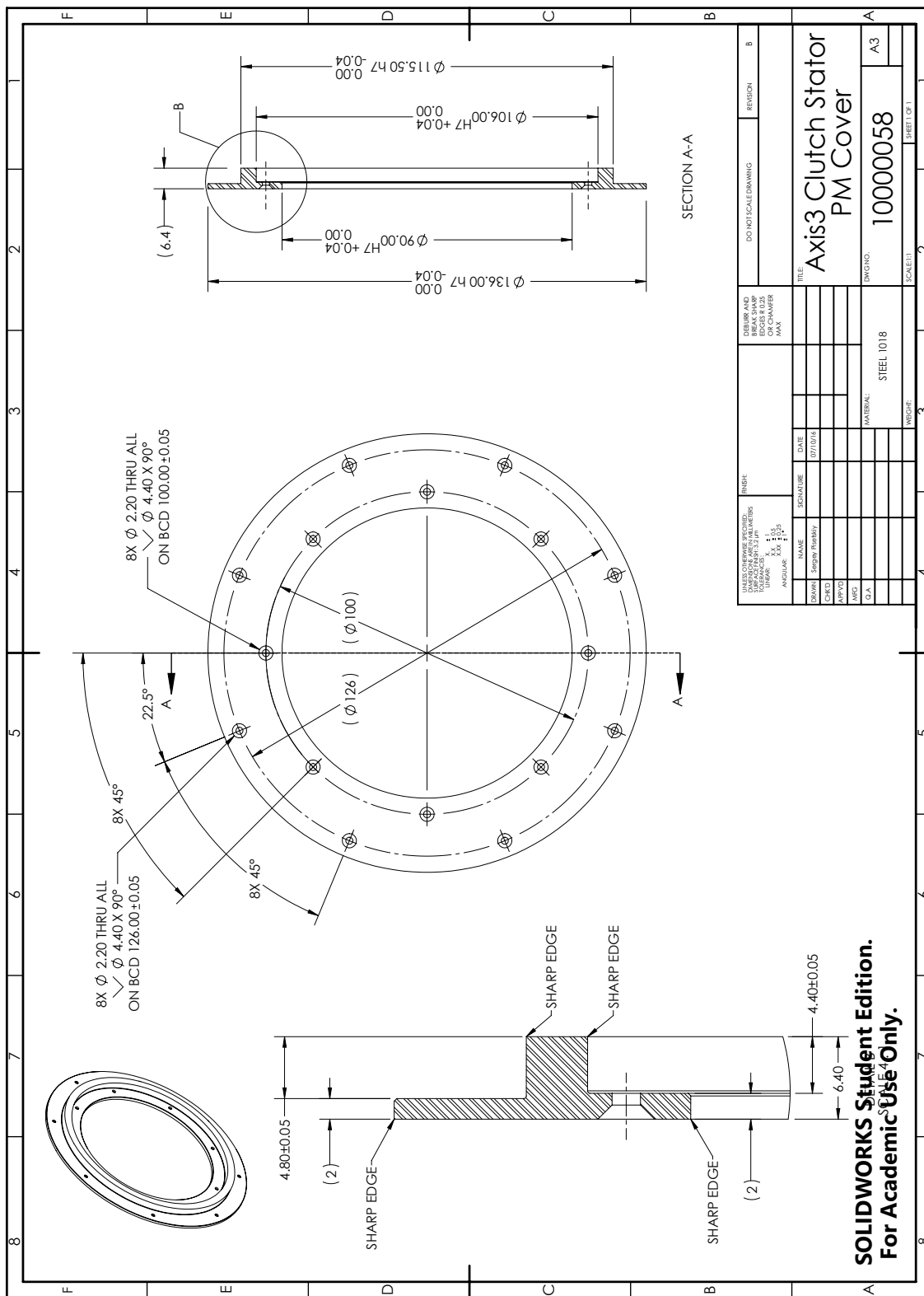
Figure B.48: Drawing: Joint 3 clutch stator permanent magnet cover.

Figure B.49: Drawing: Joint 5 clutch stator flange.

Figure B.50: Drawing: Joint 3 clutch stator side.
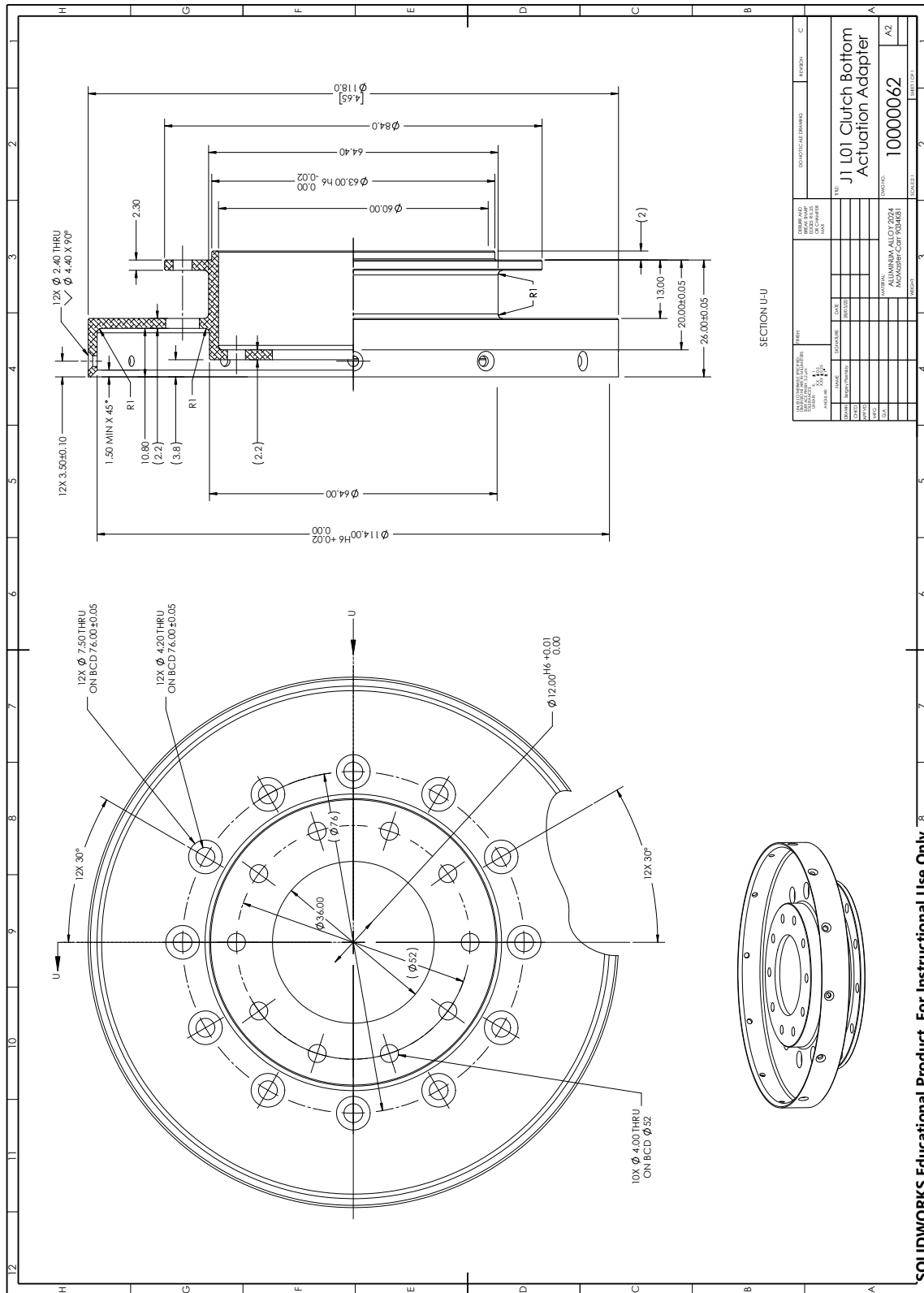
Figure B.51: Drawing: Joint 1 bottom clutch actuation adapter.

Figure B.52: Drawing: Joint 1 top clutch actuation adapter.
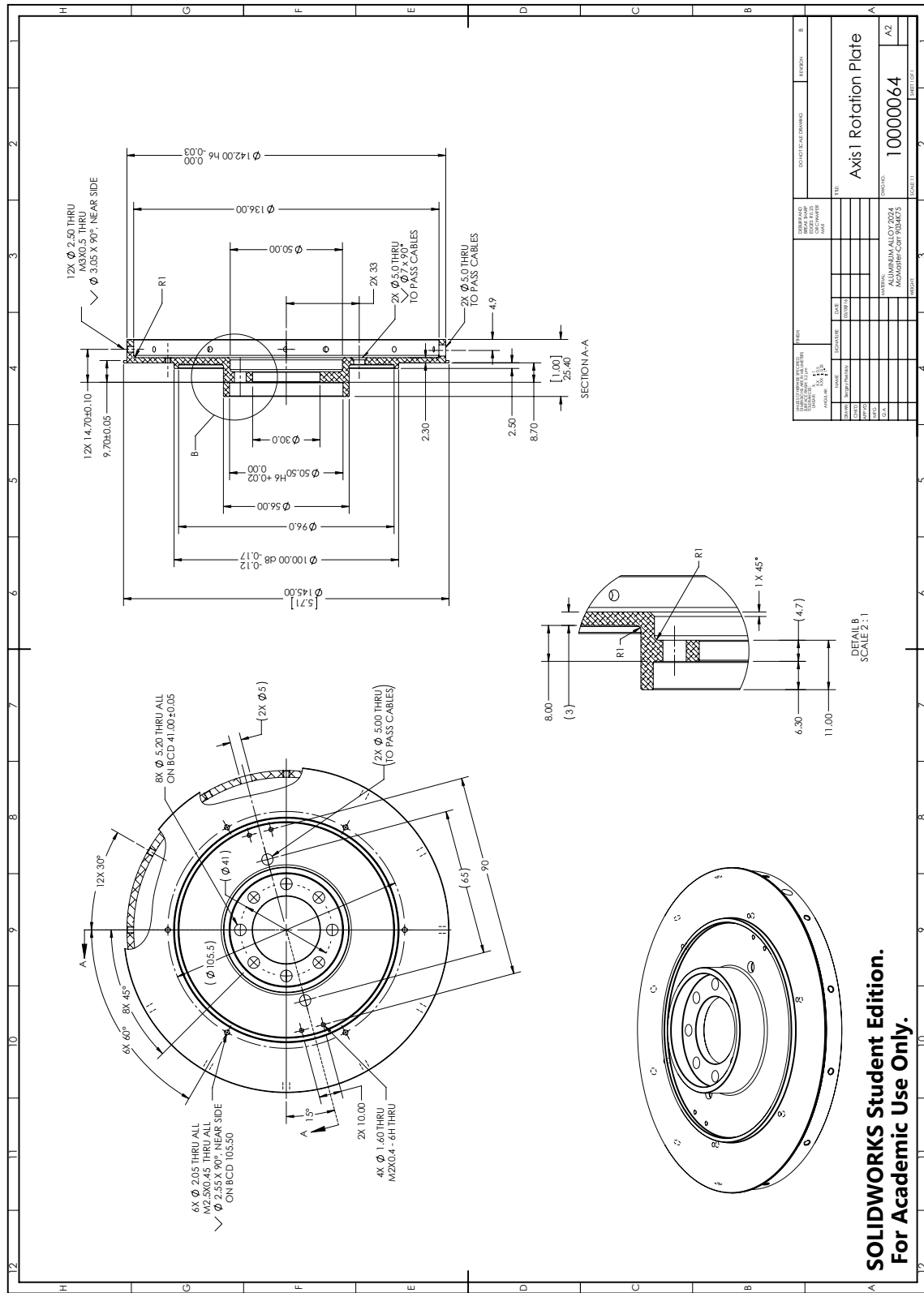
Figure B.53: Drawing: Joint 1 rotation plate.
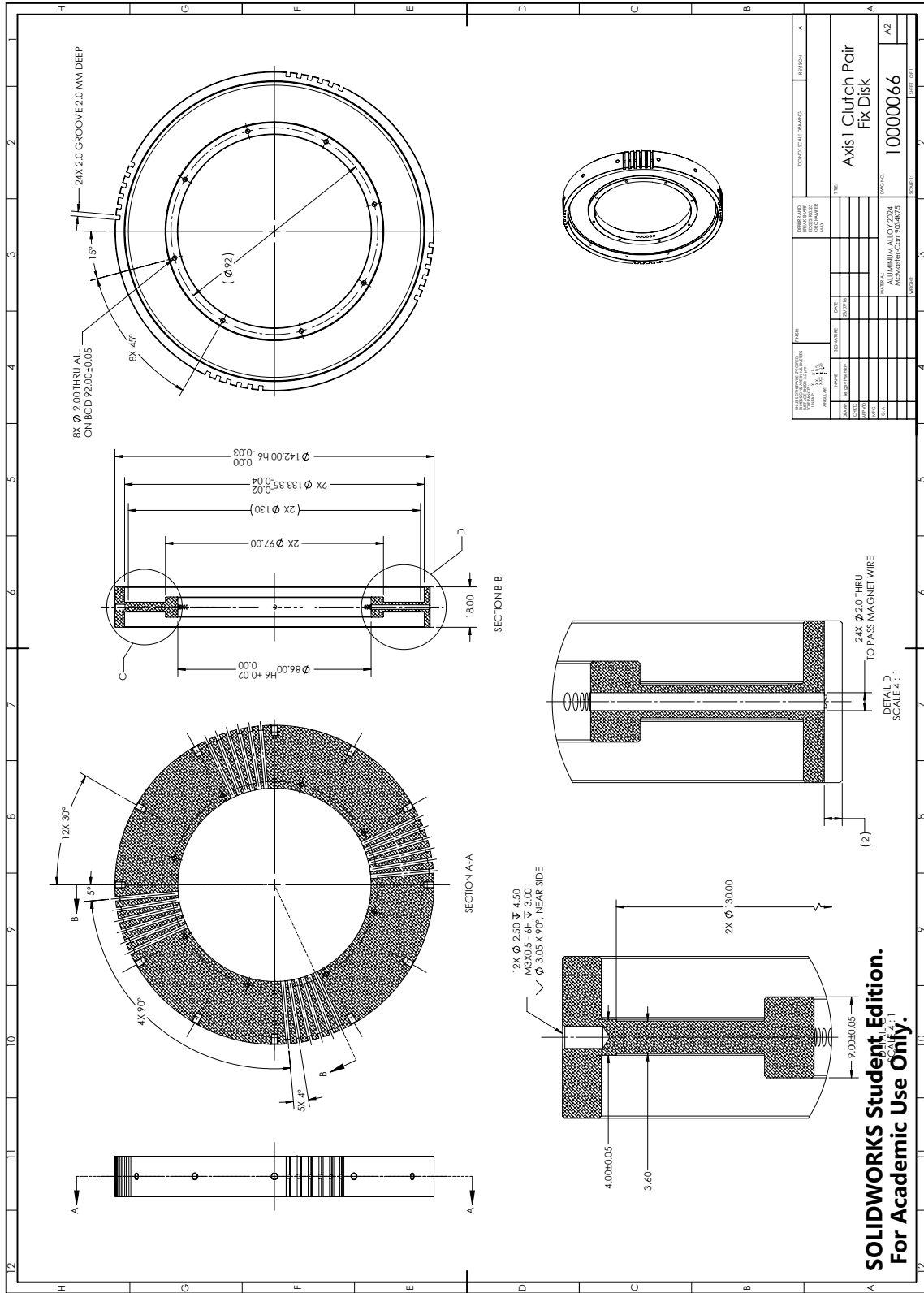
Figure B.54: Drawing: Joint 1, 4 clutch pair central frame.
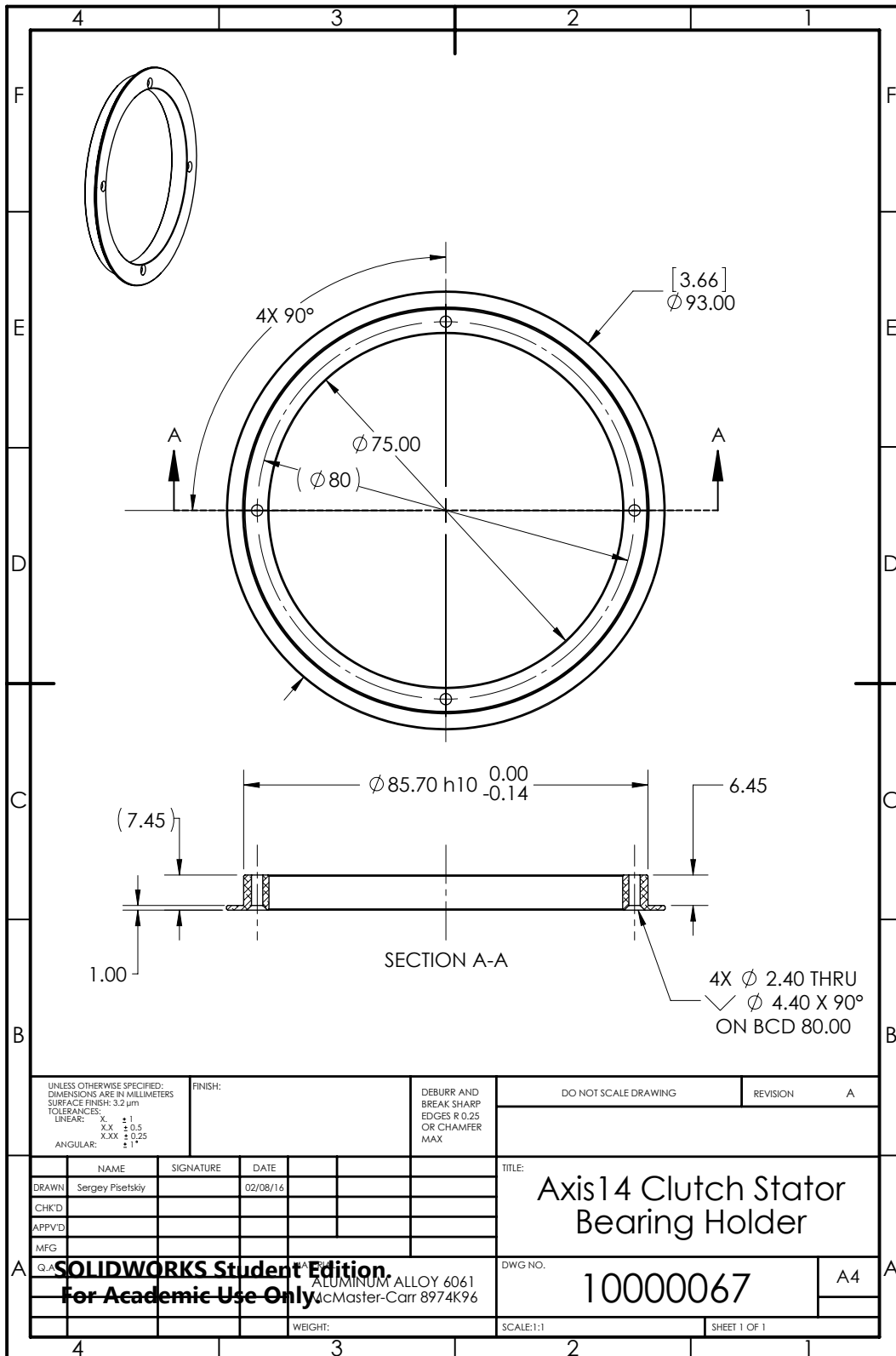
Figure B.55: Drawing: Joint 1, 4 clutch stator bearing holder.
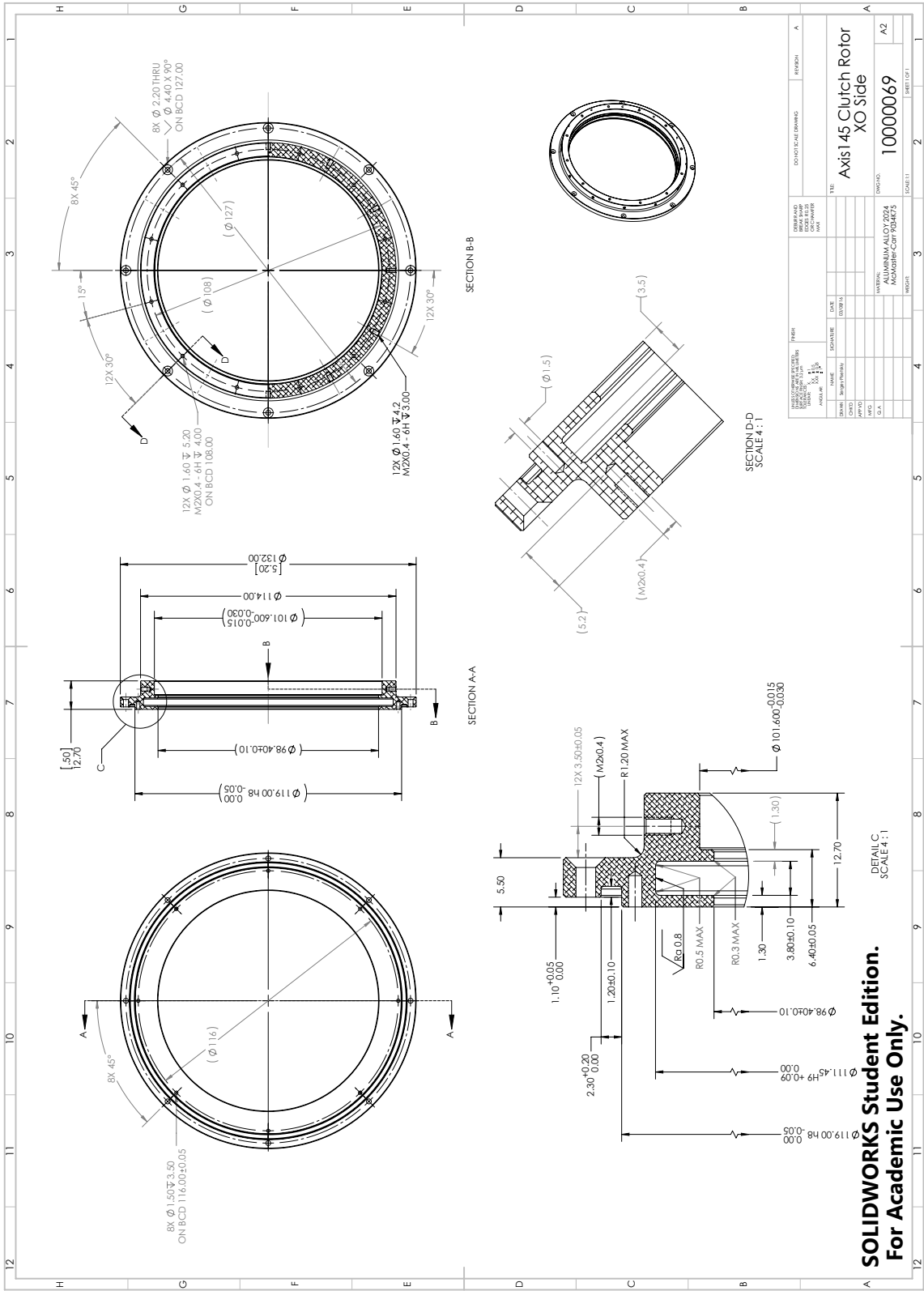
Figure B.56: Drawing: Joint 1, 4, 5 clutch rotor side.
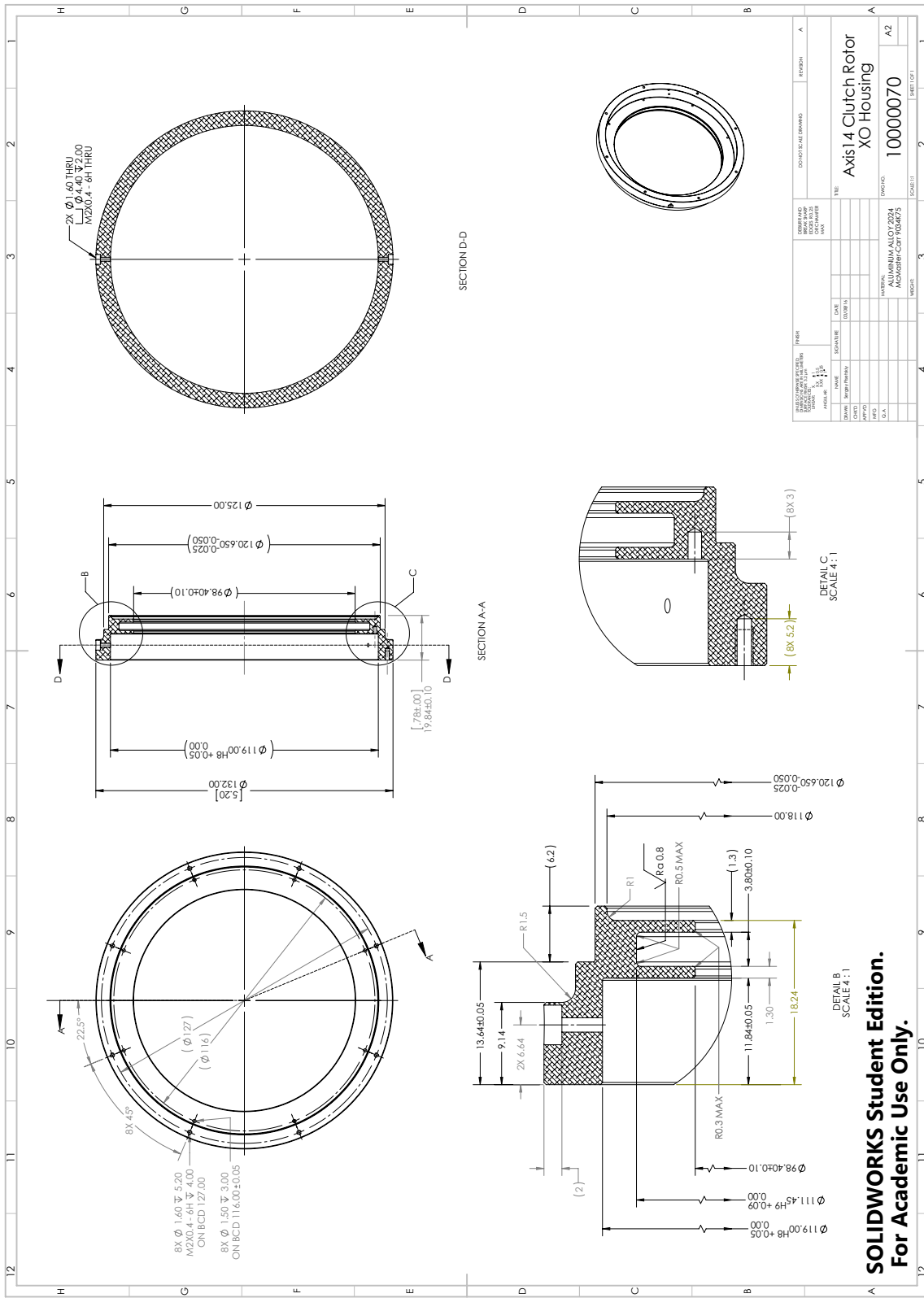
Figure B.57: Drawing: Joint 1, 4 clutch rotor housing.
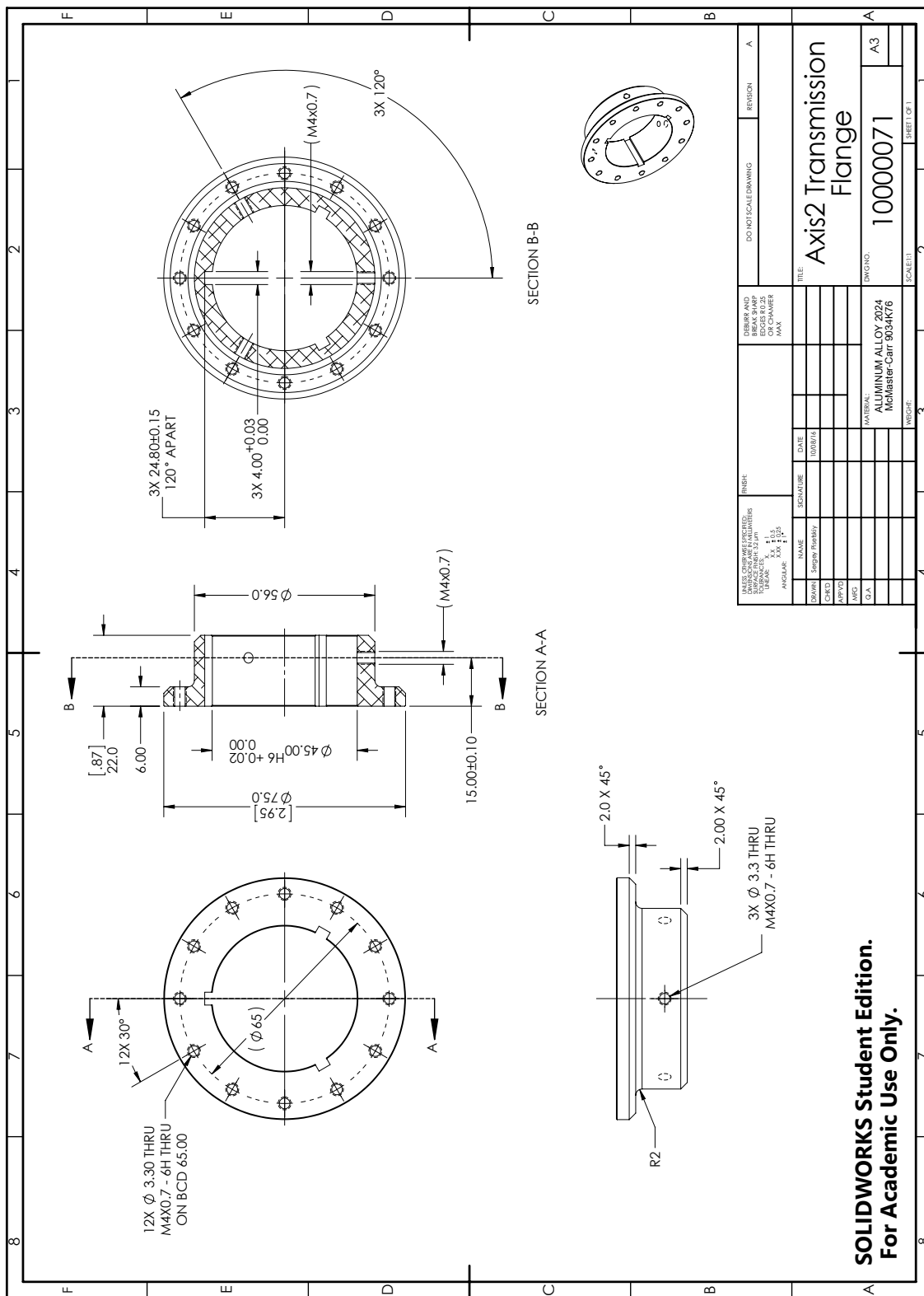
Figure B.58: Drawing: Joint 2 transmission flange.
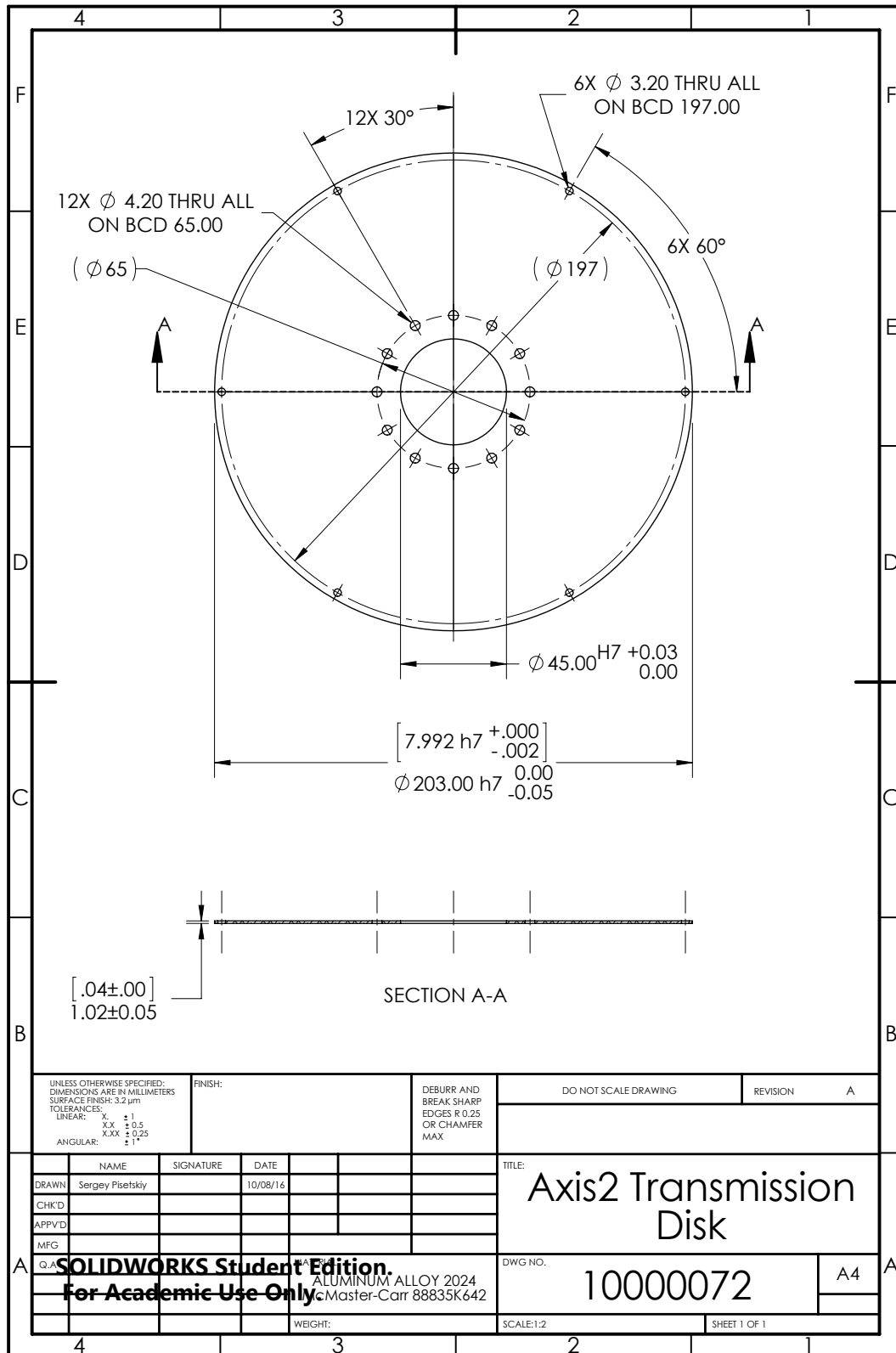
Figure B.59: Drawing: Joint 2 transmission disk.
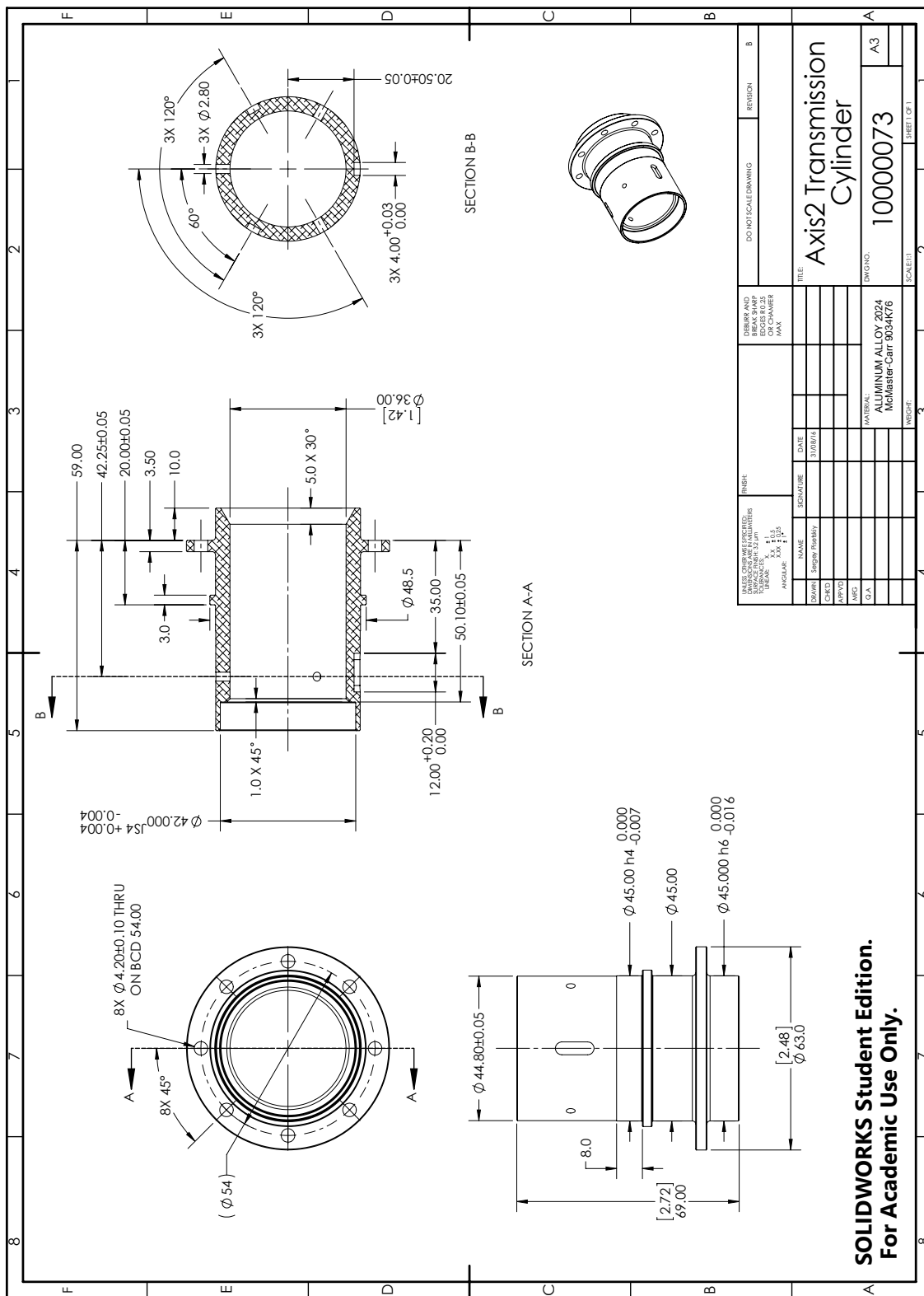
Figure B.60: Drawing: Joint 2 transmission cylinder.
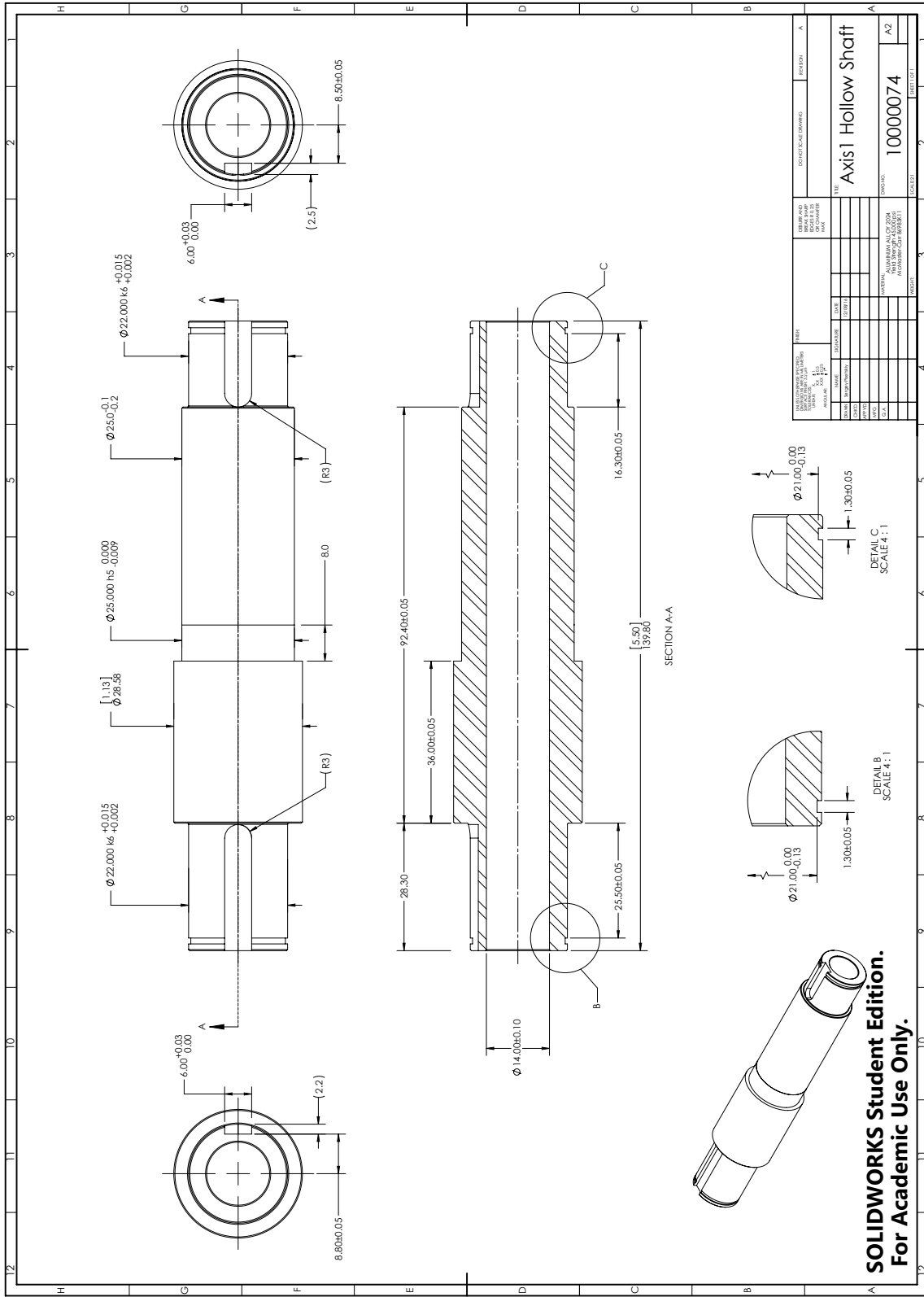
Figure B.61: Drawing: Joint 2 hollow shaft.
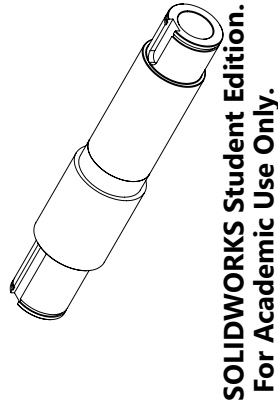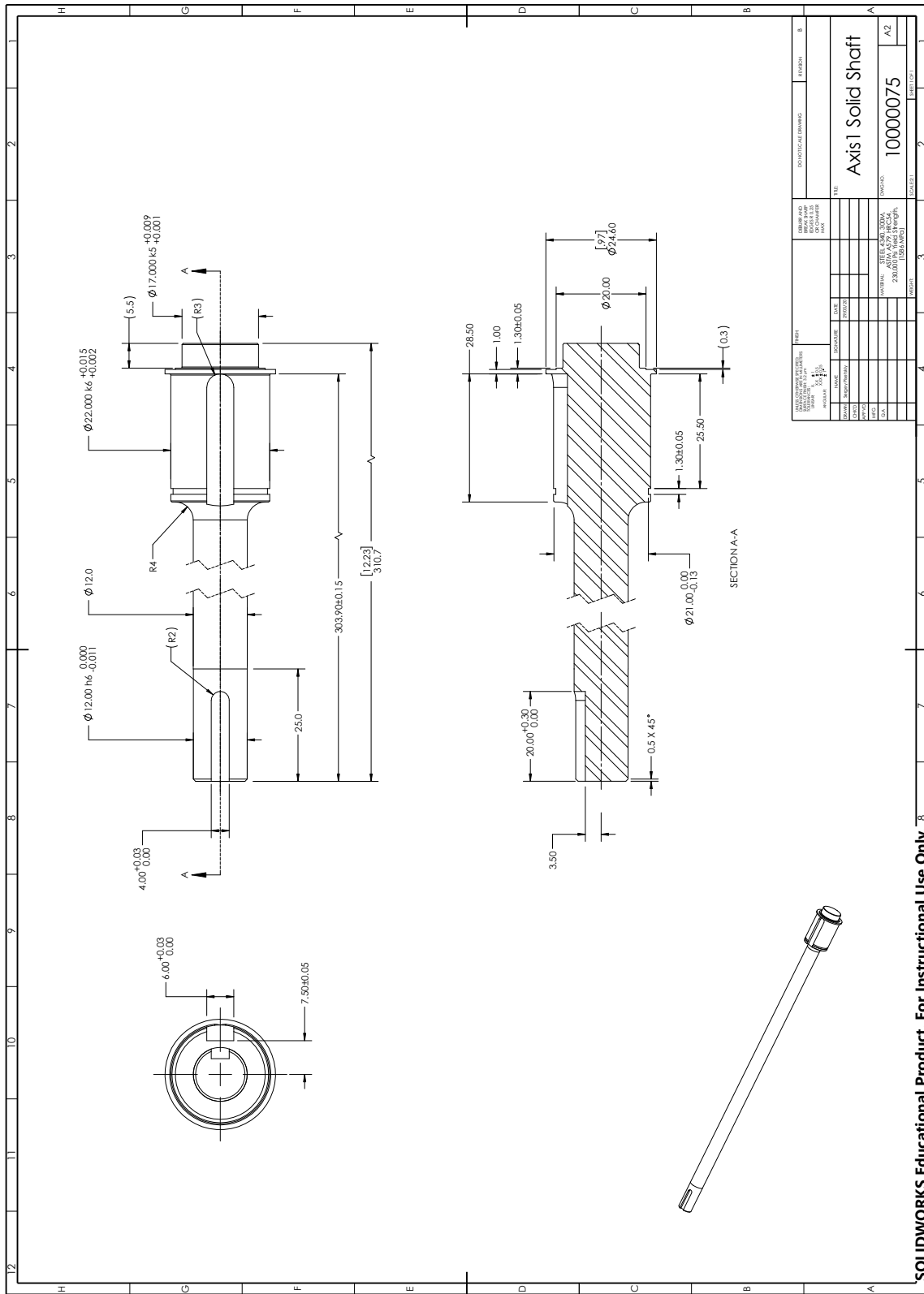
Figure B.62: Drawing: Joint 2 solid shaft.
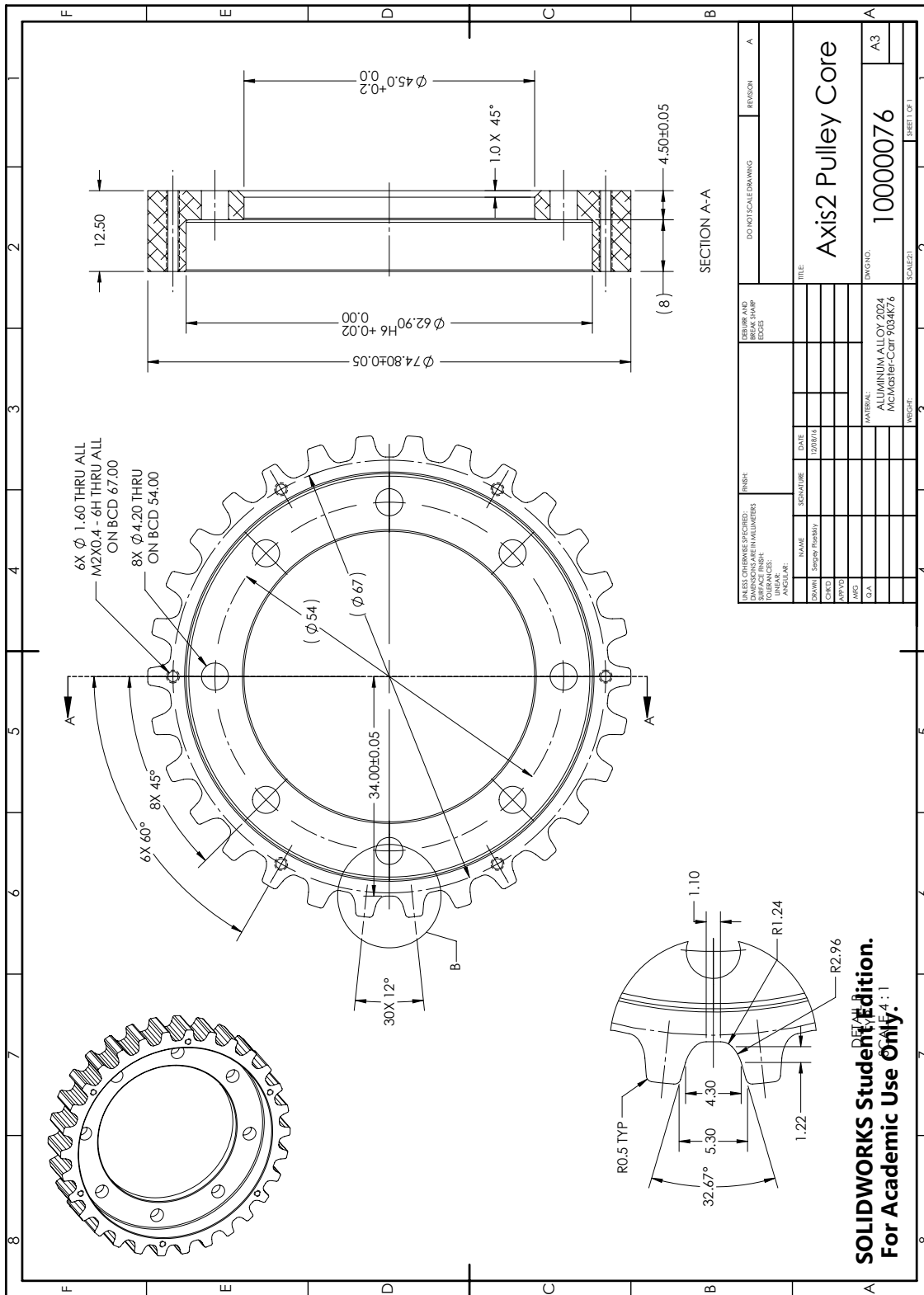
Figure B.63: Drawing: Joint 2 timing belt pulley core.
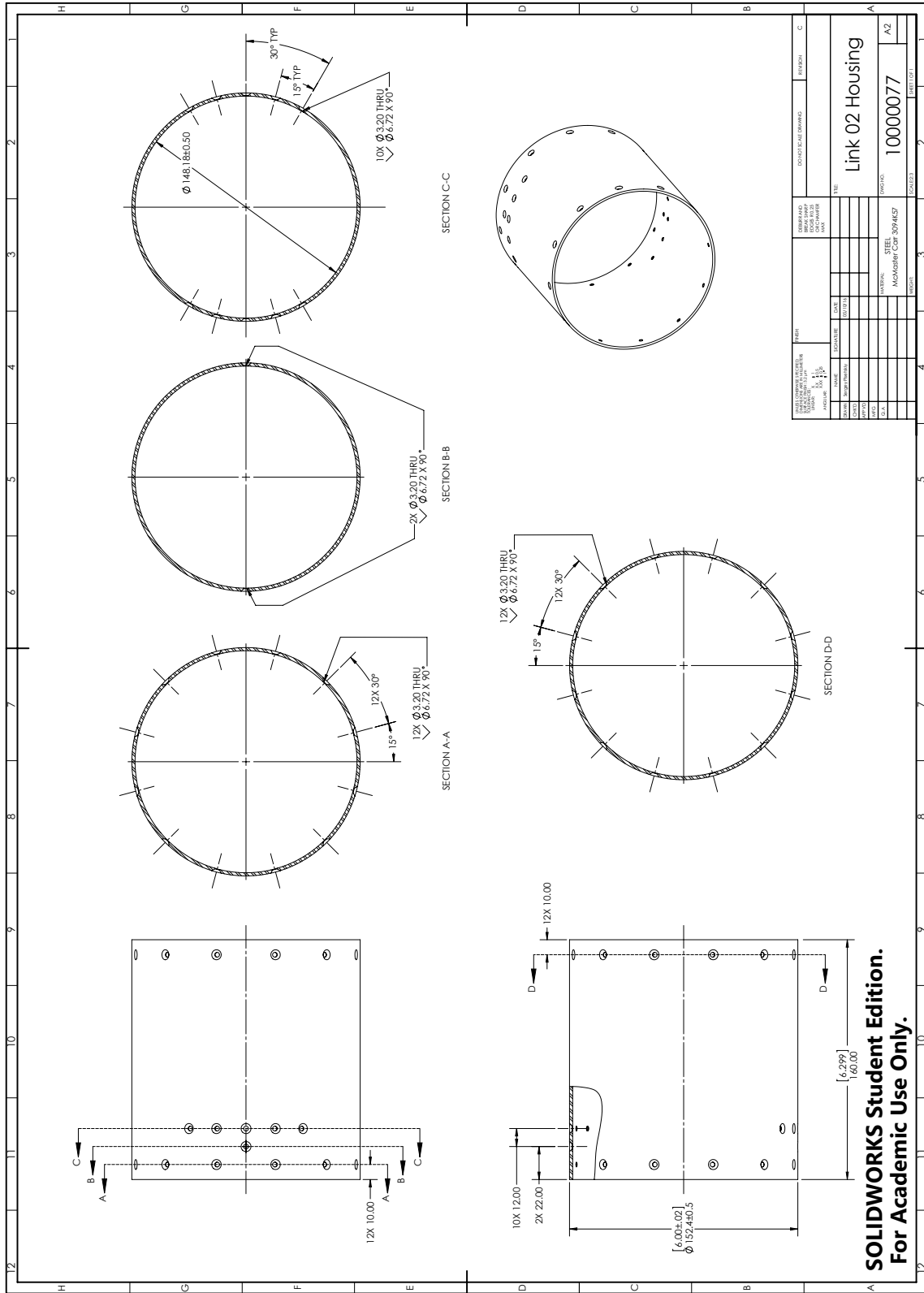
Figure B.64: Drawing: Link 2 housing.
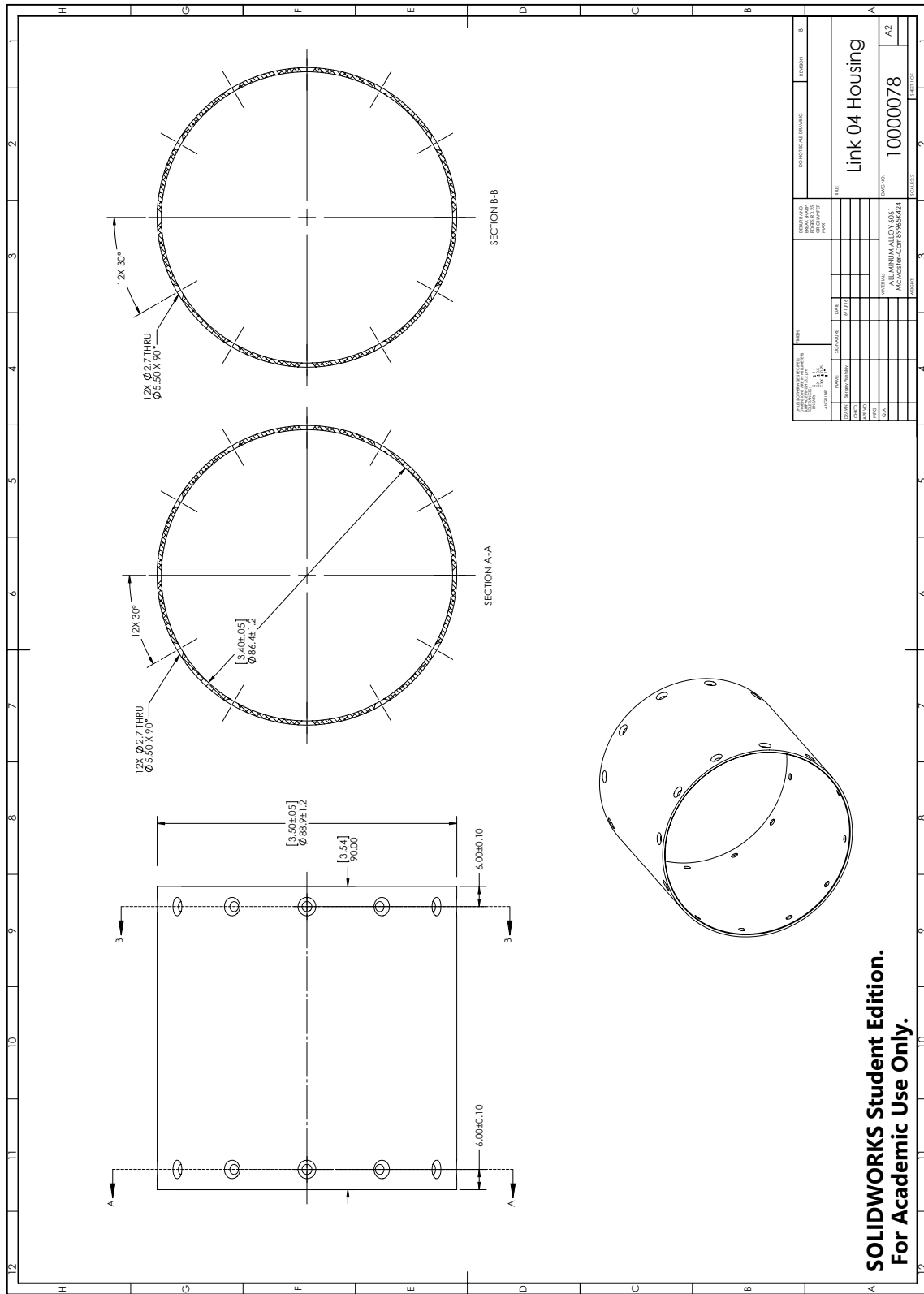
Figure B.65: Drawing: Link 4 housing.

Figure B.66: Drawing: Link 5 housing.
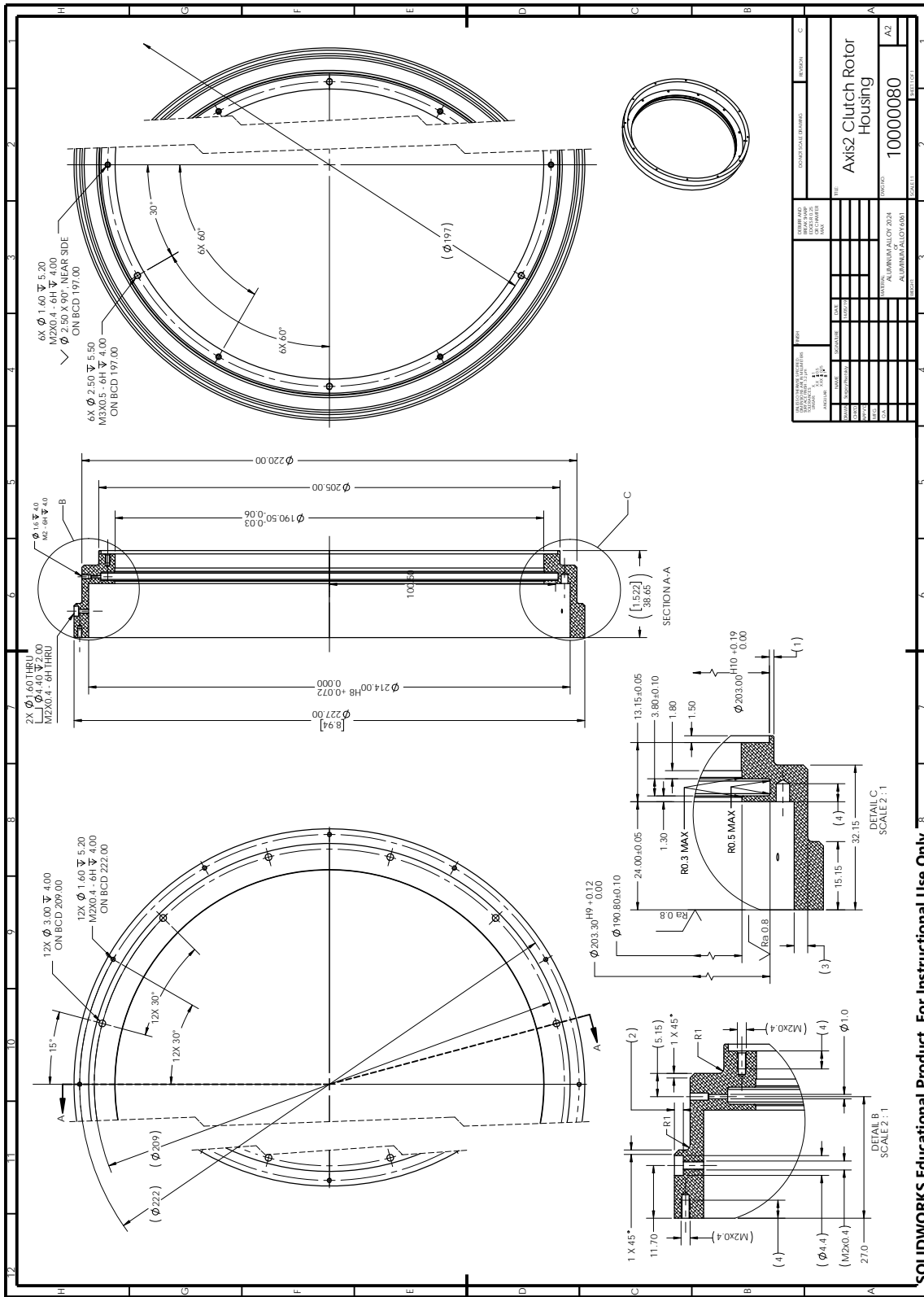
Figure B.67: Drawing: Join 2 clutch rotor housing.
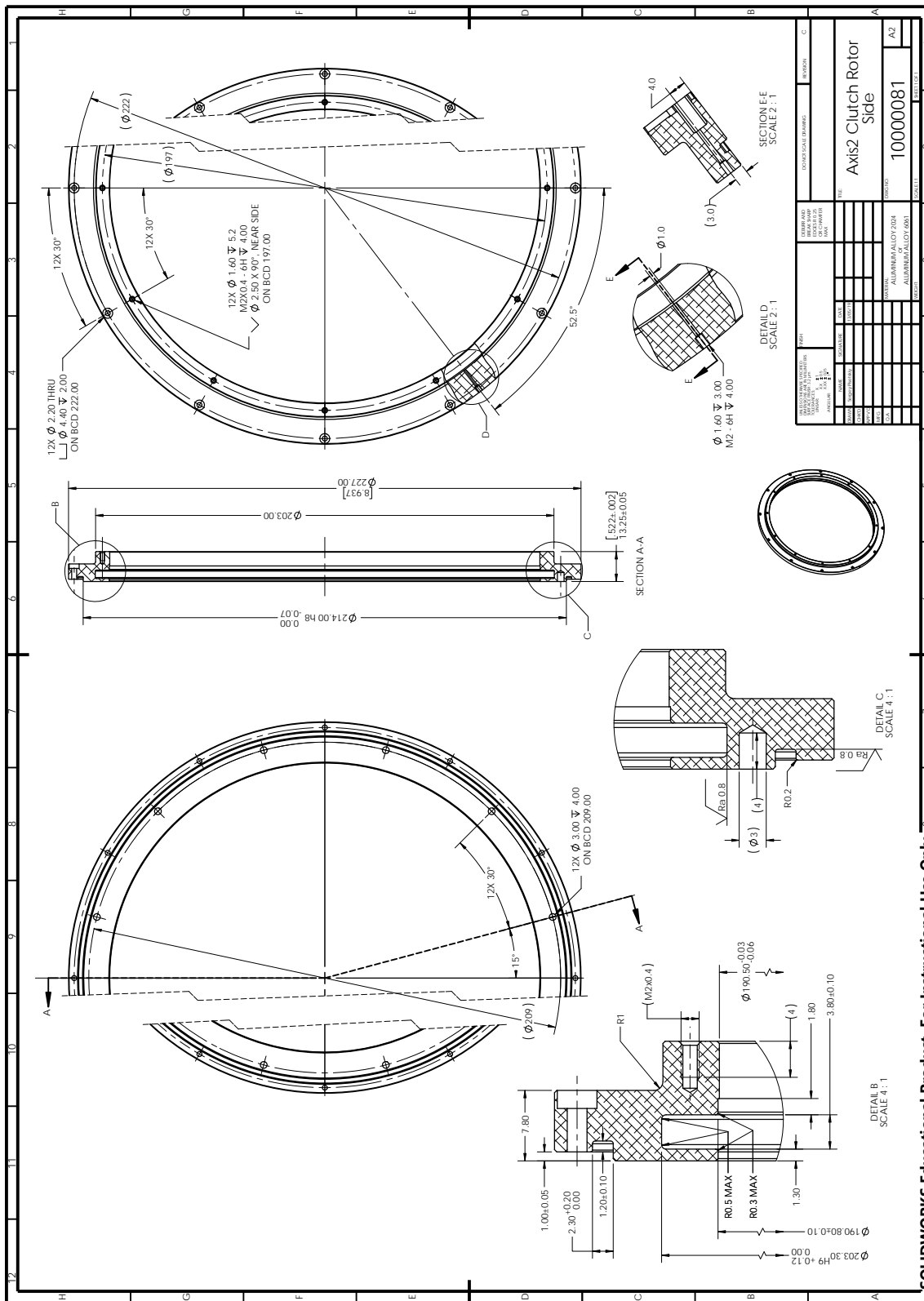
Figure B.68: Drawing: Join 2 clutch rotor side.
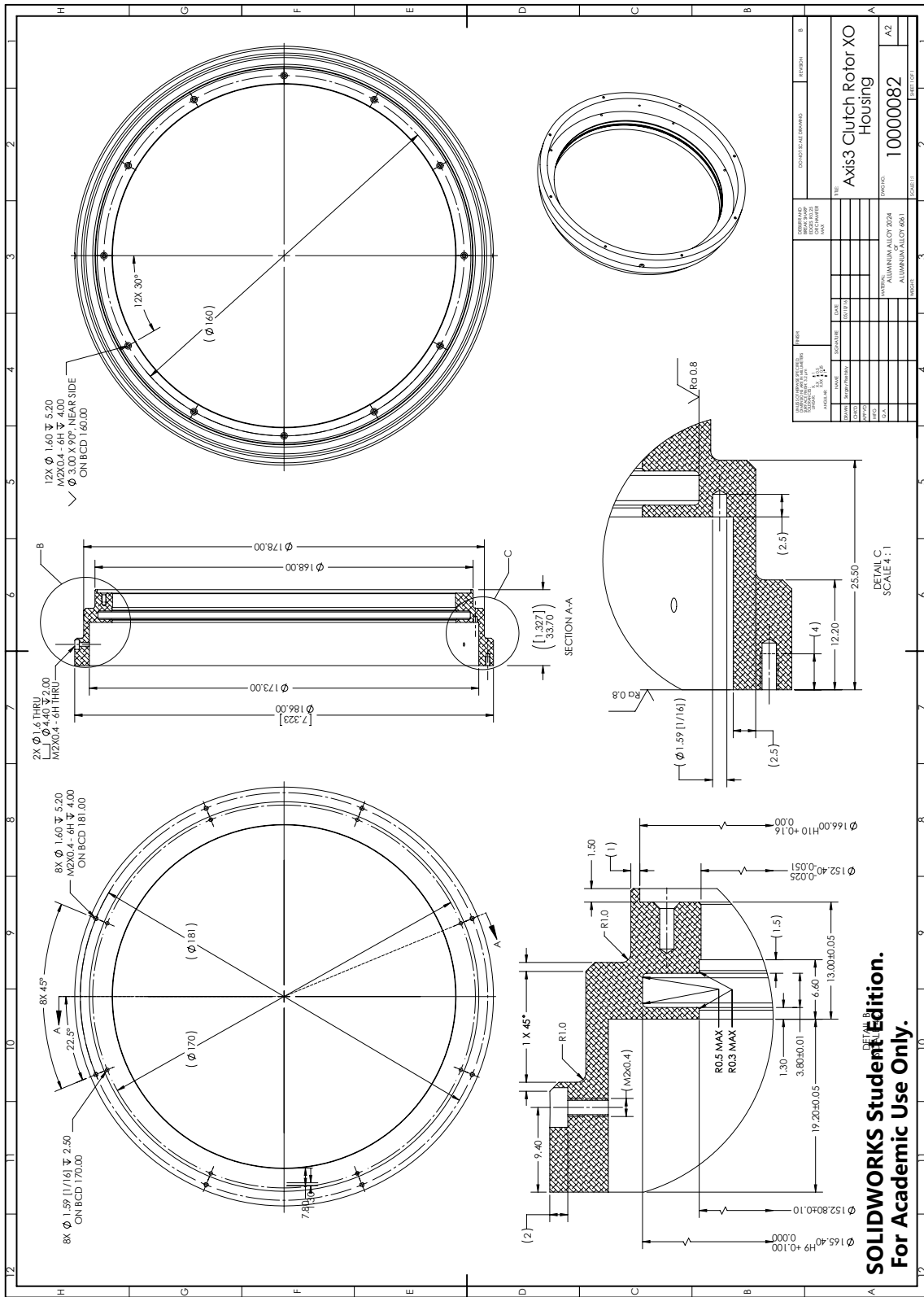
Figure B.69: Drawing: Join 3 clutch rotor housing.
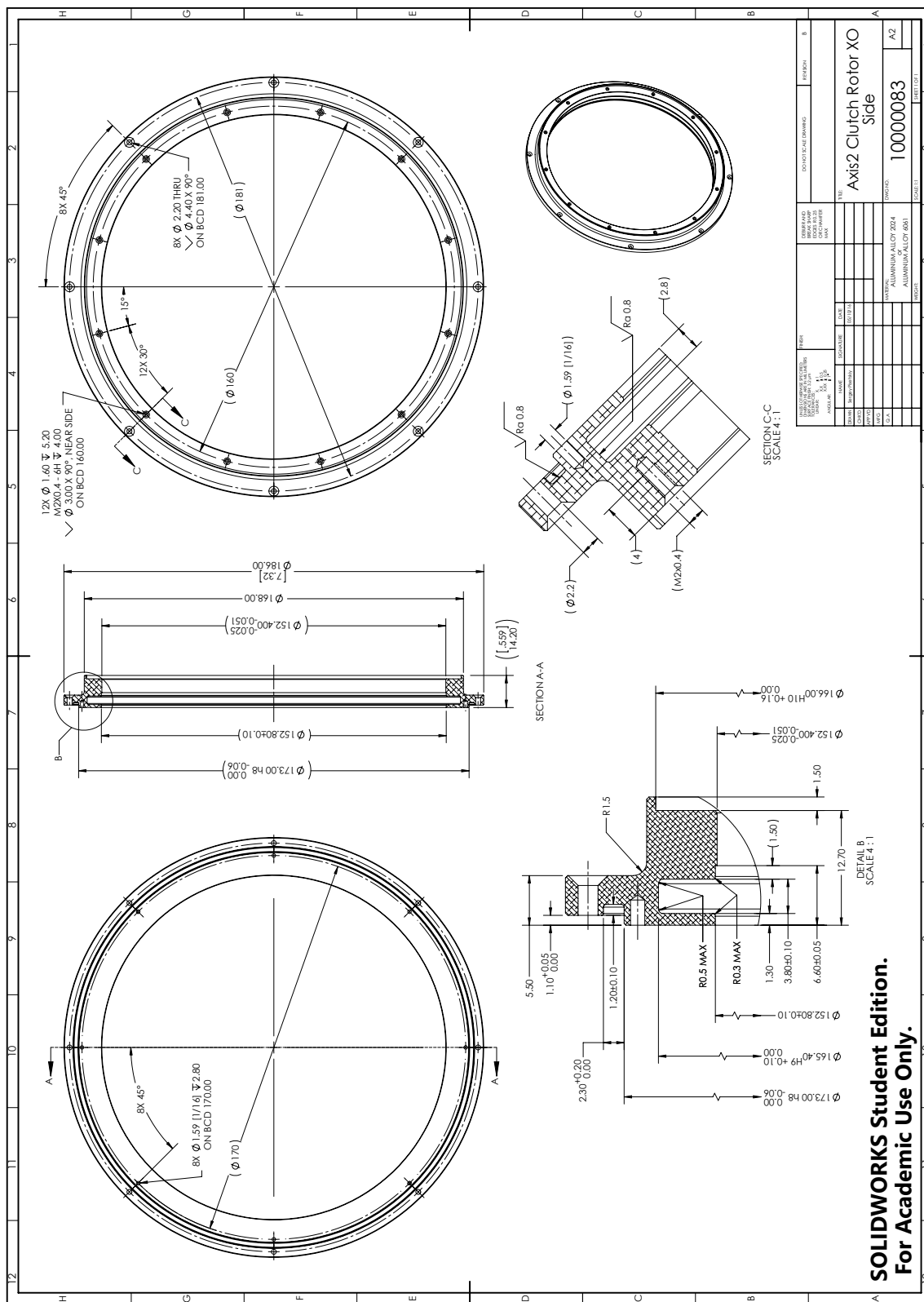
Figure B.70: Drawing: Join 3 clutch rotor side.
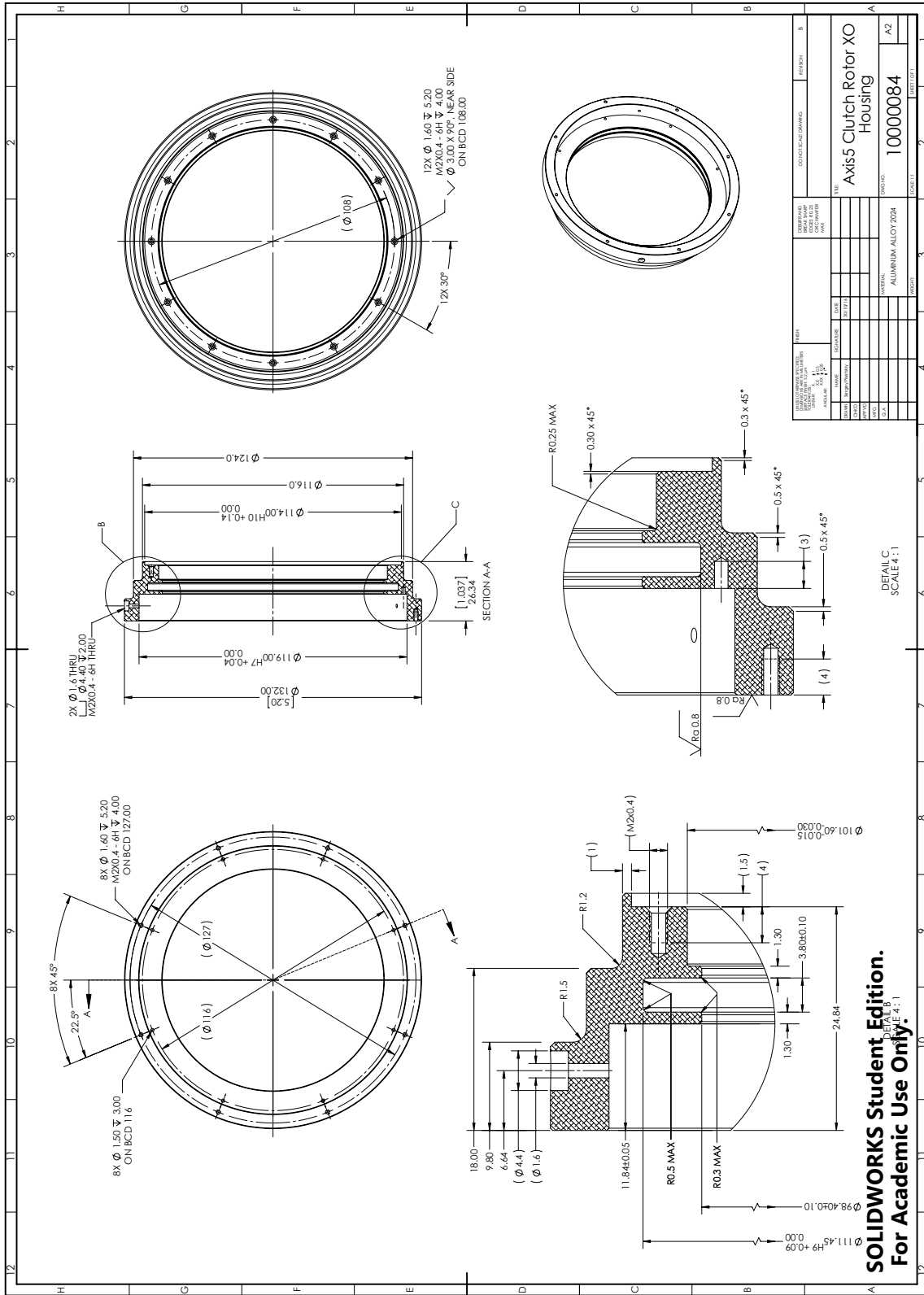
Figure B.71: Drawing: Join 5 clutch rotor housing.
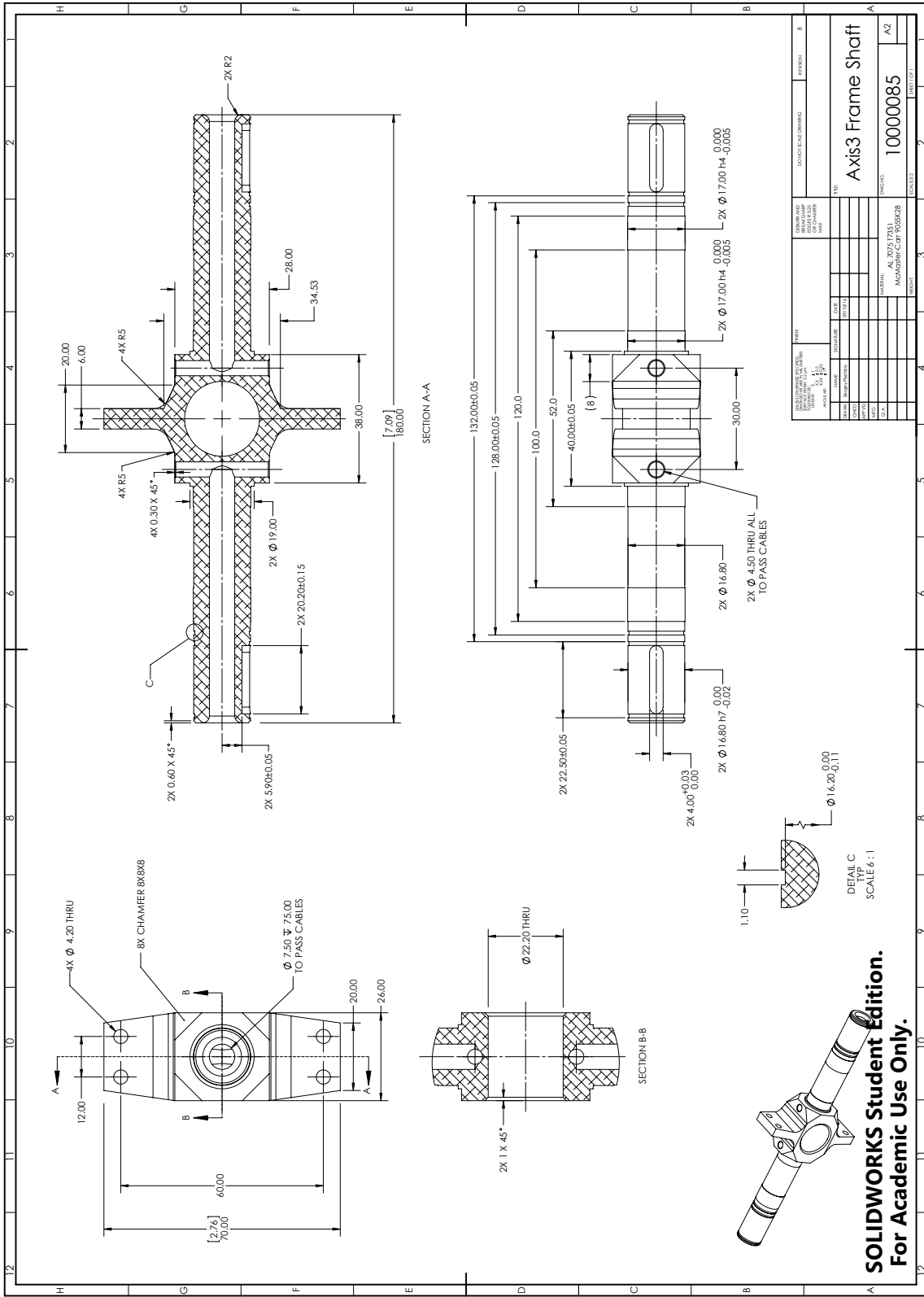
Figure B.72: Drawing: Join 3 frame shaft.
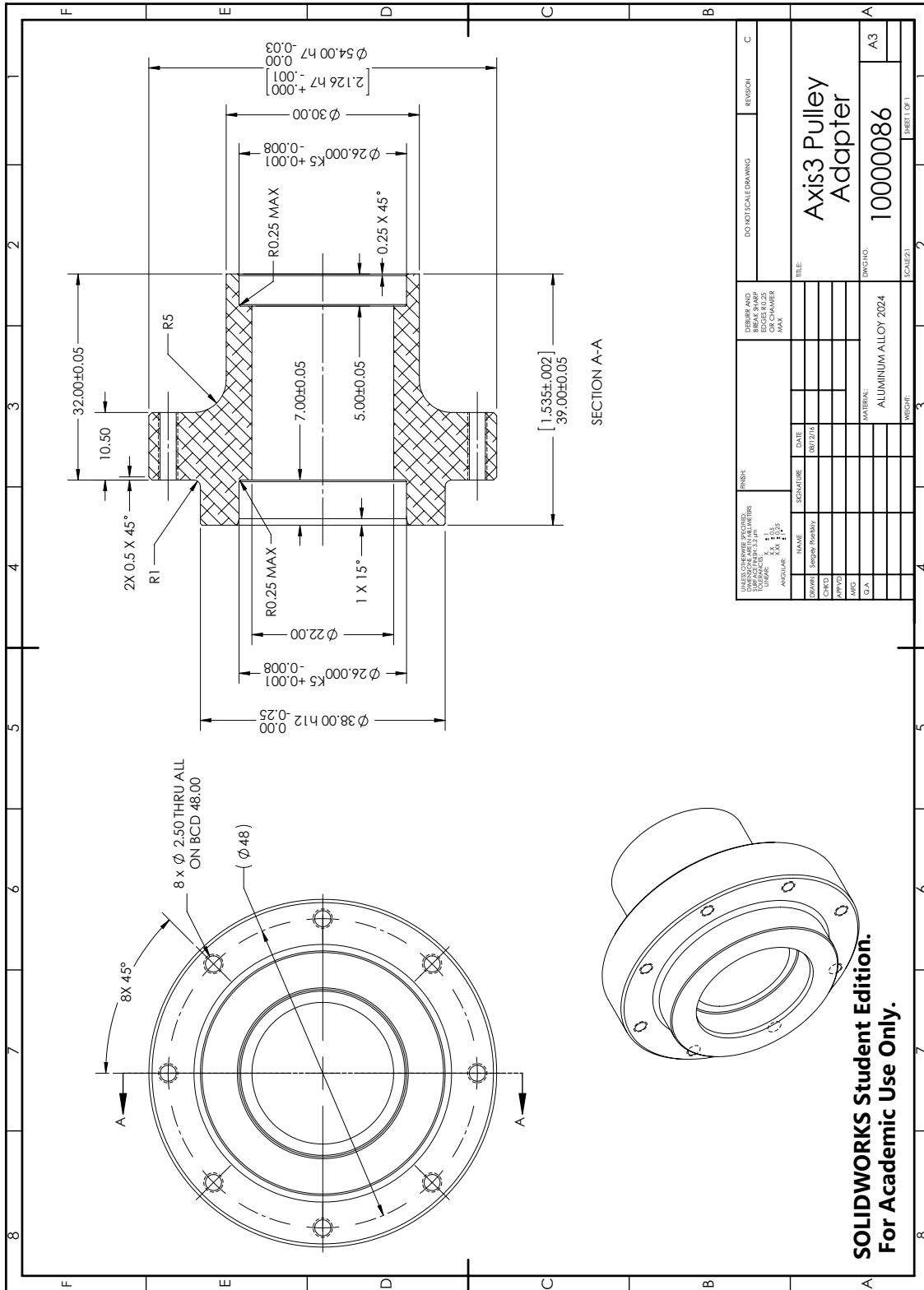
Figure B.73: Drawing: Join 3 timing belt pulley adapter.
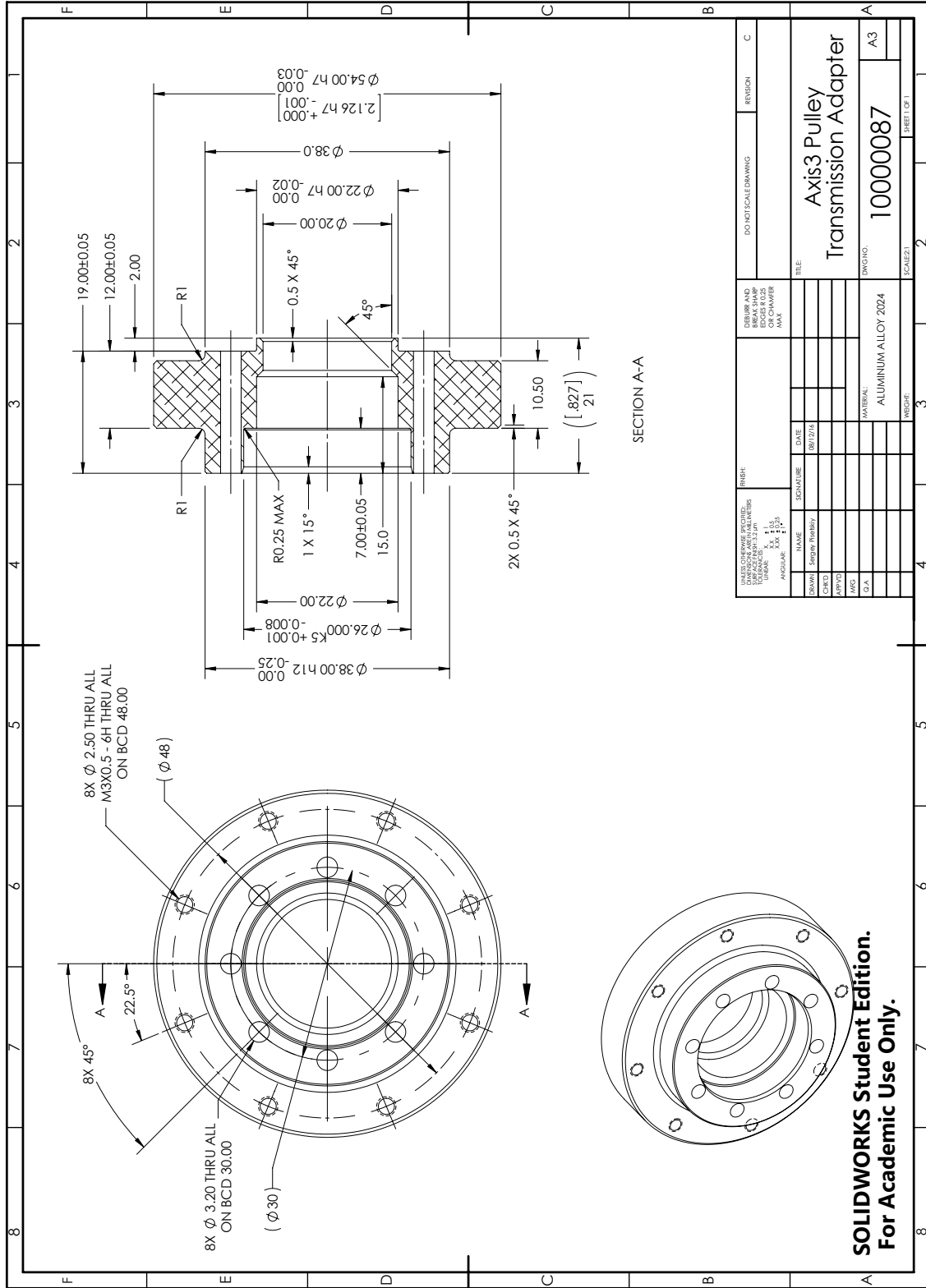
Figure B.74: Drawing: Join 3 timing belt pulley transmission adapter.
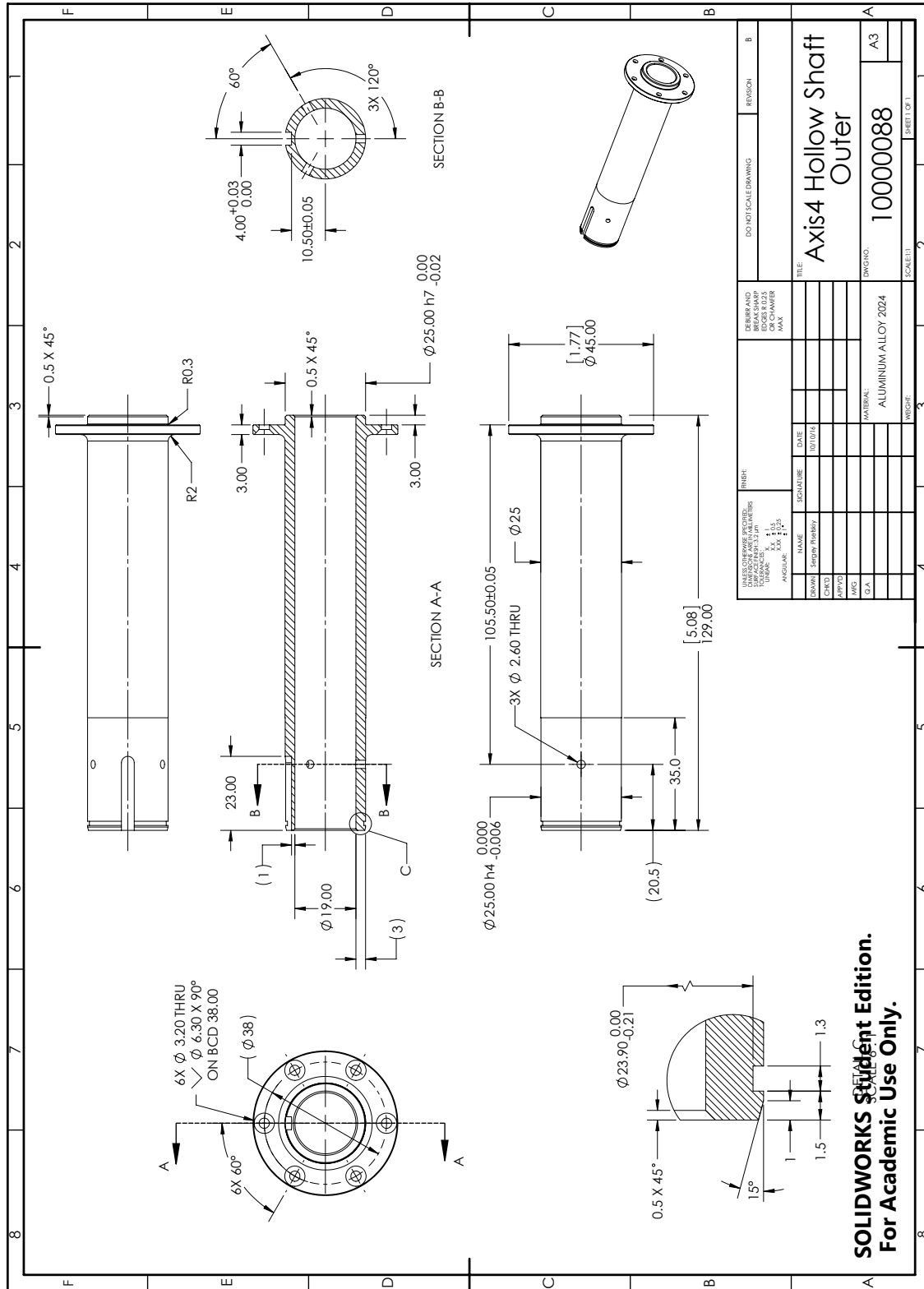
Figure B.75: Drawing: Join 4 outer hollow shaft.
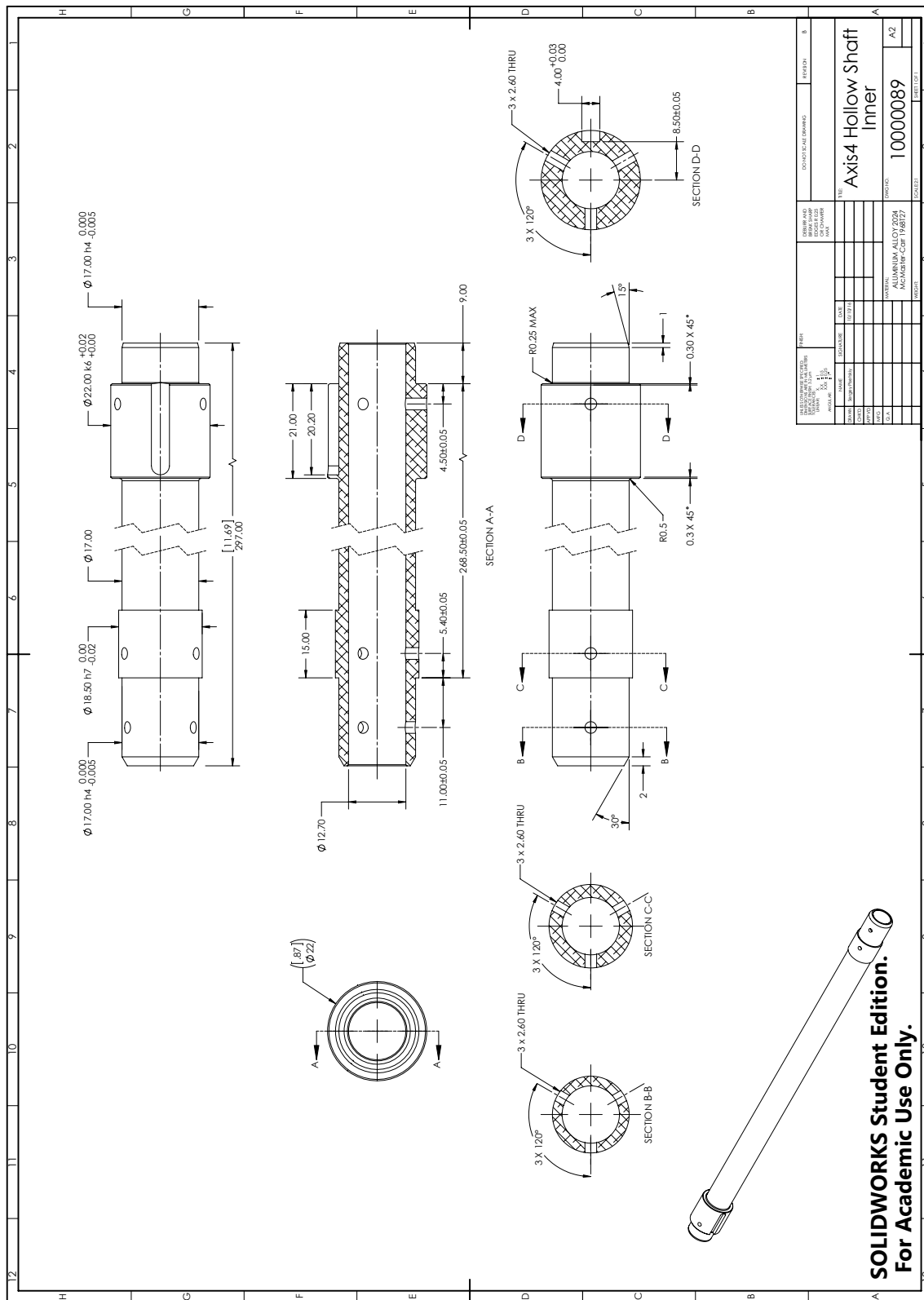
Figure B.76: Drawing: Join 4 inner hollow shaft.
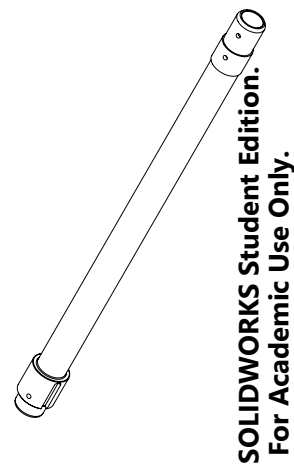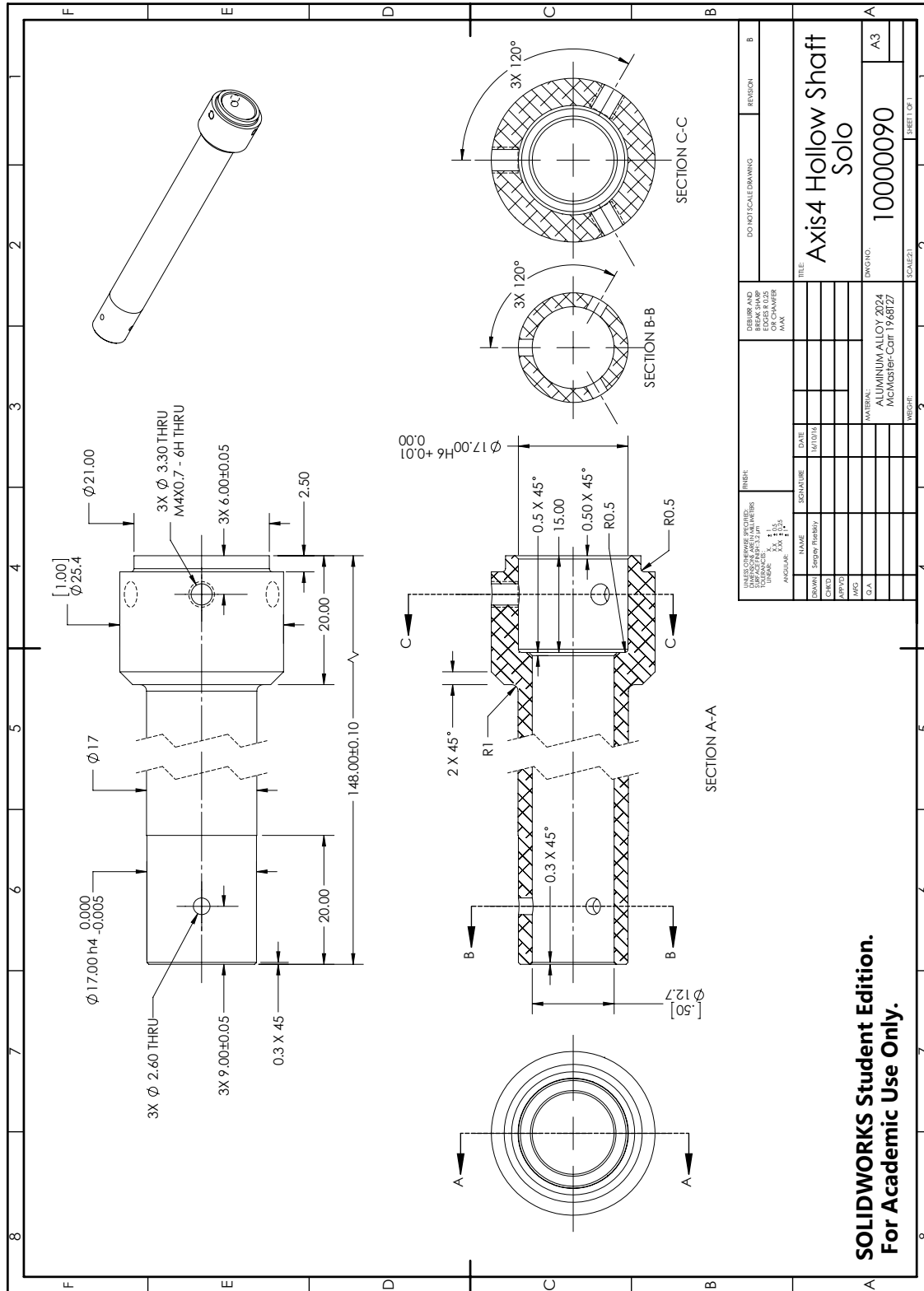
Figure B.77: Drawing: Join 4 hollow shaft.
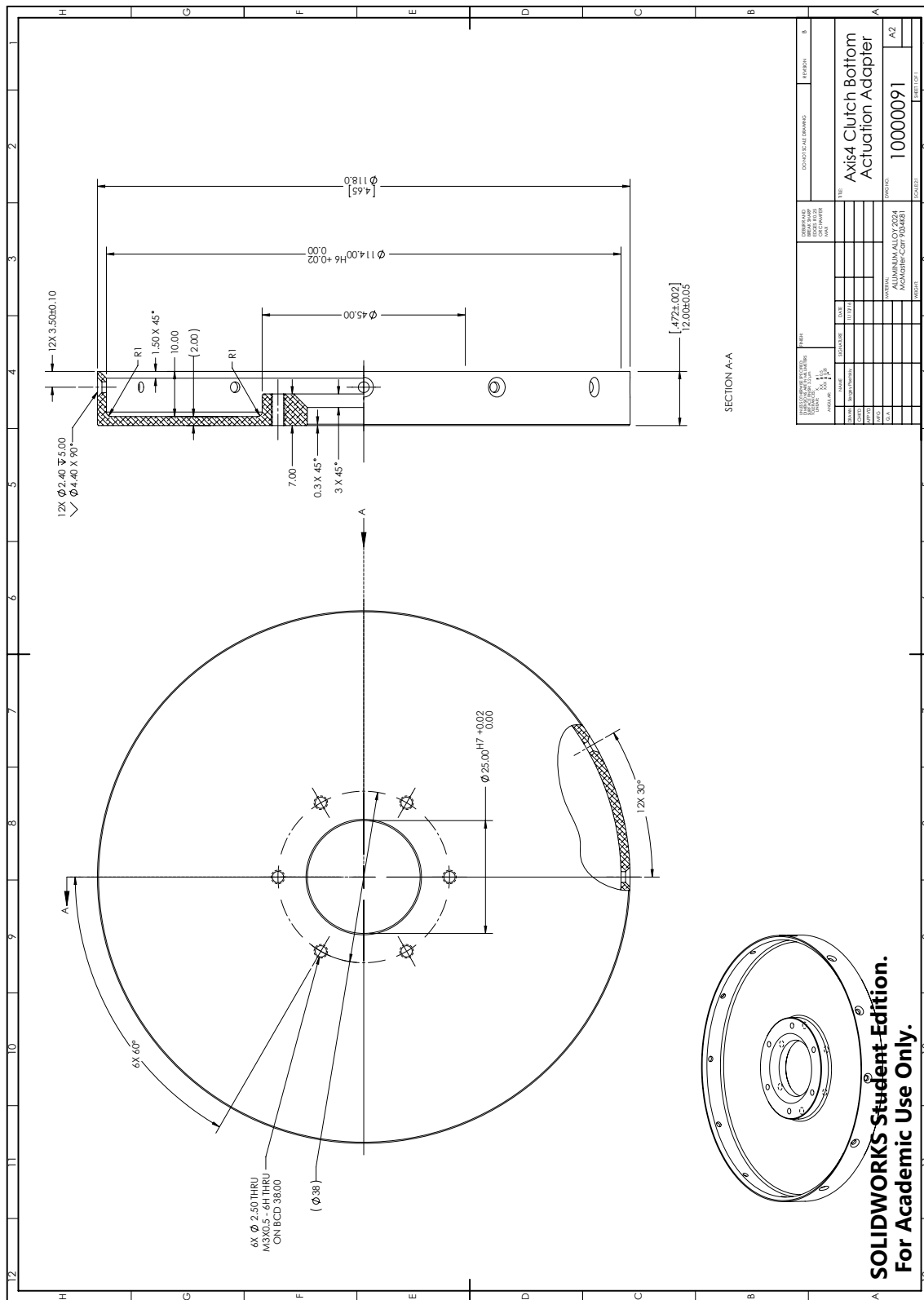
Figure B.78: Drawing: Join 4 clutch pair bottom actuation adapter.
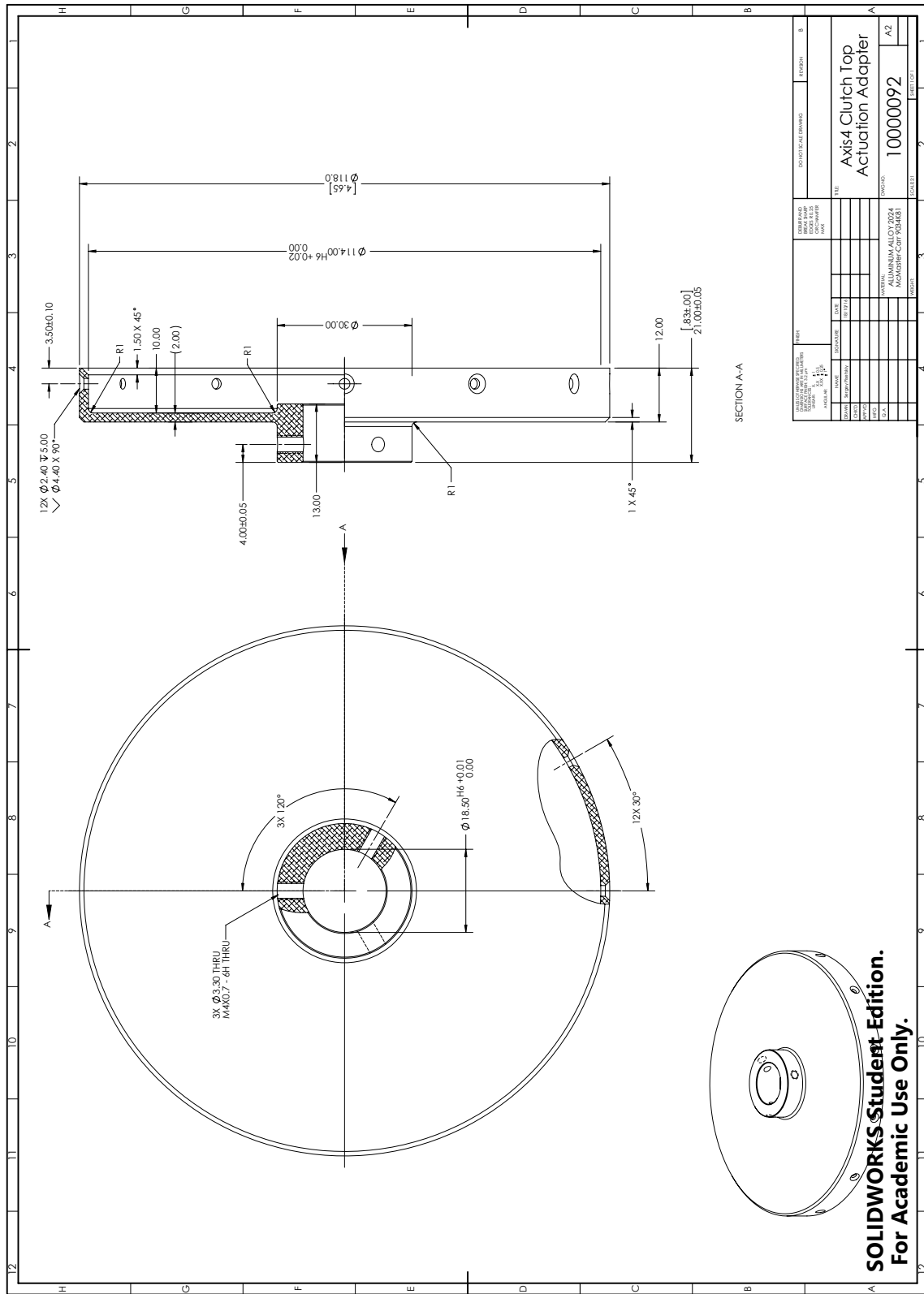
Figure B.79: Drawing: Join 4 clutch pair top actuation adapter.

215
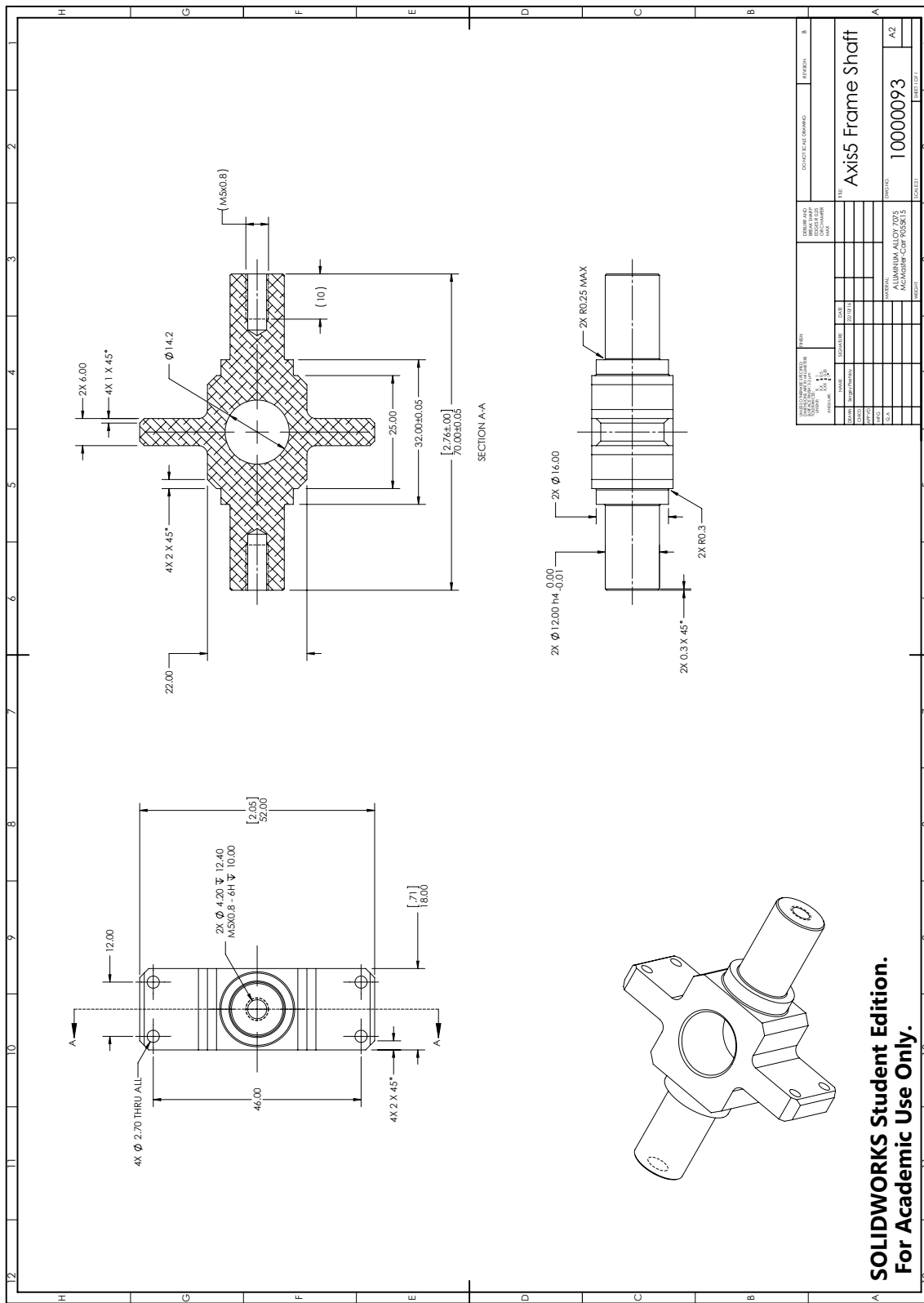
Figure B.80: Drawing: Join 5 frame shaft.
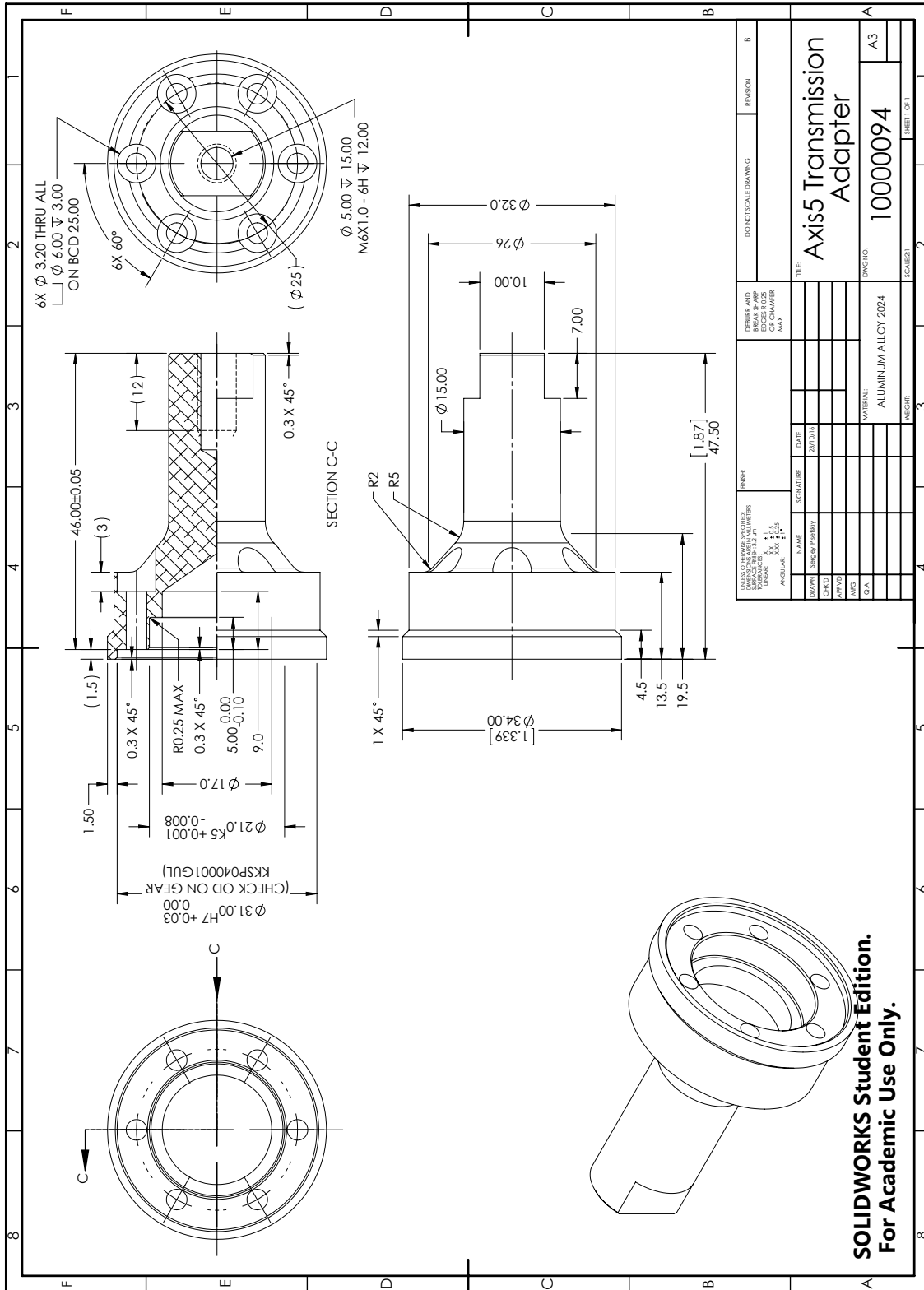
Figure B.81: Drawing: Join 5 transmission adapter.
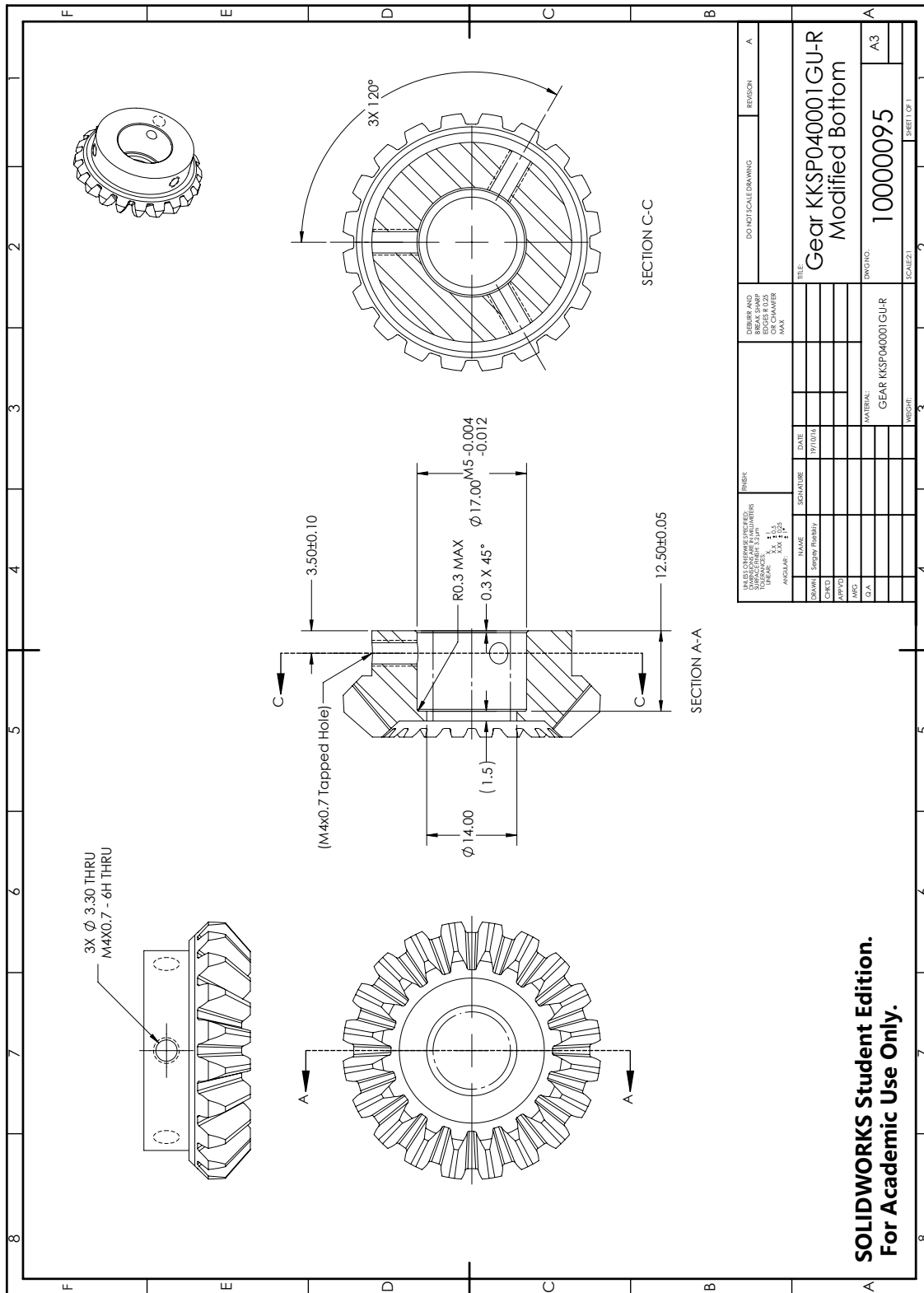
Figure B.82: Drawing: Gear KKSP040001GUR modified, bottom.
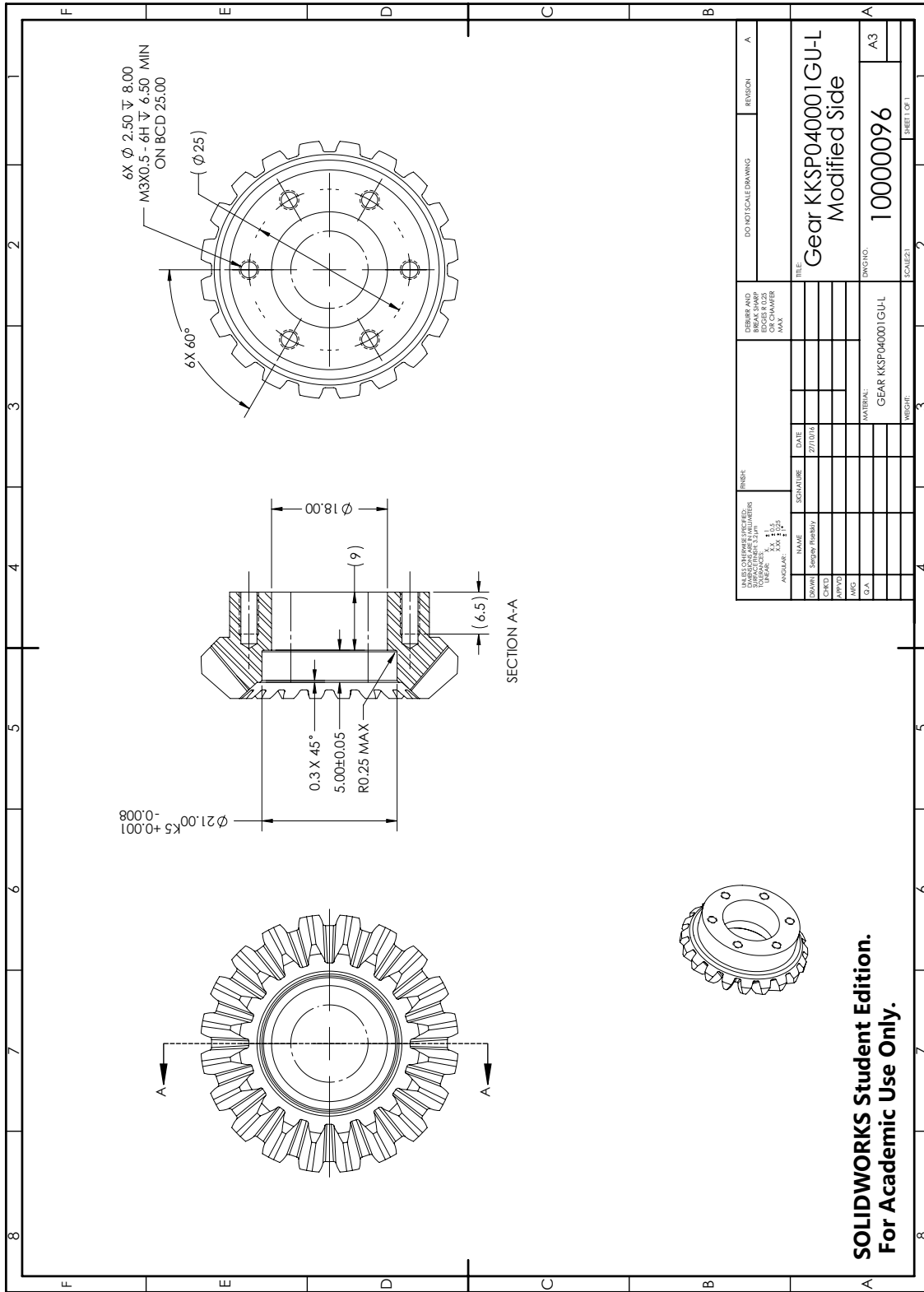
Figure B.83: Drawing: Gear KKSP040001GUL modified, side.
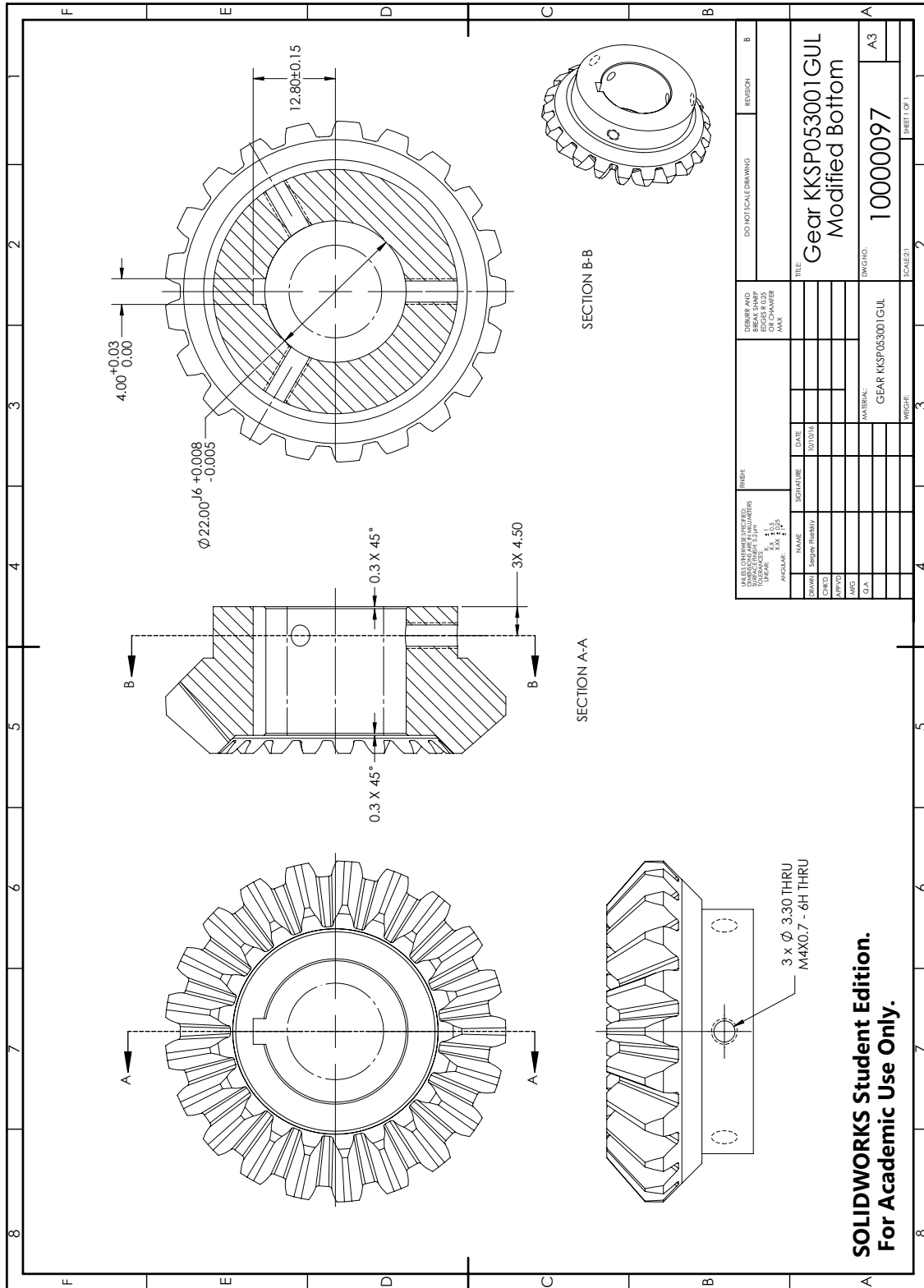
Figure B.84: Drawing: Gear KKSP053001GUL modified, bottom.
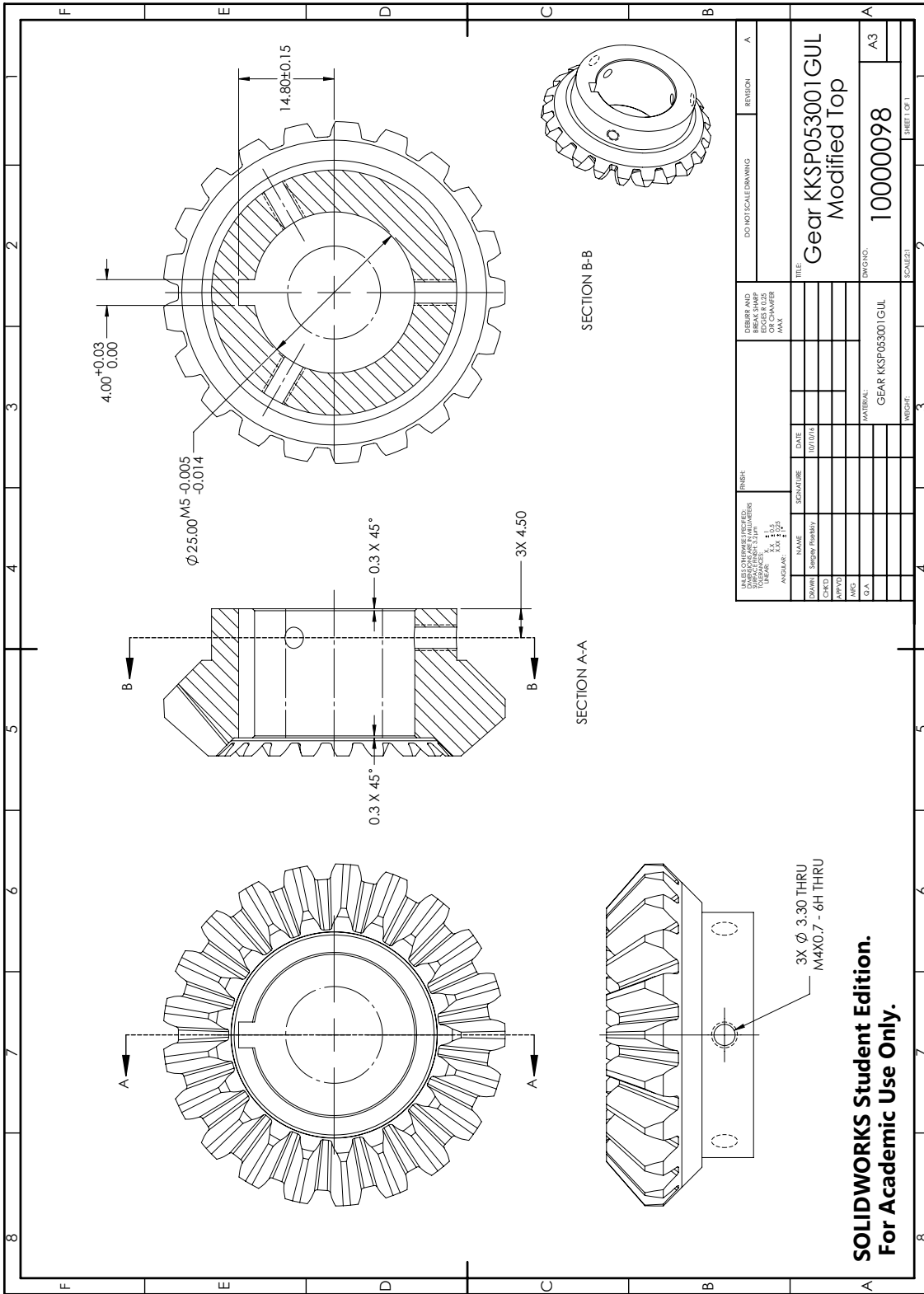
Figure B.85: Drawing: Gear KKSP053001GUL modified, top.
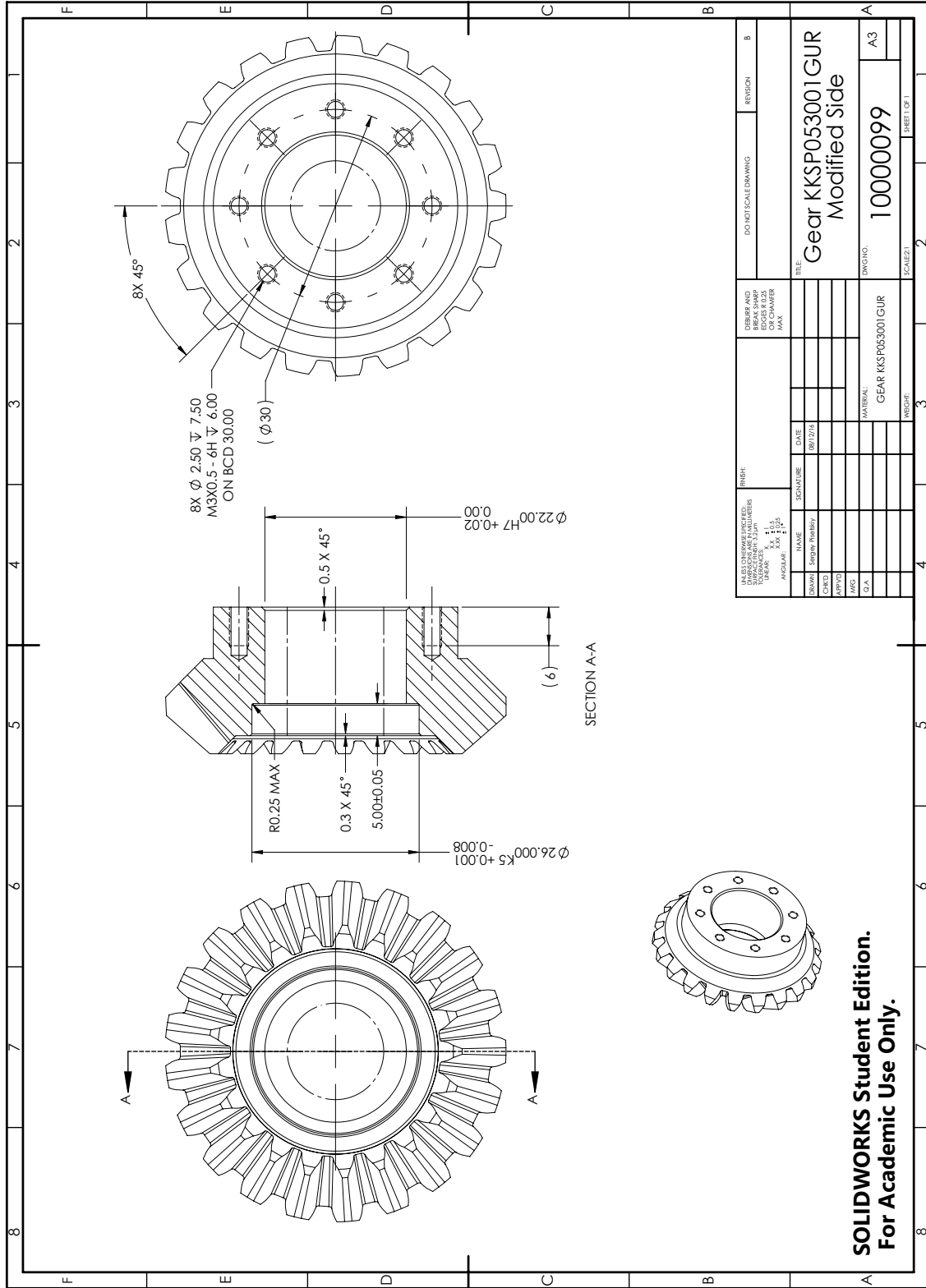
Figure B.86: Drawing: Gear KKSP053001GUR modified, side.
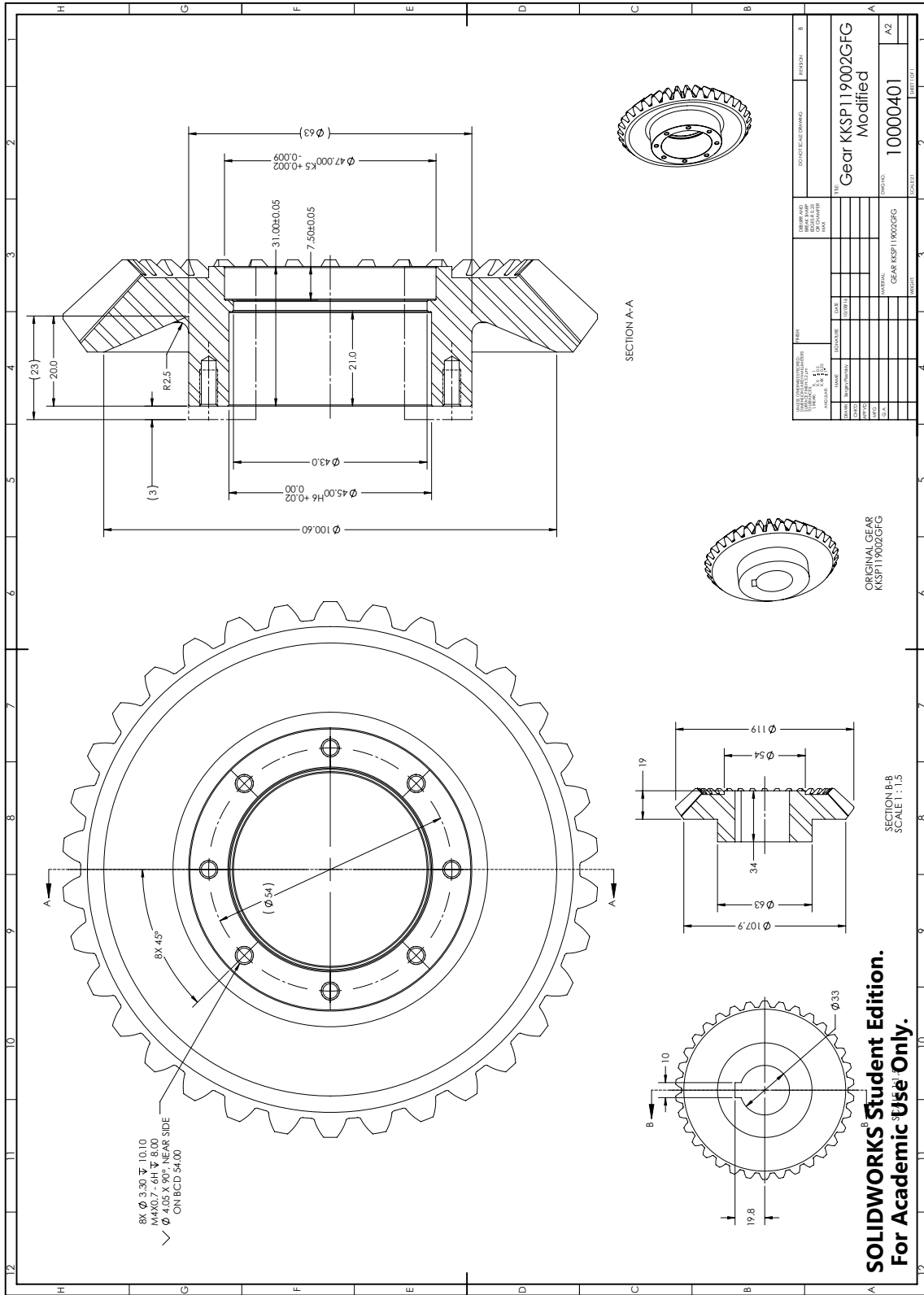
Figure B.87: Drawing: Bevel gear KKSP119002GF-G modified.
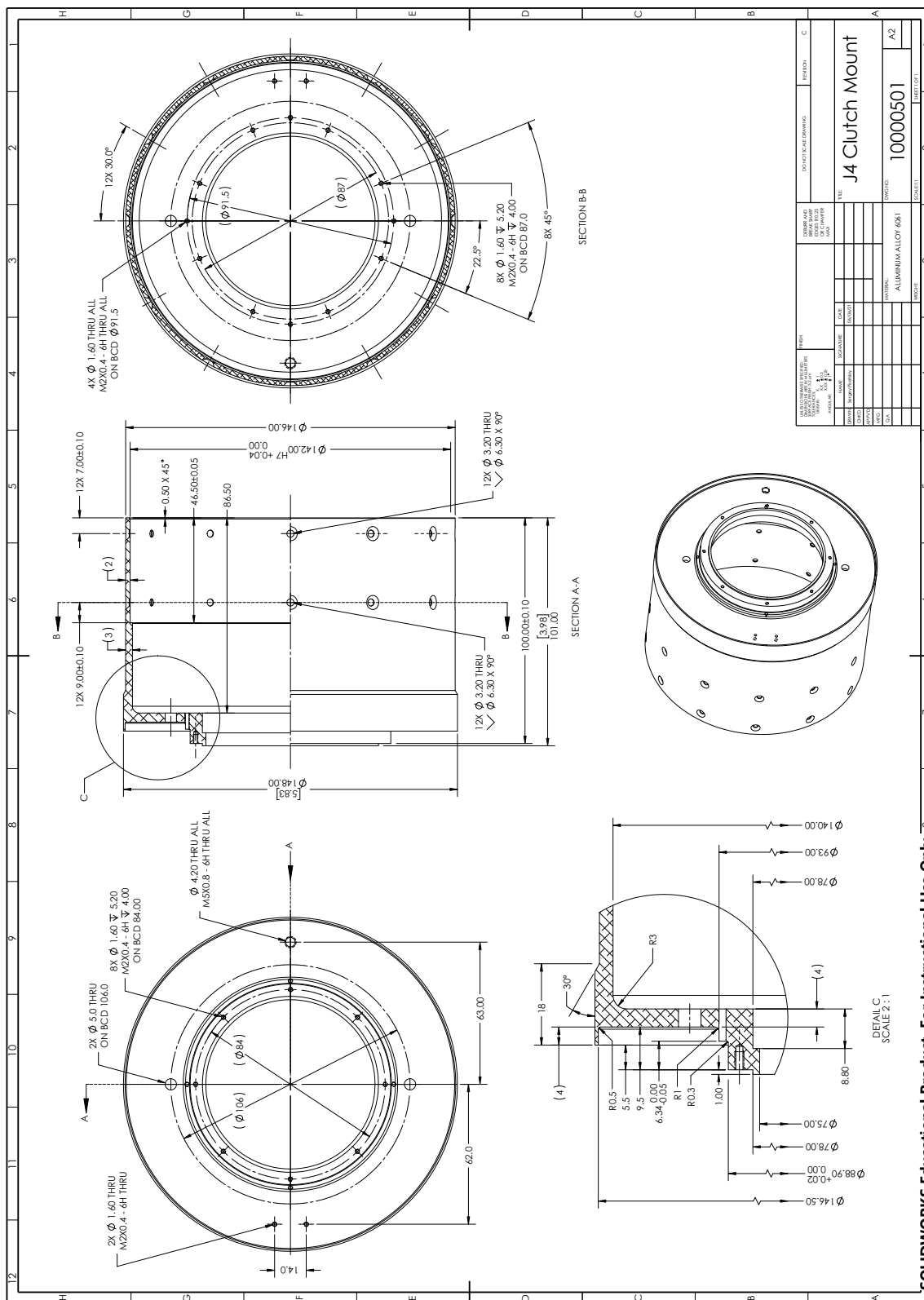
Figure B.88: Drawing: Joint 4 clutch mount.
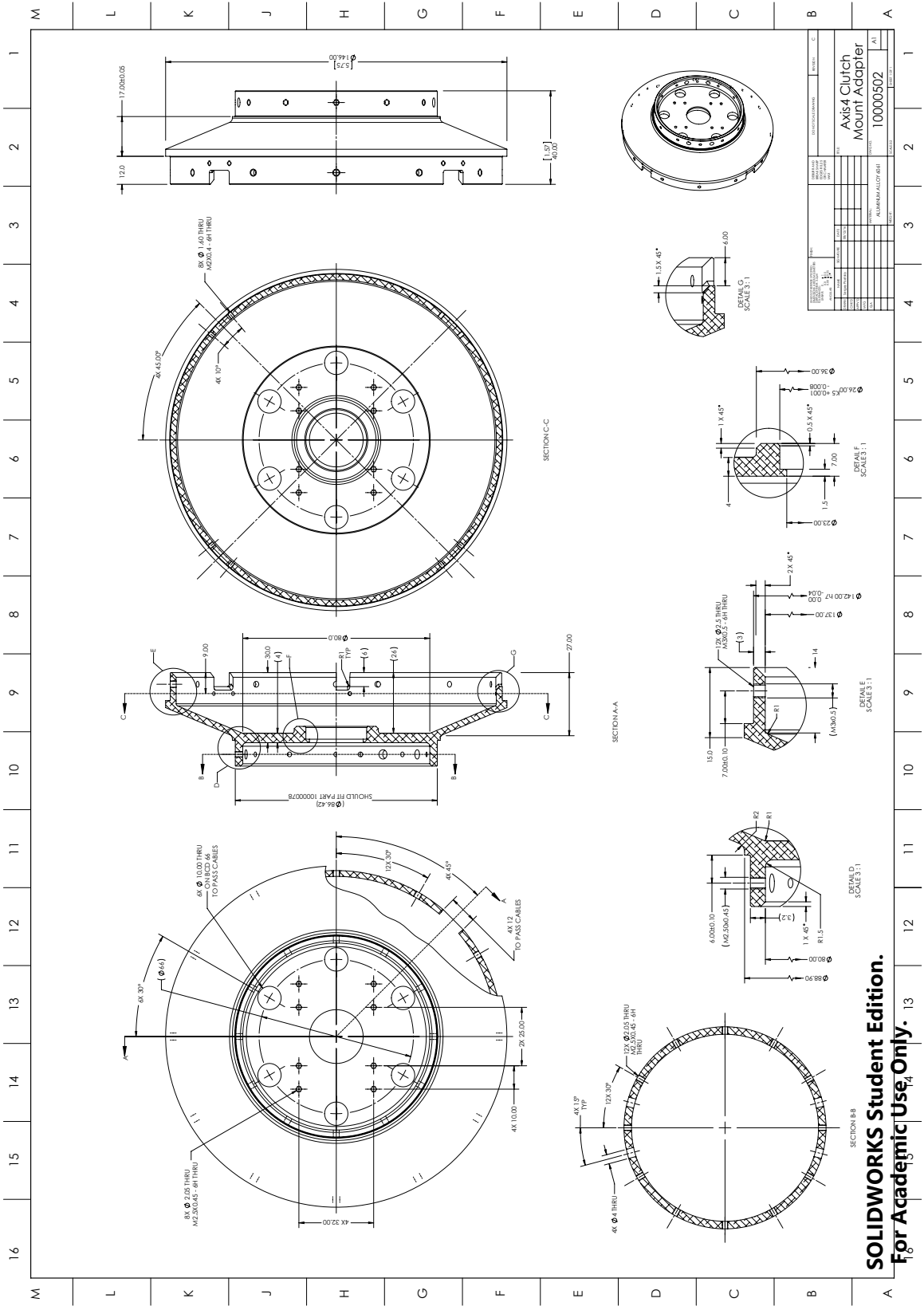
Figure B.89: Drawing: Joint 4 clutch mount adapter.
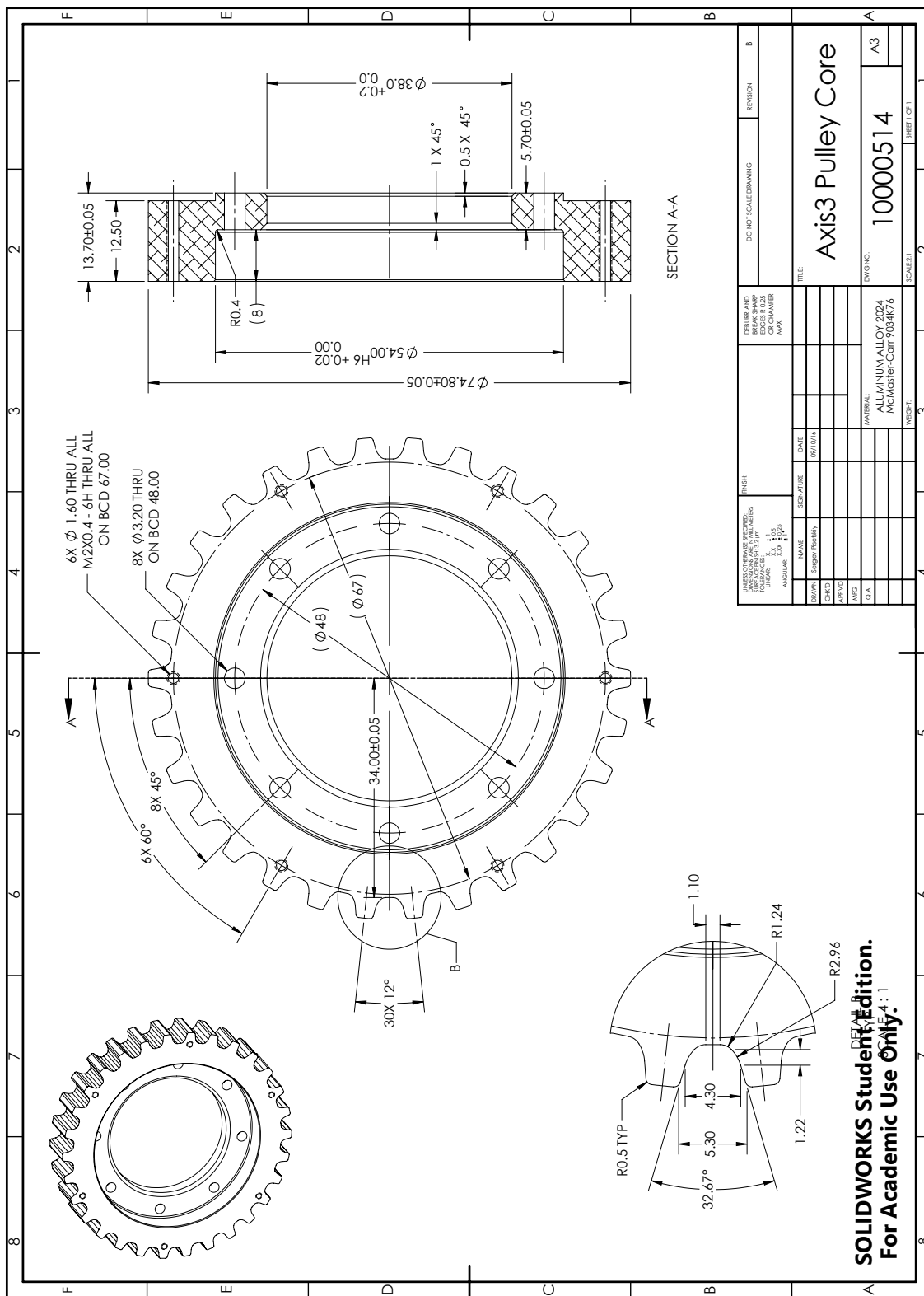
Figure B.90: Drawing: Joint 3 timing belt pulley core.
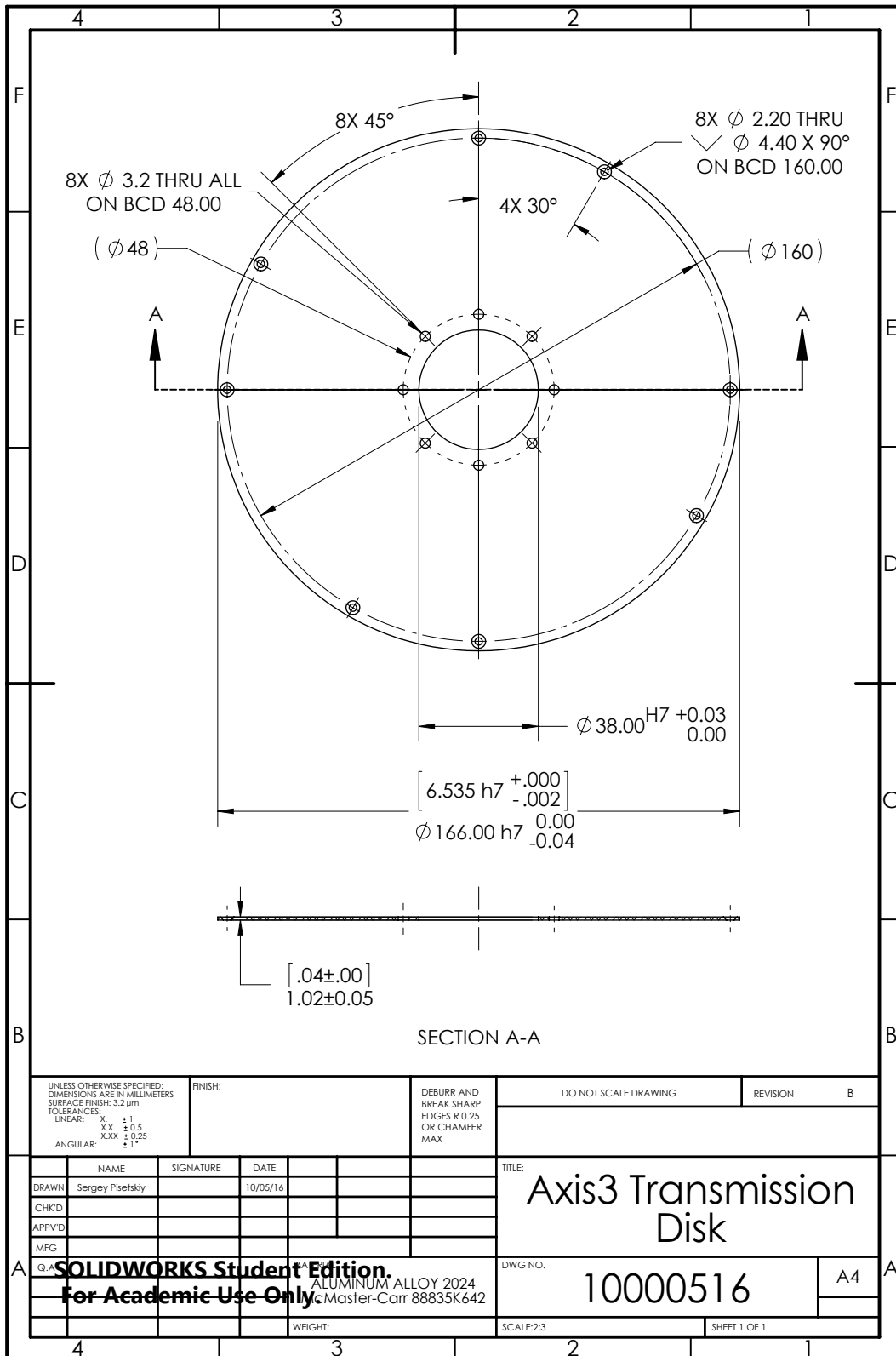
Figure B.91: Drawing: Joint 3 clutch transmission disk.
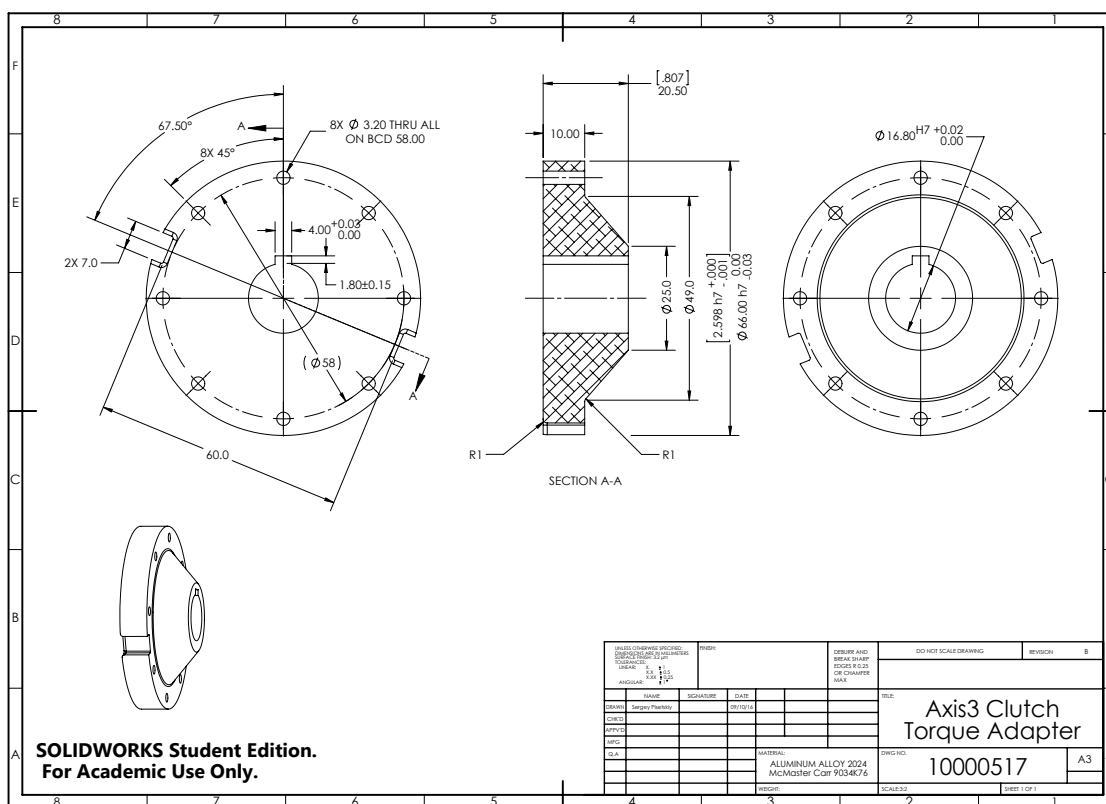
Figure B.92: Drawing: Joint 3 clutch torque adapter.
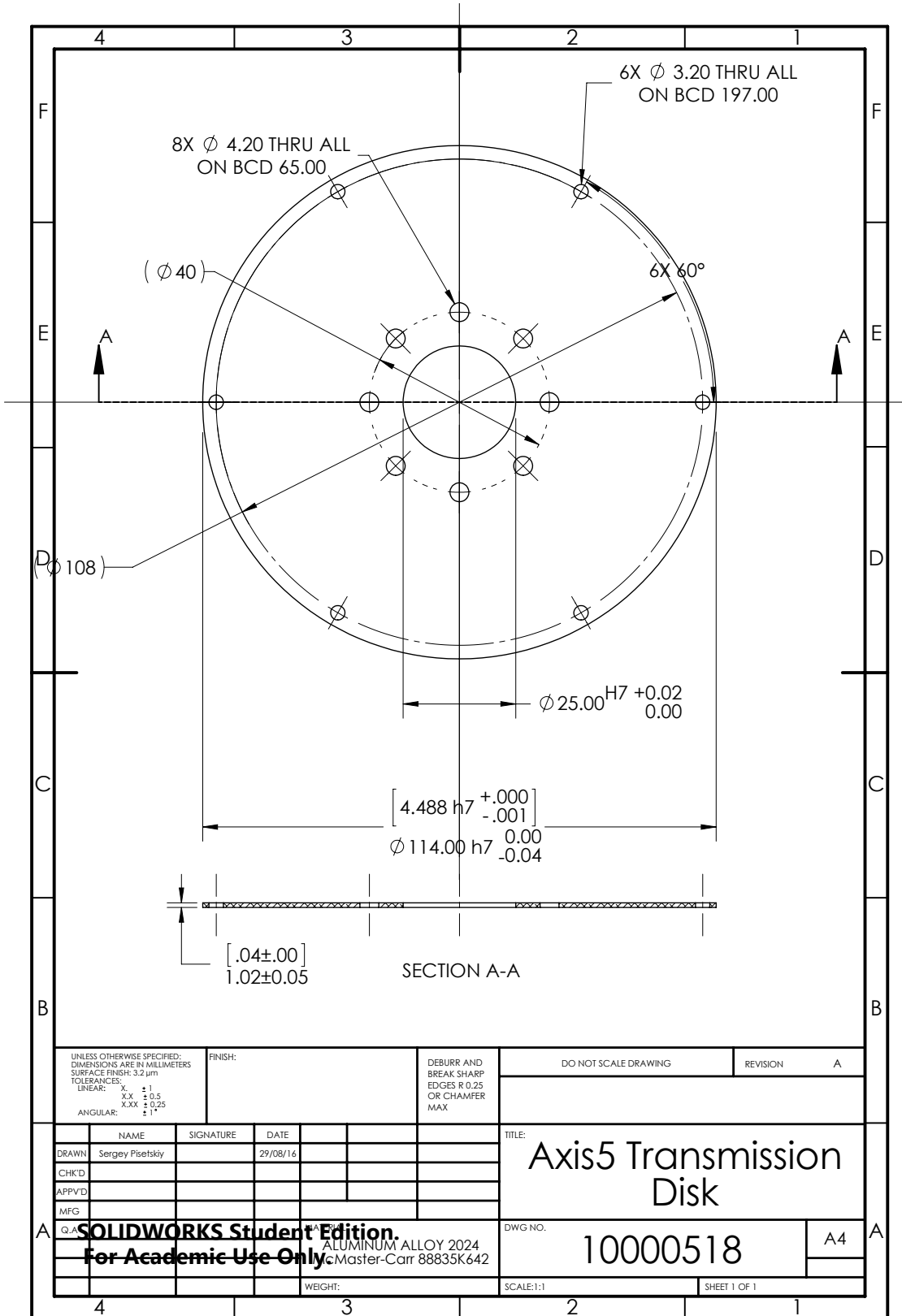
Figure B.93: Drawing: Joint 5 clutch transmission disk.
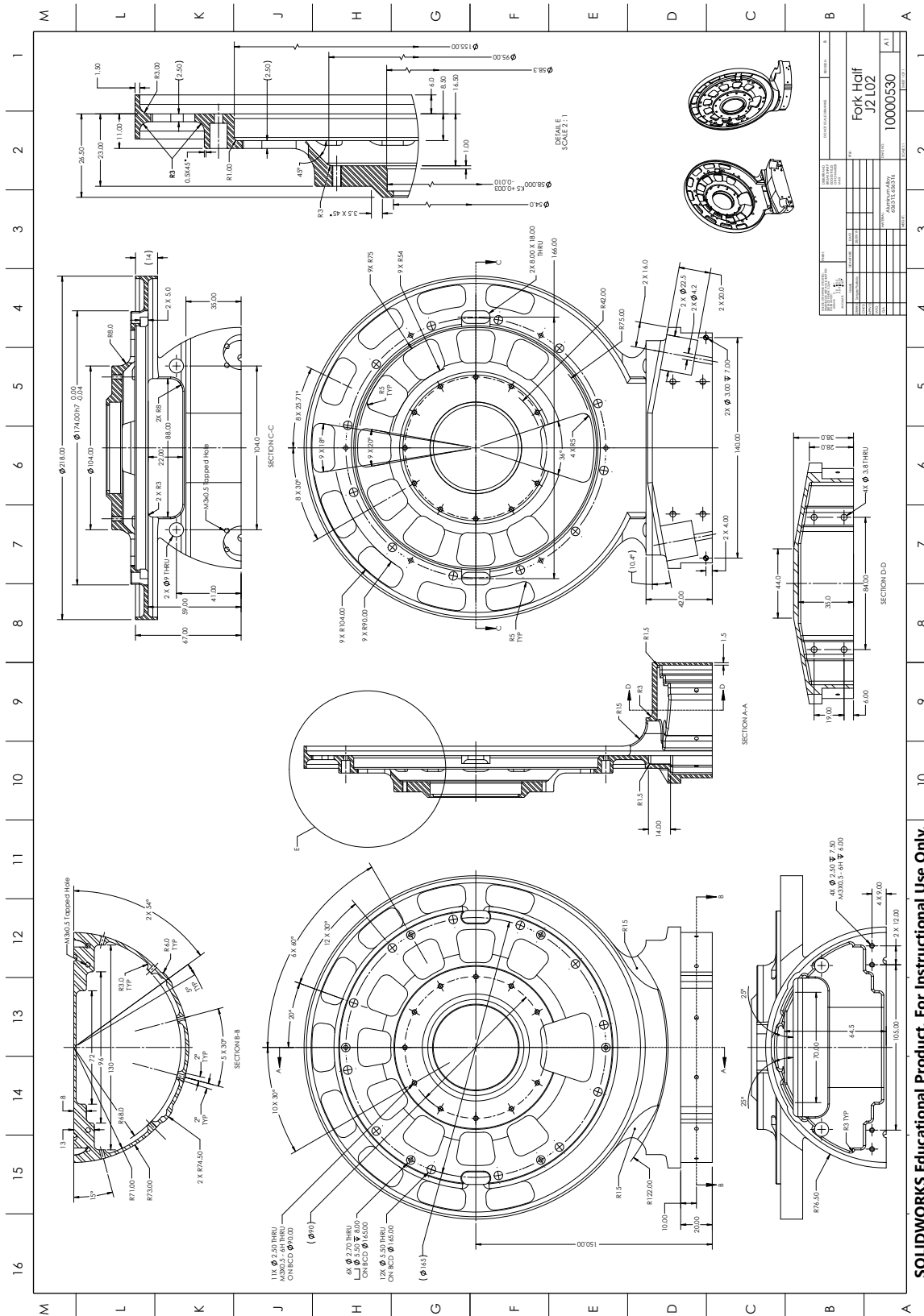
Figure B.94: Drawing: Link 2 Joint 2 fork half.
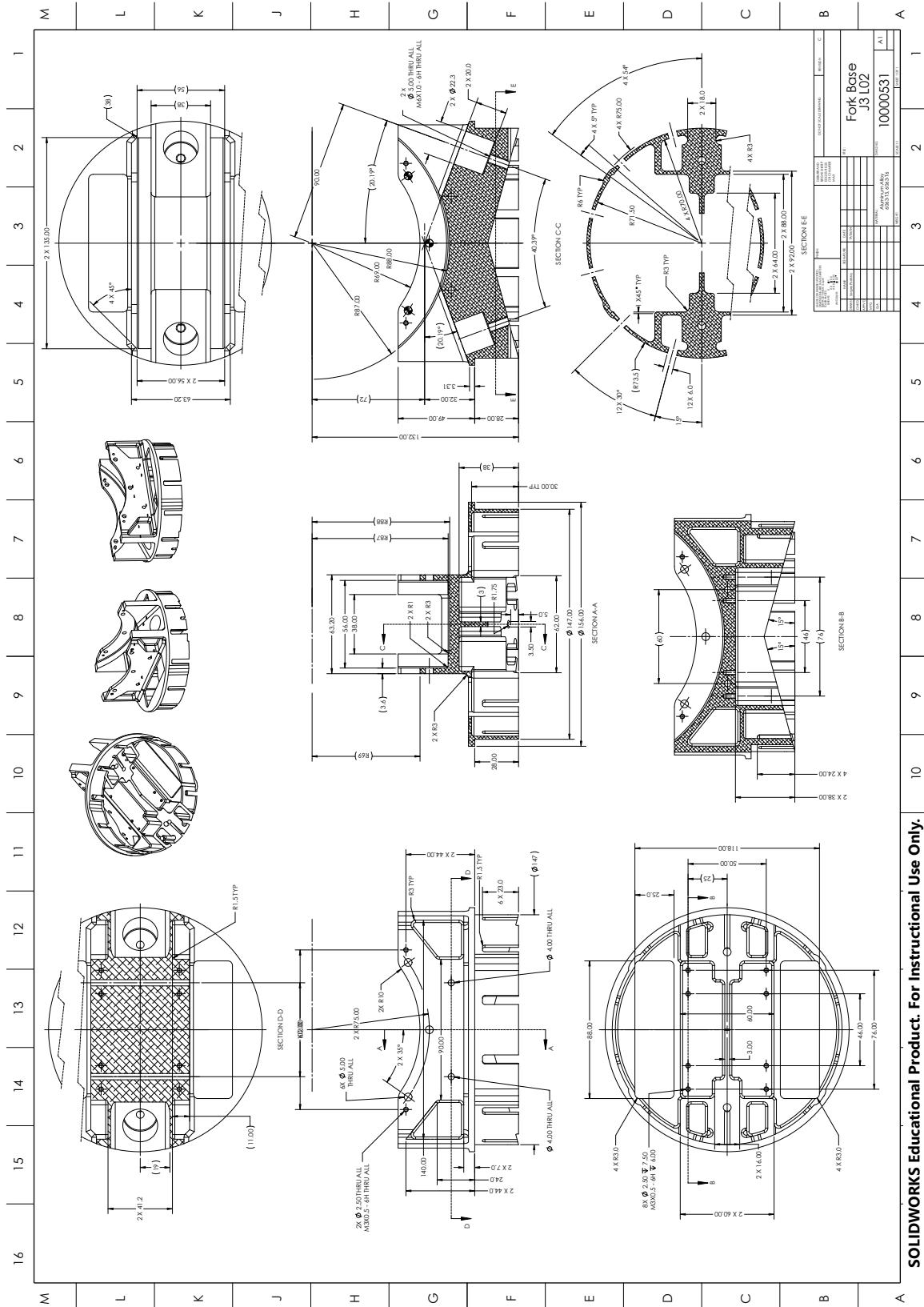
Figure B.95: Drawing: Link 2 Joint 3 fork base.
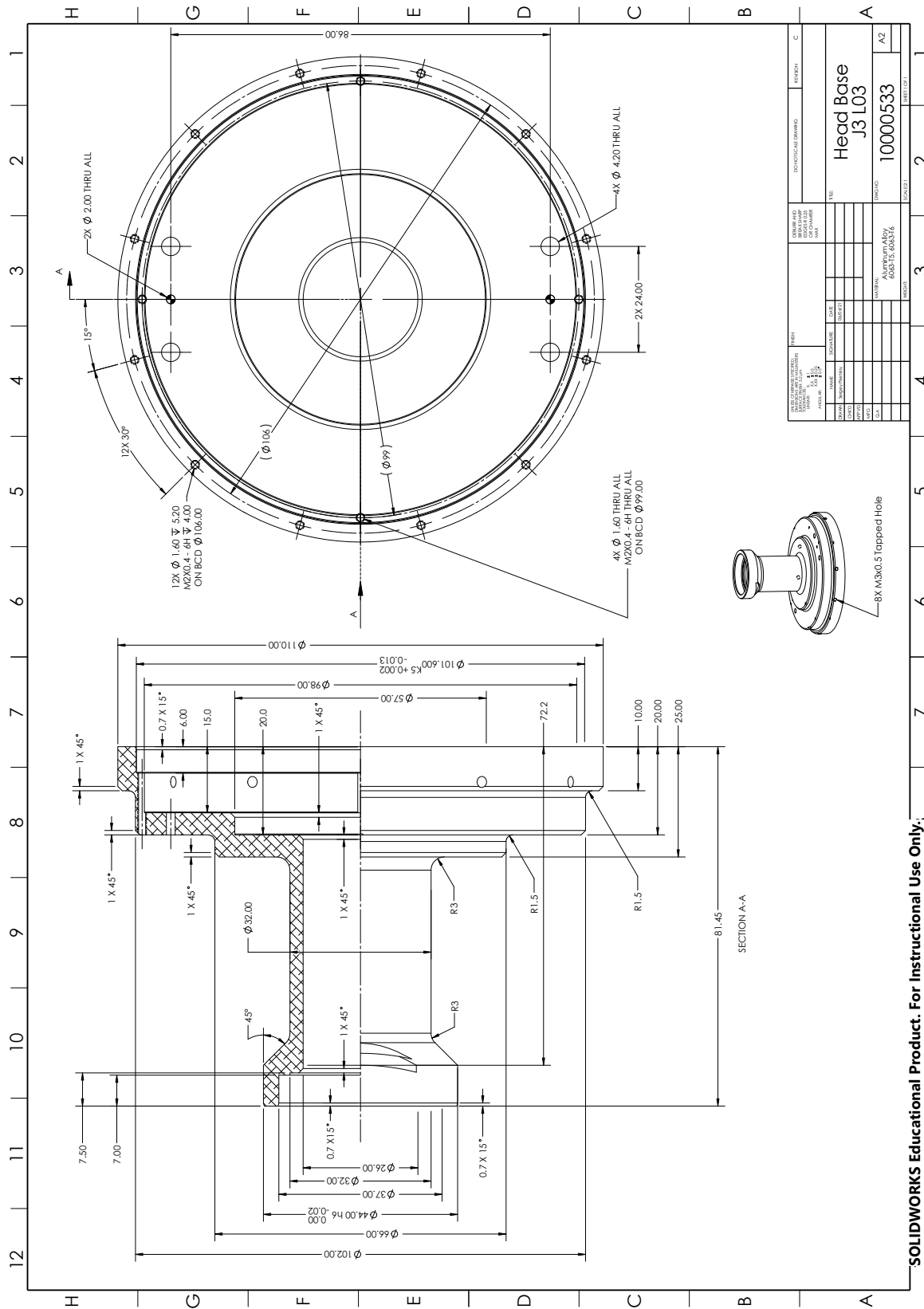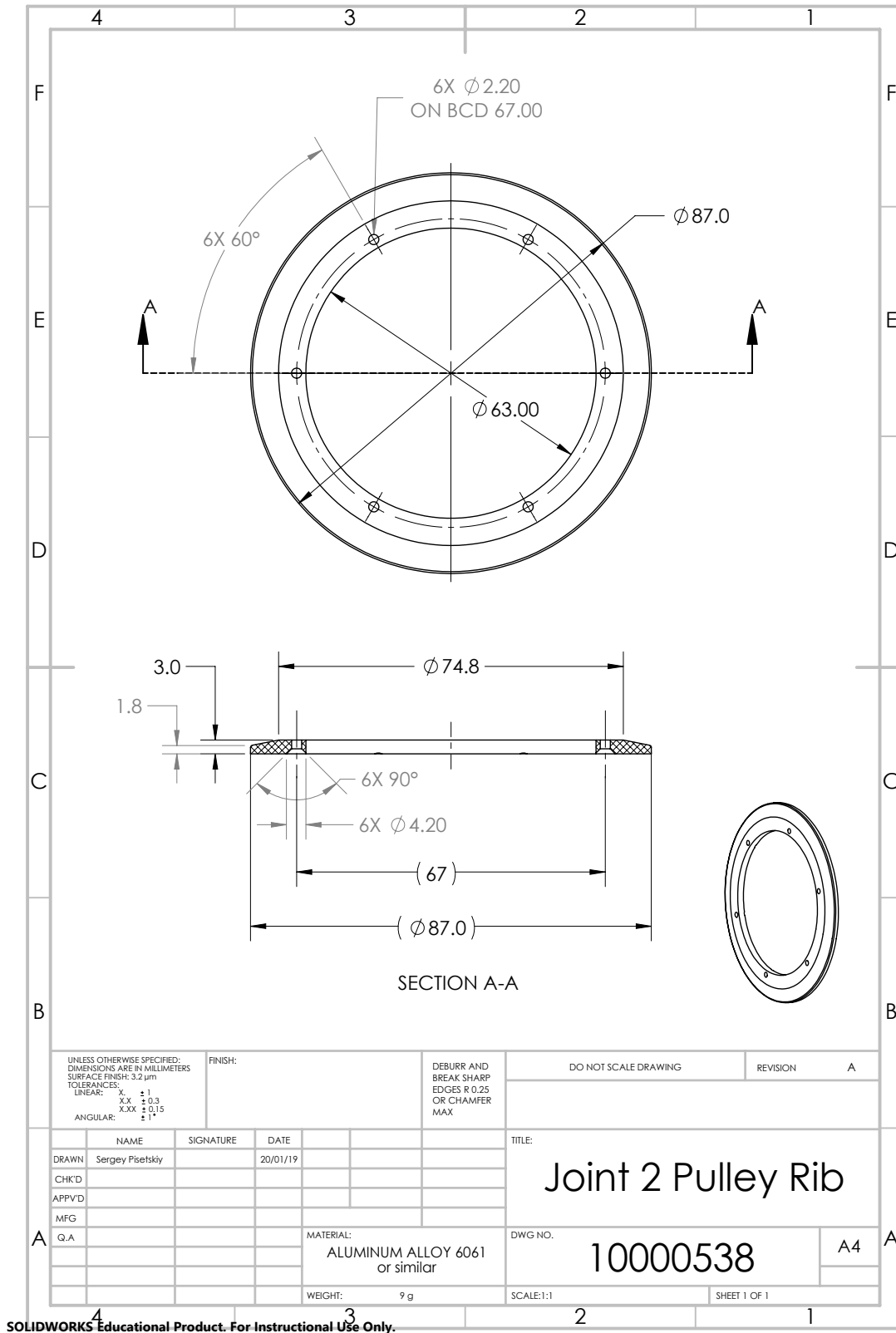
Figure B.96: Drawing: Link 3 Joint 3 head base.

Figure B.97: Drawing: Joint 2 timing belt pulley rib.

6X ⌀ 2.2 THRU ALL
ON BCD 67.00

⌀ 82.0

6X 60°

A

A

⌀ 54.00

⌀ 74.8

1.2

0.2

(⌀ 82)

SECTION A-A

	NAME	SIGNATURE	DATE			TITLE:		
DRAWN	Sergey Pisetskiy		20/01/19			**Joint 3 Pulley Rib**		
CHK'D								
APPV'D								
MFG								
Q.A				MATERIAL: ALUMINUM ALLOY 6061 or similar		DWG NO. **10000539**		A4
				WEIGHT: 9 g		SCALE:1:1	SHEET 1 OF 1	
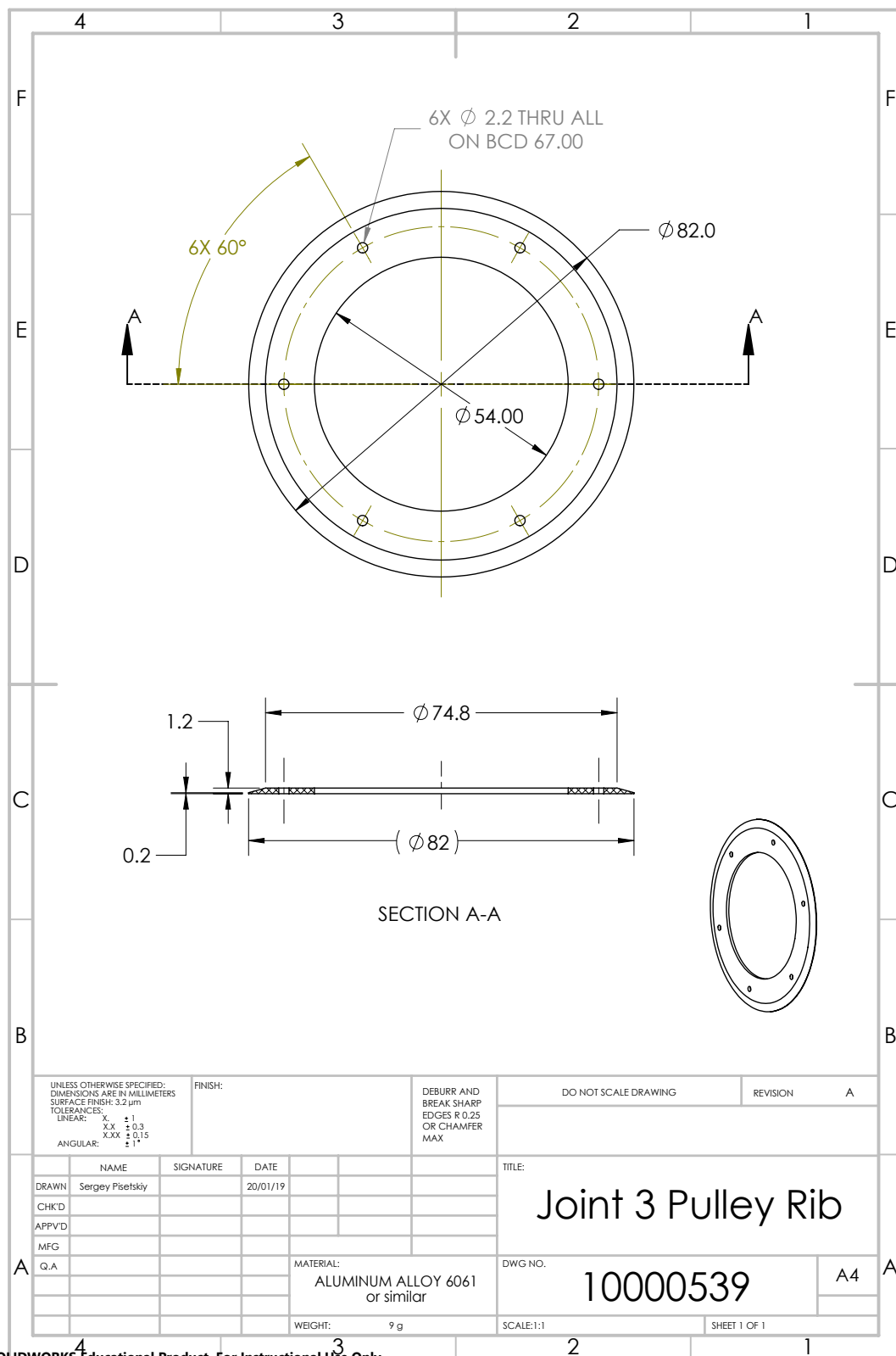
Figure B.98: Drawing: Joint 3 timing belt pulley rib.
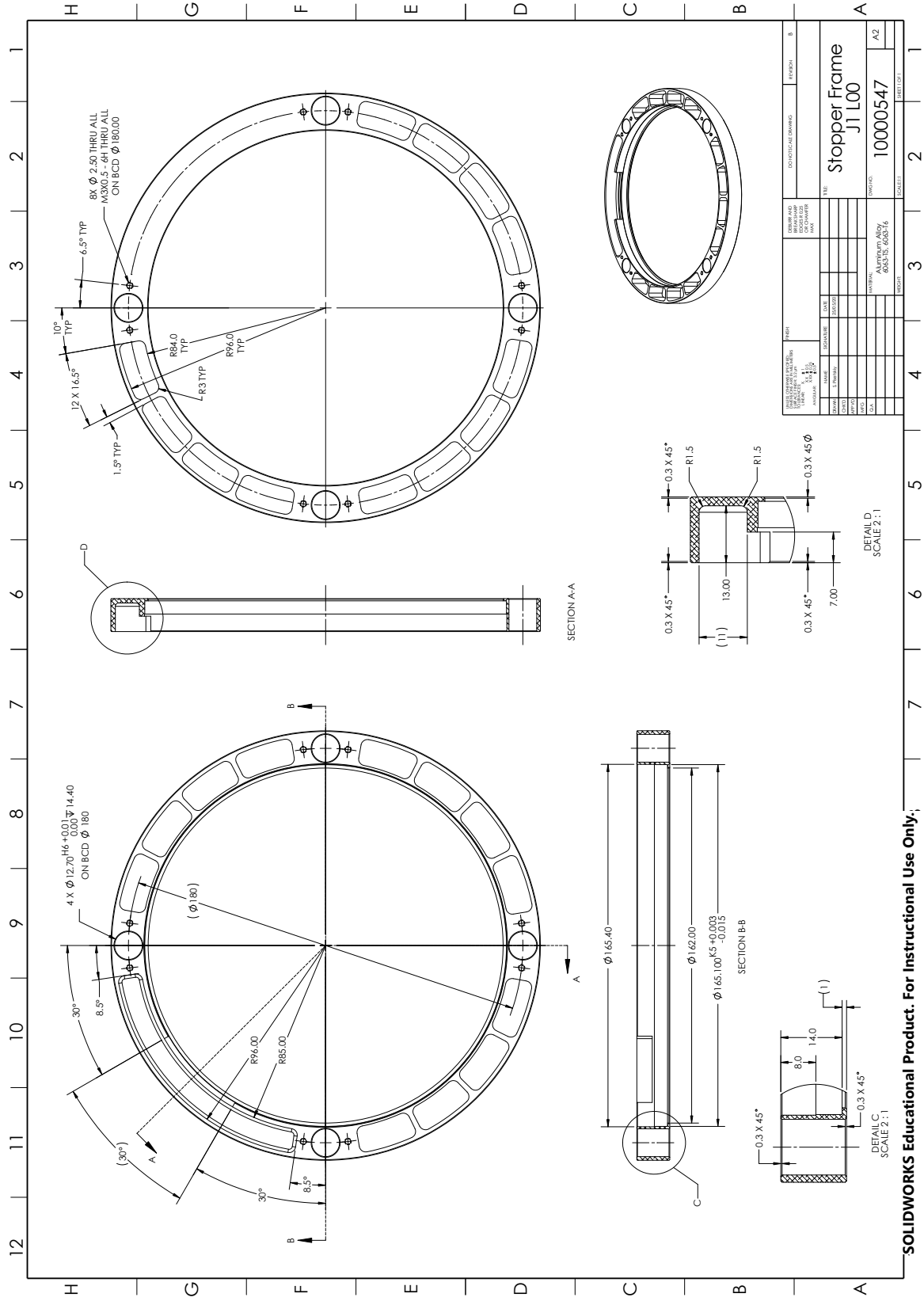
Figure B.99: Drawing: Joint 1 stopper frame.

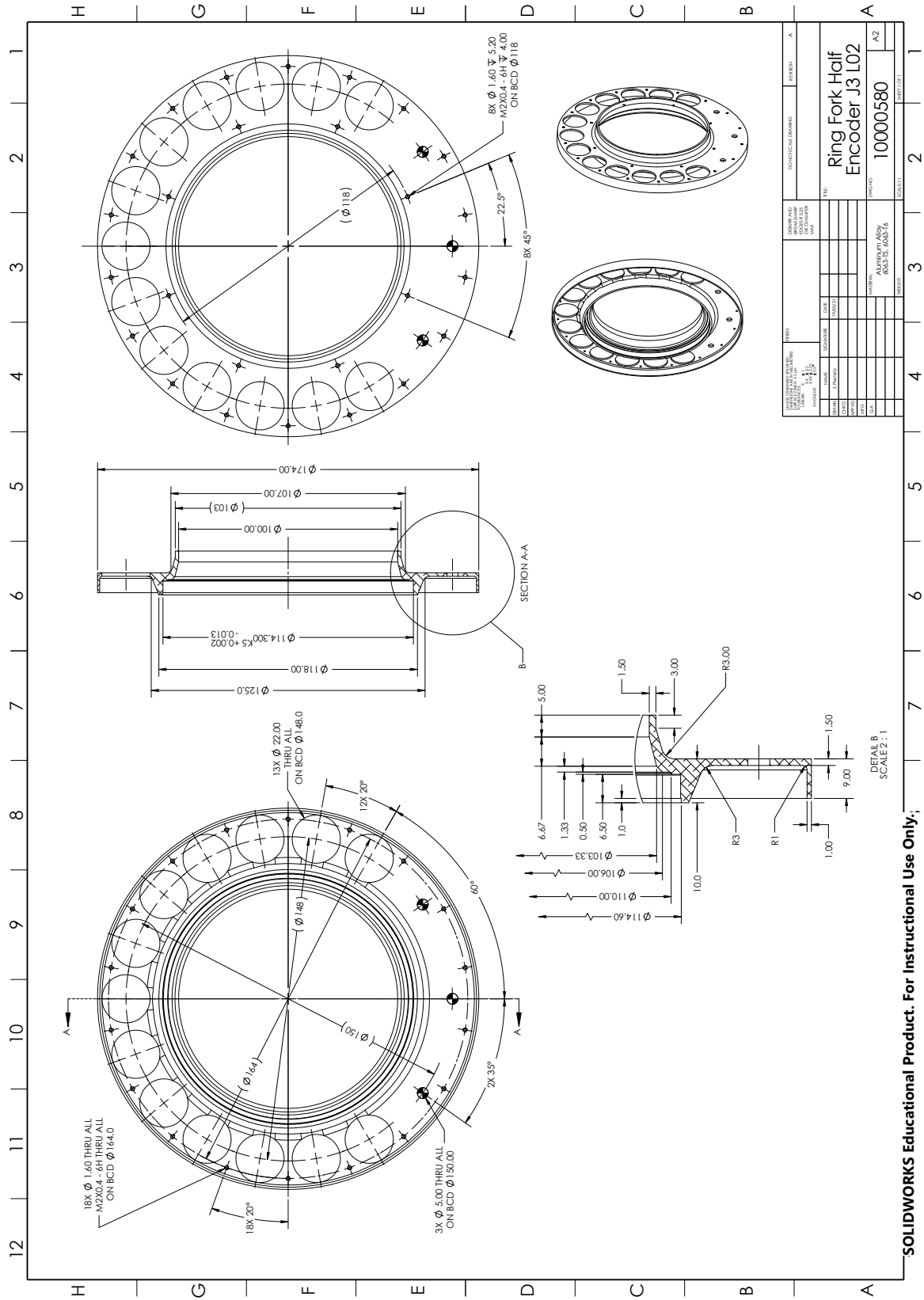Figure B.100: Drawing: Link 2 Joint 3 fork half ring.

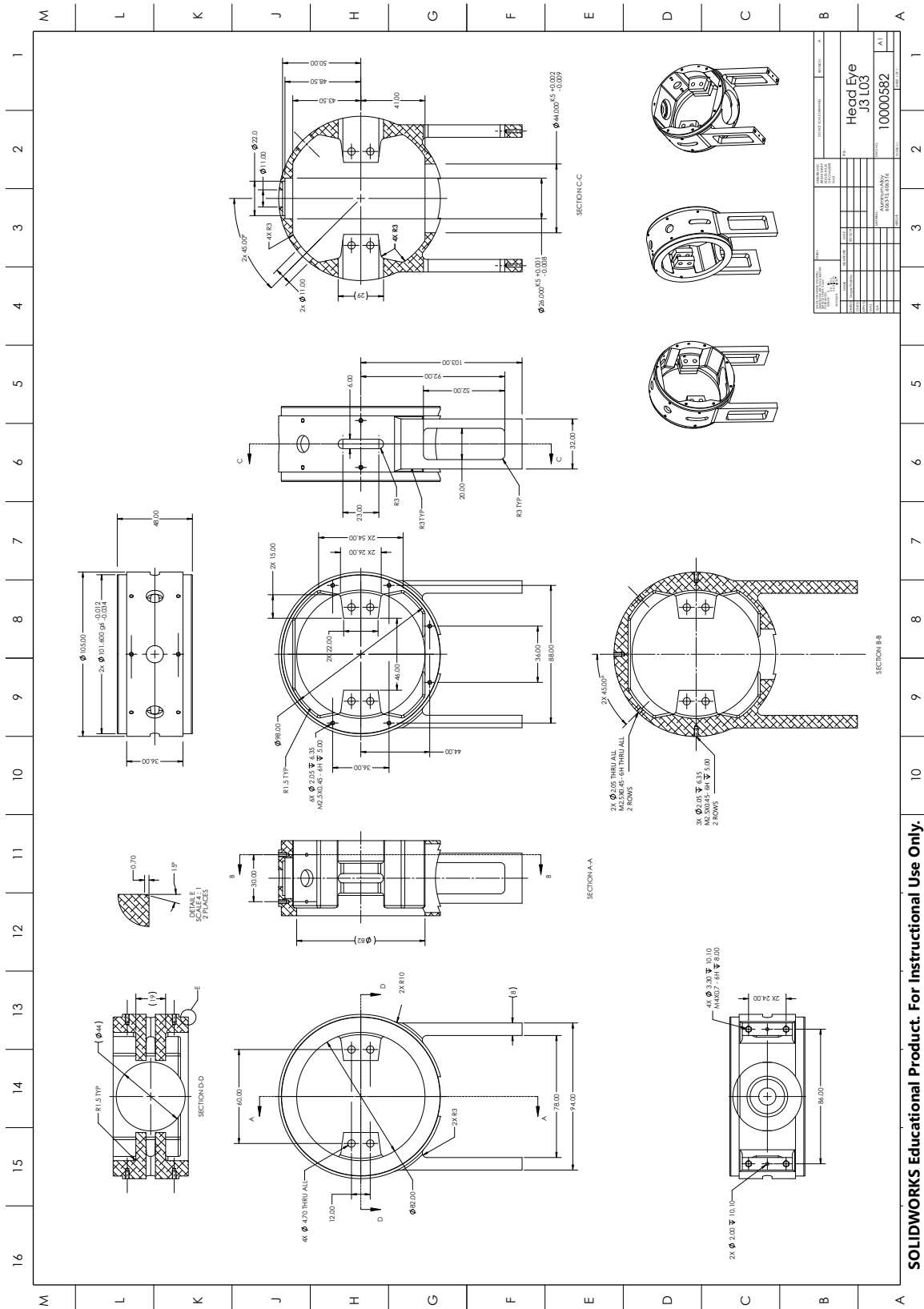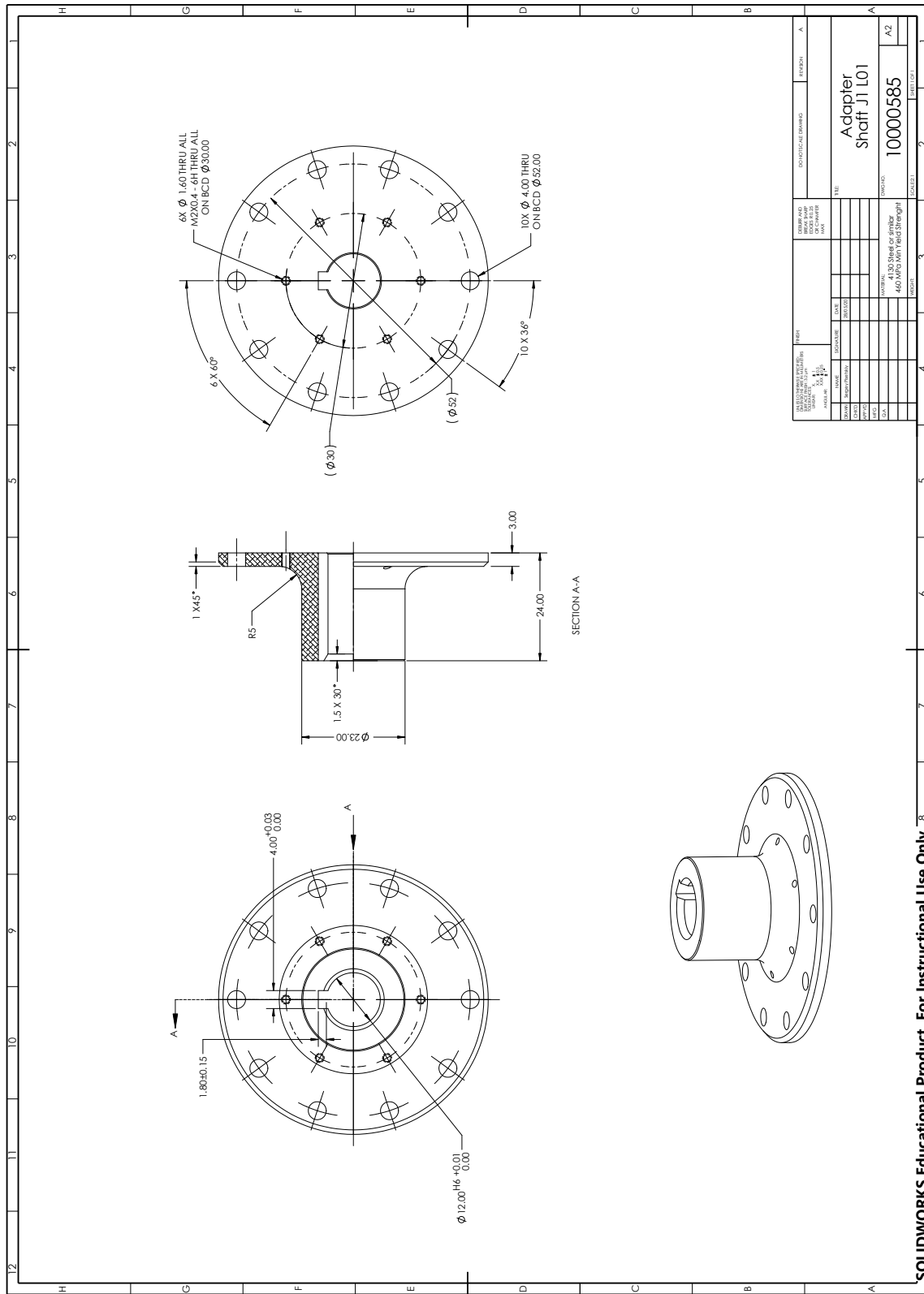Figure B.101: Drawing: Link 2 Joint 3 fork half encoder ring.

Figure B.102: Drawing: Link 3 Joint 3 head.

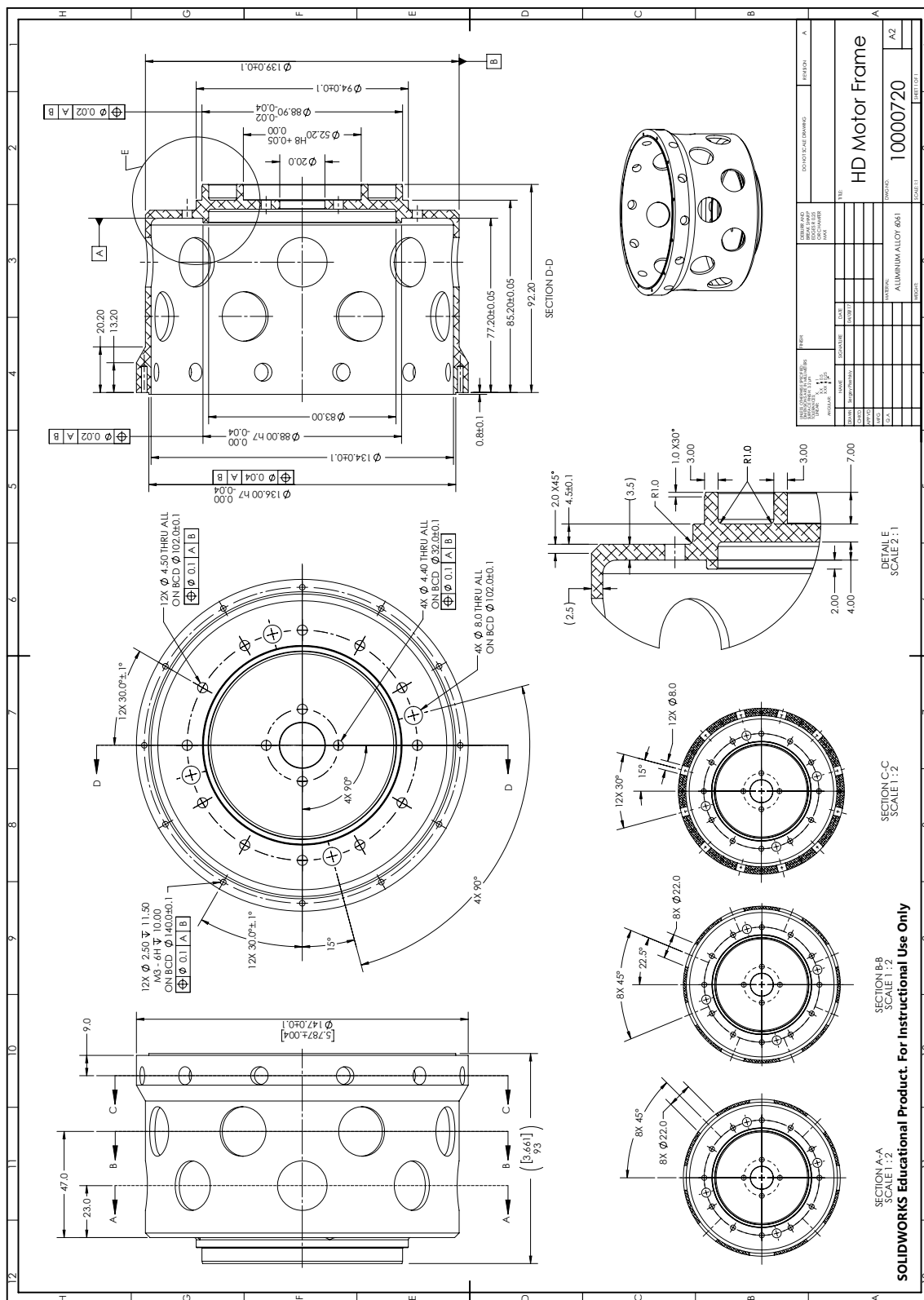Figure B.103: Drawing: Joint 1 shaft adapter.
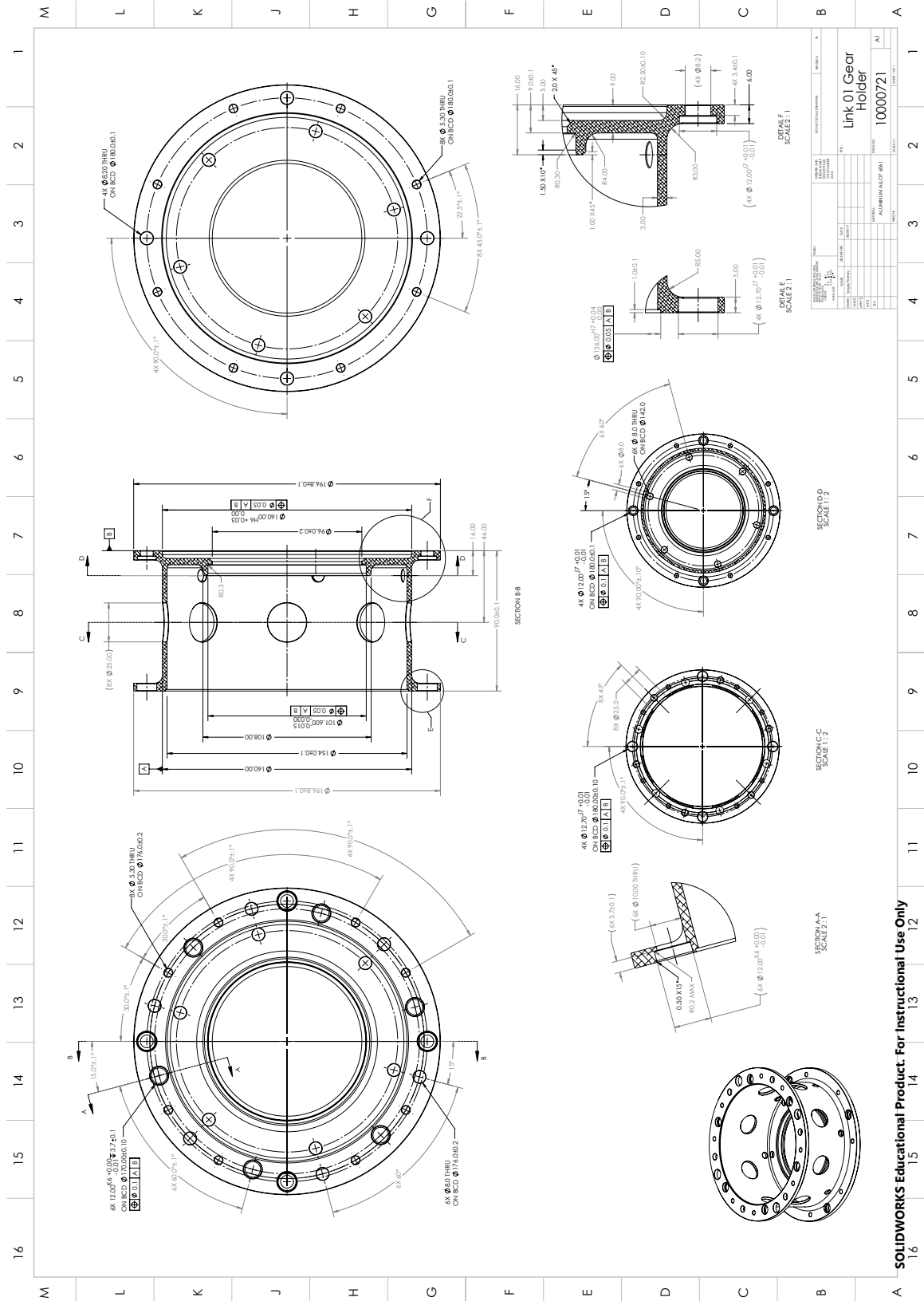
Figure B.104: Drawing: Link 1 HD motor frame.

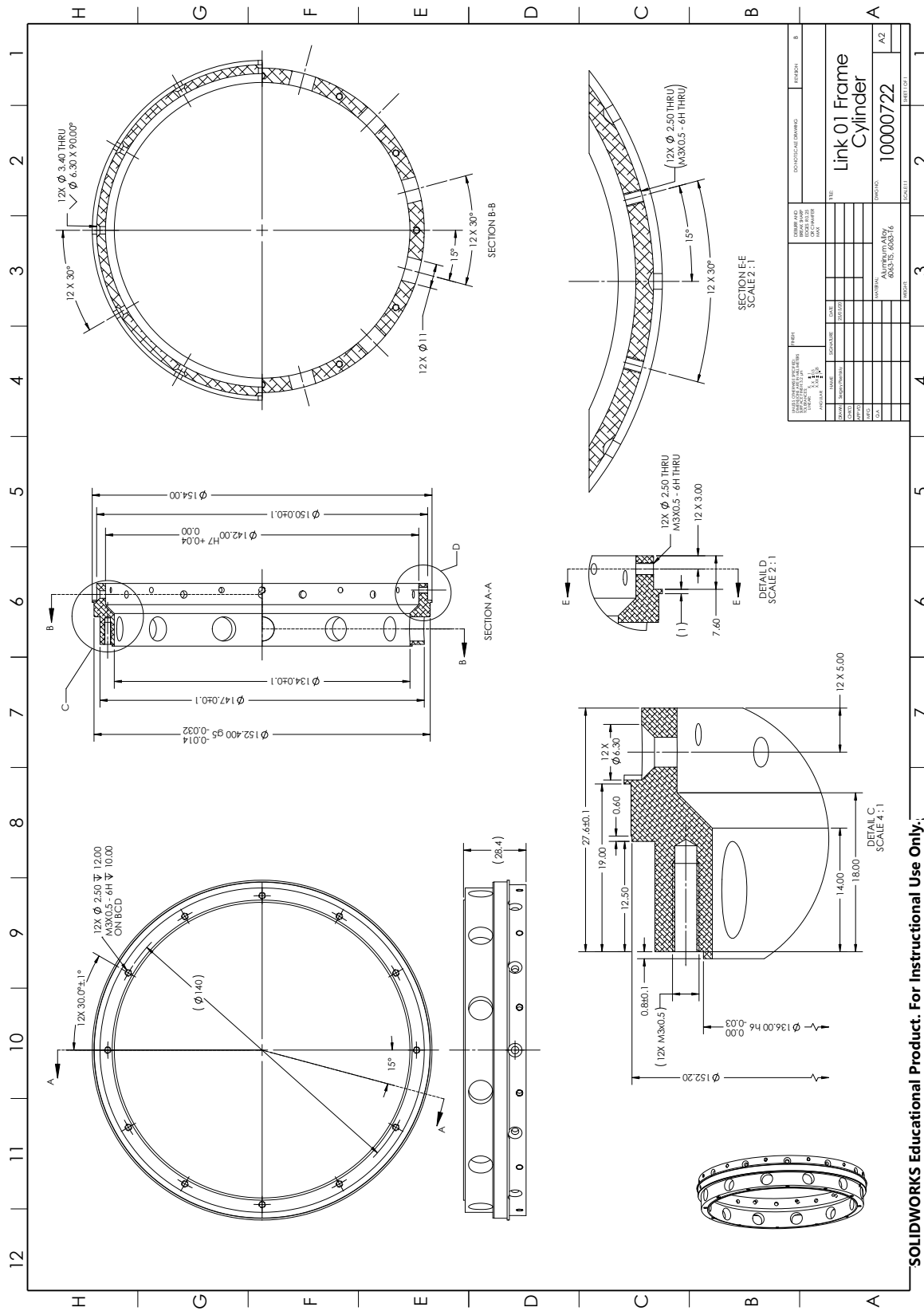Figure B.105: Drawing: Link 1 gear holder.

Figure B.106: Drawing: Link 1 frame cylinder.
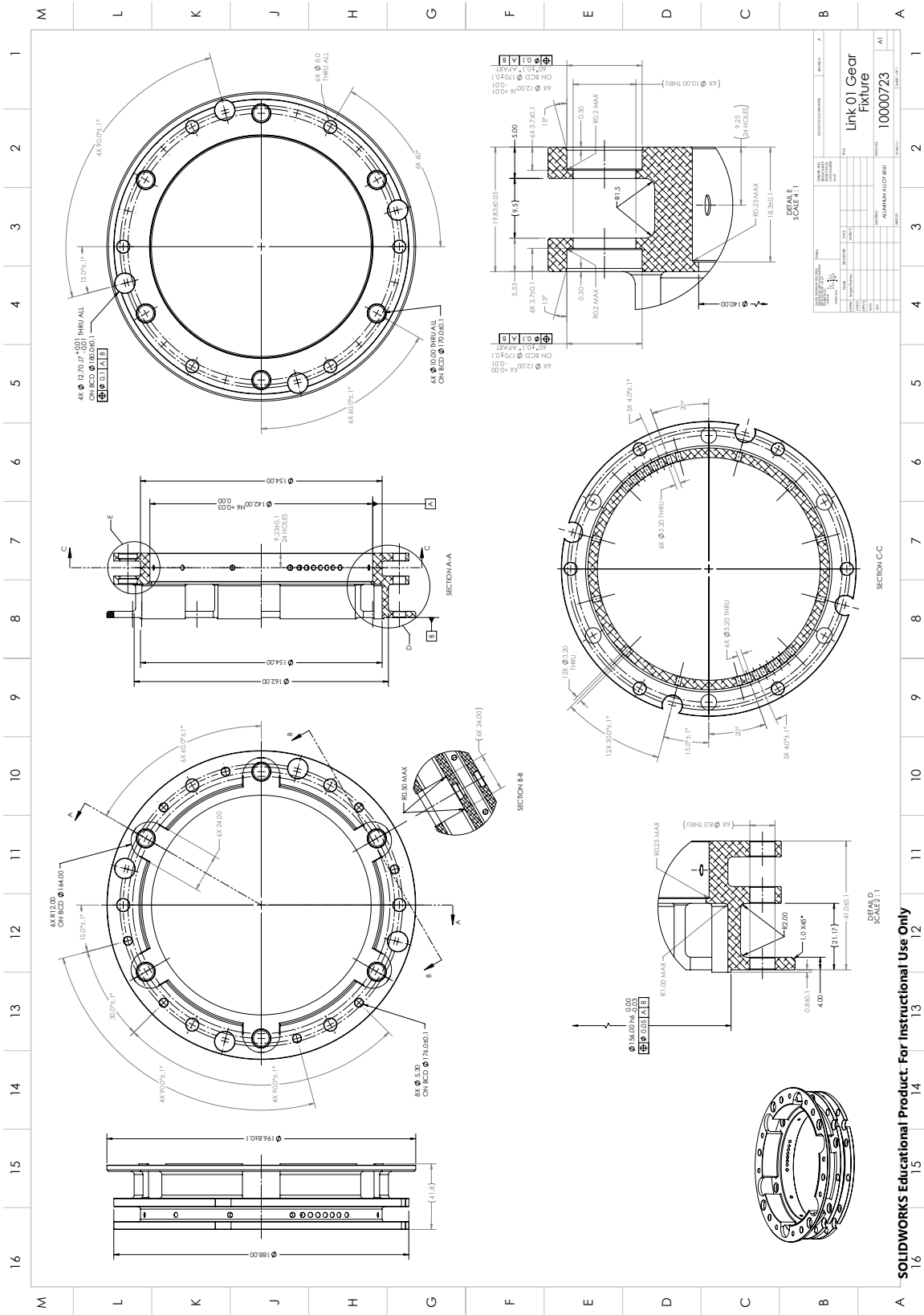
Figure B.107: Drawing: Link 1 gear fixture.

Appendix C

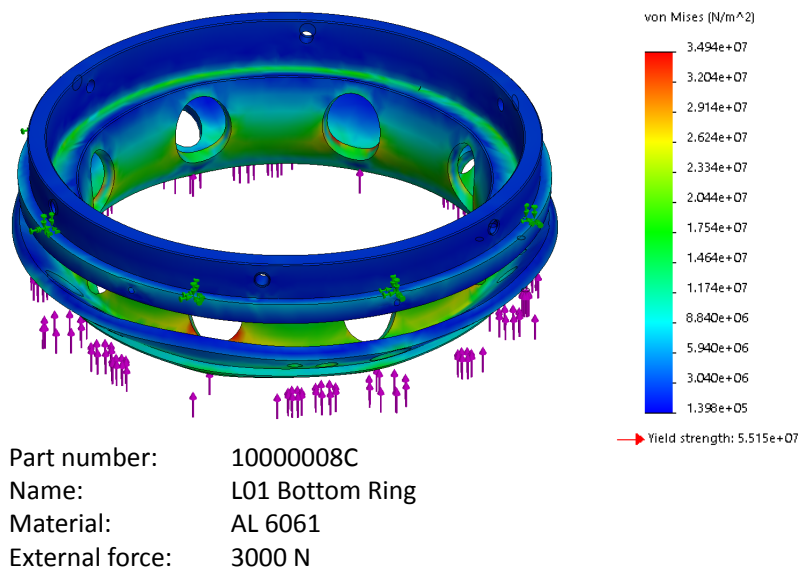# 5-DOF Manipulator components stress calculations

Part number: 10000008C
Name: L01 Bottom Ring
Material: AL 6061
External force: 3000 N

Figure C.1: Static stress simulation for Link 0 bottom ring: 3000 N external force.

Part number: 10000061B
Name: J1 HD Adapter
Material: AL 2024
External torque: 250 N·m
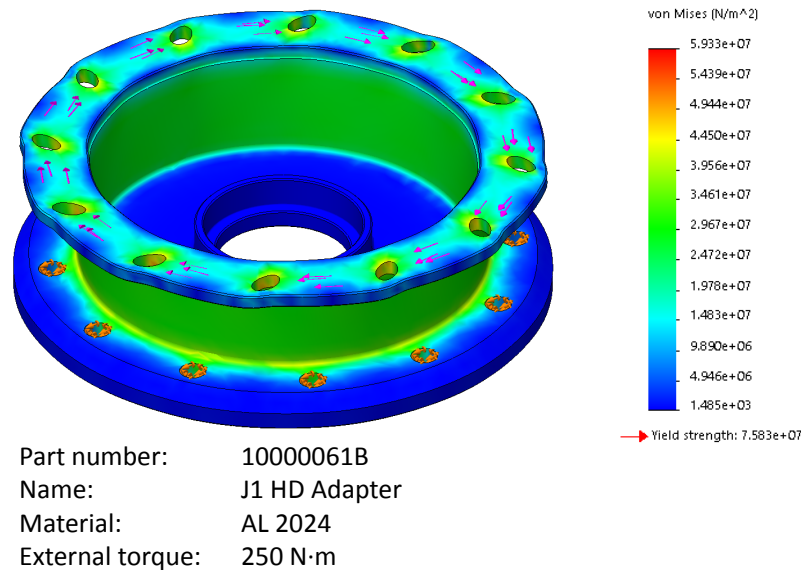
Figure C.2: Static stress simulation for joint 1 HD adapter: 250 N·m external torque.

Part number: 10000062C
Name: J1 MRC Adapter
Material: AL 2024
External torque: 200 N·m
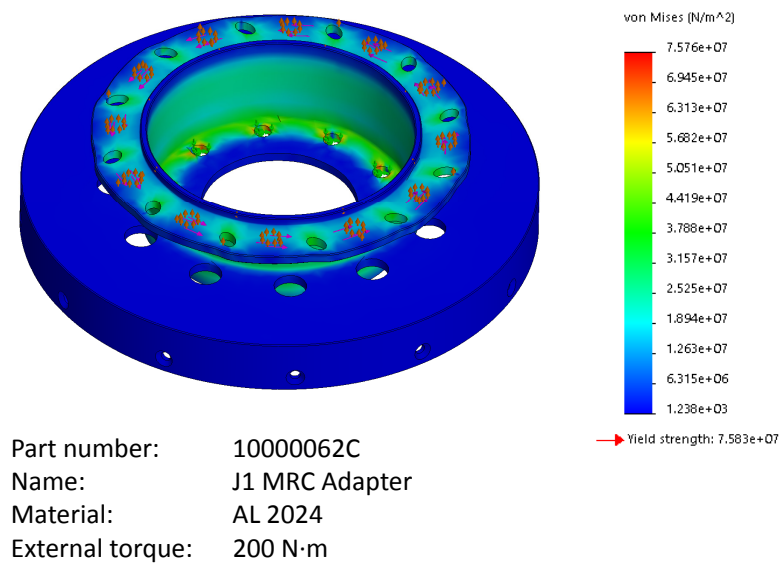
Figure C.3: Static stress simulation for joint 1 MR clutch adapter: 200 N·m external torque.

Part number:	10000074A
Name:	J1 Hollow Shaft
Material:	AL 2024-T37
External torque:	25 N·m
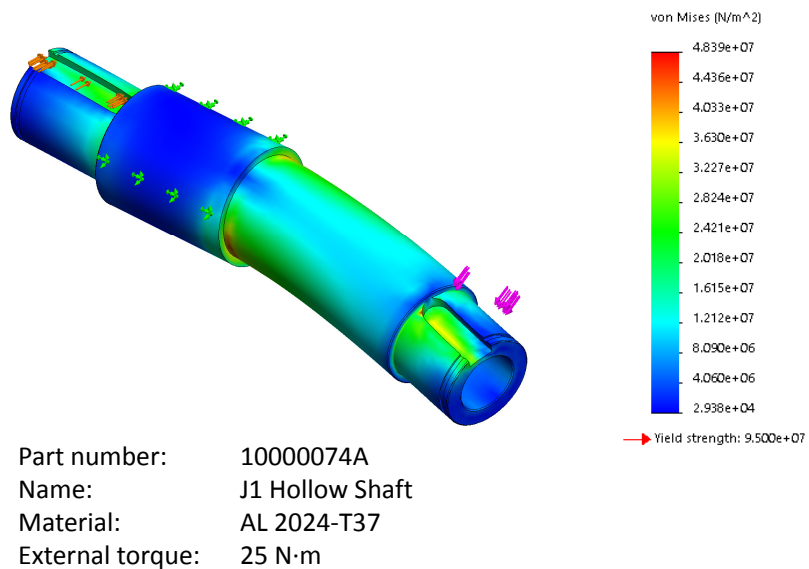
Figure C.4: Static stress simulation for joint 1 MR hollow shaft: 25 N·m external torque.

Part number:	10000077E
Name:	L02 Housing
Material:	AL 6061
External torque:	250 N·m
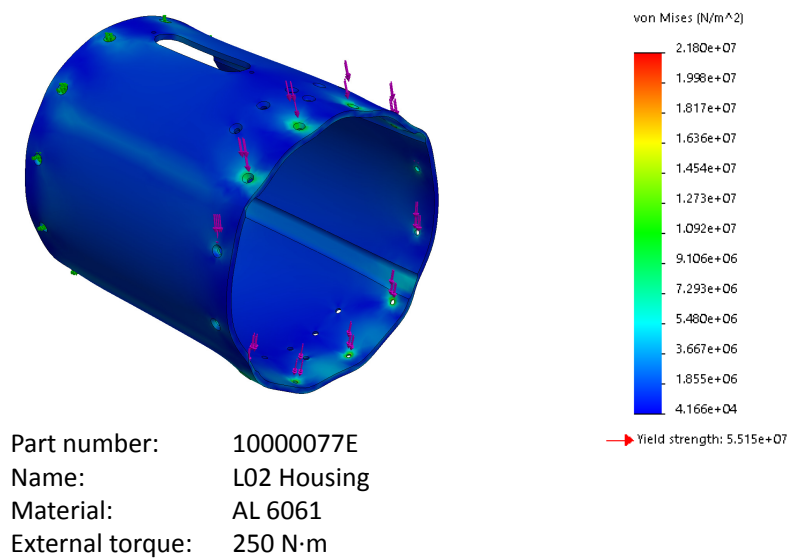
Figure C.5: Static stress simulation for link 1 housing: 250 N·m external torque.

Part number: 10000085C
Name: J3 Frame Shaft
Material: 7075-T6
External torque: 100 N·m
External force: 1500 N

Figure C.6: Static stress simulation for joint 3 frame shaft: 100 N·m external torque, 1500 N external force.

Part number: 10000516B
Name: J3 Transmission Disk
Material: AL 6061-T6
External torque: 100 N·m

Figure C.7: Static stress simulation for joint 3 transmission disk: 100 N·m external torque.

Part number: 10000530B
Name: J2 L02 Fork Half
Material: AL 6061-T6
External torque: 250 N·m
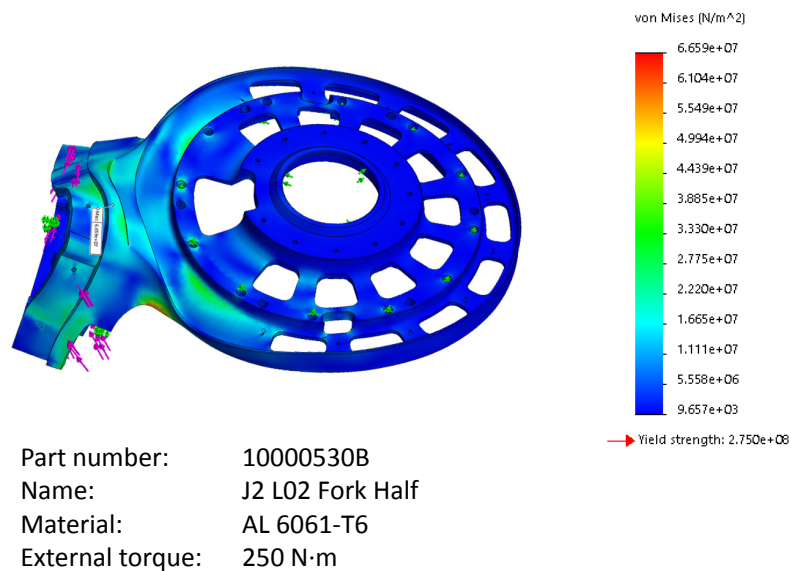
Figure C.8: Static stress simulation for link 2 joint 3 fork half: 250 N·m external torque.

Part number: 10000585A
Name: J1 Shaft Adapter
Material: 4130 Annealed
External torque: 200 N·m

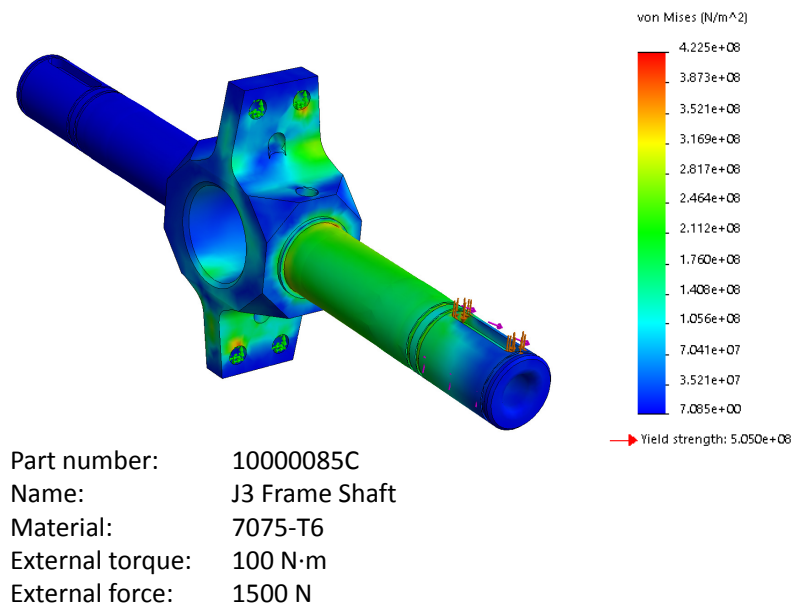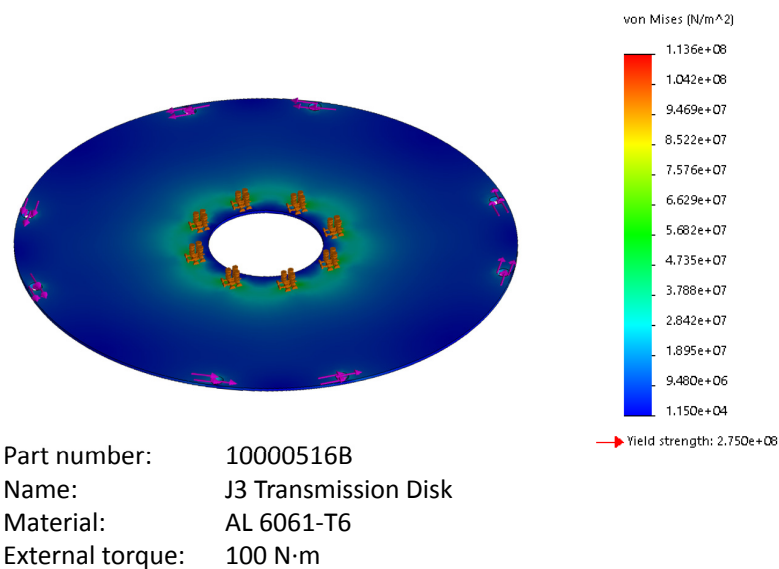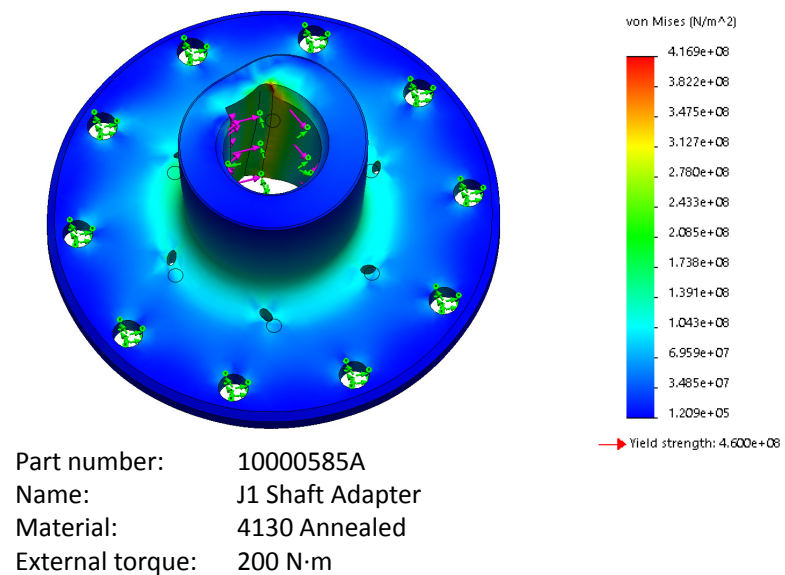Figure C.9: Static stress simulation for joint 1 shaft adapter: 200 N·m external torque.

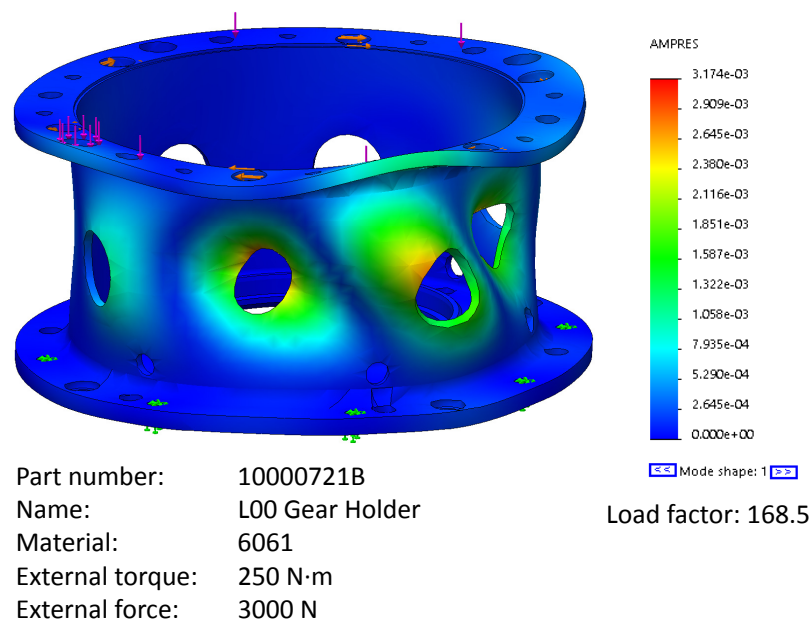| Part number: | 10000721B |
Name:	L00 Gear Holder
Material:	6061
External torque:	250 N·m
External force:	3000 N

Load factor: 168.5

Figure C.10: Buckling simulation for Link 0 gear holder: 3000 N·m external force and 250 N·m external torque.

Curriculum Vitae

Name:	Sergey Pisetskiy
Post-Secondary Education and Degrees:	University of Western Ontario London, Ontario, Canada Robotics and Control 2016 - 2021 Ph.D. Bauman Moscow State Technical University Rocket Engineering Moscow, Russia 1993-2000 M.Sc.
Related Work Experience:	Teaching Assistant The University of Western Ontario 2016 - 2020 New Product Development Engineer Schlumberger Technology Corporation 2006 - 2015 Aerospace Engineer Engineering Center Airbus Russia (ECAR) 2003 - 2006

Publications:

. **S. Pisetskiy** and M. R. Kermani, "Design and simulation of the first joint for a prospective 5degrees of freedom manipulator with MR actuators," in *The Canadian Society for Mechanical Engineering (CSME) International Congress.* CSME-SCGM, 2018.

   S. Pisetskiy and M. R. Kermani, "Compliant 5-DOF Robot: Mechanical Design," in *"Workshop on Physical human-robot interaction: a design focus" at "2019 International Conference on Robotics and Automation (ICRA),"* 2019.

S. Pisetskiy and M. R. Kermani, "Development of MR Clutch for a Prospective 5 DOF Robot," in *2018 IEEE/RSJ International Conference on Intelligent Robots and Systems (IROS)*. IEEE, 2018, pp. 5900-5905

S. Pisetskiy and M. R. Kermani, "A concept of a miniaturized MR clutch utilizing MR fluid in squeeze mode," in *2020 IEEE/RSJ International Conference on Intelligent Robots and Systems (IROS)*. IEEE, 2020, pp. 6347–6352.

S. Pisetskiy and M. R. Kermani, "High-performance magneto-rheological clutches for direct-drive actuation: Design and development," *Journal of Intelligent Material Systemsand Structures,* p. 1045389X211006902, 2021.